

2019-01-01

Shining Light On An Amygdala -- Brainstem Connection Important For Attention Processing

Jose Carlos Cano
University of Texas at El Paso

Follow this and additional works at: https://digitalcommons.utep.edu/open_etd



Part of the [Biology Commons](#), and the [Neuroscience and Neurobiology Commons](#)

Recommended Citation

Cano, Jose Carlos, "Shining Light On An Amygdala -- Brainstem Connection Important For Attention Processing" (2019). *Open Access Theses & Dissertations*. 2835.
https://digitalcommons.utep.edu/open_etd/2835

This is brought to you for free and open access by ScholarWorks@UTEP. It has been accepted for inclusion in Open Access Theses & Dissertations by an authorized administrator of ScholarWorks@UTEP. For more information, please contact lweber@utep.edu.

SHINING LIGHT ON AN AMYGDALA – BRAINSTEM CONNECTION
IMPORTANT FOR ATTENTION PROCESSING

JOSE CARLOS CANO

Doctoral Program in Biosciences

APPROVED:

Michael Kenney, Ph.D., Chair

Karine Fenelon, Ph.D., Co-chair

Arshad M. Khan, Ph.D.

Anita Quintana, Ph.D.

Edward Castaneda, Ph.D.

Stephen Crites, Ph.D.
Dean of the Graduate School

Copyright ©
by
Jose Carlos Cano
2019

Dedication

To the immaculate quintessence of maternal sacrifice, unwavering strength, devout
perseverance, and infinite love (B. R.).

To the bright muse ravaging with daily beautiful light the uncertainty of the future (O. S.).

Dedicatoria

A la inmaculada quintaesencia del sacrificio materno, la fuerza inquebrantable, la
perseverancia devota y el amor infinito (B. R.).

A la brillante musa que asola con hermosa luz diaria la incertidumbre del futuro (O. S.).

SHINING LIGHT ON AN AMYGDALA – BRAINSTEM CONNECTION IMPORTANT
FOR ATTENTION PROCESSING

by

JOSE CARLOS CANO, B.S.

DISSERTATION

Presented to the Faculty of the Graduate School of
The University of Texas at El Paso
in Partial Fulfillment
of the Requirements
for the Degree of

DOCTOR OF PHILOSOPHY

Department of Biological Sciences
THE UNIVERSITY OF TEXAS AT EL PASO
December 2019

Acknowledgements

There are three key people that guided me through the divine comedy of my Ph.D. odyssey. First, I cannot express the immense gratitude, respect and admiration I have for Dr. Joanne T. Ellzey, who gave me the opportunity and privilege to work in her Analytical Cytology Core Facility and to be in charge of her precious Zeiss EM-10. In there, I was constantly amazed by the unmatched magnificence and delicacy of electron microscopy. I greatly treasure Dr. Ellzey and Dr. Lawrence Ellzey, and their continuous support and motivation to pursue a Ph.D. degree. Dr. Arshad Khan, the embodiment of all mad scientists in cartoons and video games (except for the evil intentions). The motivation, ambition, joy and ideas that Dr. Khan emits in every conversation is mind-blowing, to the point that I picture myself picking pieces of my brain from the wall and floor after every conversation. I want to thank Dr. Khan for introducing me to Neuroscience, for the constant support, for the scientific input, and for being an unparalleled role model at UTEP. Then, to complete the Triforce was the young, driven, innovative and enthusiastic Dr. Karine Fenelon. I want to thank Dr. Fenelon for the opportunity to work under her mentorship, for always setting an example, for inviting me to Amherst to continue working on my research project, for helping my professional and scientific development, and for providing me with a unique opportunity to continue my career.

I especially want to thank Dr. Michael Kenney for taking over the time-consuming mentor responsibilities, for his experienced insight and for co-sponsoring the NIH grant! I want to thank my committee: Dr. Edward Castaneda, Dr. Anita Quintana and Dr. Kristin Gosselink (former advocate and author of extremely helpful committee meeting notes!) for their incredible support and scientific contribution. I greatly appreciate the of support

from Dr. Giulio Francia, Dr. Manuel Llano, Dr. Gosselink; and the support and input of Dr. Joseph A. Gogos and Dr. Amy MacDermott from Columbia University. I want to thank my comrades in research for sharing the joy and pain at UTEP: fellow “guinea pig” Andy (a.k.a. Sebastian), the always driven and intense L. Patricia, the fer-1 enthusiast V. Ines, the pokemon-master Eddie, the holiday enforcer Mireya, and Carla Loyola; the present labmates at UMass Amherst: Dr. Wan Yun Huang (and her never-ending questions that have made me a better mentor), Ernie, Erika, Bryan, Ethan and Brittany; Dr. Ellen Walker for the confocal microscopy mentoring, Ken Negishi for the mapping and Illustrator tutoring. I also want to commend the patch-clamp recording ‘deities’ for allowing me, after an initial frustrating semester, to ‘break the seal’ and achieve whole-cell recordings.

This journey would have been overwhelming without the support and love of my incredible family. I want to thank: Bertha Rodriguez, my mother and co-owner of this degree, for her unconditional love, sacrifice and prayers; my sister Susana for always being there to help me and discipline me to be better; my sister Vero for her mice drawings and graphic design skills, companionship, and along with my brother Omar and my nephew Jose Pablo, for the relaxing, yet thrilling and much-needed, video game Sundays; to all the “zarigüeyas” (Sofia, Mariana, Isabella, Valeria and Angel) for the joy you create with a single glance or a funny face. I want to thank Olga B. Soto for being my shelter in the many times of desperation, for always asking the questions I never thought of, and for the unwavering love and support through time and distance.

Abstract

We are continuously being exposed to an exorbitant amount of sensory information, which should result overwhelming. However, the nervous system operates several intrinsic sensory filtering mechanisms that allow us to cope with such sensory cluttering and shape appropriate behavior. Sensorimotor gating is a pre-attentive neuronal filtering mechanism that gates superfluous sensory information, and orients attentional resources towards salient information processing. Its relevance becomes in individuals suffering from schizophrenia and several otherwise unrelated neuropsychiatric disorders where sensorimotor gating is impaired. To understand the neural impaired mechanisms, extensive research studies have focused on first identifying the neural substrates underlying sensorimotor gating. This doctoral research project focuses on a connection, centrally located in the sensorimotor gating circuit, for its potential role in pre-attentive processing. In mice, we first characterized the neuroanatomy and neurochemistry of a connection from the central nucleus of the amygdala (CeA) to the caudal pontine reticular nucleus (PnC), at the core of the sensorimotor gating circuit. Secondly, we analyzed the synaptic properties of an excitatory subset of CeA-PnC synapses, and whether it modulates PnC activity *in vitro*. We then assessed the role of this connection in sensorimotor gating *in vivo*. Lastly, to provide a mechanistic basis for the role of this excitatory connection in an inhibitory mechanism, we investigated the identity of the PnC components receiving CeA excitatory inputs. Results from this dissertation research project contribute to the knowledge of the neural substrates underlying sensorimotor gating. Ultimately, a better insight on this matter might reveal potential therapeutic targets to be tested in models of diseases associated with sensorimotor gating deficits.

Table of Contents

Acknowledgements	v
Abstract.....	vii
Table of Contents.....	viii
List of Tables.....	xii
List of Figures.....	xiii
Abbreviations	xv
Prologue.....	xx
Chapter 1: Introduction.....	1
1.1 Sensorimotor gating	1
1.1.2 The relevance of sensorimotor gating	2
1.2 The startle reflex	4
1.2.1 Neural basis of the acoustic startle reflex	6
1.2.2 Plasticity of the startle reflex: a tool to evaluate sensory information processing.....	10
1.2.2.1 Habituation and sensitization	10
1.3 Prepulse inhibition: the gold standard of sensorimotor gating	13
1.3.1 The prepulse inhibition of the acoustic startle reflex paradigm	14
1.3.2 A clinical and experimental tool	19
1.3.2.1 Schizophrenia.....	20
1.3.2.2 Other neuropsychiatric disorders	23
1.3.3 Neural basis of PPI.....	26
1.3.3.1 PPTg: the dogmatic substrate mediating PPI	26
1.3.3.2 CSPP network modulating PPI	30
1.4 Enter: the central nucleus of the amygdala (CeA)	32
1.4.1 Neuronal architecture of the CeA	32
1.4.2 CeM: output station of the amygdalar complex.....	34
1.4.3 CeA-PnC connection	35
1.5 Hypothesis	38
1.6 Specific Aims.....	39

Chapter 2: Methodology	40
2.1 Subjects	40
2.2 Tissue preparation for transmission electron microscopy.....	40
2.3 Neuronal tract-tracers and viral vectors.....	41
2.4 Stereotaxic Injections	42
2.5 Tissue preparation for immunohistochemistry/microscopy analysis	44
2.6 Immunohistochemistry	44
2.7 Nissl staining	45
2.8 Tissue preparation for extracellular field recordings	46
2.9 Tissue preparation for whole-cell recordings	48
2.10 Extracellular field recordings	49
2.10.1 Light-evoked fEPSPs at the PnC.....	49
2.10.2 Application of glutamate receptor antagonists	49
2.10.3 Electrical stimulation of auditory fibers	50
2.10.4 In vitro PPI.....	51
2.10.5 Presynaptic contribution of CeA inputs to Cochlear fibers in the PnC .	51
2.11 Whole-cell recordings	51
2.11.1 vHPC recordings	52
2.11.2 PnC and CeA recordings.....	52
2.12 Acute brain slice preparation for microscopy analysis	53
2.13 Behavioral testing	54
2.13.1 Animal cohorts.....	54
2.13.2 Cannula guide implantation	54
2.13.3 Behavioral testing setup	55
2.13.4 ASR task	56
2.13.5 PPI task	56
2.14 Microscopy.....	57
2.14.1 Transmission electron microscopy	57
2.14.2 Fluorescence microscopy	57
2.14.3 Laser scanning confocal microscopy	57
2.15 Data analysis	58
2.15.1 Tract-tracing and immunohistochemistry analyses.....	59
2.15.2 Electrophysiological recordings analysis	59

2.15.3 Behavioral testing data analysis	60
Chapter 3: Results.....	62
3.1 Dissecting the anatomical and neurochemical profile of a central amygdalar input to the core of sensorimotor gating	62
3.1.1 PnC receives direct anatomical CeA input: a retrograde tracing analysis	62
3.1.2 CamKII α CeA neurons project to the PnC: an anterograde tracing approach	63
3.1.3 Neurochemistry of CamKII α -dependent CeA-PnC synapses	68
3.2 Characterization of CeA-PnC synapses and their contribution to an in vitro version of the prepulse inhibition task	73
3.2.1 An ultrastructural analysis of synapses in the PnC.....	73
3.2.2 Physiological properties of CeA-PnC excitatory synapses ...	78
3.2.3 Excitatory CeA input regulates PnC activity in vitro	78
3.3 Optogenetic manipulation of the CeA-PnC excitatory pathway during PPI in vivo: mimicking a sensorimotor gating deficit?	84
3.3.1 Excitatory CeA-PnC connection does not alter basal ASR... ..	84
3.3.2 Excitatory CeA input to the PnC contributes to PPI	88
3.4 Unraveling the identity of the PnC cells receiving CeA excitatory inputs.....	93
3.4.1 Distribution of GlyT2+ neurons in the PnC: a mapping analysis.....	93
3.4.2 A PPI-relevant neurochemical profile of PnC GlyT2+ neurons	94
3.4.3 Putative synaptic contacts: Imaging CamKII α CeA fibers on PnC GlyT2 neurons.....	101
3.4.4 CamKII α CeA input activates PnC GlyT2 cells	101
Chapter 4: Discussion	114
4.1 Neuroanatomy and neurochemistry of an excitatory CeA-PnC connection... ..	115
4.2 Synaptic properties of CeA-PnC connection and their relevance to sensorimotor gating.....	117
4.3 CeA-PnC connection as a gating substrate.....	119
4.3.1 Presynaptic filtering	119
4.3.2 Post-synaptic gating	120
4.4 Proposed amygdalar control underlying sensorimotor gating.....	125
4.5 Methodological considerations	127
4.6 Future directions	130

References.....	133
Appendix	170
Vita.....	187

List of Tables

Table 2.1: Viral vectors and tracer dyes for optogenetics and tract-tracing.....	43
Table 2.2: Antibodies for immunohistochemistry.....	46
Table 2.3: Nissl staining protocol	47
Table 2.4: Receptor blockers used during electrophysiological recordings.....	50
Table 3.1: Passive membrane properties of PnC GlyT2+ cells.	106

List of Figures

Figure 1.1: The primary ASR and PPI pathways.....	12
Figure 1.2: Prepulse inhibition of the startle reflex task.....	17
Figure 1.3: The PPI neural network.....	31
Figure 3.1: The PnC receives monosynaptic projections from the CeA..	64
Figure 3.2: Sample FluoroGold injections represented on PnC anatomical levels.	65
Figure 3.3: PnC receives cholinergic and non-cholinergic inputs from the PPTg	66
Figure 3.4: CeA sends direct CamKII α -dependent axonal projections to the PnC	67
Figure 3.5: CamKII α -expressing cell bodies in the medial CeA.....	68
Figure 3.6: Sample AAV injections represented on CeA anatomical levels.....	69
Figure 3.7: PnC-projecting neurons in the CeA are not cholinergic.....	70
Figure 3.8: CamKII α -eYFP CeA fibers projecting to the PnC are not GABAergic	71
Figure 3.9: CeA projections activate ionotropic glutamate receptors in the PnC.....	72
Figure 3.10: Ultrastructure of PnC synapses.....	74-77
Figure 3.11: Basal transmission and plasticity of CeA-PnC excitatory synapses	79
Figure 3.12: Electrical stimulation of auditory fibers elicit fEPSPs in the PnC	80
Figure 3.13: Excitatory CeA input to the PnC contributes to PPI <i>in vitro</i>	81
Figure 3.14: CeA inputs do not inhibit vesicle release from auditory fibers in the PnC .	83
Figure 3.15: Optogenetic manipulation of CeA-PnC during behavioral testing.....	84
Figure 3.16: Rep. PnC coronal sections with lesions from optic fiber implants	85
Figure 3.17: Arch3.0 photoinhibition of CeA-PnC synapses reduces PPI <i>in vivo</i>	86
Figure 3.18: NpHR3.0 photoinhibition of CeA-PnC synapses reduces PPI <i>in vivo</i>	87
Figure 3.19: Photostimulation of CeA-PnC synapses as a prepulse elicits a PPI effect	88

Figure 3.20: NpHR3.0 photoinhibition of hippocampal neurons	90
Figure 3.21: Photostimulation of CeA-PnC synapses does not potentiate acoustic PPI	92
Figure 3.22: Distribution of GlyT2+ interneurons in the PnC and adjacent regions ..	95-98
Figure 3.23: PnC GlyT2+ interneurons express PSD-95.....	99
Figure 3.24: PnC GlyT2+ interneurons express PV and PRODH.....	100
Figure 3.25: Putative synaptic app. between CeA fibers and PnC interneurons ..	102-104
Figure 3.26: Imaging analysis of a putative CeA-PnC synaptic contact	105
Figure 3.27: Strategy for whole-cell patch-clamp recordings of PnC GlyT2 neurons ..	107
Figure 3.28: sEPSC and IPSC amplitude distribution of PnC GlyT2 interneurons	108
Figure 3.29: Light responsive and unresponsive cells display similar spiking activity .	109
Figure 3.30: Spatial-dependent light-evoked activity of PnC GlyT2 interneurons.....	110
Figure 3.31: Light-evoked activity of PnC GlyT2 interneurons	111
Figure 3.32: CeA excitatory inputs act. ionotropic receptors on GlyT2 interneurons...	112
Figure 3.33: sEPSCs, spiking and light-evoked activity of CeA CamKII α cells.....	113
Figure 4.1 Proposed parallel amygdalar pathways regulating ASR and PPI	126

Abbreviations

6N	abducens nucleus
7n	facial nerve or its root
AAV-DJ	adeno-associated virus serotype DJ
Arch3.0	archaerhodopsin
AMPA	α -amino-3-hydroxyl-5-methyl-4-isoxazolepropionic acid
AP5	(2R)-amino-5-phosphonovaleric acid
ASR	acoustic startle reflex
au	arbitrary units
BLA	basolateral amygdaloid nucleus, anterior part
BSTIA	bed nucleus of the stria terminalis, intra-amygdaloid division
CamKII α	calcium/calmodulin-dependent protein kinase II alpha
cc	corpus callosum
CeA	central amygdaloid nucleus
CGPn	central gray of the pons
ChAT	choline acetyltransferase
ChR2	channelrhodopsin-2
CN	cochlear nuclei
CNQX	6-cyano-7-nitroquinoxaline-2,3-dione
CPu	caudate putamen
CRNs	cochlear root neurons
DEn	dorsal endopiriform nucleus
DPO	dorsal periolivary region

eGFP	enhanced green fluorescent protein
EPSC	excitatory post-synaptic current
EPSP	excitatory post-synaptic potential
EVe	nucleus of origin of efferents fibers of the vestibular nerve
eYFP	enhanced yellow fluorescent protein
fEPSP	field excitatory post-synaptic potential
GABA	gamma-aminobutyric acid
GiA	gigantocellular reticular nucleus, alpha part
GlyT2	glycine transporter 2
HPC	hippocampus
I	intercalated nuclei of the amygdala
IC	inferior colliculus
ic	internal capsule
IPSC	inhibitory post-synaptic current
IPSP	inhibitory post-synaptic potential
ISI	interstimulus interval
IRt	intermediate reticular nucleus
ITI	intertrial interval
LADL	lateral amygdaloid nucleus, dorsolateral part
LAVL	lateral amygdaloid nucleus, ventrolateral part
LC	locus coeruleus
LGP	lateral globus pallidus
LPBC	lateral parabrachial nucleus, central part

LPBV	lateral parabrachial nucleus, ventral part
LSO	lateral superior olive
LV	lateral ventricle
LVPO	lateroventral periolivary nucleus
MePD	medial amygdaloid nucleus, posterodorsal part
MePV	medial amygdaloid nucleus, posteroventral part
MGP	medial globus pallidus
Mlf	medial longitudinal fasciculus
MPB	medial parabrachial nucleus
MPBE	medial parabrachial nucleus, external part
mPFC	medial prefrontal cortex
Mve	medial vestibular nucleus
MveMC	medial vestibular nucleus, magnocellular part
MvePC	medial vestibular nucleus, parvicellular part
MVPO	medioventral periolivary nucleus
NAcc	nucleus accumbens
NMDA	N-methyl-D-aspartate
NMDAR	NMDA receptor
NpHR3.0	halorhodopsin
Ocb	olivocochlear bundle
opt	optic tract
Pa6n	paraabducens nucleus
PCRtA	parvicellular reticular nucleus, alpha part

Pir	piriform cortex
PnC	caudal pontine reticular nucleus
PnO	oral pontine reticular nucleus
PPD	paired-pulse depression
PPF	paired-pulse facilitation
PPI	prepulse inhibition
PPR	paired pulse ratio
PPTg	pedunculopontine tegmental nucleus
Pr5DM	principal sensory trigeminal nucleus, dorsomedial part
Pr5VL	principal sensory trigeminal nucleus, ventrolateral part
PRh	perirhinal cortex
PRODH	proline dehydrogenase
PSD95	post-synaptic density protein 95
PV	parvalbumin
rlu	relative light units
RMg	raphe magnus nucleus
RtTg	reticulotegmental nucleus of the pons
SC	superior colliculus
scp	superior cerebellar peduncle (brachium conjunctivum)
SN	substantia nigra
SPO	superior paraolivary nucleus
sox	supraoptic decussation
st	stria terminalis

SuVe	superior vestibular nucleus
TBS	Tris-buffered saline
Tz	nucleus of the trapezoid body
VEn	ventral endopiriform nucleus
vHPC	ventral hippocampus
VP	ventral pallidum
VTA	ventral tegmental area

Prologue

The purpose of this dissertation is to outline an original investigation focused on the role of an unexplored neural substrate in the context of sensorimotor gating. The results from this dissertation will contribute to the knowledge of neural network underlying pre-attentive processing mechanisms. The multi-scale study presented here was performed on a wild-type mouse strain (C57BL/6J), and two C57BL/6J transgenic mouse strains. Compelling evidence shows that mice exhibit prepulse inhibition (PPI) of the startle reflex, the operational measure of sensorimotor gating, and have identified key brain regions anatomically and functionally homologous to human brain regions. In light of this, the work presented here postulates a novel neural substrate of sensorimotor gating in mice, and provides a methodology blueprint that can be applied to experimental systems of neuropsychiatric disorders associated with sensorimotor gating deficits.

Chapter 1 introduces sensorimotor gating, the spectrum of neurological diseases associated with sensorimotor gating and the impact of its clinical relevance. This section then delves into the extensive research on the neural network underlying PPI, under normal and pathological conditions. In an attempt to contribute to these research efforts, this section then focuses on a connection centrally located in the sensorimotor gating pathway, presents the hypothesis, and outlines the specific aims. **Chapter 2** describes the techniques and approaches used to address the specific aims. **Chapter 3** presents the results for each specific aim. In **Chapter 4**, results are summarized, interpreted and placed into the context of sensorimotor gating and other gating mechanisms responsible for integration of sensory information. In this section, methodological considerations, alternatives and future directions for this project are discussed.

Chapter 1: Introduction

On a daily basis, we are continuously bombarded by an immense stream of multimodal (e.g. acoustic, tactile, visual, vestibular, etc.) sensory information. Through several physiological mechanisms, the nervous system efficiently gates excessive and redundant sensory input, integrates salient information, and shapes behavior. At the periphery, gating starts with sensory receptors that adjust in response to excessive sensory stimuli, and reduce the load of information conveyed to the central nervous system. On the opposite end, higher cognitive centers integrate salient information, generate perception and regulate attention, which can be controlled to focus on or ignore sensory stimuli. However, the majority of sensory input is thought to be gated by inbuilt mechanisms along the sensory information processing pathway, that is, between the peripheral sensory receptors and cognition centers. In fact, attention hinges on the autonomic ability to properly filter out sensory information. In this manner, higher cognitive centers responsible for attention are relieved from an excess of sensory stimuli, and solely focus on salient information processing. One of these autonomic and intrinsic mechanisms is denominated sensorimotor gating.

1.1 Sensorimotor gating

Sensorimotor gating refers to a continuously active neuronal filtering process that suppresses irrelevant sensory information. In doing so, sensorimotor gating prevents a sensory overload, conveys only salient sensory information to higher cognitive centers, and orients attention towards salient stimuli for further processing (Graham, 1975). Sensorimotor gating employs central, inbuilt, and inhibitory mechanisms that require no

conscious effort to be operated. Since it precedes the conscious effort of focusing attention, sensorimotor gating is categorized as a pre-attentive processing mechanism (Swerdlow *et al.*, 1999).

1.1.2 The relevance of sensorimotor gating

Essential to allocate attention, the significance of sensorimotor gating becomes more evident in individuals exhibiting impairments in this mechanism. In a seminal study by Braff and colleagues (1978), authors documented for the first time impaired sensorimotor gating in patients diagnosed with schizophrenia. These deficits reflected their inability to properly filter out unnecessary sensory information, and being easily overwhelmed by a sensory cluttered environment (Braff *et al.*, 1978; Dawson *et al.*, 1993). Such deficient processing of sensory information compromises their attentional resources, which significantly impacts their daily activities, such as social insertion, academic success and work performance. Since then, deficient sensorimotor gating has been established as a hallmark of schizophrenia. The splitting of the mind, etymology of schizophrenia, is greatly attributed to the abundant and bombarding 'noise' commonly described by patients suffering from schizophrenia, which reflects impaired inhibitory mechanisms (i.e. sensorimotor gating; Dawson *et al.*, 1993). In addition, sensorimotor gating deficits have also been documented in several neurological and neuropsychiatric disorders, such as Huntington's disease (HD), Gilles de la Tourette's syndrome (TS), autism spectrum disorders (ASD), obsessive compulsive disorder (OCD), post-traumatic stress disorder (PTSD), substance abuse and bipolar disorder with manic symptoms (Ahmari *et al.*, 2012; Ahmari and Dougherty, 2015; Cavanna *et al.*, 2017; Dawson *et al.*, 1993; Hoenig *et al.*, 2005; Holstein *et al.*, 2013; Swerdlow *et al.*, 1995; Swerdlow, 2013; Zebardast *et al.*,

2013). Although still debated, decreased sensorimotor gating has also been observed in major depressive disorder (MDD) and generalized anxiety disorders (Kohl *et al.*, 2013; Ludewig *et al.*, 2002; Ludewig *et al.*, 2003). In these disorders, impaired sensorimotor gating is associated with the disruption of cognitive processes. In fact, the impaired inhibition of sensory information is thought to result in a sensory overload of neocortical regions, which then contributes to the development of several symptoms, such as delusions, hallucinations, tics, obsessions and compulsions (Dawson *et al.*, 1993; Hoenig *et al.*, 2005; Javanbakht, 2006; Mena *et al.*, 2016; Swerdlow *et al.*, 1993).

The relatively low incidence of schizophrenia (affecting 21 million persons worldwide, and 4 million in the United States) and other neuropsychiatric diseases results in a perplexing economic burden, estimated at 63 billion per year just in the U.S. (Chong *et al.*, 2016; Cloutier *et al.*, 2016; GBD, 2017; Wu *et al.*, 2006). Several factors beyond direct healthcare are likely to contribute to the disproportionately high economic burden of schizophrenia. For instance, the early onset of the treatable, but persisting, symptoms of schizophrenia (Mena *et al.*, 2016). Remarkably, up to one-half of all homeless adults suffer from schizophrenia. These individuals end up homeless due to the high healthcare expenses, inaccurate diagnosis and treatment, social stigma, and the symptomatology of schizophrenia (Desai *et al.*, 2013a; Desai *et al.*, 2013b). This results in loss of productivity, and increased social welfare and law enforcement costs. Additionally, 50% of people diagnosed with schizophrenia are concomitantly afflicted by other neuropsychiatric disorder, which add up to the indirect costs. OCD, PTSD, MDD and substance abuse are the major co-morbid disorders associated with schizophrenia (GBD, 2017; NAMI, 2019; Tsai *et al.*, 2013). Interestingly, sensorimotor gating deficits are the common denominator

among all these, otherwise unrelated, neuropsychiatric disorders. Therefore, further investigation on the neural substrates underlying sensorimotor gating, with the ultimate goal to find and test therapeutic targets, will greatly impact the lives of patients and economy, both nationally and internationally.

For clinical and experimental purposes, sensory information processing is measured by behavioral paradigms assessing the plasticity of the startle reflex. Under normal or pathological conditions, the prepulse inhibition (PPI) of the startle reflex is the gold standard to measure sensorimotor gating in patients and animal models (Li *et al.*, 2009; Kohl *et al.*, 2003; Swerdlow *et al.*, 1999). Therefore, in order to understand how the brain filters out irrelevant sensory information prior to focusing attention, extensive research has focused on the neural network underlying the startle reflex and its plasticity events.

1.2 The startle reflex

The startle response is an evolutionarily-conserved, innate and protective motor response of animals to potentially threatening stimuli (Davis, 1984; Landis and Hunt, 1939; Frankland *et al.*, 1995). The startle reflex has been documented in a wide spectrum of organisms in the animal kingdom, from invertebrates (e.g. *Caenorhabditis elegans* and mollusks) to vertebrates (e.g. zebrafish, rodents, cats and primates), in which is described as a whole-body motor response (Eaton, 1984; Hoffman and Ison, 1980; Kandel, 1976). In mammals, this defensive response is characterized by rapid and robust muscular activation. Once triggered, the startle reflex stops ongoing behavior, allows orientation towards stimuli and, if necessary, is followed by a fight-or-flight response (Davis, 1984; Eaton 1991; Koch and Schnitzler, 1997). As an innate behavior, the startle reflex does

not require conditioning or motivation, and is triggered by the presentation of multimodal sudden startling stimuli, including tactile, acoustic and vestibular (Eaton 1984, Landis and Hunt, 1939; Swerdlow *et al.*, 1999). Furthermore, the startle reflex exhibits inherent plasticity mechanisms, such as habituation, sensitization, potentiation and prepulse inhibition, which have been used to explore the bases of information processing across species (Davis, 1984; Eaton *et al.*, 1991; Graham, 1975; Kandel, 1976; Frost *et al.*, 2003; Takahashi *et al.*, 2017). Altogether, these characteristics make the startle response an essential research tool to evaluate information processing in animal models with an important translational potential.

Due to its short-latency and simple neural pathway, most studies using PPI as an operational measure of sensorimotor gating use a startle reflex triggered by a sudden loud acoustic stimulus, called the acoustic startle response (ASR). Experimentally, the ASR has been widely investigated in several animal models. The neurophysiological characteristics of the startle response, and its plasticity events, are commonly studied in invertebrates or “lower” vertebrates. Their comparatively simpler neural system and “ethical” accessibility provide an optimal framework to characterize in detail the neural networks and mechanisms underlying these behaviors.

Zebrafish, an emerging vertebrate animal model, offers unparalleled advantages for neurodevelopmental studies due to the rapid and external development of transparent embryos, high fertility, distinguishable nervous system and genetic malleability (Burgess and Granato, 2007; Gupta *et al.*, 2018; Koster and Sassen, 2015; Medan and Preuss, 2014). In addition, because of its relatively high genetic (~70%) and neuroanatomic homology to humans, zebrafish lines of human diseases are of particular and translational

interest. This organism also displays several translational behavior traits, such as ASR and PPI. The startle response in larval zebrafish, and in some other fish and amphibians, is characterized by an all-or-nothing, short-latency and lateral C-shaped body flexion (Burgess and Granato, 2007; Takahashi *et al.*, 2017). This short-latency C-bend (SLC) response occurs 3-16ms after the presentation of a startling acoustic, tactile or vestibular stimulus, and it initiates an escape maneuver (Medan and Preuss, 2014). This observation in similar organisms is one of the reasons why the startle reflex in mammals is thought to also initiate a fight-or-flight (defensive) response, or it may be an evolutionary remnant response encoded in a neural circuit underlying a similar task. Regardless, zebrafish also exhibit multimodal plasticity of the startle response, which is mediated by a neural network similar to the one in mammals (Bergeron *et al.*, 2015; Burgess and Granato, 2007; Tabor *et al.*, 2018). Often, observations from ASR and PPI studies in these animal models are then pursued in mammal neural systems, such as rodents.

1.2.1 Neural basis of the acoustic startle reflex

First proposed in rats, the mammal primary ASR pathway is clearly understood (Davis, 1982; Figure 1.1, 1.3, in red). In rodents, the ASR elicits a whole-body flexor response characterized by muscular contraction of paws, back and tail (Hoffman and Fleshler, 1963; Hoffman and Searle, 1963; Davis, 1984). For experimental purposes, the ASR in rodents is assessed in a chamber with a motion sensor that detects the animal movement. In this manner, the whole-body startle response can be digitized and analyzed in detail. Interestingly, the parameters to elicit and record the ASR in these animal models have been successfully applied in humans (Swerdlow and Geyer, 2016). In humans, the ASR is mainly characterized by an eye blink reflex and contraction of facial (e.g. orbicularis

oculi) and neck muscles (e.g. trapezius and sternocleidomastoid; Davis, 1984; Graham, 1975; Martin *et al.*, 1990). In clinical settings, the ASR is measured by attaching EMG electrodes ventral to the eye and neck (Braff *et al.*, 1978; Braff *et al.*, 2001; Swerdlow and Light, 2016).

As a short latency motor response to sudden stimuli, the ASR pathway relies on few central synapses with fast neurotransmission. In humans, muscular contraction by the ASR begins in average 9-15ms after the onset of the startle pulse; while in rodents, it may take 6-8ms (Braff *et al.*, 2001; Davis *et al.*, 1982; Koch and Schnitzler, 1997; Lingenhöhl and Friauf, 1992; Martin *et al.*, 1990). In a pioneer lesion and stimulation study, Davis and colleagues (1982) outlined for the first time the neural basis of the ASR pathway in rats, which was later sculpted by electrophysiological recordings and tract-tracing strategies.

Following mechano-electrical transduction to the inner ear, input from the startling sound excites hair cells in the cochlea. Hair cells then activate spiral cochlear ganglion cells of the vestibulocochlear nerve, which enter the CNS at the level of the brainstem and synapse on cochlear root neurons (CRNs; Davis *et al.*, 1982; Gomez-Nieto *et al.* 2014; Lee *et al.*, 1996; Lingenhöhl and Friauf, 1994). At this time point (approximately 2ms in rodents), if the acoustic input surpasses the startle threshold, CRNs send the information via contralateral axonal projections that decussate through the trapezoidal body (TB; Gomez-Nieto *et al.* 2014; Lingenhöhl and Friauf, 1994). These thick myelinated fibers emerge from the lateroventral periolivary nucleus (LVPO), pass through the superior olivary complex (sending collaterals), and terminate in the caudal pontine reticular nucleus (PnC). At the PnC, CRN afferents activate giant reticulospinal neurons, approximately 5ms after presentation of startling sound (in rats; Gomez-Nieto *et al.* 2014;

Koch *et al.*, 1999 Lingenhöhl and Friauf, 1994). PnC giant reticulospinal neurons are directly connected to facial, cranial and spinal motor neurons that, upon activation, elicit the motor ASR (6-8ms; Gomez-Nieto *et al.* 2014; Lee *et al.*, 1996, Yeomans *et al.*, 2006). The short-latency on the three central synapses of the ASR pathway (i.e. cochlear ganglion cells-CRNs, CRNs-PnC, PnC-motor neurons) relies on ionotropic glutamate transmission (Figure 1.3, in red; Koch *et al.*, 1999; Lee *et al.*, 1996; Lingenhöhl and Friauf, 1994). In humans, PnC giant neurons are also directly connected to motor nuclei in the head and spinal cord that trigger the eye blink reflex and contraction of facial and shoulder muscles (Martin *et al.*, 1990).

Extensive lesion and electrophysiological studies in rodents have established the pivotal role of the PnC in the acoustic and tactile startle responses. Interestingly, startling tactile or acoustic stimuli trigger a similar motor response in humans, which suggests a related and potentially conserved neural basis. Tactile startling stimulus activates neurons in the principal sensory nucleus (Pr5), which projects to the lateral caudal pontine reticular formation (Peterson and Felpel, 1971; Yeomans *et al.*, 2002). In fact, electrical stimulation of the ventrolateral part of the Pr5 evokes excitatory post-synaptic currents (EPSCs) in the giant reticulospinal neurons (Schmid *et al.*, 2003). It is still debated whether vestibular startling information from the lateral vestibular nucleus is processed in the PnC (Koch and Schnitzler, 1997; Steidl *et al.*, 2004; Yeomans *et al.*, 2006). In addition, the PnC also receives inputs from the “limbic and cortico-striato-thalamic-pallido-pontine” circuit, which modulates startle information processing (Koch, 1999). Therefore, the PnC giant reticulospinal neurons serve as the sensorimotor interface in the startle response pathway, integrating sensory information and initiating a behavioral output.

In zebrafish, other *teleostei* and amphibians, Mauthner cells are homologous to the mammalian PnC (Burgess and Granato, 2007; Medan and Preuss, 2014). Mauthner cells are a pair of easily-detectable giant reticulospinal neurons in the hindbrain that initiate the SLC in response to startle stimuli. Similar to mammals, startling acoustic or vestibular input excites neurons of the vestibulocochlear (VIII) nerve (Eaton *et al.*, 1991; Takahashi, *et al.*, 2017). Startling input travels via electrical junctions and glutamate synapses from VIII nerve neurons to the relatively gigantic lateral dendrites of Mauthner cells (Burgess and Granato, 2007; Tabor *et al.*, 2018). As the PnC giant neurons, the startle-driven Mauthner cells send contralateral output to motor neurons that elicit the SLCs. Furthermore, startling input also activates a collateral inhibitory network to control firing of Mauthner cells. This inhibitory network consists of ipsilateral commissural interneurons and contralateral neurons, which form electrical junctions and glycine synapses by the axon hillock of Mauthner cells (Eaton, 1984; Medan and Preuss, 2014). For instance, a startling stimulus delivered to the right side of a zebrafish elicits an avoidance SLC to the left (i.e. contraction of the left side of the fish). Therefore, the startling stimulus delivered to the right side activates VIII nerve and inhibitory commissural neurons synapsing on the ipsilateral Mauthner cell and inhibitory contralateral neurons to the left side Mauthner cell. This results in startling input traveling down only the right Mauthner cell axon, which relays the motor output to left-side descending interneurons that excite left-side motor neurons. At the end, this results in contraction of the left side only (i.e. left-side SLC) that initiates the escape maneuver away from the startling stimulus (Eaton *et al.*, 1991; Medan and Preuss, 2014; Takahashi *et al.*, 2017). Unlike the startle response in mammals, the SLC

is an all-or-nothing event; therefore, PPI or habituation are displayed as a decrease in the probability of eliciting an SLC (Bergeron *et al.*, 2015; Burgess and Granato, 2007).

1.2.2 Plasticity of the startle reflex: a tool to evaluate sensory information processing

As demonstrated in landmark studies on the gill withdrawal reflex in *Aplysia californica*, the startle response is an archetypal behavior to investigate the molecular, cellular and neural underpinnings of short-term and long-term plasticity (Kandel, 1976). Enhancement of a startle response can be achieved through sensitization, prepulse facilitation; while attenuation includes habituation and PPI. The delicate balance between these ‘opposite’ plasticity events (i.e. habituation and sensitization, or prepulse facilitation and PPI) promotes survival (Davis, 1984; Medan and Preuss, 2014). For instance, tipping the scale towards enhanced plasticity of the startle reflex results in hypervigilant conditions, such as hyperekplexia (exaggerated startle). In fact, testing these plasticity events in individuals suffering from neurological and neuropsychiatric disorders, or animal models of disease, has shed light on some of the neural mechanisms and pathways essential for sensory information processing.

1.2.2.1 Habituation and sensitization

Habituation refers to the exponential attenuation of a startle response after repetitive presentation of the startle stimulus (Davis, 1984; Pilz and Schnitzler, 1996). Interestingly, habituation is not exclusive to startle responses as it can be observed in most behaviors. This plasticity event is thought to be a measure of sensory filtering, which decreases the amount of redundant sensory information to be processed. In this manner, an organism

learns that the repeated stimulus does not require expending attentional resources (Pilz and Schnitzler, 1996). Sensitization occurs when the startle response is enhanced by an unconditioned stimulus (Davis, 1984; Pilz and Schnitzler, 1996). This enhanced effect has been observed to be caused via presynaptic facilitation (Kandel, 1976). Although previous investigations revealed the neural mechanisms underlying sensitization in mollusks, the homologous mechanisms in mammals remain unclear.

The notion that habituation and sensitization act as counterparts originates from the dual-process theory. This theory states that repeated stimulation travels two separate neural pathways (habituation and sensitization), which converge at a brain region to integrate sensory information and generate a behavioral output (Groves and Thompson, 1970). This theory depends on further investigations to expand the knowledge of the sensitization and habituation neural mechanisms.

ASR habituation is thought to occur along the primary ASR pathway, possibly in the PnC, since lesions confined to brain regions involved in the primary ASR alter habituation (Davis *et al.*, 1982; Koch and Schnitzler, 1997; Yeomans *et al.*, 2006). In fact, activity of giant PnC neurons decays during habituation, and repeated electrical stimulation *in vitro* of auditory fibers (mimicking acoustic startle) that synapse on these neurons results in synaptic depression (Lingenhöhl & Friauf, 1994; Weber *et al.*, 2002). Similarly, repeated electrical stimulation of Pr5 fibers (mimicking tactile startle) results in an exponential depression of excitatory post-synaptic currents (EPSCs) of giant PnC neurons (Schmid *et al.*, 2003). However, the precise neuronal underpinnings driving habituation of the startle reflex are still not completely understood.

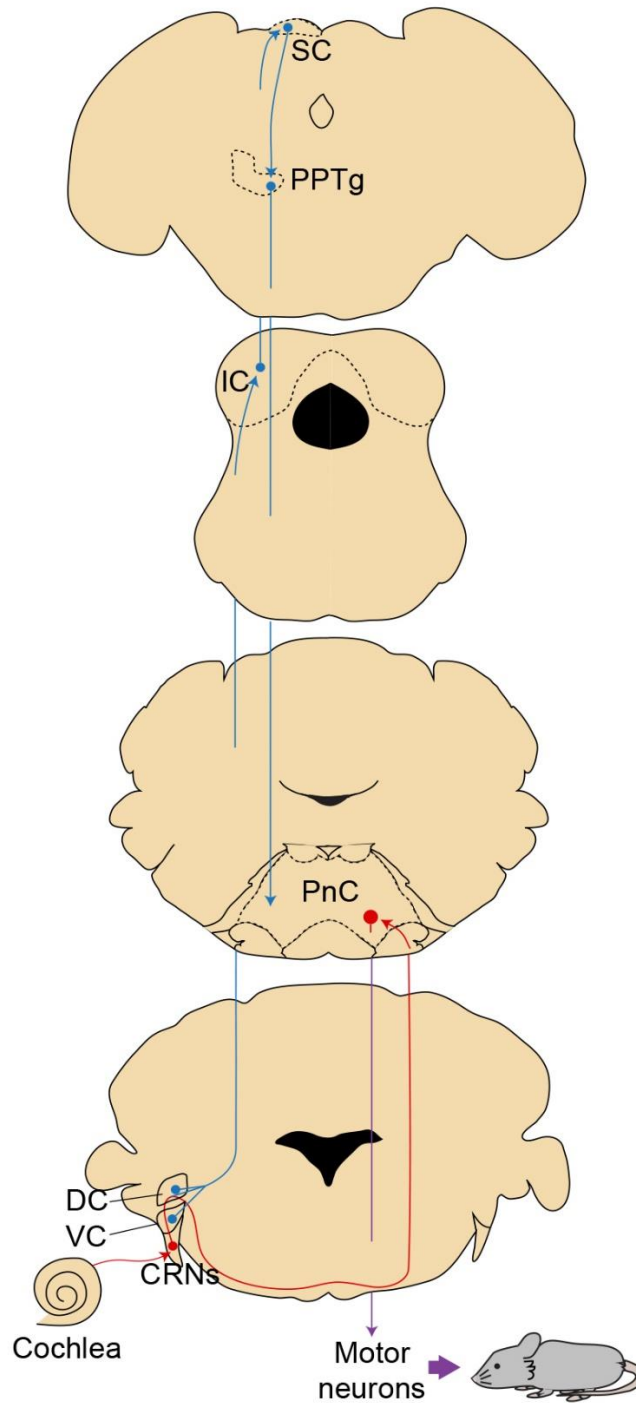


Figure 1.1. The primary ASR and PPI pathways. In red, the primary ASR pathway consists of three synapses: cochlear ganglion cells-CRNs, CRNs-PnC and PnC-motor neurons, which generate the startle response. In blue, the primary PPI pathway diverges from the ASR pathway to mesopontine nuclei, which then inhibit acoustic startle input in the PnC attenuating the motor output and startle response

1.3 Prepulse inhibition: the gold standard of sensorimotor gating

First noted by Sechenov (1863), rediscovered by Hoffman and Searle (1963), and coined “prepulse inhibition” by Ison and Hammond (1971); PPI occurs when a weak and non-startling “lead stimulus” (or prepulse) attenuates a startle response triggered by a subsequent startling stimulus (Figure 1.2). Although both PPI and habituation refer to an attenuation of a startle response, PPI does not require learning. Also, unlike other forms of startle plasticity, PPI is a non-associative behavior (Valsamis and Schmid, 2011). PPI occurs in the first trial without conditioning. In her influential studies on PPI in humans, Frances Graham hypothesized that the acoustic prepulse creates a small time window (approximately 30ms-500ms) in which the information carried by the prepulse is protected to be properly processed (Graham, 1975, Swerdlow *et al.*, 1999). If the startling sound is presented during this sensory gating window, the resulting startle response is attenuated. Alternatively, the time window is used to allocate attentional resources to properly process any subsequent stimuli (Graham, 1975; Hoffman and Ison, 1980; Norris and Blumenthal, 1996). These hypotheses are supported by the facilitation of the startle response (i.e. eye blink and whole-body flexor) when the startling pulse is presented before or after the gating period (Graham, 1975, Swerdlow *et al.*, 1999). Regardless, the prepulse is thought to activate inbuilt and evolutionarily-conserved sensory processing mechanisms that facilitate orienting attention (Graham, 1975; Hoffman and Ison, 1980). Therefore, PPI is a valuable operational tool to assess the integrity of intrinsic inhibitory brain circuits employed for sensorimotor gating.

1.3.1 The prepulse inhibition of the acoustic startle reflex paradigm

The PPI behavioral task consists of two main steps. First, the acoustic startle response is measured by presenting an intense and sudden sound pulse (Figure 1.2, top panel). In the second step, a brief and non-startling sound pulse is presented several milliseconds (interstimulus interval; ISI) before the startling stimulus. The PPI effect is the percent difference between the startle responses of the two tasks (Figure 1.2, bottom panel; Blumenthal *et al.*, 1996; Geyer and Dulawa, 2003; Valsamis and Schmid, 2011). However, there are several essential parameters that can alter the PPI effect.

Although not mentioned above, and not usually depicted in PPI task diagrams, a key factor in the ASR and PPI task is the presentation of background noise before and throughout the extent of the behavioral testing session. The vast majority of ASR and PPI studies use background noise for at least 5 minutes to acclimatize the subject (human or animal models) to the experimental setting before behavioral testing. The background noise usually consists of continuous white noise at 60-70dB above sound pressure level (SPL) also presented during the ISI and intertrial (ITI) periods (Blumenthal *et al.*, 1996; Flaten *et al.*, 2005; Valsamis and Schmid, 2011). Originally, background noise was used to isolate the subject from external stimuli, mimic daily ambience (50-70dB) and reduce variability of startle responses. However, in a series of pioneer studies in rats, Hoffman and colleagues first noted the relevance of broadband background noise during the ASR and PPI tasks. Continuous background noise significantly enhanced ASR and PPI, as opposed to silence or background sound pulses (Hoffman and Fleshler, 1963). Also, the magnitude of the ASR increased (even during the PPI task) with longer lead time intervals of background noise (Hoffman and Wible, 1969; Schmajuk *et al.*, 2006). Along these lines,

the facilitation effect on the ASR decreased when the background noise was interrupted before the onset of the startle pulse. The difference between the sound pulses and the background noise, denominated signal-to-noise ratio, can mask or increase the salience of the stimuli. Therefore, when comparing different sound intensities of background noise, the weaker sound intensity (i.e. greater signal-to-noise ratio) elicits stronger ASR and PPI. Lastly, the frequency (or pitch) of the background noise, prepulse or pulse does not modify ASR or PPI (Hoffman and Fleshler, 1963; Hoffman and Wible, 1969). These initial findings in rats have been successfully replicated in human subjects, where it was hypothesized that a lower signal-to-noise ratio increases the difficulty to properly process the prepulse. This intriguing hypothesis may help explain why in the absence of background noise, the characteristic PPI deficits of schizophrenia patients are negligible (Hsieh *et al.*, 2006). The added continuous stimulation by the background noise may be enough to overwhelm the impaired pre-attentive mechanisms of schizophrenia patients, which results in PPI deficits. Hence, the application of background noise, which can represent the continuous stream of sensory information on a daily basis, during these two tasks is crucial to discern abnormalities in pre-attentive processing mechanisms (Flaten *et al.*, 2005; Hoffman and Wible, 1969; Hsieh *et al.*, 2006).

Commonly, acoustic modality for startle pulse is used because the primary neural pathway underlying the acoustic startle response is well understood. However, a sudden and intense air puff or light flash can also trigger a tactile or visual startle response, respectively. In the PPI of the ASR task, a 40ms sound pulse with an intensity of 100-120dB above SPL is commonly used (MacLaren *et al.*, 2014; Valsamis and Schmid, 2011). However, there are studies in which shorter (e.g. 20ms), longer (e.g. 150ms) and

milder (e.g. 95dB above SPL) sound pulses successfully elicited a motor startle response (Swerdlow *et al.*, 2007; Blumenthal, 1996; Valsamis and Schmid, 2011). Under normal circumstances above the startling threshold, the magnitude of the startle response is proportional to the sound intensity. Moreover, bigger ASR occur with larger signal-to-noise ratio. On the other hand, slow rise times to onset and shorter sound pulses greatly decrease the startle response (Blumenthal, 1996; Blumenthal *et al.*, 1996). The ASR task tested at different intensities can also single out hearing impairments that may be misinterpreted as PPI or facilitation. Therefore, it is primordial to first assess the ASR with different parameters, especially sound intensity, and select optimal startling sound pulse parameters to be used in the PPI task (Hoffman and Searle, 1968; Swerdlow *et al.*, 2007; Valsamis and Schmid, 2011).

As accurately denominated, PPI is the short-term plastic attenuation of a startle response by a prepulse. Foundational studies observed the inhibitory effect of the prepulse when applied 50-300ms prior to the startling pulse, with a prepulse lasting 10-40ms with an intensity (lower than but) close to that of the startling pulse (Fendt *et al.*, 2001; Graham, 1975; Hoffman and Searle, 1965; Hoffman and Searle, 1968; Hoffman and Wible, 1970). Usually, a 20ms sound pulse with a 65-85dB intensity above SPL is applied to significantly attenuate the startling effect of the subsequent loud sound pulse. Previous studies demonstrated that shorter prepulses decrease the PPI effect. In addition, the PPI effect is directly dependent on the prepulse intensity. As the main requirement, the prepulse must not elicit a startle response; with this in mind, the closer the prepulse intensity to the startle threshold, the larger the PPI effect. In fact, the PPI effect is greater when the difference in sound intensity between the prepulse and pulse

is minimal (Fendt *et al.*, 2001; Hoffman and Wible, 1970; Li *et al.*, 1998). Due to the obvious importance of the prepulse intensity on PPI, studies commonly test different prepulse intensities varying by 3-5dB. Additionally, different prepulse intensities may be regulated by specific neurochemical systems (Valsamis and Schmid, 2011).

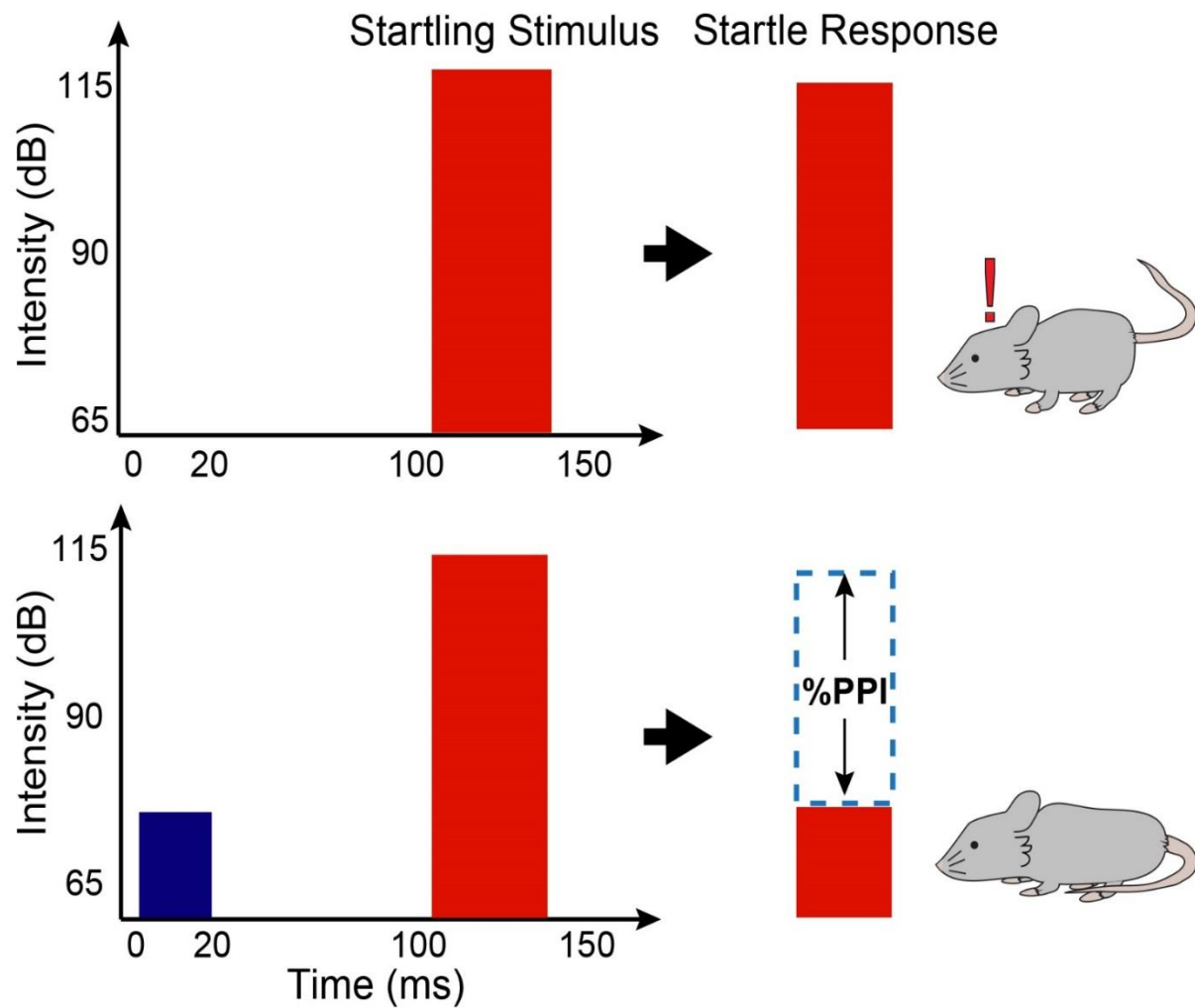


Figure 1.2. Prepulse inhibition of the startle reflex task. *Top.* The ASR task consists of presenting a sudden acoustic startling stimulus (also visual, vestibular or tactile), which elicits a motor startle response. *Bottom.* Presenting a mild non-startling stimulus several milliseconds before the startling stimulus greatly attenuates the startle motor response. PPI is the percent difference of the startle response between the two tasks.

Aside from the signal-to-noise ratio, the difference in modality between the stimuli can alter PPI values. Flaten and colleagues (2005) demonstrated that the signal-to-noise ratio of the prepulse is irrelevant when the prepulse is in a different sensory modality from the background noise.

Previous studies in normal human subjects demonstrated that a monaural prepulse elicits a stronger PPI than binaural delivery. Although not completely understood, it is hypothesized that a monaural prepulse exerts less spatial attention resources to attempt locating the stimulus (Kumari *et al.*, 2007; Marsh *et al.*, 1976). This hypothesis may also explain why patients diagnosed with schizophrenia exhibited abnormal binaural PPI values, but normal monaural PPI in a clinical setting. In this case, it is hypothesized that the impaired pre-attentive mechanisms may be sufficient to properly process the monaural prepulse. However, the significance of a stronger monaural PPI effect remains unclear. Previous studies in a prototypical model of sound processing and localization, the barn owl, showed that monaural acoustic stimulation drastically reduced accurate sound localization when compared to binaural stimulation (Knudsen and Knudsen, 1985). Therefore, as a mechanism essential for orienting attentional resources, the importance of stronger PPI with monaural prepulse stimulation remains to be revealed.

The last important variable to consider in the PPI task is the ISI between the prepulse and the startling pulse. The importance of the ISI resides in the hypothetical gating window created by the prepulse. At short ISI (<10ms, likely before the gating window), the prepulse has been shown to facilitate the ASR (i.e. prepulse facilitation; Fendt *et al.*, 1999; Ison *et al.*, 1973). Similarly, the PPI effect disappears at long ISI (>500-2000ms). Furthermore, the weight of the ISI on PPI is species-dependent, which may be due to the

difference in size of the nervous systems. Maximal PPI in rodents is regularly observed at 30-50ms ISI; while in humans is observed at 100ms (Fendt *et al.*, 2001; Swerdlow and Light, 2016). Furthermore, these ISI of maximal PPI have been shown to be dependent on prepulse intensity. It is hypothesized that the time extent of the gating window increases as the prepulse intensity and its signal-to-noise ratio increases. Furthermore, as observed with prepulse intensities, several studies suggest that different neurochemical systems are responsible for PPI at different ISI (Valsamis and Schmid, 2010; Weber *et al.*, 2003). Therefore it is crucial to test genetic or drug manipulations, specifically targeting a neurochemical system, at different ISI.

In conclusion, a detailed study of previous protocols and careful adjustment of the described parameters should be performed when applying the ASR and PPI behavioral tasks. Doing so can allow the analysis of the neurochemical and physiological properties of the mechanisms underlying the ASR and PPI.

1.3.2 A clinical and experimental tool

Being the operational measure of sensorimotor gating, which is dysregulated in several neuropsychiatric disorders, PPI has been applied as a clinical assessment to shed light on the pathophysiology of these disorders. As mentioned before, rodents exhibit PPI, and the majority of the brain regions involved in the ASR and PPI in rodents (or other organisms) are anatomically and functionally homologous to human brain regions (Swerdlow *et al.*, 1999; Swerdlow and Light, 2016). In addition, PPI deficits are also present in transgenic animal models of diseases associated with sensorimotor gating deficits. In fact, recent findings on the pathogenesis of these disorders, spanning from genetic to environmental factors, have been made possible by generating transgenic

animal models (Stefansson *et al.*, 2014; Swerdlow and Light, 2016). This genetic technology allows to isolate and study the contribution of each factor to the disease. Furthermore, recent and more translational approaches allow the analysis of cell type-specific roles in a disorder and genomic analyses to identify susceptibility genes (Benraiss *et al.*, 2016; Windrem *et al.*, 2017). Taken together, this evidence endorses the “ethically sound” option to study the PPI circuit in animal models. Ultimately, by employing these resources, we can gain a better insight on the sensorimotor gating network, under both normal and pathological circumstances.

1.3.2.1 Schizophrenia

The PPI task was first utilized as a clinical tool in individuals diagnosed with schizophrenia. In this study, the eye blink component of the startle response in individuals suffering from schizophrenia was not attenuated by the prepulse (Braff *et al.*, 1978). Along with previous findings in schizophrenia patients showing cortical hyperactivity, it was then hypothesized that deficient sensory filtering results in sensory flooding of higher order brain regions (Braff *et al.*, 1977; Braff *et al.*, 1978; Braff and Geyer, 1990). More recent studies, using EMG to measure other components of the startle response, have further confirmed that patients suffering from schizophrenia are not able to properly process the prepulse resulting in reduced PPI values (Dawson *et al.*, 1993). This empirical observation reflects the characteristically deficient sensorimotor processing, which is associated to the development of other cognitive deficits and symptoms of schizophrenia, such as thought disorder, high distractibility, hallucinations and delusions (Hoenig *et al.*, 2005; Javanbakht, 2006; Mena *et al.*, 2016; Swerdlow *et al.*, 1999;). In fact, extensive

human and animal studies have established sensorimotor gating impairments as an endophenotype of schizophrenia.

Endophenotypes are quantifiable neurobehavioral traits that reflect a genetic susceptibility to develop a disorder. Although still debated, an endophenotype is further defined as a heritable, state-independent, measurable trait that reflects the dysfunctionality of a system in a complex disorder (Flint and Munafo, 2007; Iacono, 2018; Kendler and Neale, 2010; Walters and Owen, 2007). Altogether, these characteristics indicate that an endophenotype is more closely related to the genetic etiology of a disease than its phenotype. Taking this definition into consideration, first, sensorimotor gating deficits are quantified by the PPI task (Braff *et al.*, 1978; Graham, 1975). Secondly, these deficits are state-independent as they can be measured in individuals undergoing the first episode of psychosis, and persist until after remission of other schizophrenia symptoms (Mena *et al.*, 2016). Clinical investigations in patients medicated with antipsychotics document persisting PPI deficits. In fact, the persisting sensorimotor gating deficits, and the resulting sensory overload, are thought to contribute to the recurrence of positive symptoms and impaired cognition (Javanbakht, 2006; Mena *et al.*, 2016). Similar deficits have been documented in individuals with a genetic susceptibility of developing schizophrenia and schizotypal disorders. Lastly, immediate unaffected relatives of a schizophrenia patients also show decreased PPI, which are much more pronounced in normal monozygotic twins (Cardno and Owen, 2014). Therefore, as a schizophrenia endophenotype, sensorimotor gating deficits reflect underlying genetic abnormalities that result in dysfunctional sensory processing mechanisms.

The genetic connotation of impaired sensorimotor gating in schizophrenia is further suggested by the 22q11.2 deletion syndrome. Although this syndrome accounts for a relatively low percentage (1-2%) of schizophrenia cases; currently, it is the most common genetic factor for the development of schizophrenia (Drew *et al.*, 2011 Ellegood *et al.*, 2014). Commonly known as diGeorge syndrome or velocardiofacial syndrome, individuals with this genetic deletion exhibit low IQ scores and impaired pre-attentive processing, as evident by low PPI values and poor performance on other attention-related tasks. These cognitive deficits and functional abnormalities may represent the volumetric reductions observed in several cortical and subcortical brain regions, such as the hippocampus, cerebellum, amygdala, prefrontal cortex and temporal lobe, among others (Ellegood *et al.*, 2014; Fenelon *et al.*, 2011; Fenelon *et al.*, 2013; Mukai *et al.*, 2015; Stark *et al.*, 2008). Most of these cognitive and neuroanatomical abnormalities are also observed in the genetically engineered mouse models of the 22q11.2 deletion syndrome. *Df(16)A^{+/-}* mice, an isomorphic animal model of schizophrenia, have been used to delve in the genetic etiology of this disorder. These mice display hyperactivity, and deficient PPI, fear conditioning and working memory. Investigations in the 22q11.2 deletion syndrome mouse model helped identify genes that may contribute to the development of schizophrenia (Fenelon *et al.*, 2011; Fenelon *et al.*, 2013; Mukai *et al.*, 2015; Stark *et al.*, 2008). These susceptibility genes were then studied separately in knock-out mouse lines. PPI deficits were observed in mutant mouse lines of T-box 1 (Tbx1), guanine nucleotide binding protein beta polypeptide 1-like (GNB1L), proline dehydrogenase (PRODH), catechol-o-methyltransferase (COMT), zinc finger DHHC-type containing 8 (ZDHHC8) and diGeorge syndrome critical region gene 8 (DGCR8), among others (Crabtree *et al.*,

2016; Drew *et al.*, 2011 Ellegood *et al.*, 2014; Fenelon *et al.*, 2011). Interestingly, mutations in orthologous genes were found in patients that exhibited the 22q11.2 deletion syndrome phenotype (Greenwood *et al.*, 2011; Prasad *et al.*, 2008). In an alternative and elegant approach, Windrem and colleagues (2017) generated patient-specific mice to investigate the role of glia in early-onset schizophrenia. This strategy relies on iPSC (induced Pluripotent Stem Cell) technology. iPSCs were first derived from reprogrammed somatic cells of schizophrenia patients, and then differentiated into glial progenitor cells (Boland *et al.*, 2012; Wang *et al.*, 2013). In one part of the study, these cells were grafted into neonatal immune-deficient mice for histological and behavioral analysis. Interestingly, the chimeric mice displayed schizophrenia phenotypic traits, such as sensorimotor gating deficits, excessive anxiety and locomotion, and antisocial behavior. In the other component of this investigation, glial progenitor cells were subjected to a genome wide analysis to identify shared susceptibility genes, which may provide the genetic basis for the neuroanatomical and behavioral abnormal traits (Windrem, *et al.*, 2017). In sum, the genetic etiology of schizophrenia is reflected in its characteristic endophenotypes, including sensorimotor gating deficits.

1.3.2.2 Other neuropsychiatric disorders

Aside from schizophrenia, OCD is another neuropsychiatric disorder commonly associated with sensorimotor gating deficits. In individuals suffering from OCD, sensorimotor gating deficits are manifested as the inability to filter out redundant thoughts and repetitive actions, which results in obsessions and compulsions, respectively (Ahmari and Dougherty, 2015; Hoenig *et al.*, 2005; Pauls, 2008). The main obstacles for sensorimotor gating deficits in the context of OCD are the limited understanding on both

the etiology of OCD and the precise neural basis of sensorimotor gating (Kohl *et al.*, 2013). As observed in schizophrenia, compelling evidence on immediate relatives of OCD patients suggests a genetic predisposition in the development of OCD. However, currently, there are no identified OCD susceptibility genes to generate an etiological valid animal model of OCD (Pauls, 2008). The three main mouse lines investigated as potential OCD models are mutants for glutamatergic components, but have not been tested or do not show PPI deficits. The knowledge on the neural substrates of OCD was derived from lesion studies in rodents, and imaging and drug testing in animal and human subjects. Abnormalities in the serotonergic and dopaminergic components of the cortico-striatal-pallido-pontine (CSPP), which has been greatly implicated in sensorimotor gating, are thought to contribute to the OCD phenotype (Fendt *et al.*, 2001; Swerdlow *et al.*, 1999; Szechtman *et al.*, 2017). A combined drug therapy consisting of selective serotonin reuptake inhibitors and dopamine receptor antagonists has been successfully tested in OCD patients. Dopamine and serotonin receptor antagonists, such as clozapine, have been shown to lessen PPI deficits in OCD and schizophrenia patients (Lim *et al.*, 2007). However, the precise mechanism behind this phenomenon needs further investigation.

In TS, sensorimotor gating deficits are displayed by the failure to gate premonitory urges which result in motor or vocal tics (Cavanna *et al.*, 2017; Swerdlow, 1993). Dysfunctional dopaminergic substrates of the CSPP are also associated to the development of TS. Concomitant abnormal GABAergic neurotransmission in the striatum, responsible for gating unnecessary and involuntary movements, results in the characteristic tics observed in TS patients (Kohl *et al.*, 2013). As in OCD, it is hypothesized that impaired sensorimotor gating stems from these dopaminergic and

disinhibition dysfunctions. However, unlike OCD, there is a better insight on the possible PPI neural substrates dysregulated in TS. The characteristic symptoms are largely attributed to the dysregulated GABAergic and dopaminergic neurotransmission in the ventral striatum (Swerdlow 1993). More specifically, the NAcc sends GABAergic input to the VP that modulates both the ASR and PPI, likely through GABA efferents from the VP to the pedunculopontine tegmental area (PPTg). In addition, this GABAergic circuit receives dopaminergic input from the ventral tegmental area (VTA; Groenewegen et al., 2003). These findings, on the relevance of a striatal dopaminergic/GABAergic circuit for PPI in rats, offer a promising candidate to be targeted in future investigations.

Along these lines, patients suffering from HD also exhibit PPI deficits, which are thought to contribute to the characteristic motor abnormalities and deteriorating cognitive processes in this disease. Similar to TS, the GABAergic striatal circuit is compromised in HD patients and animal models. Striatal lesions in rats result in phenotypic abnormal PPI values and motor behavior. In fact, patients suffering from HD show a progressive degeneration of medium spiny GABAergic striatal cells (Carter *et al.*, 1999). This observation suggests a potential cell-specific endophenotype of HD, and a platform to direct therapeutic efforts. Therefore, the GABAergic circuit from the ventral striatum, and its dysregulated disinhibition, is a potential target for further investigations of sensorimotor gating deficits present in OCD, TS and HD patients.

In sum, better understanding the PPI circuit under physiological and pathological conditions will allow us to identify neuronal targets in disease animal models.

1.3.3 Neural basis of PPI

In 1997, Koch and Schnitzler gleaned findings from numerous studies to propose a “hypothetical” and central PPI of the ASR pathway that, once activated by a mild and non-startling prepulse, suppresses a subsequent evoked startle response (Figure 1.1, in blue). According to this pathway, the information from the prepulse enters the brain at the level of the cochlear nuclei, which includes the dorsal, ventral and cochlear root nuclei. Similar to the ASR pathway, at the cochlear nuclei the information by the prepulse is first processed. If the prepulse intensity falls below the startle threshold, the information then diverges from the primary ASR, and activates the inferior colliculus and the superior colliculus. The superior colliculus then directly activates the pedunculopontine tegmental area (PPTg), which inhibits the PnC (Fendt, 1999; Koch et al., 1993; Koch and Schnitzler, 1997; Swerdlow et al., 1993). As a result of this PnC inhibition, the output to motor neurons and the motor response is greatly attenuated (Bosch and Schmid, 2006; Bosch and Schmid, 2008; Davis et al., 1982; Koch et al., 1993). The PnC is at the core of the sensorimotor gating circuit, since it is where the two pathways converge (ASR and PPI; Figures 1.1 and 1.3, in dark blue). This PPI pathway is further modulated by a larger and more intricate network of cortical, striatal, pallidal and pontine regions denominated the CSPP network (Figure 1.3, light blue). However, the precise neural circuits connecting the CSPP network to the central PPI and ASR pathways are still debated.

1.3.2.1 PPTg: the dogmatic substrate mediating PPI

As one of the mesopontine nuclei in the second largest cholinergic network in the CNS, the cytoarchitectural borders of the PPTg in mammals are dictated by its cholinergic chemoarchitecture. These PPTg cholinergic neurons contribute to REM sleep, arousal

and associative learning behaviors, such as reward learning and prediction, and decision making (Cyr *et al.*, 2015; Diederich and Koch, 2005; Gut and Winn, 2016; Kroeger *et al.*, 2017; Xiao *et al.*, 2016). In addition, a cholinergic PPTg-PnC connection was thought to be the main neural substrate mediating PPI.

In 1993, two contemporary reports co-established a cholinergic dogma in PPI. First, Swerdlow and Geyer demonstrated that electrolytic lesions in the PPTg significantly potentiated startle, and decreased PPI and habituation in rats. In this same study, disrupting subpallidal GABAergic ionotropic transmission also reduced PPI. Considering previous studies showing that subpallidal regions send GABAergic projections to the PPTg, authors hypothesized that cortical and limbic systems modulate PPI through subpallidal efferents to the PPTg (Swerdlow and Geyer, 1993). At this point, the PPTg was strictly identified as a mesopontine cholinergic nucleus with few studies documenting glutamate neurons in the PPTg (Clements and Grant 1990). Then, Koch and colleagues (1993) identified a direct cholinergic connection from the PPTg to the PnC. Taking into consideration separate evidence indicating some cholinergic innervation to giant PnC neurons and close apposition of PPTg boutons to these PnC neurons, the authors ventured to hypothesized that the PPTg sends direct cholinergic input to the “startle” neurons in the PnC. In fact, muscarinic agonists attenuated activity of the “startle” PnC neurons, and quinolinic acid (QA) lesions in the PPTg reduced cholinergic cells and PPI without significantly affecting (mildly attenuating) basal ASR in rats (Koch *et al.*, 1993). From this evidence, Koch and colleagues concluded that acetylcholine PPTg neurons are involved in PPI via a direct attenuation of PnC startle neurons. More recent studies *in vitro* further explored the mechanistic basis of this PPI cholinergic dogma. Acoustically-driven

giant PnC neurons express both muscarinic and nicotinic receptors, and its activation can inhibit giant PnC neuron activity evoked by electrical stimulation of auditory or trigeminal fibers innervating the PnC (Bosch and Schmid, 2006; Bosch and Schmid, 2008). In addition, evidence from human and animal studies supported the contribution of acetylcholine in PPI. For instance, cigarette smoking significantly improved PPI in schizophrenia patients; while rats fed with choline-free chow showed reduced PPI (Kumari *et al.*, 2001; Wu *et al.*, 1993). Altogether, these observations helped establish the dogmatic role in PPI of acetylcholine PPTg neurons.

Despite this, the study by Koch and others presents two major caveats in the specificity of the strategies used. Using a FluoroGold tract-tracing and immunohistochemistry approach, authors showed that some PPTg neurons directly connected to the PnC (FluoroGold-labeled) were cholinergic. Nevertheless, the majority of the FluoroGold-labeled cell bodies in the PPTg were not cholinergic (Koch *et al.*, 1993). Then, based on a relative specificity of QA to ablate cholinergic neurons, only acetylcholine neurons were quantified and compared in the lesion experiments, which led to the speculation that the ablation of these neurons caused the decrease in PPI. However, contemporary investigations on PPI used QA to effectively ablate dopamine and GABA neurons (Kodsi and Swerdlow, 1994; Kodsi and Swerdlow, 1995; Wan and Swerdlow, 1997). QA, an excitotoxin, is a potent agonist of the NMDA receptor (NMDAR). Since NMDAR have been observed on the axon and presynapse, QA may have also affected fibers *en passant* and PPTg afferents. Therefore, other non-cholinergic (FluoroGold-labeled) PPTg neurons directly connected to the PnC and also affected by QA administration may also contribute to changes in PPI and basal ASR. In fact, *in situ* hybridization studies in rodent tissue

revealed interspersed glutamatergic and GABAergic neurons among the distinctive PPTg acetylcholine neurons (Steinkellner *et al.*, 2018; Wang and Morales, 2009), which may be “the other non-cholinergic PPTg neurons” involved in PPI. Recent studies focusing on the cell-type specific role of PPTg neurons revealed their precise contribution to PPI.

First suggested by vesicular acetylcholine transporter knockdown mice exhibiting normal PPI values (Schmid *et al.*, 2011), recent investigations revisited the cholinergic dogma using cell-type specific manipulations. In rats, infusions of a modified neurotoxin to specifically ablate acetylcholine neurons in the PPTg almost abolished the basal startle response without altering PPI (Clark *et al.*, 2007; MacLaren *et al.*, 2014). Similarly, optical stimulation of PPTg cholinergic neurons did not alter PPI and potentiated startle, which is in line with the role of these neurons in arousal (Azzopardi *et al.*, 2018). In contrast, chemical lesions targeting all PPTg neurons and chemogenetic inhibition of glutamate PPTg neurons significantly decreased PPI in rodents (Fulcher *et al.*, 2019; MacLaren *et al.*, 2014). Similar optogenetic approaches in larval zebrafish highlighted the relevance of Gsx1-expressing neurons in a region homologous to the mammal mesopontine. Gsx1 is a neurodevelopmental transcription factor chiefly expressed in excitatory neurons, and also important for inhibitory interneuron development (Pei *et al.*, 2011; Toresson and Campbell, 2001). Optogenetic inhibition of Gsx1 neurons in rhombomere 4 of larval zebrafish and in the rodent PPTg greatly attenuates PPI (Bergeron *et al.*, 2015). These neurons are activated by an acoustic prepulse, and its optogenetic stimulation can mimic prepulse activation and attenuate the startle response (Tabor *et al.*, 2018). In the goldfish, another animal model of PPI, glutamatergic and GABAergic receptor in Mauthner cells mediate PPI (Curtin and Preuss, 2015). These studies using novel and more targeted

approaches highlight the importance of a previously uninvestigated and paradoxical glutamatergic substrate in PPI.

1.3.2.2 CSPP network modulating PPI

In the literature, a modulatory brain region refers to a neural substrate connected to the primary PPI pathway and indirectly regulating PPI (Figure 1.3, light blue). Several investigations on the neural substrates underlying sensorimotor gating gleaned a constellation of CSPP regions modulating PPI (and ASR), some of which are consistently associated with the pathology of schizophrenia and other related disorders (Koch and Schnitzler, 1997).

In the CSPP network, the NAcc plays an integrative role by converging inputs from the mPFC, hippocampus, VTA and BLA, and projecting to the PPI primary pathway. The NAcc is largely characterized for GABAergic medium spiny neurons (MSNs) that receive dopaminergic input from the VTA, and mediate reward-seeking and aversive behaviors. MSNs also receive glutamatergic inputs from the hippocampus, BLA and mPFC, which help regulate reward-seeking and aversive behaviors (Britt *et al.*, 2012; Pennartz and Kitai, 1991; Scudder *et al.*, 2018; Swerdlow *et al.*, 1995). Interestingly, dopamine infusion in the NAcc disrupts PPI; while infusion of glutamate agonists can enhance or reduce PPI, depending on the infused NAcc region (Koch and Schnitzler, 1997; Swerdlow *et al.*, 1992). The importance of accumbal MSNs in PPI becomes evident by concomitant HD endophenotypes, sensorimotor gating deficits and MSNs depletion (Carter, *et al.*, 1999; Swerdlow *et al.*, 1995). As mentioned above, in a study by Forcelli and colleagues (2012), authors observed that a BLA-NAcc-VP pathway regulated both ASR and PPI. It was then hypothesized that this circuit relays input to the PPTg, which now is known to mediate

both ASR and PPI through cholinergic and glutamatergic neurons, respectively (Azzopardi *et al.*, 2018; Forcelli *et al.*, 2012; Fulcher *et al.*, 2019; Tabor *et al.*, 2018).

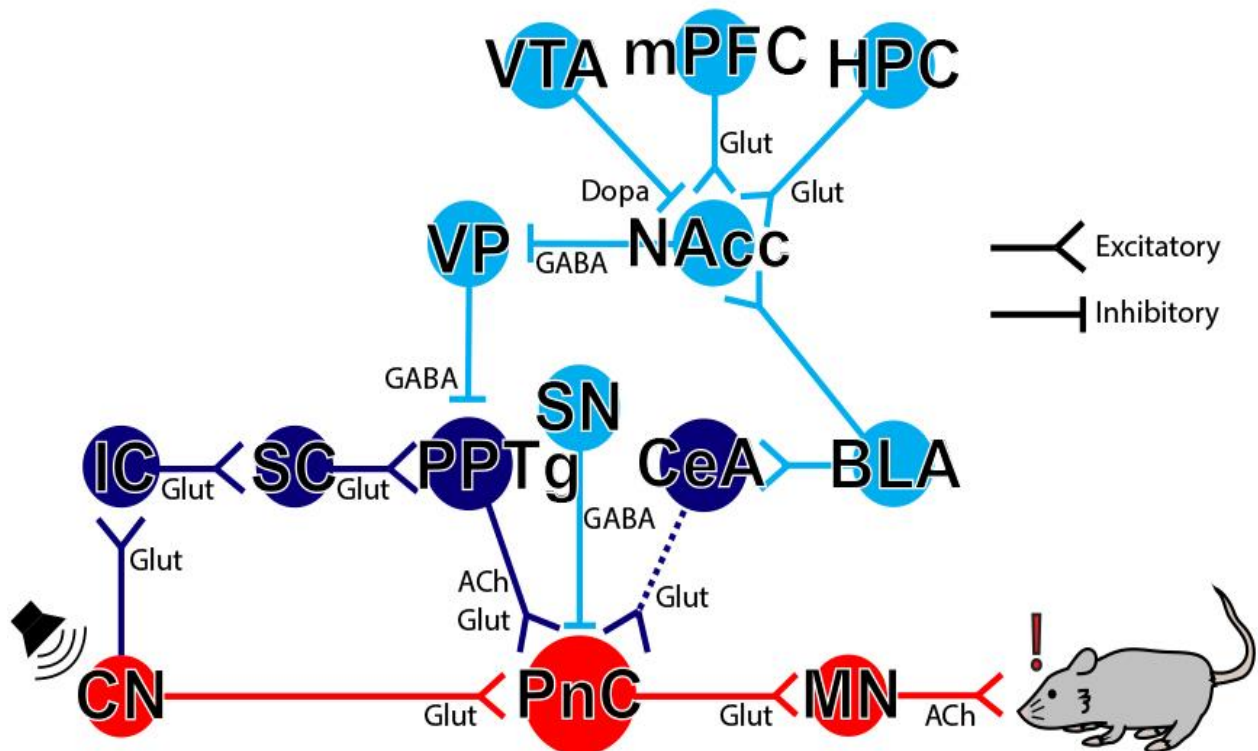


Figure 1.3. The PPI neural network. In red, the primary acoustic pathway activated by a startling sound pulse depends on fast glutamatergic neurotransmission to elicit a short-latency startle response. In dark blue, the primary PPI pathway with the dogmatic PPTg-PnC connection *directly* mediates PPI. In parallel, we propose that a glutamatergic CeA-PnC connection (dotted line) also mediates PPI. In light blue, the CSPP network indirectly modulates both ASR and PPI. Modified from Swerdlow *et al.*, 1999.

In the amygdala, the contribution of the BLA to PPI is the most investigated. Chemical and electrical lesions in the BLA did not alter basal ASR and inhibited not only PPI, but other forms of startle plasticity, such as fear-potentiation and sensitization (Davis *et al.*, 1993; Decker *et al.*, 1995; Keifer *et al.*, 2015; Sananes and Davis, 1992; Wan and Swerdlow, 1997). However, a more recent aforementioned study demonstrated that muscimol infusion in the BLA separately attenuated both ASR and PPI (Forcelli *et al.*,

2012). Remarkably, the central nucleus of the amygdala (CeA) has been previously observed to project directly to the PnC (Rosen *et al.*, 1991).

1.4 Enter: the central nucleus of the amygdala (CeA)

As described by Swanson and Petrovich (1998) in the rat brain, the amygdala is a controversially delineated group of chemically and functionally distinct nuclei that are involved in a wide array of functions. One of these nuclei is the CeA, which serves as the main output station of the amygdala. The CeA receives and integrates information from numerous cortical and subcortical, including intra-amygdalar, circuits. Then, by virtue of its widespread connections to the brainstem and hypothalamus, the CeA coordinates the acquisition, consolidation and expression of several autonomic behavioral responses to stimuli including attention and arousal (Akmaev *et al.*, 2004; Davis and Shi 1999; Fadok *et al.*, 2018; LeDoux *et al.*, 1988; Kim *et al.*, 2017; Swanson and Petrovich, 1998).

1.4.1 Neuronal architecture of the CeA

In rodents, the CeA consists of four major subdivisions, medial (CeM), intercalated/intermediate (CeI), lateral (CeL) and capsular (CeC) (Akmaev *et al.*, 2004; Cassell *et al.*, 1986; McDonald 1982, Paxinos and Franklin, 2004). The CeM is the subdivision with the largest cell bodies in the CeA, it is located ventral to the CP and the LGP and medial to the CeL and CeC, and it includes the caudal stria terminalis. The CeC is the most lateral subdivision of the CeA and it is delineated by the cc and BLA; while the CeL is confined by the CeL and CeM (Cassell *et al.*, 1986; McDonald 1982).

Commonly described as a GABAergic nucleus, the neurochemical and peptidergic profile of the CeA also consists of galanin, substance P/glutamate, enkephalin and corticotropin-releasing factor (CRF) neurons (Cassell *et al.*, 1986; Gray and Magnuson, 1987). A closer examination on the expression profile of GABAergic neuronal subtypes, CeA neurons expressing somatostatin, neurotensin, cholecystokinin, vasoactive intestinal protein are mainly located in the CeL and CeM (Kim *et al.*, 2017). Interestingly, the chemoarchitecture of the GABAergic neurons in the CeL and CeM was shown to be correlated with a hodological profile that controlled innate and learned behaviors.

Electrophysiological analyses further categorized the neurons located in each CeA subdivisions based on their firing rate. Neurons with low threshold-bursting, late-firing, fast spiking and regular spiking rate were consistently found in the CeA (Chieng *et al.*, 2006; Martina *et al.*, 1999). Most CeM neurons were categorized as late-firing, and some interspersed low-threshold bursting and fast spiking neurons. On the other hand, neurons in the CeL displayed all types of firing rate neurons, with late-firing and regular spiking being the most predominant. Interestingly, the late-firing neurons within the CeM are thought to contribute to the integrative role of this CeA subdivision.

The hodology of the CeA subdivisions consists of cortical, subcortical and intra-amygdalar afferents, as well as, reciprocal connections with hindbrain nuclei. The CeA receives input from the mPFC, ITC, PVT, PBN, BNST, hippocampus, VTA and NAcc, among others; then, the CeM and CeC integrate this information and relay the output to premotor hindbrain nuclei, such as the PAG, PCRtA, NTC, and LC (Akmaev *et al.*, 2004; Cassell *et al.*, 1986; Fadok *et al.*, 2018, Han *et al.*, 2017; Isosaka *et al.*, 2015; McDonald, 1982; Saha *et al.*, 2000; Swanson and Petrovich, 1998; Tillman *et al.*, 2018). For these

circuits, the CeM provides amygdalar output to hindbrain nuclei through the ventral amygdalofugal pathway (VAF). CeM efferents entering the VAF also send collaterals to the adjacent BNST, which has projections to similar brain regions through the stria terminalis. Therefore, the CeA, more specifically the CeM, is the interface between the input from higher cognitive regions and the integrated output to downstream autonomic regions that then initiate the motor response.

1.4.2 CeM: output station of the amygdalar complex

As the major amygdalar output station, the CeM drives the expression of innate and learned defensive behaviors. For example, following input from serotonin-2A receptor-expressing lateral CeA cells, computations to elicit innate and learned behaviors have been shown to be initiated in the CeM, in which an innate-induced behavioral response is prioritized over a learned-induced behavior (Isosaka *et al.*, 2015). Similarly, CeM-PAG and CeM-PCRtA GABAergic circuits have been shown to initiate and regulate innate predatory motor behaviors (Han *et al.*, 2017).

Along these lines, a feed-forward inhibitory intra-amygdalar microcircuit contributes to anxiety-related behaviors. BLA glutamatergic afferents to the CeL activate inhibitory “interneurons”, which then inhibit CeM output eliciting in anxiolytic effects. In parallel, direct BLA glutamatergic efferents to the CeM (i.e. by passing the CeL) were shown to override the BLA-CeL-CeM inhibitory effect (Tye *et al.*, 2011). In this case, it is speculated that CeM output through the VAF pathway activates several stress- and fear-related premotor hindbrain regions, such as the LC, PAG and NTS (Kamali *et al.*, 2016; LeDoux *et al.*, 1988; Reyes *et al.*, 2011; Valentino and Van Bockstaele, 2008). This same feed-forward inhibitory microcircuit has been demonstrated to control appetitive behaviors.

However, the output from this pathway is hypothesized to travel through the stria terminalis to hypothalamic regions (Cai *et al.*, 2014; Kim *et al.*, 2017).

Imperative for fear conditioning, the CeA processes fear-related input and coordinates innate and fear-conditioned responses through its VAF efferents (Davis *et al.*, 1997; Fadok *et al.*, 2018; Keifer *et al.*, 2015; Kim *et al.*, 2016). Furthermore, synaptic plasticity in the CeL contributes to acquisition of conditioned fear; while in the CeM synaptic plasticity drives fear extinction (Duvarci *et al.*, 2011; Hitchcock and Davis 1986; Li *et al.*, 2013). Electrolytic lesions to each CeA subdivision abolishes fear learning and expression (Wilensky *et al.*, 2006). Despite these intra-amygdalar computations, it is the output from the CeM that operates the fear responses. CeM output bifurcates to the LH and the PAG, with the former controlling the autonomic fear response (i.e., increased heart rate and blood pressure) and the latter controlling the characteristic fear-induced freezing behavior (LeDoux *et al.*, 1988). To reconcile the electrophysiological findings with the integrative role of the CeM, it is hypothesized that the abundant CeM late-firing neurons require activation to relay the output through VAF efferents. Such input can originate from the BLA glutamatergic excitatory inputs, cortical regions or reciprocal hindbrain connections.

1.4.3 CeA-PnC connection

In rats, a direct amygdalar connection to the PnC potentiates the fear-conditioned startle response (Rosen *et al.*, 1991; Hitchcock and Davis, 1991; Koch and Ebert, 1993; Yeomans and Pollard, 1993). In these studies, electrical stimulation of the amygdaloid complex enhanced a startle response in rats (Rosen and Davis, 1988a; Rosen and Davis, 1988b; Rosen and Davis, 1990; Koch and Ebert, 1993). In the same manner, lesions to

the central amygdala “restricted” to the CeA altered the startle response (Melia *et al.*, 1992; Young and Leaton, 1996).

When studied in the context of fear processing using rats, this connection between the amygdaloid complex and the PnC was speculated to be direct and excitatory (Davis *et al.*, 1997; Koch and Ebert, 1993; Miserendino and Davis, 1993). In a separate study, CRF inputs from the CeA to the PnC were also shown to contribute to a fear-potentiated startle response (Fendt *et al.*, 1997). However, the upstream substrates underlying this behavior remain uninvestigated. It is hypothesized that acoustic stimulus from the primary pathway activates a thalamo-amygdalar circuit, which then employs the CeA-PnC connection to potentiate the startle response (Iwata *et al.*, 1986; LeDoux *et al.*, 1988).

In a study by St Andre and Reilly (2007), lesions to the CeA did not affect the conditioned taste aversion in a latent inhibition design. However, in a later rat study by Kuramashi and colleagues (2013), the antipsychotic blonanserin was shown to ameliorate methamphetamine-induced disruption of latent inhibition. To evaluate latent inhibition, the authors used a conditioned emotional response in which a tone (conditioned stimulus) was paired with a mild foot shock (unconditioned stimulus). Immunohistochemical examination showed blonanserin increased c-Fos expression in the shell area but not in the core area of the NAcc while methamphetamine produced the opposite expression pattern. Interestingly, blonanserin also increased the number of c-Fos expressions in the central amygdala nucleus but not in the basolateral amygdala (BLA) nucleus or the prefrontal cortex. The different results obtained by the two studies might be related to the different stimuli employed: taste (St Andre and Reilly, 2007) and sound (Kuramashi *et al.*, 2013). Because we also use tones in our current study, it is tempting to speculate that a

subset of excitatory CeA neurons might specifically be involved in auditory-dependent behaviors associated with a filtering/inhibitory component; while the CeA as a whole might be involved in mediating attention and other associative learning processes (Gallagher *et al.*, 1994, Holland and Gallagher, 1993; Maddux *et al* 2007). Along these lines, photoinhibition of the central, lateral and basolateral amygdalar complex impairs olfactory processing. This impairment was replicated by inhibiting amygdalar efferents to the LC (Fast and Gann 2017), likely through the VAF pathway. Despite this, a potential contribution of the CeA-PnC pathway in the context of sensorimotor gating has not been investigated.

Altogether, for its unique sensory input integration in the amygdala roles and hodology, the CeA is an intriguing and potential PPI substrate. Therefore, the proposed study aims to further characterize the CeA-PnC connection and its role in sensorimotor gating in mice.

1.5 Hypothesis

Sensorimotor gating is a pre-attentive mechanism that prevents sensory information overload and helps orient attention. Patients diagnosed with psychiatric and neurological disorders, such as schizophrenia, exhibit sensorimotor gating deficits. Currently, there is no treatment for sensorimotor gating deficits, and the associated attention impairment, mainly because the sensorimotor gating circuit is not completely understood, even in healthy subjects. Previous studies identified a connection from the CeA to the PnC, the core of sensorimotor gating. However, whether the CeA-PnC pathway contributes to sensorimotor gating remains unknown.

Our *hypothesis* is that direct CeA input to the PnC mediates sensorimotor gating. Our hypothesis is based on previous studies showing that: 1) the PnC is at the core of the sensorimotor gating circuit, 2) the amygdala is anatomically connected to the PnC, 3) lesions of the amygdaloid complex can disrupt sensorimotor gating, and 4) patients and mouse models of schizophrenia show sensorimotor gating deficits and amygdalar dysfunctions.

1.6 Specific aims

To address our hypothesis, the following specific aims were developed and tested:

Specific Aim 1: Establish the chemical identity of the CeA-PnC anatomical connection

Inject tracers to identify CeA neurons directly connected to the PnC. Use *in vitro* electrophysiological recordings with ChR2 photostimulation to selectively activate CeA efferents to the PnC, and apply receptor antagonists to determine the chemical identity of a subset of CeA-PnC synapses.

Specific Aim 2: Characterize how the CeA neurons modify the PnC activity in vitro

Use the *in vitro* electrophysiological with optogenetics approach from *Aim 1* to characterize the synaptic properties of a subset of the CeA-PnC connection, and investigate if excitatory CeA efferents modulate PnC activity evoked by auditory input.

Specific Aim 3: Establish how CeA-PnC synapses underpin sensorimotor gating in vivo

Silence CeA-PnC excitatory synapses with inhibitory opsins during the ASR and PPI tasks *in vivo*. Use photostimulation of CeA-PnC excitatory synapses as a prepulse during the ASR and PPI tasks *in vivo*. These experiments will reveal whether excitatory CeA input to the PnC contributes to PPI.

Specific Aim 4: Identify the PnC components receiving CeA excitatory inputs

Use tract-tracers to image putative synaptic contacts between excitatory CeA efferents and PnC inhibitory interneurons. To complement the imaging analysis, perform whole-cell recordings of PnC interneurons with photostimulation of CeA fibers. These experiments will provide mechanistic evidence for the contribution of excitatory CeA-PnC synapses in PPI.

Chapter 2: Methodology

2.1 Subjects

Experiments were performed on C57BL/6 mice (The Jackson Laboratory, Bar Harbor, ME), GlyT2-eGFP mice (transgenic mouse line acquired from Dr. Manuel Miranda-Arango, The University of Texas at El Paso, El Paso, TX) and GlyT2-Cre^{+/-} mice (transgenic mouse line acquired from Dr. Jack Feldman, University of California, Los Angeles). Mice received food and water *ad libitum* in a 12 hour light/12 hour dark cycle. Litters were weaned at PND 21 and housed together until stereotaxic microinjections were performed at PND 70-84 (adult). This age corresponds to the age of the animals used in the Paxinos and Franklin Mouse Brain Atlas, from which all the stereotaxic coordinates were derived and brain regions delineated (2004). Following surgical procedures, mice were single-housed and monitored for the duration of the recovery period. All experiments presented in this section were performed in accordance with the Institutional Animal Care and Use Committee (IACUC) and the Laboratory Animal Resources Center (LARC) at The University of Texas at El Paso (UTEP), and the IACUC at the University of Massachusetts Amherst (UMass).

2.2 Tissue preparation for transmission electron microscopy

Acute brain slices (300µm) at the level of the PnC of 2 mice were immersed in Karnovsky's fixative (in 0.12M PBS, pH 7.4) for 20 mins at -4°C. Tissue slices were then rinsed with 0.06M PBS (3 rinses, 10 mins each), and immersed in 2% osmium tetroxide in 0.06M PBS (pH 7.4) for 20 mins at -4°C in darkness. Following rinses (3 rinses, 10 mins each), tissue slices were incubated in 2% uranyl acetate (pH 5.2) for 15 mins at room temperature in darkness, and rinsed (3 rinses, 10 mins each). For embedding, slices

were sequentially incubated in 70/30%, 50/50% and 30/70% of acetone/PolyBed 812 followed by 100% PolyBed 812 for 30mins each. Tissue sections were then transferred to a flat mold, covered in 100% PolyBed 812, and placed in a 60°C oven for 48 hours. Once plastic hardened, excess plastic was shaved off to gain access to the tissue. Using an ultramicrotome (Leica Ultracut UCT, Wetzlar, Germany) and a glass knife, 50-60nm thin serial sections of the PnC were cut and collected on copper grids. Post-staining of thin sections to enhance contrast consisted on a 5mins incubation period with 2.5% uranyl acetate, rinsed with distilled water for 2 mins, lead citrate incubation for 2 mins, and rinsed with distilled water. Copper grids with tissue sections were air-dried overnight.

2.3 Neuronal tract-tracers and viral vectors

FluoroGold (Molecular Probes, Eugene, OR, catalog# H22845, lot# 1611168), a monosynaptic retrograde tract tracer, was suspended in 0.9% saline solution and stored at -80°C. Adeno associated viral constructs (serotype DJ; 4×10^{12} particles/mL; obtained from the Deisseroth Lab/Optogenetics Innovation Lab Stanford University, Stanford, CA) were used on separate animal cohorts as indicated in *Table 2.1*. To manipulate CeA-PnC excitatory synapses, mice were injected with three pAAV DJ-CamKII α -*Opsin*-eYFP vectors in the CeA. To silence CeA-PnC excitatory synapses at the PnC, the inhibitory opsins Archaelhodopsin (Arch3.0) or Halorhodopsin (NpHR3.0) were used. Conversely, to activate this subset of the CeA-PnC connection, Channelrhodopsin-2 (ChR2) was used. As a control and for tract-tracing purposes, mice were injected with a control vector lacking the opsin gene (pAAV DJ-CamKII α -eYFP or pAAVDJ-CamKII α -mCherry). In a transgenic mouse line expressing Cre recombinase under the GlyT2 promoter, a Cre-

dependent AAV vector (pAAVDJ-CAG-FLEX-tdTomato-WPRE) was injected in the PnC. In this manner, GlyT2⁺ cells in the PnC were visible during whole-cell recordings.

2.4 Stereotaxic Injections

Ten-to-twelve week old mice were sedated by inhaling 5% isoflurane vapors (Piramal Critical Care, Bethelhem, PA, catalog# 26675-46-7); then placed in a stereotaxic apparatus (David Kopf, Tujunga, CA, model 900), and immobilized using ear bars and a nose cone. Mice were maintained under anesthesia (1.5%-2% isoflurane in oxygen) throughout the duration of the surgical procedure, and administered an intraperitoneal injection of 0.1ml of dexamethasone. Following scalp sterilization and incision, the head was leveled and zeroed on all three planes (anterior-posterior - AP, medial-lateral - ML and dorsal-ventral – DV) using the anatomical points on the skull, bregma and lambda, as reference. A craniotomy was then performed by drilling a small hole in the skull located directly dorsal to the injection site. Using a pressure microinjector (Stoelting Co., Wood Lane, IL, catalog# 53311) with a 5µl Hamilton syringe (Hamilton Company Inc., Reno, NV, catalog# 80016) and a 32 gauge steel needle, a unilateral injection of 50-80nl of FluoroGold was targeted to the PnC (Coordinates: -5.35mm AP; +0.5mm ML, -5.6mm DV). In separate animal cohorts, 100-125nl of a viral vector were injected unilaterally in the CeA (-1.4mm AP, +2.46mm ML, -4.6mm DV) or PnC. FluoroGold and viral particles were infused at a rate of 50nl/min. After tracer infusion was completed, the microinjection syringe remained in place for 10 minutes to limit spillover during needle retraction. The craniotomy was covered with antibiotic ointment, the incision was sutured, and antibiotic ointment was applied on the sutured area. Mice were then administered subcutaneous

injections of 0.05ml GentaVed antibiotic (Vedco Inc., St. Joseph, MO, catalog# 200-037) and 0.1ml Flunazine analgesic (Norbrook, Overland Park, KS catalog# 200-308). Following surgical procedures, mice were monitored for 5 days. FluoroGold-injected mice recovered for 5 days postoperatively, time period during which the transport of this retrograde tracer to the site of interest was completed. AAV-injected mice recovered for 3-4 weeks, time period required for maximal reporter gene expression at the target site. For NpHR3.0 injections in the ventral hippocampus (vHPC), the following coordinates were used: 1) -3.05mm AP, -2.40 ML, 2.55mm and -3.75mm DV; 2) -3.05mm AP, 2.65mm ML, -1.85mm, -3.00mm and -4.40mm DV; 3) -3.05mm AP, 3.00mm ML, -2.15mm and -4.25mm DV; 4) -3.05mm AP, 3.35mm ML, -2.55mm and -3.92mm DV; 5) -3.05mm AP, 3.55mm ML, -2.95mm DV. Mice injected in the vHPC recovered for 2 weeks.

Table 2.1 Viral vectors and tracer dyes for optogenetics and tract-tracing

Viral Construct	Use	Addgene ID/OIL #	
pAAVDJ-CamKII α -eYFP	Anterograde tract-tracing Electrophysiology - control Behavioral testing - control	114469 (other)/GVVC-AAV-8	
pAAVDJ-CamKII α -mCherry	Anterograde tract-tracing in GlyT2-eGFP mice	114469 (other)/GVVC-AAV-9	
pAAVDJ-CamKII α -Chr2-eYFP	Field and whole-cell recordings Behavioral testing - experimental	26969/GVVC-AAV-36	
pAAVDJ-CamKII α -Arch3.0-eYFP	Behavioral testing - experimental	35516/GVVC-AAV-53	
pAAVDJ-CamKII α -NpHR3.0-eYFP	Behavioral testing – experimental Whole-cell recordings in the vHPC	26971/GVVC-AAV-57	
pAAVDJ-CAG-FLEX-tdTomato-WPRE	Whole-cell recordings in the PnC	51503	
Tracer	Source	Catalog/Lot#	Concentration
FluoroGold	Molecular Probes	H22845/1611168	2% in saline solution

2.5 Tissue preparation for immunohistochemistry/microscopy analysis

Mice were lethally sedated with isoflurane, and exsanguinated transcardially by perfusion of 100ml of 0.9% saline solution followed by 150ml of chilled 4% paraformaldehyde (PFA) solution (pH 9.5 at 4°C) in phosphate buffer saline (PBS) at the level of the left ventricle. Mice were then decapitated, and brains were extracted. Brains were post-fixed overnight in 12% sucrose in the 4% PFA solution. Following post-fixation, brains were blotted to remove excess fixative, frozen in chilled hexane for 1 minute, and stored at -80°C. Using a microtome (Leica, Wetzlar, Germany, model SM200R), four 1-in-5 series of 30µm coronal sections were cut through the entire brain, and stored in a cryoprotectant solution at -20°C. One of the series was rinsed with Tris-buffered saline (TBS, pH 7.4), mounted and coverslipped to image injection site and projection sites. An adjacent series of brain sections was mounted on gelatin-coated slides for Nissl staining to determine plane of section, delineate cytoarchitectural boundaries, and map injection and projection sites. The two remaining series were used for immunohistochemistry.

For GABA immunohistochemistry, mice were transcardially perfused with Karnovsky's fixative. Brains were then immersed in this fixative with 12% sucrose overnight at 4°C.

2.6 Immunohistochemistry

Tissue sections were rinsed with TBS (five rinses, five minutes each), then incubated in blocking solution (2% normal donkey serum, 0.1% Triton X-100; in TBS) for 1-2 hours at room temperature. Tissue sections were then incubated in the primary antibodies of interest for 60 hours at 4°C. Following TBS rinses (five rinses, five minutes each), tissue sections were incubated in respective secondary antibody-fluorophore conjugates for 4-5 hours at room temperature, and rinsed with TBS. In the case of AAV injected mice,

tissue sections were then incubated in NeuroTrace™ (1:100 in TBS, ThermoFisher, catalog# N21483). NeuroTrace™, a fluorescent Nissl stain, was alternatively used to determine plane of section and cytoarchitecture. Tissue sections were then rinsed with TBS (five rinses, five minutes each), mounted on glass slides, coverslipped with mounting media (sodium bicarbonate buffered glycerol), and sealed with nail polish. Controls consisted of tissue sections incubated with blocking solution instead of primary antibody. Primary and secondary antibodies were diluted in blocking solution. *Table 2.2* contains the details of the primary antibodies and corresponding secondary antibodies used in this project

2.7 Nissl staining

Tissue slices mounted on gelatin-coated slides were immersed on a series of solutions (*Table 2.3*). The Nissl stain method used in this project consisted of three main sets of steps. The first set of steps dehydrates the tissue in ascending concentrations of ethanol to make it compatible with xylenes, which removes fat from the tissue. The second set of steps rehydrates tissue in descending concentrations of ethanol to be stained with a thionin acetate solution. The third set of steps dehydrates tissue to make it compatible with DPX, the mounting medium. Then, inside a fume hood, slides were then coverslipped with DPX, and air-dried overnight.

Table 2.2 Antibodies for immunohistochemistry

Antigen	Source	Catalog/Lot#	Host	Dilution
ChAT	Millipore	AB144P-200UL/2854034	Goat	1:200
GABA	abcam	ab17413/GR3274793	Guinea Pig	1:500
GFP	abcam	ab13970/GR236651-13	Chicken	1:1000
mCherry	abcam	ab205402/GR225123-3	Chicken	1:1000
Parvalbumin	abcam	ab11427/GR3250017-1	Rabbit	1:1000
PRODH	Sigma Aldrich	SAB2501795-100UG/7166P1	Goat	1:1000
PSD-95	abcam	ab12093/GR317630-1	Rabbit	1:500
RFP (tdTomato)	abcam	ab62341/GR193835-2	Rabbit	1:500

Antibody/Protein	Source	Catalog/Lot#	Conjugate	Dilution
Donkey anti-goat	Jackson-ImmunoResearch	705-165-147/115611	Cy3	1:500
Donkey anti-rabbit	Jackson-ImmunoResearch	705-545-147/125100	Cy5	1:500
Donkey anti-rabbit	Jackson-ImmunoResearch	711-165-152/13947	Cy3	1:500
Donkey anti-chicken	Jackson-ImmunoResearch	703-545-155/130357	Alexa Fluor 488	1:500
Donkey anti-chicken	Jackson-ImmunoResearch	703-165-155/130328	Cy3	1:500
Donkey anti-guinea pig	Jackson-ImmunoResearch	706-175-148/23021	Cy5	1:500
Streptavidin	Jackson-ImmunoResearch	016-170-084/138512	Cy5	1:500
Neurotrace™	ThermoFisher Scientific	N21483/1837175	640/660	1:100

2.8 Tissue preparation for *in vitro* extracellular field electrophysiological recordings

Four-to-five weeks after viral injection, mice were anesthetized with isoflurane, and rapidly decapitated after cervical dislocation. The brain was harvested and chilled in ice-cold dissection solution (in mM): sucrose (195), NaCl (10), KCl (2.5), NaH₂PO₄ (1), NaHCO₃ (25), glucose (10), MgCl₂ (5), MgSO₄ (1), CaCl₂ (0.5) constantly bubbled with 5%CO₂/95%O₂ (carbogen). The olfactory bulb and part of the prefrontal cortex were cut

off, the brain was glued to a magnetic platform caudal part facing up, and 300µm coronal brain sections were cut with a vibratome (Leica, Wetzlar, Germany, model VT1200S). Acute brain slices at the level of the CeA or PnC were cut and immediately transferred to a beaker with artificial CSF (aCSF; constantly bubbled with carbogen) at room temperature with the following composition (in mM): NaCl (124), KCl (2.5), NaH₂PO₄ (1), NaHCO₃ (25), Glucose (10), MgSO₄ (1), CaCl₂ (2). Acute brain slices were transferred to an interface chamber (Harvard Apparatus, Holliston, MA, catalog #65-0073) to recover for at least 2hrs at 31–32°C. Carbogenated aCSF was continuously fed by gravity at a rate of ≈2mL/minute. The interface chamber was mounted on a M165FC apochromatic corrected stereoscope (Leica Microsystems Inc., Buffalo Grove IL).

Table 2.3 Nissl staining protocol

First set of steps		Second set of steps		Third set of steps	
Time	Solution	Time	Solution	Time	Solution
3 min	DI Water	2 min	Xylene 1	20 dips	DI water
3 min	50%	2 min	100%*	20 dips	50%
3 min	70%	2 min	100%*	20 dips	70%
3 min	95%*	2 min	100%*	3 min	95%*
3 min	95%*	2 min	95%*	3 min	95%*
3 min	100%*	2 min	95%*	3 min	100%*
3 min	100%*	2 min	70%	3 min	100%*
3 min	100%*	2 min	50%	3 min	100%*
5 min	Xylene 1	2 min	DI Water	3 min	Xylene 1
30 min	Xylene 2	8-20 dips**	Thionin	3 min	Xylene 2

%: percentage of ethanol in DI water.

*steps with same ethanol concentration were done in separate containers.

**number of dips depended on staining intensity observed in between dips.

2.9 Tissue preparation for *in vitro* whole-cell recordings

Whole cell recordings were performed on acute brain slices from adult mice 2 weeks after the intracranial injection of NpHR3.0 in the vHPC of WT mice, or tdTomato in the PnC of GlyT2-Cre^{+/-} mice. Mice were anesthetized, followed by cervical dislocation and rapid decapitation. The brain was harvested and placed in a constantly carbogenated ice-cold dissection solution (in mM): sucrose (210), KCl (2), KH₂PO₄ (1.2), NaHCO₃ (26), glucose (10), MgCl₂ (2), MgSO₄ (1.3), CaCl₂ (0.5), Myo-inositol (3), Sodium pyruvate (2) and Ascorbic acid (0.4). CaCl₂ was added after 30mins of carbogenation, which buffers pH to 7.3-7.4. Using a vibratome, 300µm-thick horizontal sections containing the vHPC or coronal sections at the PnC and CeA level were cut. These sections were immediately transferred to a beaker filled with carbogenated aCSF in a hot water bath at 34°C. The aCSF was composed of (in mM): NaCl (124), KCl (2.5), NaH₂PO₄ (1), NaHCO₃ (25), Glucose (10), MgSO₄ (1) and CaCl₂ (1). After tissue slices were transferred to the beaker, 80µl of 2mM CaCl₂ were added. After 30 minutes at 34°C, the beaker was placed at room temperature for the duration of the recording session. One acute slice was transferred to a recording chamber and secured with a nylon mesh submerged in aCSF fed by gravity at a rate of ≈2mL/minute. CaCl₂ concentration for the recording aCSF bathing the acute slices was 2mM, which was added following 30mins of carbogenation. The recording chamber was mounted on the stage of a Nikon FN1 physiostation (Micro Video Instruments, Avon, MA) equipped with a CFI Plan 4x objective, a Apochromat NIR 40X objective, GFP and Texas Red fluorescent filters, a Cool LED pE300 light source and a PCO Panda 4.2 sCMOS camera.

2.10 Extracellular electrophysiological field recordings

The recording electrode was placed in the medial CeA or the lateroventral area of the PnC (dorsal to the DPO). Data was acquired with pClamp10 software (Molecular Devices LLC, Sunnyvale, CA), using an extracellular amplifier (Cygnus Technologies, Southport, NC, model ER-1) and a Digidata 1440A digitizer (Molecular Devices LLC, Sunnyvale, CA).

2.10.1 Light-evoked fEPSPs at the PnC

Field excitatory post-synaptic potentials (fEPSPs) were evoked by delivering a 1ms blue light pulse with a 200 μ m optical fiber (Plexon, Dallas, TX, item# 94062) mounted on a micromanipulator (Narishige, Amityville, NY, catalog# MWS-31) and connected to blue LED module (473 nm; Plexon, Dallas, TX). The optical fiber was in close proximity to a glass micropipette recording electrode (1-3M Ω ; Warner Instruments, LLC, Hamden, CT, item# 64-0827) filled with aCSF and placed within the CeA or PnC. Basal CeA-PnC synaptic transmission was assessed at 0.033Hz, by gradually increasing the light intensity from 1-11 relative light units (1rlu = 0.43mW). For the following protocols, the light intensity generating a half maximum response was used. Paired optical pulses every 15 seconds with different interstimulus intervals (ISI in ms; 2, 5, 10, 20, 50, 100, 200, 300, 500, 1000, 1500) were applied to analyze the presynaptic efficacy of vesicle release.

2.10.2 Application of glutamate receptor antagonists

Glutamate ionotropic receptor antagonists, AP5 and CNQX, and GABA_A receptor antagonist, Gabazine, were stored as stock solutions at -20°C, then freshly diluted at the indicated concentrations (*Table 2.4*) prior to use. Initially, a pre-treatment recording session of 10 minutes was performed. The solution was then fed by gravity to bathe the acute brain slices for 20 minutes, followed by a 10-minute recording session. The

antagonists were washed out with aCSF for 20 minutes, followed by a 10-minute recording session.

Table 2.4 Receptor blockers used during electrophysiological recordings

Antagonist	Receptor blocked	Source	Catalog/Lot#	Solvent	Concentration
AP5	Glutamate – NMDA	abcam	ab120003/GR43480-11	aCSF	50 μ M
CNQX	Glutamate – AMPA	abcam	ab120017/GR69180-7	aCSF	25 μ M
DNQX	Glutamate – AMPA	Tocris		aCSF	25 μ M
Gabazine	GABA – GABA _A	abcam	ab120042/GR202999-53	DMSO	10 μ M

2.10.3 Electrical stimulation of auditory fibers

Auditory fibers were electrically stimulated with a bipolar stimulating electrode (tip diameter 0.2 mm, FHC, Bowdoin, ME, catalog# CBBRC75) placed on the LVPO (ventral to the LSO, ~1.25mm ML) of acute slices at the level of the PnC. Similar to the recordings with photo-stimulation, the recording electrode was placed in the lateroventral area of the PnC. Evoked fEPSPs in the PnC in response to auditory fiber stimulation were recorded, which simulates the physiological stimulation of the auditory fibers by the startling sound during the ASR. Basal synaptic transmission of auditory fibers in the PnC was characterized at 0.033 Hz, with increasing stimulation intensities and a pulse duration of 0.1ms. The subsequent protocols were performed at the stimulus intensity that elicited a fEPSP one-third of the maximum fEPSP recorded. Paired pulses were applied every 15 seconds with different ISIs (in ms: 2, 5, 10, 20, 50, 100, 200, 300, 500, 1000, 1500) to analyze the probability of vesicular neurotransmitter release from auditory fibers onto PnC neurons.

2.10.4 *In vitro* PPI

With the recording electrode placed on the lateroventral PnC (just dorsal to the DPO and medial to the 7n), the PPI task *in vitro* consisted of a 1ms light pulse (“prepulse”) to stimulate CeA fibers, followed by a 0.1ms electrical pulse (“startling pulse”) to activate auditory fibers. The light pulse followed by electrical stimulation were delivered at different ISI (in ms): 10, 20, 50, 100, 200, 300, 500, 1000, 1500 to determine at which ISI the CeA modifies auditory-evoked activity in the PnC.

2.10.5 Presynaptic contribution of CeA inputs to Cochlear fibers in the PnC

To determine presynaptic filtering of auditory fibers by CeA inputs, paired electrical stimulation separated by 50 or 100ms at the LVPO was preceded by a 1ms light pulse at different ISI (in ms): 5, 10, 20, 50, 100, 200, 300, 500, 1000.

2.11 Whole-cell recordings

Whole-cell recordings were performed using glass pipettes (3–5 M Ω) filled with intracellular solution (in mM): KMeSO₄ (125), KCl (10), HEPES (10), NaCl (4), EGTA (0.1), MgATP (4), Na₂GTP (0.3), Phosphocreatine (10), Biocytin (0.1%) (pH=7.3; osmolarity=285–300 mosm). The glass microelectrode was mounted on a patch clamp headstage (Molecular Devices LLC, Sunnyvale, CA; catalog# CV-7B), which was attached to a multi-micromanipulator (Sutter Instrument, Novato, CA; catalog# MPC-200). Data was acquired with pClamp10 software using a MultiClamp™ 700B amplifier (Molecular Devices LLC, Sunnyvale, CA) and a Digidata 1550B digitizer (Molecular Devices LLC, Sunnyvale, CA). EYFP-expressing cells in the pyramidal layer of the vHPC or within the CeA, or tdTomato-expressing cells in the PnC were imaged and targeted using NIS-Elements Basic Research software (version 5.11, Nikon Instruments Inc.,

Melville, NY). Only cells with an initial seal resistance greater than $1\text{G}\Omega$, a resting membrane potential between -60mV and -70mV , a holding current within -100pA to 100pA at resting membrane potential and overshooting action potentials were used.

2.11.1 vHPC recordings

In vHPC slices, 15pA depolarizing current steps were injected for 500ms to induce action potentials in hippocampal neurons. To photo-inhibit these action potentials, 5Hz light pulses were delivered during the current injection using a $200\mu\text{m}$ mounted on a micromanipulator connected to an orange LED (620nm ; Plexon, Dallas, TX).

2.11.2 PnC and CeA recordings

First, the intrinsic properties of the cells were assessed under voltage clamp configuration. The cells were clamped at -70mV (close to their resting potential), and spontaneous excitatory postsynaptic currents (sEPSC) were recorded for 5mins . Then at 0mV , inhibitory postsynaptic currents (IPSCs) were recorded for 5mins . In current clamp mode, 15pA depolarizing current steps (from -150pA to 150pA) were injected for 500ms to analyze the spiking properties of the cells.

Optical stimulation was then used to activate CeA fibers while recording synaptic responses in PnC GlyT2⁺ neurons, which were held at -70mV . One millisecond blue light pulses were applied to elicit EPSPs and EPSCs. Paired light pulses with 50 and 100ms ISI were then delivered to characterize short-term plasticity. Similarly, at 0mV , light pulses were delivered to isolate and record inhibitory post-synaptic potentials (IPSPs) and IPSCs. In voltage clamp mode, light pulses were delivered at -70mV and -30mV to evaluate NMDA- and AMPA-mediated currents, respectively.

Similar to the field recordings, glutamate receptor antagonists, AP5 and DNQX, were freshly diluted at the indicated concentrations (Table 2.4) prior to use. Initially, a pre-treatment recording session of 10 minutes was performed. The solution was then fed by gravity to bathe the acute brain slices for 20 minutes, followed by a 10-minute recording session. The antagonists were then washed out with aCSF for 20 minutes, followed by a 10-minute recording session.

Once all recordings were obtained from a cell, the cell membrane was sealed by forming an outside-out patch. The glass microelectrode was slowly retracted, and as the series resistance increased, the membrane potential was clamped at -40mV. This allowed subsequent immunostaining, imaging and morphological analysis of the patched cells.

2.12 Acute brain slice preparation for microscopy analysis

Immediately after electrophysiological experiments, the 300µm-thick acute brain slices (at the level of the CeA or PnC) were immersed in 4% PFA solution overnight. Tissue slices used for extracellular field recordings were frozen in chilled hexane for 30 seconds. Then, three 1-in-5 series of 30µm coronal sections were cut through the entire 300µm-thick brain slices, and stored in cryoprotectant at -20°C. To confirm fluorescence within injection (CeA) and projection (PnC) sites, tissue sections were then prepared mounted and coverslipped.

Following PFA fixation overnight, tissue slices used for whole-cell recordings were rinsed with PBS (3 times, 5mins each). Slices were then incubated in anti-RFP and/or anti-GFP antibodies and complementary secondary antibodies to enhance fluorescence of the vectors used. Following PBS rinses, Cy3- or Cy5-conjugated streptavidin (a biotin-

binding protein; *Table 2.2*) diluted in PBS (with 0.1% Triton X-100) at room temperature for 4-5 hours or overnight at 4°C. Slices were then rinsed with PBS, mounted on glass slides, coverslipped and sealed with ProLong™ Gold antifade reagent (Invitrogen by ThermoFisher Scientific, Waltham, MA, catalog# P36934, lot# 1943081), and air dried overnight in the dark (Booker *et al.*, 2014; Sweietek *et al.*, 2016).

2.13 Behavioral testing

2.13.1 Mice cohorts

Behavioral testing was performed on five animal cohorts. Two groups of mice were used as controls: 1) a non-injected group of 14-16 week-old mice, which corresponded to the age of the injected mouse groups after the cannula implantation procedure, and 2) a control group of mice injected with a viral vector lacking the opsin gene (pAAVDJ-CamKIIa-eYFP). Two experimental groups each injected with an inhibitory opsin vector, archaerhodopsin (pAAVDJ-CamKIIa-eArch3.0-eYFP) or halorhodopsin (pAAVDJ-CamKIIa-NpHR3.0-eYFP) were used to silence the CeA-PnC connection. A third experimental group injected with Channelrhodopsin (pAAVDJ-CamKIIa-hChR(H134R)-eYFP) was used to photo-stimulate CeA-PnC synapses.

2.13.2 Cannula guide implantation

Three weeks after the injection, a cannula guide was implanted in the PnC. Mice were sedated with 5% isoflurane vapors, placed in a stereotaxic apparatus, and immobilized using ear bars and a nose cone. Mice were maintained under anesthesia (1.5%-2% isoflurane) throughout the duration of the surgical procedure. Following head leveling, a craniotomy was performed by drilling a small hole in the skull located directly dorsal to

the implantation site. A cannula guide (Doric Lenses Inc. Quebec, Canada), consisting of a ferrule and a 200 μ m (in diameter) optical fiber was cut to no less than 6.5mm long. The optical fiber end was then inserted into the PnC (AP -5.35mm, ML +0.5mm, DV -5.2mm), and attached to the skull with dental cement (Parkell, Edgewood, NY, item# S380). Mice were then administered subcutaneous injections of 0.05ml GentaVed antibiotic and 0.1ml Flunazine analgesic and monitored for 5 days post-surgery before behavioral testing.

2.13.3 Behavioral testing setup

One week after cannula guide implantation, the behavioral testing was performed using a startle response system (PanLab System; Harvard Apparatus, Holliston, MA). Behavioral testing protocols were created, and data were collected using PACKWIN V2.0 (Harvard Apparatus, Holliston, MA). Sound pressure levels were calibrated using a standard SPL meter (model 407730, Extech, Nashua, NH). Behavioral testing was divided into four experimental tasks: ASR, ASR with optogenetics, PPI, and PPI with optogenetics (see below). During all trials, an optical fiber (Thorlabs, Newton, NJ, item# RJPFF2) was connected to a 593.5nm laser (Opto Engine LLC, Midvale, UT, catalog# MGL-F-593.5-100mW) for mice injected with NpHR3.0, a 473nm laser (Opto Engine LLC, Midvale, UT, catalog# MBL-III-473-100mW) for mice injected with ChR2, or a green LED (532nm; Plexon, Dallas, TX) for mice injected with Arch3.0-injected; while the other end was attached to the cannula implant on the mouse with a zirconia sleeve (Thorlabs, Newton, NJ, item# ADAF1). Each testing session started with a 10min acclimatization period with background white noise (65dB) during which the animal was exposed to the startle chamber.

2.13.4 ASR task

During ASR trials, mice were presented with 40ms sound pulses at different intensities (in dB: 70, 80, 90, 100, 110 and 120). Immediately after the presentation of the sound pulse, a 1s recording period was examined for any motor response. Each pulse intensity was presented 5 times in pseudorandomized order with a 15s interval (with 65dB background noise) in between pulses. For the ASR with optogenetics task, 5Hz light pulses (and 20Hz for the ChR2 group only) were presented 1s before and through the onset of the sound pulse.

2.13.5 PPI task

Following an acclimatization period of 10mins, PPI trials started with seven 120dB sound pulses presented every 29s (with 65dB background noise) to establish basal ASR level. Then, PPI trials consisted of a 75dB non-startling sound pulse (prepulse) followed by a 120dB startling pulse at different and pseudorandomized ISIs. The ISIs between the prepulse and the startling pulse tested here were (in ms): 10, 30, 50, 100, 200, 300, 500, and 1000. Aside from PPI trials, there were trials where no stimulation was presented, trials with startle pulses presented alone and trials with prepulses presented alone. Each trial was presented 7 times in a pseudorandomized order, every 29s with a 65dB background noise between trials. For the PPI task with optogenetics, 5Hz light pulses (and 20Hz for the ChR2 group only) were presented 1s before the prepulse and lasting until the presentation of the startling pulse. Light pulses alone trials were also included. As in ASR tasks, immediately after each trial, a 1s recording period was examined for any motor response. Mice were then anesthetized, perfused transcardially (as mentioned above), and brains extracted. Histological analyses were performed to confirm that: 1- the injected viral particles targeted the CeA, and 2- the cannula guide placement was

successfully aimed at the PnC. If these criteria were not met, the subject was excluded from the study.

2.14 Microscopy

2.14.1 Transmission electron microscopy

Ultrastructure micrographs were captured in a Zeiss 10A Transmission Electron Microscope (Carl Zeiss Inc., Thornwood, NY) adapted with an Erlangshen ES1000W CCD camera (Gatan, Pleasanton, CA) and Digital Micrograph software (Gatan, Pleasanton, CA) previously located at the Analytical Cytometry Core Facility of the BBRC at UTEP.

2.14.2 Fluorescence microscopy

Imaging of tissue sections from FluoroGold injected mice was performed on an Axio Observer.Z1 inverted epifluorescence microscope (Carl Zeiss Inc., Thornwood, NY) equipped with FG, GFP, Cy3, and Cy5 filters, 10x and 40x objectives, and Axiovision Rel. 4.8 software (Carl Zeiss Inc., Thornwood, NY) located in the Miranda Lab at UTEP. These tissue sections were imaged isolating a single Z-plane. To create photomontages, single Z-plane images were obtained with the MosaiX module of the Axiovision Rel. 4.8 software at 10x for each fluorophore sequentially or with bright-field for Nissl-stained sections (1024 × 1024 pixel resolution).

2.14.3 Laser scanning confocal microscopy

Tissue sections from AAV-injected mice were imaged with a LSM 700 Confocal Microscope (Carl Zeiss Inc., Thornwood, NY) equipped with four lasers (405, 488, 555 and 639 nm), 10X, 20X, 40X, 63X, and 100X objectives, and Zen 2009 software (Carl Zeiss Inc., Thornwood, NY) located within the Cytometry, Screening and Imaging Core

Facility of the Border Biomedical Research Center (BBRC) at UTEP. Tissue sections from GlyT2-eGFP mice were imaged on a Nikon A1 Resonant Confocal microscope (Nikon Instruments Inc., Melville, NY) equipped with: 10x, 20x, 40x, 60x, 100x objectives, six laser lines (in nm: 405, 435, 488, 514, 561, 640), one transmitted light detector, 2 high-sensitivity photomultiplier detectors, 2 gallium arsenide phosphide (GaAsP) detectors, a high resolution Andor camera (Model Zyla 5.5; Andor Technologies, Oxford Instruments, Abingdon, United Kingdom), and NIS-Elements High Content Analysis software (version 5.02, Nikon Instruments Inc., Melville, NY) located in the Light Microscopy Facility (LMF) of the Institute of Applied Life Sciences (IALS) at UMass. Tissue sections mice were first examined on a single Z-plane with the 10x objective to survey the tissue section on a single Z-plane. Using the 60x objective, an area (212.56 μ m width x 212.56 μ m height) within the lateroventral PnC was then sequentially scanned by the 488, 561 and 640nm laser lines in 0.1 μ m Z-steps throughout the 30 μ m tissue section. This same strategy with the 40x objective was used to three dimensionally reconstruct biocytin-filled cells, from which whole-cell recordings were obtained.

2.15 Data analysis

Statistical analyses were performed and graphs/plots were created in SigmaPlot (Systat Software, Inc., San Jose, CA). Sample sizes were chosen based on expected outcomes and variances. Normality and equal variance of data were first tested using the Shapiro-Wilk test and Levene's mean test, respectively. If normality and equal variance were violated, a non-parametric test was conducted. Data are presented as means \pm SEM. N indicates number of mice, n indicates total number of tissue slices (in tract-tracing

and electrophysiological recordings) or trials (in behavioral testing). A criteria of $p < 0.05$ was considered significant for all statistical analyses. Adobe Illustrator (Adobe, San Jose, CA) was used to delineate cytoarchitectural borders of bright-field and fluorescence images, for mapping analysis, and to prepare/edit all figures.

2.15.1 Tract-tracing and immunohistochemistry analyses

Quantification of FluoroGold-labeled or eYFP-expressing cells in the CeA and adjacent regions was performed in ImageJ (U.S. National Institutes of Health, Bethesda, MD). T-tests were used for pair-wise comparisons of FluoroGold or eYFP cell count (CeA vs. adjacent regions).

Z-stacks were analyzed with NIS-Elements 5.0 Advanced Research software (version 5.02, Nikon Instruments Inc., Melville, NY) installed in the computer workstations of the LMF at UMass. To examine if CeA axons (mCherry-labeled) are in close contact with GlyT2⁺ neurons (GFP-labeled), a binary layer was configured to segregate putative synaptic contacts of >50nm in distance (due to technical limitations). These contacts were imaged in split-channels and orthogonal views. Then, Z-stacks were three-dimensionally reconstructed and rendered volume. Images and three-dimensional animations were acquired after orthogonal and adjusted angle sectioning. Similarly, images and z-stacks from the co-localization analysis of PV and PRODH in GlyT2⁺ neurons were visualized in split channels and reconstructed.

2.15.2 Electrophysiological recordings analysis

The fEPSPs were quantified by measuring the initial slope of the peak negativity of the synaptic responses using Clampfit (Molecular Devices LLC, Sunnyvale, CA). Events from whole-cell recordings were quantified by the amplitude of the peak. Data was then

transferred and organized in Microsoft Office Excel (Microsoft Corporation, Redmond, Washington). For electrophysiological recordings with receptor antagonists, one-way repeated measures ANOVA followed by Tukey post-hoc test were used to determine the effect of the antagonists on the light-evoked events. Paired-pulse ratio was calculated for all ISI by dividing the slope or peak of the second event by the slope or peak of the first event ($PPR = fEPSP2 \text{ slope}/fEPSP1 \text{ slope}$ or $PPR = \text{event 2 amplitude}/\text{event 1 amplitude}$). For PPI *in vitro* and presynaptic filtering of auditory fibers, one way ANOVAs and Tukey post-hoc testing were used to reveal at which ISI the electrically-evoked fEPSPs or PPRs were altered by optical stimulation of CeA-PnC excitatory synapses. For vHPC whole-cell recordings, a paired t-test was conducted to determine the effect of light on evoked spiking activity. For PnC whole-cell recordings with photostimulation, a pairwise comparison of the spiking activity of light unresponsive and responsive cells was assessed with a two-way ANOVA, with light/no light response and current as factors. Differences in sEPSC and IPSC amplitudes of these two groups was evaluated with a paired t-test.

2.15.3 Behavioral testing data analysis

For each subject, PPI was measured as: $[1 - (\text{startle amplitude in PPI trials}/\text{startle amplitude on "startling pulse alone" trials})] \times 100$. For optical inhibition, two-way repeated-measures ANOVA was used to assess the effect of the vector used, light, the sound intensity/ISI and light interaction, then Tukey testing was applied for post-hoc comparisons. Similarly, for optical stimulation as a prepulse *in vivo*, two-way repeated-measures ANOVA was used to assess the effect of the prepulse stimulation

modality/frequency used, ISI, ISI and stimulation modality/frequency interaction, then Tukey testing was applied for post-hoc comparisons.

Chapter 3: Results

3.1 Dissecting the anatomical and neurochemical profile of a central amygdalar input to the core of sensorimotor gating

Earlier studies (Koch *et al.*, 1993; Swerdlow *et al.* 1993) indicating that acetylcholine PPTg neurons were chiefly, but not solely, responsible for PPI suggested that other chemical systems and brain regions also mediate PPI. Since PPI is a relatively short-latency phenomenon (within milliseconds), we hypothesized that contribution from other brain regions may occur via a direct connection to the PnC. Previous rat studies identified a direct CeA-PnC connection underlying fear potentiated startle (Rosen *et al.*, 1989; Rosen *et al.*, 1991); while its contribution to PPI remains uninvestigated. Here, we investigate this CeA-PnC connection for its potential contribution to sensorimotor gating.

3.1.1 PnC receives direct anatomical CeA input: a retrograde tracing analysis

We first confirmed the presence of this connection in our mouse model. Unilateral FluoroGold injections in the PnC resulted in FluoroGold-labeled cell bodies clustered within the ipsilateral CeA (Figure 3.1; N=4). As shown in figures 3.1C-D, the gliotic lesion and fluorescent halo of the FluoroGold deposit, used to pinpoint the extent of the injection site, were confined within the PnC cytoarchitectural borders. This was then corroborated by mapping the injection site to the Mouse Brain Atlas (Figure 3.1E; Paxinos and Franklin, 2004). A closer examination of several FluoroGold injections throughout all PnC levels, to consider the injection variability, helped optimize the PnC coordinates that resulted in labeled neurons within the CeA (i.e. where the CeA axonal terminals are in the PnC). As shown in figure 3.2, injections sites encompassing the lateral area of the PnC and brain regions lateral to the 7n resulted in retrograde labeling in the CeA. PnC injections were further confirmed by examining the PPTg, known to be connected to the PnC (Figure 3.3).

In accordance with the study by Koch and colleagues (1993), we detected some FluoroGold-labeled PPTg cell bodies (i.e. neurons connected to the PnC) that expressed ChAT, a cholinergic marker used to delineate the cytoarchitecture of the largely cholinergic PPTg. Other FluoroGold-labeled PPTg cells did not show ChAT labeling and are possibly glutamatergic or GABAergic (Figure 3.3D). At all anatomical levels containing the CeA, FluoroGold-labeled cell bodies clustered near the border of the dorsomedial portion of the anterior amygdalar complex (Figure 3.1G-I). Although mostly observed within the CeA (307 ± 20 cells), Fluoro-Gold labeled neurons were also located in adjacent brain regions (76 ± 6 cells), such as the BSTIA, CPu and LH.

3.1.2 CamKII α CeA neurons project to the PnC: an anterograde tracing approach

Whether FluoroGold is specifically taken up by axon terminals, or also by fibers *en passant* damaged by needle insertion, is still debated (Falgairolle and O'Donovan, 2015). Therefore, to confirm our previous observation, an anterograde approach consisting of a unilateral injection of pAAV-CamKII α -eYFP particles in the CeA was implemented (Figure 3.4A; N=4). These AAV particles contained a plasmid coding for eYFP under control of CamKII α , a promoter to predominantly target excitatory components. A successful targeted injection was, in part, evident by the presence of several cell bodies within the medial CeA expressing EYFP (Figure 3.4B-D; Figure 3.5). Similar to FluoroGold injections, the lesion by the needle insertion was used to map the injection site, observed within the CeA (Figure 3.4D). At the level of the PnC, we observed EYFP-expressing axonal projections that coursed in a lateral-to-medial fashion from the Pr5VL, Pr5DM and PCRtA (lateral to the 7n) and into the PnC (Figure 3.4F-H). These fibers were denser at the lateroventral area of the PnC, just dorsal to the superior olivary complex (Figure 3.4G).

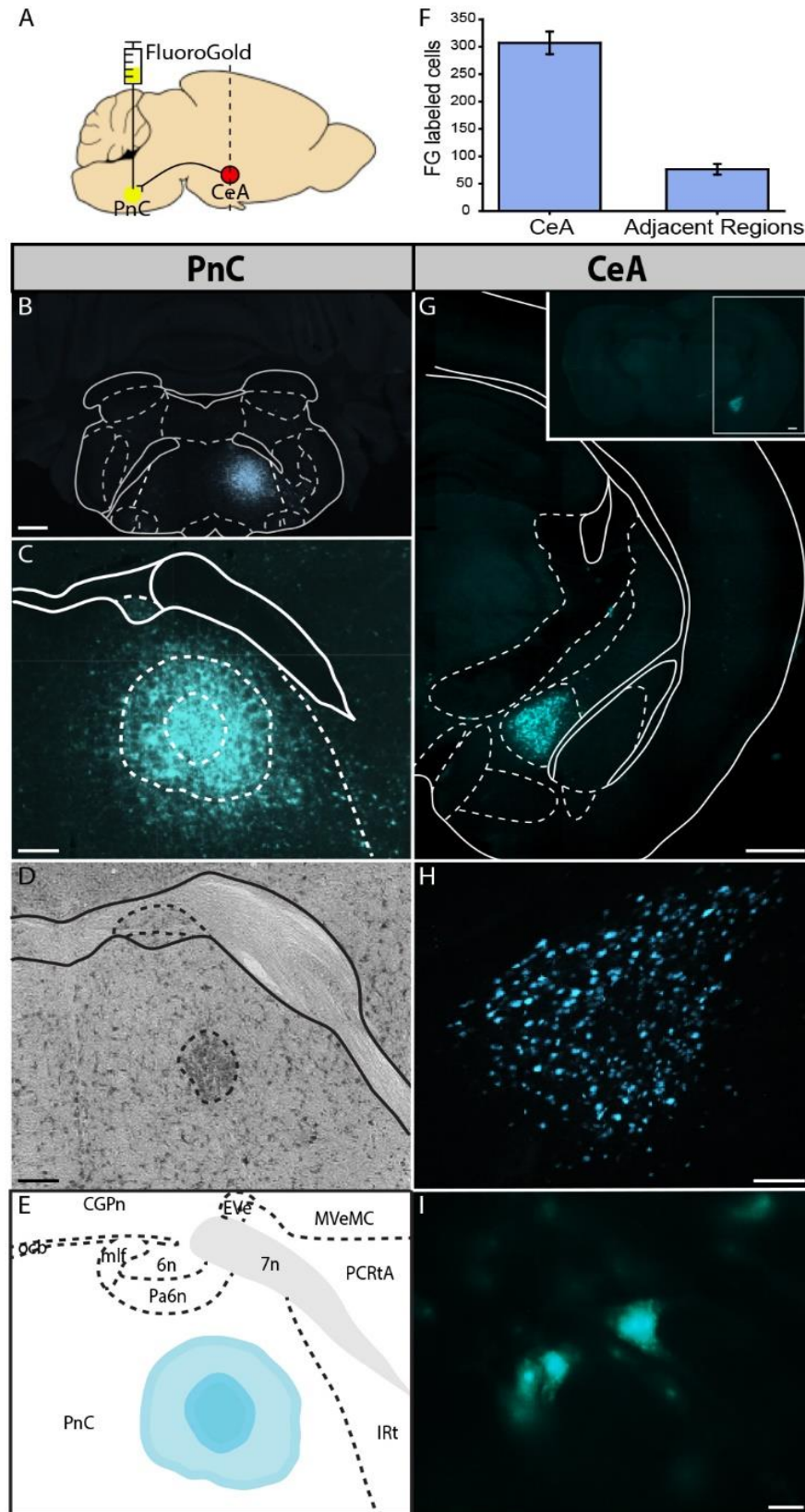


Figure 3.1. The PnC receives monosynaptic projections from the CeA. **(A)** Sagittal representation of the mouse brain illustrating the retrograde tract-tracing approach: FluoroGold was injected in the PnC (yellow circle), and retrograde labeling was observed in the CeA (red circle). **(B)** Representative coronal brain slice with a unilateral injection site of Fluoro-Gold (cyan) within the PnC, medial to the 7th cranial nerve. **(C)** The extent of the Fluoro-Gold injection is delineated by the fluorescent halo (outer dotted circle) surrounding the gliotic lesion (inner dotted circle) caused by the injection. **(D)** Nissl-staining of an adjacent section to the one shown in (C) makes the gliotic lesion more evident (dark spot). **(E)** Injection site in the PnC mapped onto level 77 of the Paxinos and Franklin Mouse Brain Atlas. **(F)** The number of Fluoro-Gold labeled cell bodies within the CeA were significantly higher than in adjacent brain regions. **(G, H)** Representative coronal section at the level of the CeA showing ipsilateral Fluoro-Gold back-filled cell bodies (cyan) within the CeA. Inset: Fluoro-Gold cell bodies were only observed ipsilateral to the injection site. **(I)** Fluoro-Gold-labeled cell bodies in the CeA shown at higher magnification. Data are represented as mean \pm SEM. Scale bars: (B, G) 500 μ m, (C, D) 200 μ m, (H) 100 μ m, (I) 10 μ m.

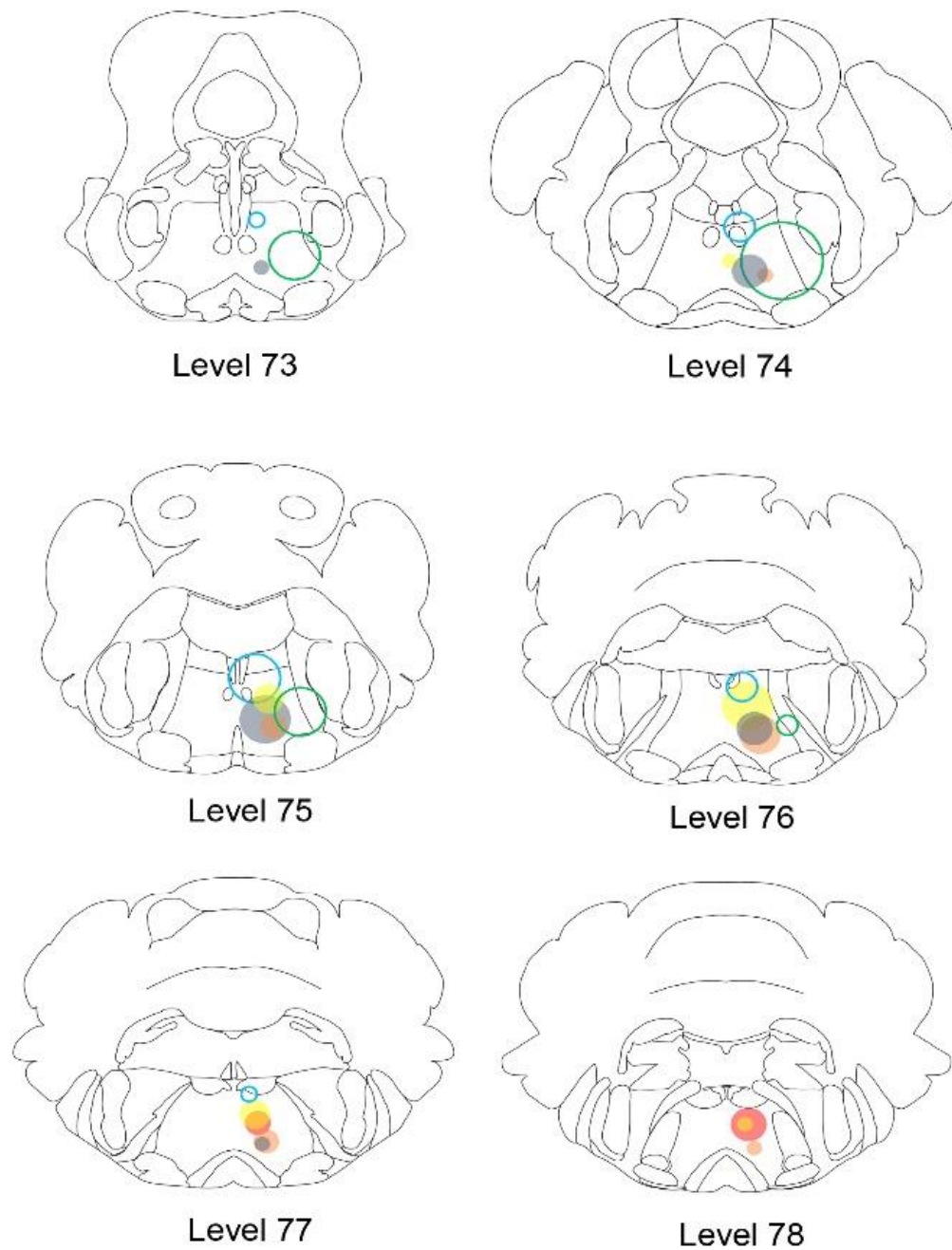


Figure 3.2. Sample FluoroGold injections represented on PnC anatomical levels. Levels 73-78 of the Paxinos and Watson Mouse Brain Atlas with filled circles corresponding to injections that resulted in FluoroGold-labeled cell bodies in the CeA. Open circles represent injections that resulted in no labeling within the CeA.

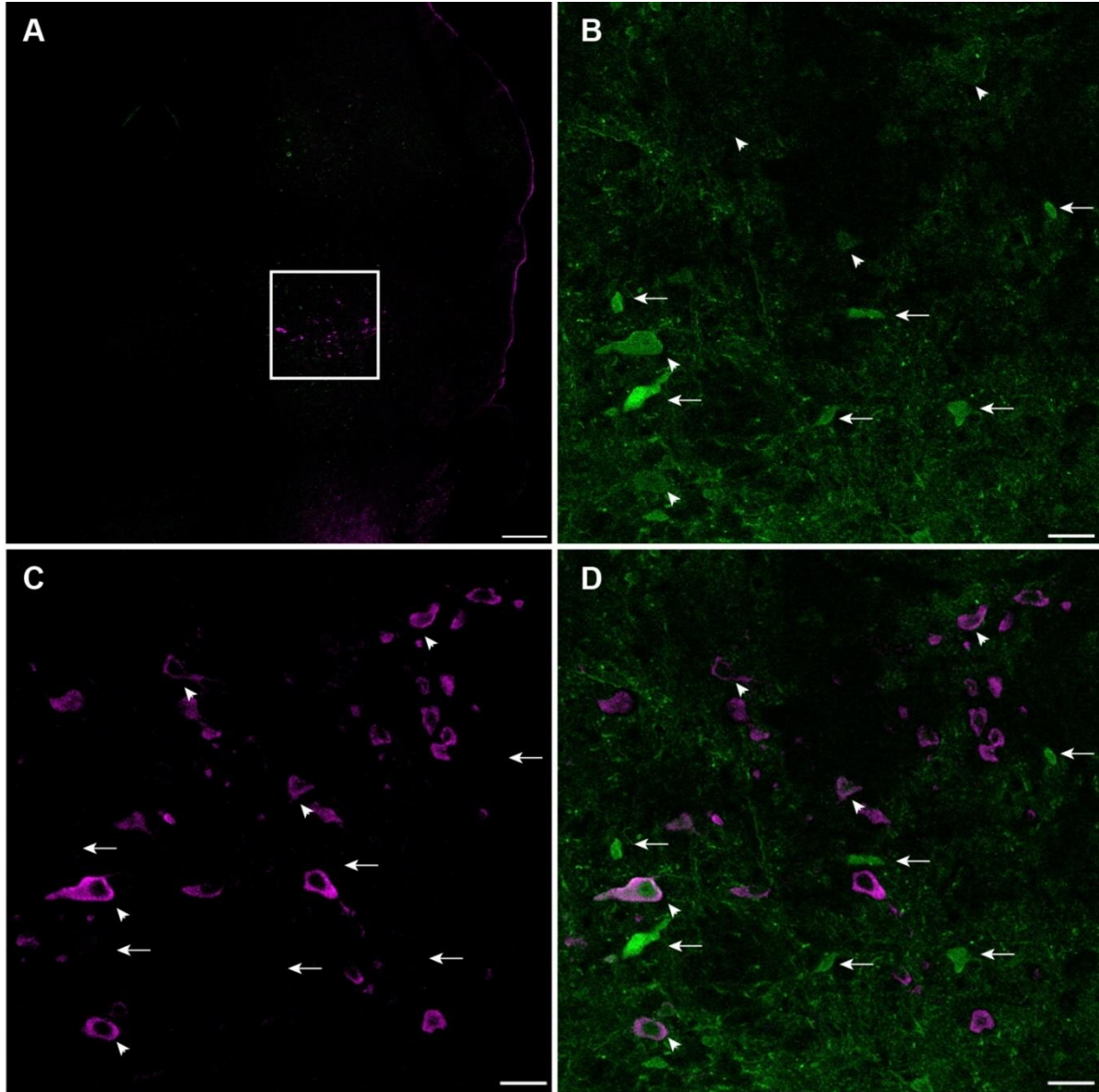


Figure 3.3. The PnC receives cholinergic and non-cholinergic inputs from the PPTg. (A) Representative coronal brain slice at the level of the PPTg, delineated by the ChAT+ neurons (magenta). White rectangle indicates the area shown in B-D. (B) Fluoro-Gold labeled PPTg cell bodies that project to the PnC (green). (C) Higher magnification of the ChAT+ cell bodies (magenta) that delineate the borders of the PPTg. (D) Merged image showing both Fluoro-Gold labeled PPTg neurons that are ChAT-negative (arrows) and others that are ChAT-positive (arrowheads). N=4. Scale bars: (A) 500 μ m, (B-D) 50 μ m.

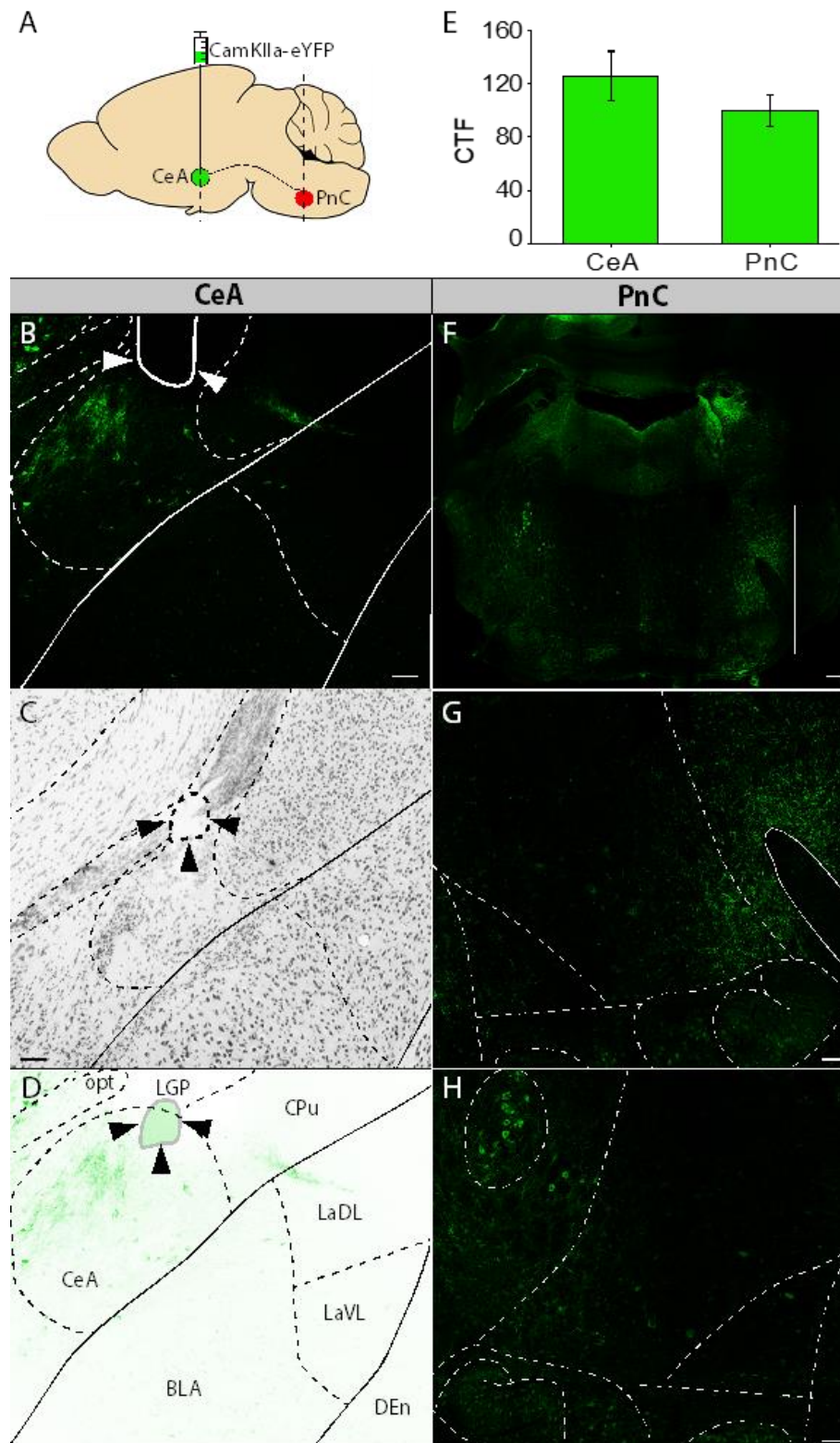


Figure 3.4. The CeA sends direct CamKIIα-dependent axonal projections to the PnC. (A) Sagittal representation of the mouse brain illustrating the anterograde approach: viral particles were injected in the CeA (green circle), and anterograde labeling of CeA axons were observed in the PnC (red circle). (B) Representative coronal slice showing injection site (white arrowheads) and transduced neurons in the CeA (green). (C) Nissl-stained section revealing the lesion (black arrowheads) caused by the injection. (D) Injection site in CeA (black arrowheads) mapped onto level 42 of the Paxinos and Franklin Mouse Brain Atlas. (E) Corrected total fluorescence (CTF) at the CeA and PnC was not statistically different. (F) eYFP-labeled CeA fibers course bilaterally within PnC boundaries. (G, H) CeA fibers coursing into the ipsilateral (G) and contralateral (H) PnC. Data are represented as mean ± SEM. Scale bars: (B, C) 150µm, (F) 300µm, (G, H) 150µm.

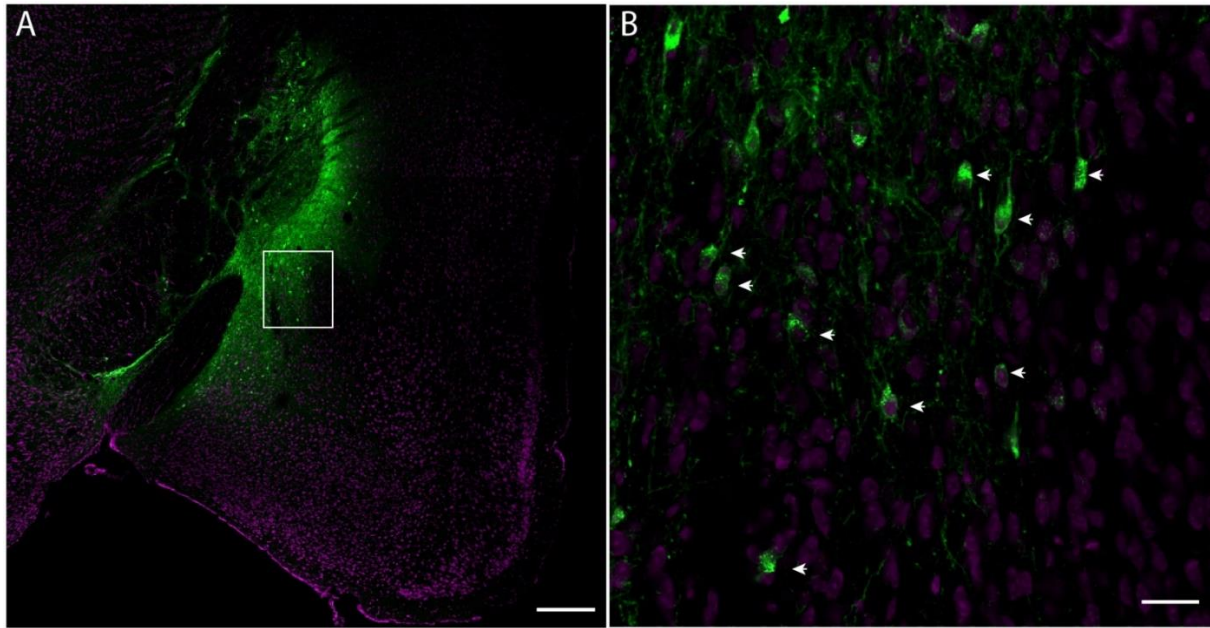


Figure 3.5. CamKII α -expressing cell bodies in the medial CeA. (A) Representative coronal section of the CeA injection site shows CamKII α -eYFP expression (green) and NeuroTraceTM staining (magenta). The white rectangle shows the area imaged in panel D. (B) Higher magnification of the CeA section in panel C shows cell bodies (white arrows) co-labeled with CamKII α -eYFP (green) and NeuroTraceTM (magenta). Scale bars: (C) 150 μ m, (D) 50 μ m

Although bilateral, eYFP-labeled axonal projections were mainly found ipsilateral to the injection site. At the coronal level of the PnC, eYFP-labeled axonal projections were also observed in the LC, MPB, LPB, scp, DRI and RMg (Figure 3.4F). A closer examination of several AAV injections throughout all CeA levels helped optimize the CeA coordinates that resulted in labeled CeA axonal terminals in the PnC (Figure 3.6).

3.1.3 Neurochemistry of CamKII α -dependent CeA-PnC synapses

In order to better understand how the CeA-PnC synapses may contribute to PPI, we investigated the neurochemical identity of this connection. Tissue slices containing FluoroGold-labeled neurons in the CeA were stained for ChAT, a cholinergic marker. At the coronal levels containing the CeA, no FluoroGold-labeled neuron was ChAT-positive

(Figure 3.6; N=4). In fact, no ChAT- positive neurons (in red) were observed within the CeA, as opposed to the adjacent ic, LGP and CPu (Figure 3.6C, E).

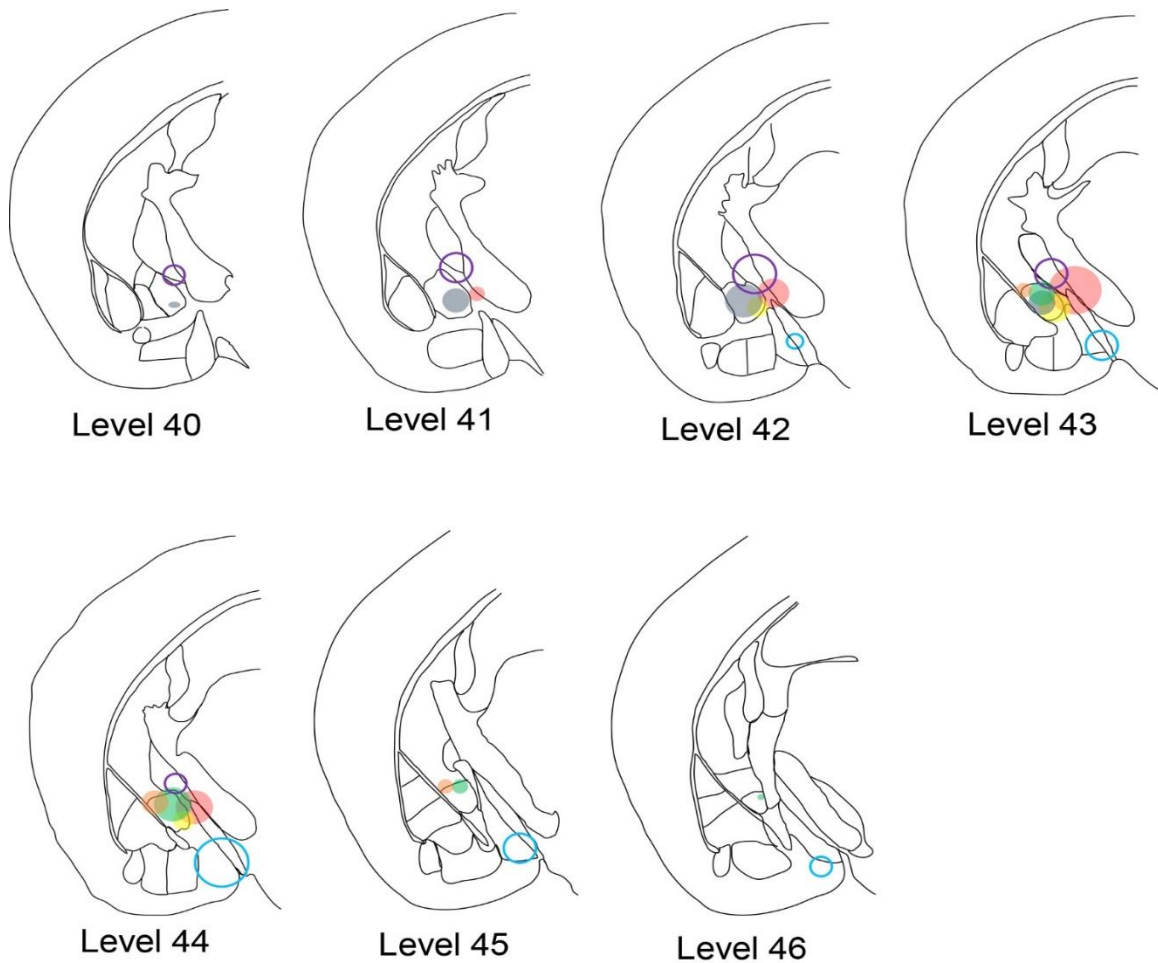


Figure 3.6. Sample AAV injections represented on CeA anatomical levels. Levels 40-46 of the Paxinos and Watson Mouse Brain Atlas. Filled circles correspond to injections that resulted in eYFP-labeled axonal projections in the PnC. Open circles represent injections that resulted in no labeling within the PnC or did not target the CeA.

While previous studies showed that most inhibitory interneurons do not express CamKII α , some GABAergic projection neurons do (Nathanson *et al.*, 2009). Therefore, to confirm whether we targeted excitatory projections with our anterograde findings, we injected an AAV construct coding for ChR2 and eYFP under the control of CamKII α (pAAV-CamKII α -ChR2-eYFP) in the CeA of mice. EYFP-expressing cell bodies, mainly

distributed in the medial CeA and adjacent regions, showed no GABA immunostaining (Figure 3.8B-D; N=4). The accuracy of the anti-GABA antibody was assessed by imaging the hippocampus at the CeA containing coronal levels (Figure 3.8E). As widely described in the hippocampus, we observed GABA-positive cell bodies were mainly distributed in the stratum radiatum, stratum lacunosum-moleculare and hilus, and scarcely interspersed among pyramidal cells in the stratum pyramidale (Figure 3.8E; N=3).

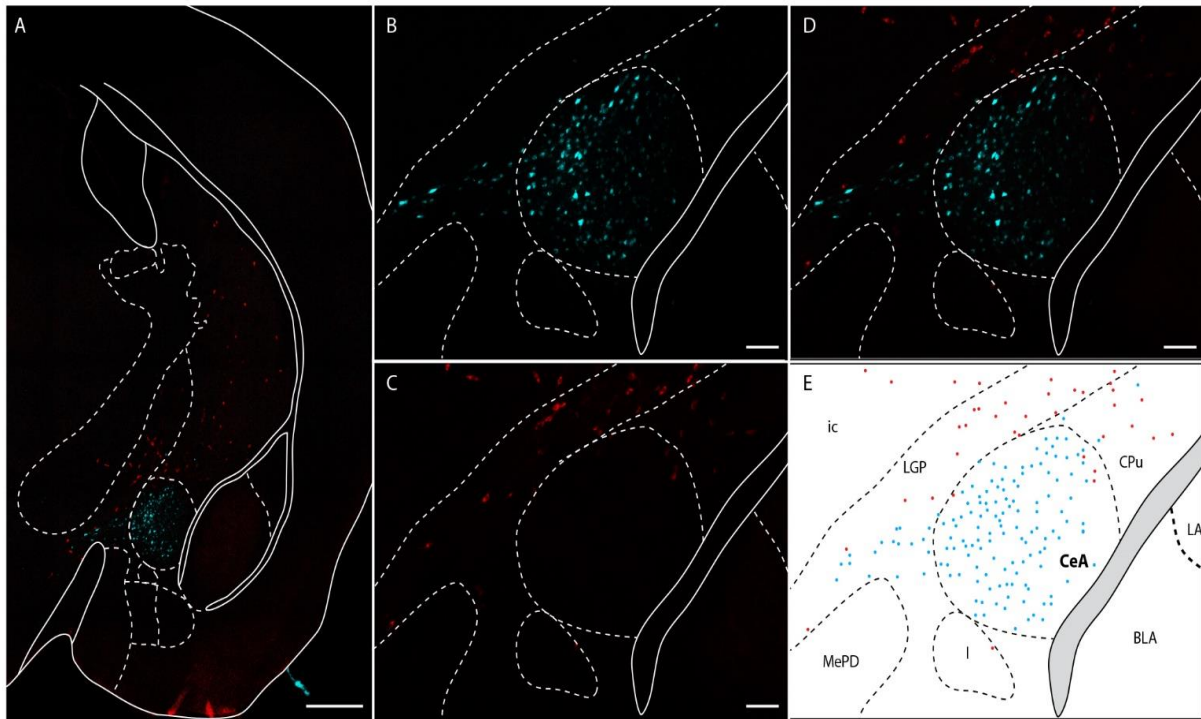


Figure 3.7. PnC-projecting neurons in the CeA are not cholinergic. (A) Representative coronal brain slice at the level of the CeA of a mouse injected with FluoroGold in the PnC. (B) FluoroGold-labeled neurons were mainly observed within the CeA and the BSTIA. (C) ChAT+ cell bodies are scarce in the CeA, and were primarily observed in adjacent regions. (D) Overlay of (B) and (C) shows no FG and ChAT co-localization at the level of the CeA. (E) FluoroGold-labeled and ChAT-expressing neurons mapped onto level 42 of the Paxinos and Watson Mouse Brain Atlas.

In parallel, to further confirm the neurochemistry of the CamKII α CeA-PnC synapses, we performed extracellular electrophysiological field recordings with photostimulation of CeA fibers coursing within acute PnC brain slices (Figure 3.8A, 3.9; N=7, n=21). First, light-evoked fEPSPs were elicited and recorded in the PnC suggesting that CeA inputs

send inputs to PnC neurons (Control: $2.646 \pm 0.044 \text{ mV}$; Washout: $2.600 \pm 0.0352 \text{ mV}$). Then, bath-application of Gabazine or its vehicle (DMSO) did not alter light evoked fEPSPs (Gabazine: $2.653 \pm 0.043 \text{ mV}$; DMSO: $2.619 \pm 0.0534 \text{ mV}$; 1-way RM ANOVA, $F=0.273$, $p=0.844$, Figure 3.8A). On the other hand, application of the ionotropic glutamate receptor antagonists abolished the light-evoked fEPSPs (AP5: $0.122 \pm 0.026 \text{ mV}$, AP5 & CNQX: $0.0758 \pm 0.0202 \text{ mV}$; 1-way RM ANOVA, $F=34.777$, $p<0.001$; Figure 3.9).

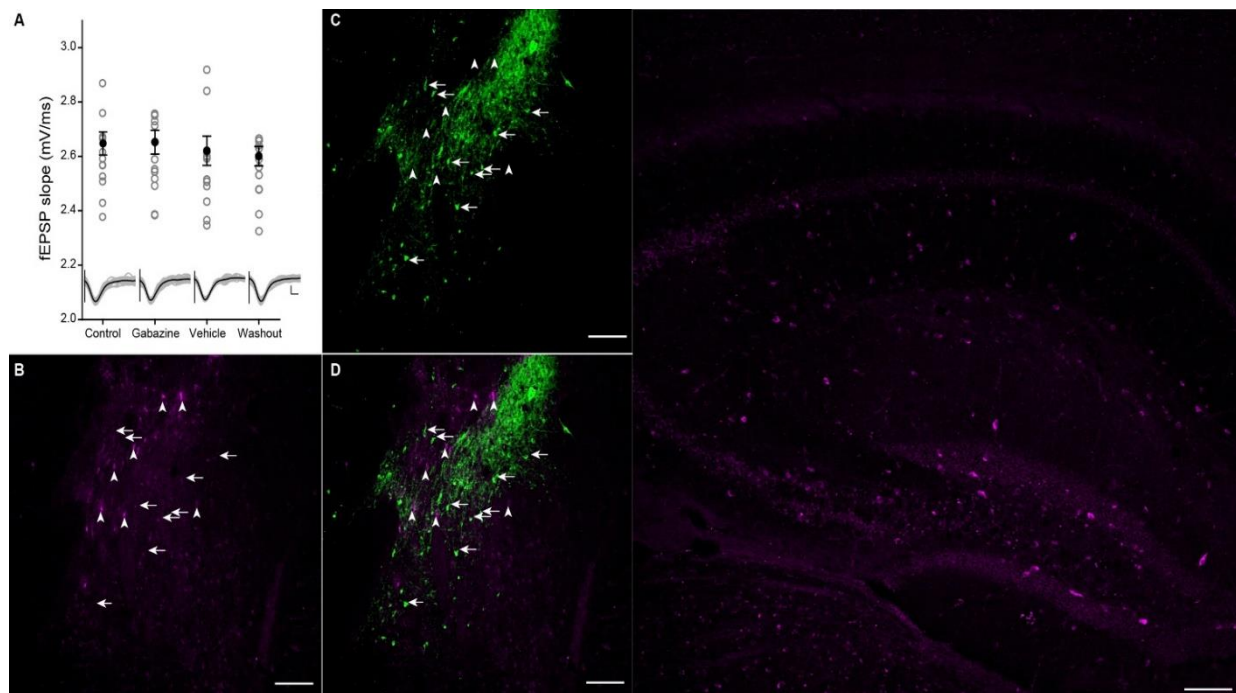


Figure 3.8. CamKII α -eYFP+ CeA fibers projecting to the PnC are not GABAergic. (A) Blue light elicited fEPSPs in the PnC of a mouse injected with CamKII α -Chr2 in the CeA. The slope of the fEPSPs was not modified by Gabazine or DMSO. *Inset*, Sample traces showing light-evoked fEPSPs under each experimental condition (gray=individual trials; black=averaged trace) (N=6, n=12). (B) High magnification of a CeA section from a mouse injected with CamKII α -eYFP in the CeA showing GABA+ cell bodies (magenta, arrowheads). (C) eYFP+ cell bodies and neurites (green, arrows) are mainly located in the medial division of the CeA. (D) Overlay of B and C show no eYFP+ cells display GABA labeling (N=4). Scale bars: (A) 0.2mV/1ms, (B-D) 250 μm . Data are represented as mean \pm SEM.

These results suggest that CeA neurons (primarily within the medial CeA) send, at least in part, direct and glutamatergic inputs to the PnC. Furthermore, these projections

were mainly observed at the lateroventral area of the PnC, ipsilateral to the injection site, where they activate ionotropic glutamate receptors on PnC cells.

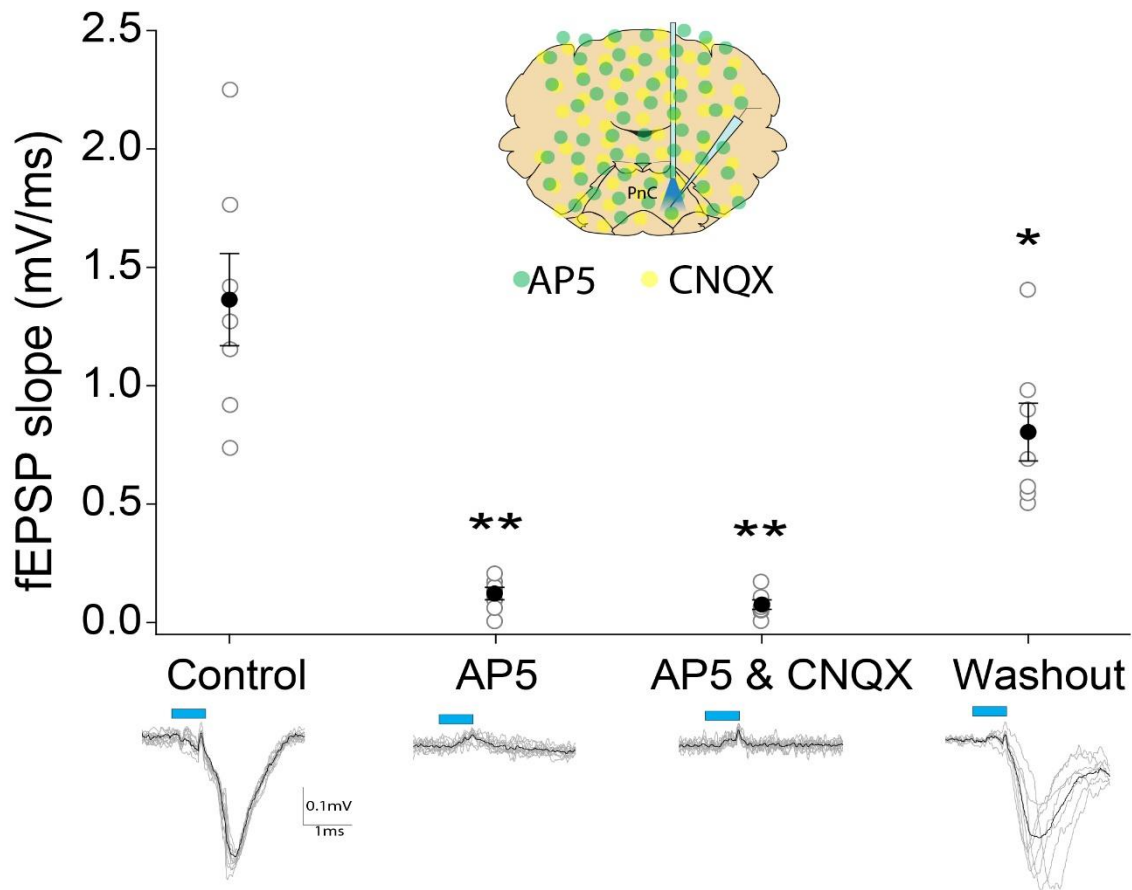


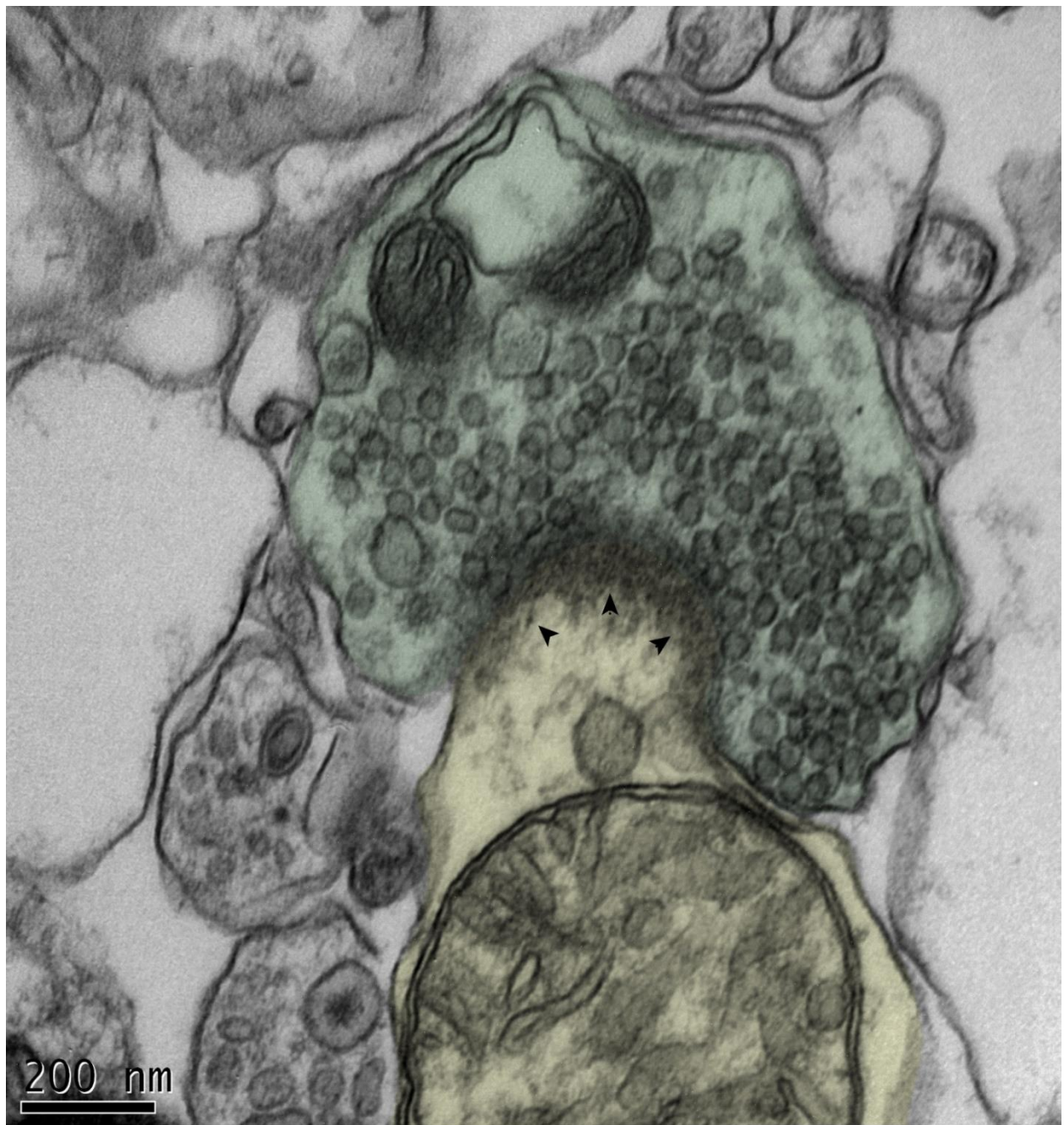
Figure 3.9. CeA projections activate ionotropic glutamate receptors in the PnC. Light-evoked fEPSPs in the PnC were abolished with bath-application of AP5 alone or AP5 & CNQX and recovered after washout. Sample traces (gray: all traces; black: averaged trace) of light-evoked fEPSPs shown under each condition. N=7 (represented by gray circles in plot). Data are represented as mean ± SEM. *p<0.05. **p<0.01.

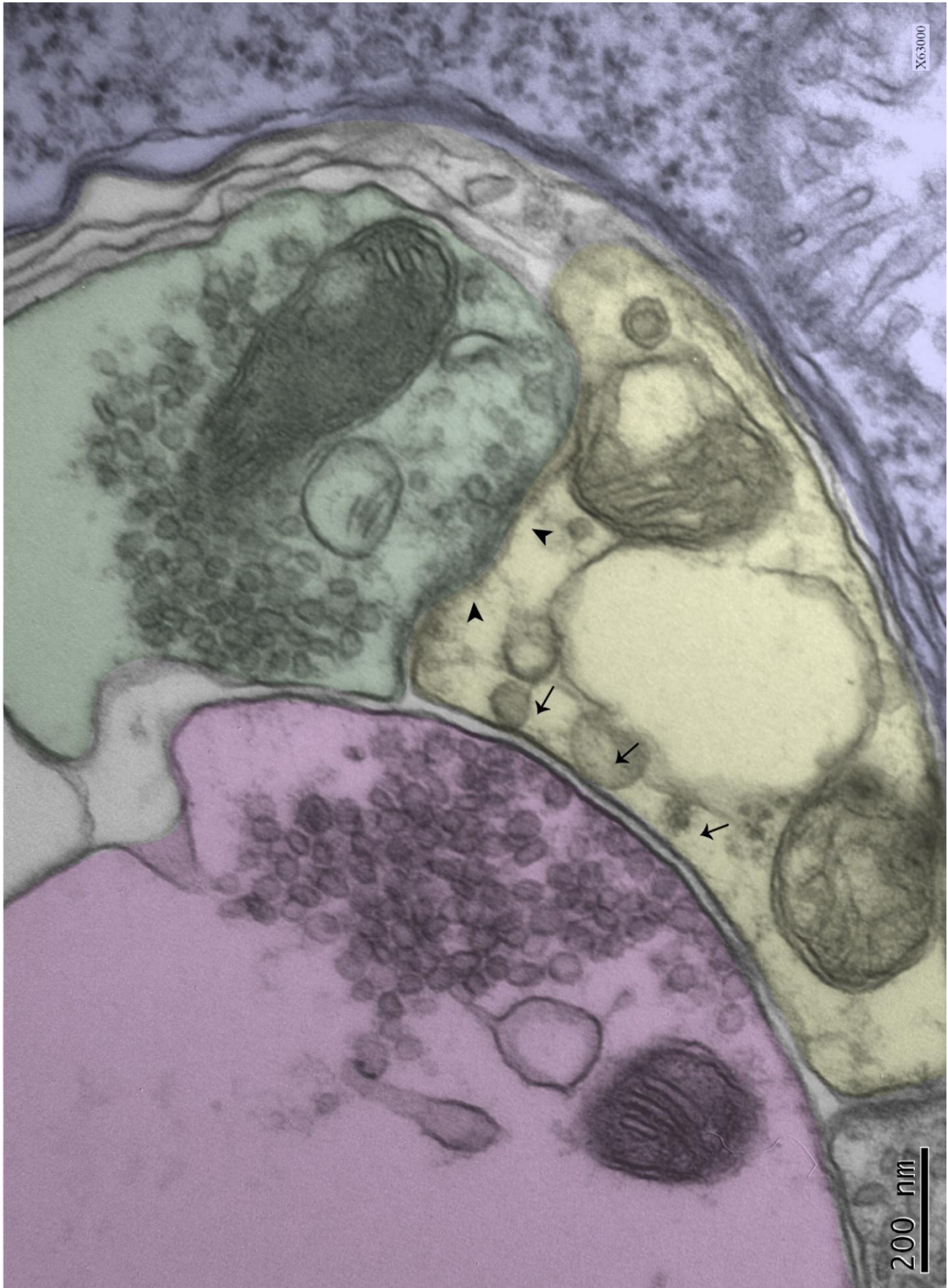
3.2 Characterization of CeA-PnC synapses and their contribution to an *in vitro* version of the prepulse inhibition task

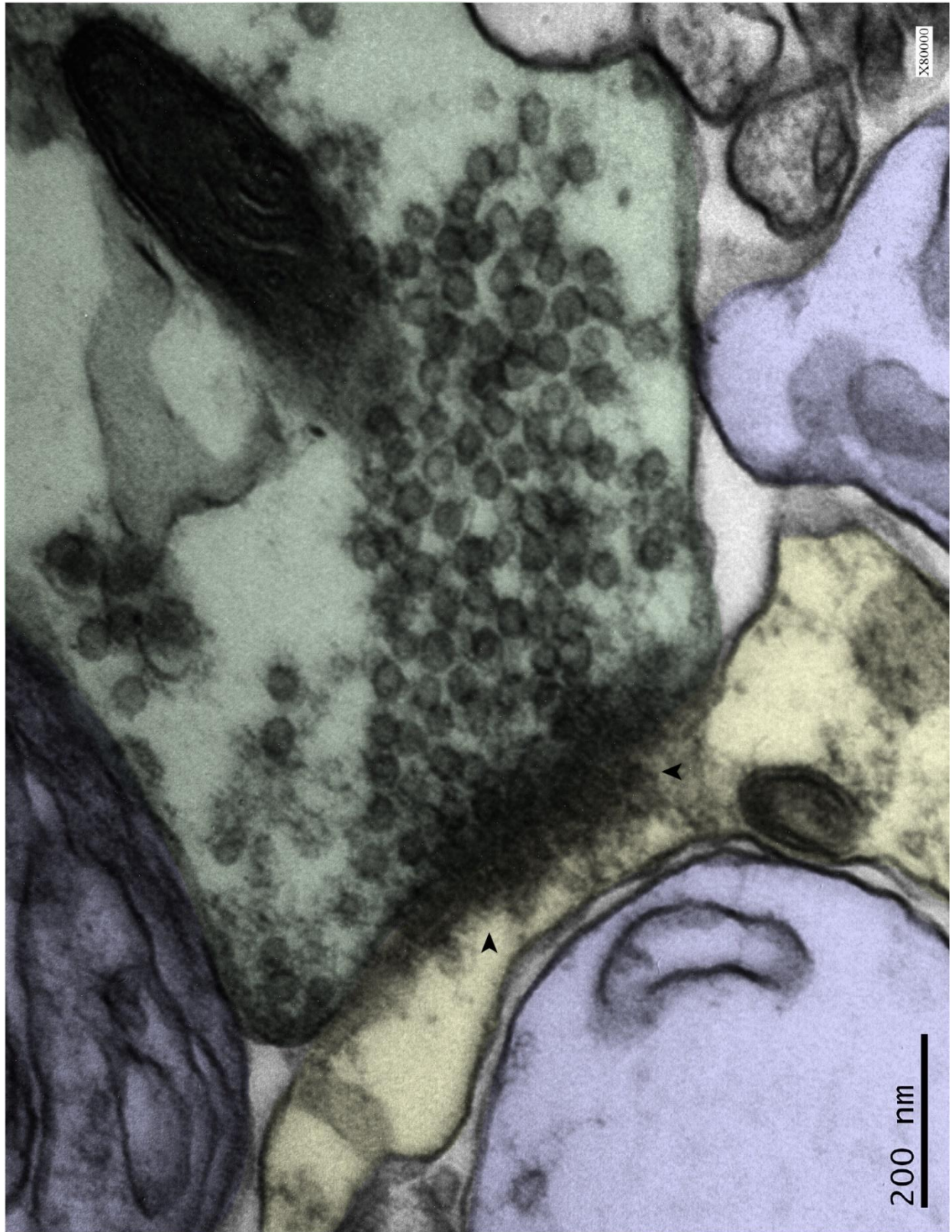
The fact that the CeA is connected to the PnC, situated at the core of the PPI pathway, makes it a prospective substrate of sensorimotor gating. To characterize in more details the CeA-PnC synaptic connection for its potential role in PPI, we investigated its synaptic morphology and physiology.

3.2.1 An ultrastructural analysis of synapses in the PnC

Ultrastructural analysis of the PnC revealed normal and canonical features of asymmetric type 1 (excitatory) and symmetric type 2 (inhibitory) synapses (N=2). As shown in figure 3.10, a canonical excitatory synapse consists of a presynaptic terminal with round neurotransmitter vesicles (green) apposed to a dendritic spine (yellow; Harris and Weinberg, 2012). Active zones refer to the presynaptic area where vesicles are docked for neurotransmitter release. At excitatory synapses, active zones align with an electron post-synaptic density (yellow with arrowheads; Landis *et al.*, 1988). This post-synaptic density represents the intricate scaffolding machinery required for anchoring and functioning of glutamate receptors in the post-synaptic membrane (Kennedy, 2000; Kim and Sheng, 2004; Wyszynski *et al.*, 1999). On the other hand, ultrastructural features of inhibitory synapses include a presynaptic terminal with round and flattened vesicles (magenta) and a translucent and symmetric synaptic gap (yellow with arrows). Although commonly axo-somatic, inhibitory synapses have been documented in the neck of dendritic processes (as shown in 3.10; Knott *et al.*, 2002; Wilson *et al.*, 1983). In these representative micrographs, we observed vicinal excitatory and inhibitory synapses on the same dendritic process. This observation illustrates dendritic integration of synaptic inputs, which is vital to initiate action potentials (Bloss *et al.*, 2016).







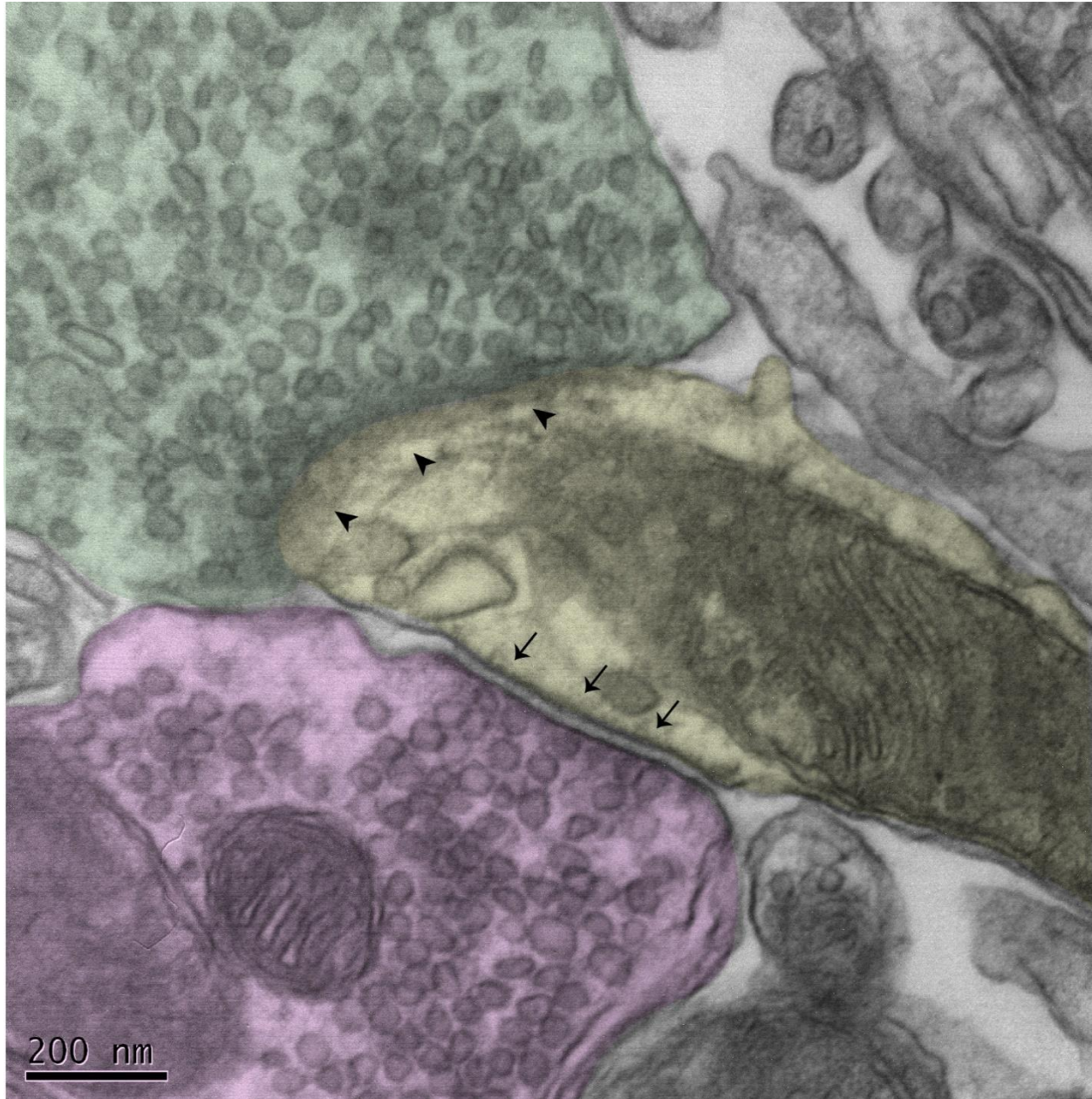


Figure 3.10. Ultrastructure of PnC synapses. Representative electron micrographs were color-coded to illustrate ultrastructural features of asymmetric type 1 (excitatory) and symmetric type 2 (inhibitory) synapses in the PnC. Excitatory synapses show characteristic round vesicles in the presynaptic terminal (green) and the post-synaptic electron dense active zone in spiny dendrites (yellow with arrowheads). Inhibitory synapses are characterized by round and flattened vesicles in the presynaptic terminal (magenta) and electron transparent synaptic cleft. Other neuropil compartments (blue) surrounding the synapse could be glial processes.

3.2.2 Physiological properties of CeA-PnC excitatory synapses

To assess basal transmission of CeA-PnC excitatory synapses, a stimulation-response protocol was used. We observed that light-evoked fEPSPs recorded within the PnC or CeA increased as light intensity increased (Figure 3.11A, B; N=7, n=21). However, at 9rlu and higher light intensities, fEPSPs in the CeA and PnC reached maximal magnitude (one-way ANOVA, CeA: $F=0.0333$, $p=0.967$; PnC: $F=0.530$, $p=0.598$, Figure 3.11B). Optical stimulation in the PnC contralateral to the injection site did not elicit fEPSPs at all the light intensities tested. Then, short-term presynaptic efficacy at CeA-PnC synapses was examined with a paired-pulse protocol at different ISI (N=7, n=21; Figure 3.11C, D). Such protocol uses two identical stimuli and is quantified as the ratio of the amplitude of the second synaptic response over the first synaptic response. The resulting paired pulse ratio (PPR) has been shown to be inversely proportional to vesicle release probability following the first stimulus (i.e. the initial release; Zucker and Regehr, 2002). Therefore, a paired pulse ratio greater than “1” reflects facilitating synapses, which typically have a relatively low vesicle release probability following the first stimulus, allowing a relatively big pool of vesicles to be released in response to the second stimulus. CeA-PnC excitatory synapses displayed facilitation at 50-200ms ISI suggesting a relatively low initial probability of neurotransmitter release (Figure 3.11C, D).

3.2.3 Excitatory CeA input regulates PnC activity *in vitro*

Before investigating its contribution to PPI *in vivo*, we first dissected how CamKII α CeA input regulates auditory information in the PnC using an *in vitro* version of PPI. Previously, an *in vitro* ASR was performed in acute brain slices by electrical stimulation of auditory fibers stemming from the LVPO into the PnC (Bosch and Schmid, 2006, Figure 3.12A). Here, to perform PPI “*in vitro*”, we first elicited an “ASR” in PnC slices by electrically

stimulating auditory fibers (mimicking a “startling pulse”) and recording a synaptic response (“startle response”) in the PnC.

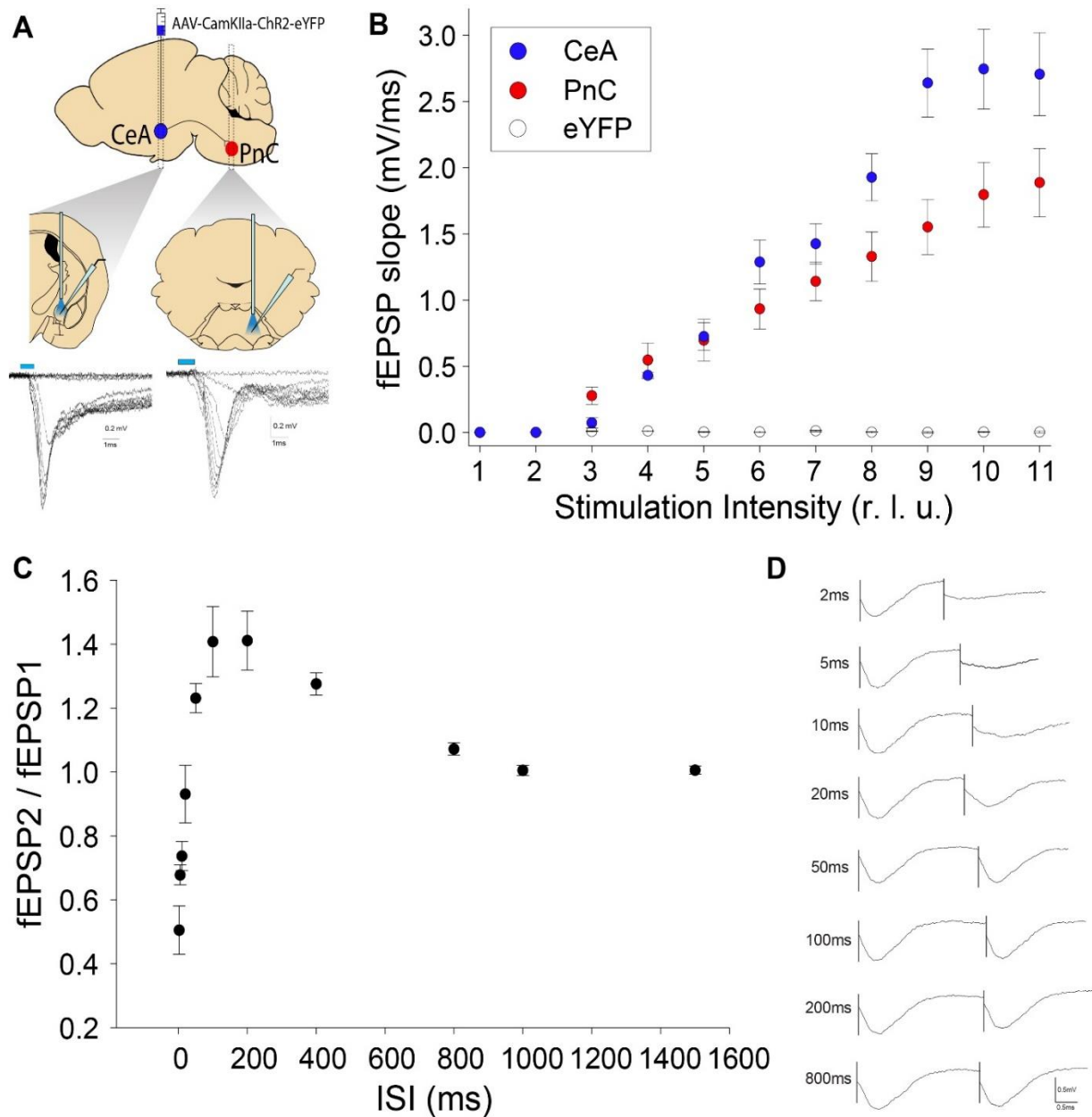


Figure 3.11. Basal transmission and short-term plasticity of CeA-PnC excitatory synapses. (A) Strategy used to transduce CeA excitatory neurons projecting to the PnC with ChR2, and record light-evoked fEPSPs (sample traces below) in the CeA and PnC. **(B)** Input-output slope of light-evoked fEPSPs as a function of stimulation intensity. **(C)** The probability of neurotransmitter release indicated by paired-pulse ratio (fEPSP2/fEPSP1) at different ISI. **(D)** Sample traces of fEPSPs evoked by paired light pulses at different ISI. Data are represented as mean \pm SEM.

As shown in figure 3.12B, electrical stimulation at the LVPO evoked fEPSPs within the PnC, which increased as stimulation increased (N=7, n=21). In addition, we also characterized the probability of neurotransmitter release of these synapses with a paired-pulse protocol. For these experiments, we used 0.6V for stimulation, which was one-third of the stimulation intensity that elicited the strongest response shown in the input-output curve. With these parameters, we observed no short-term plasticity (Figure 3.12C).

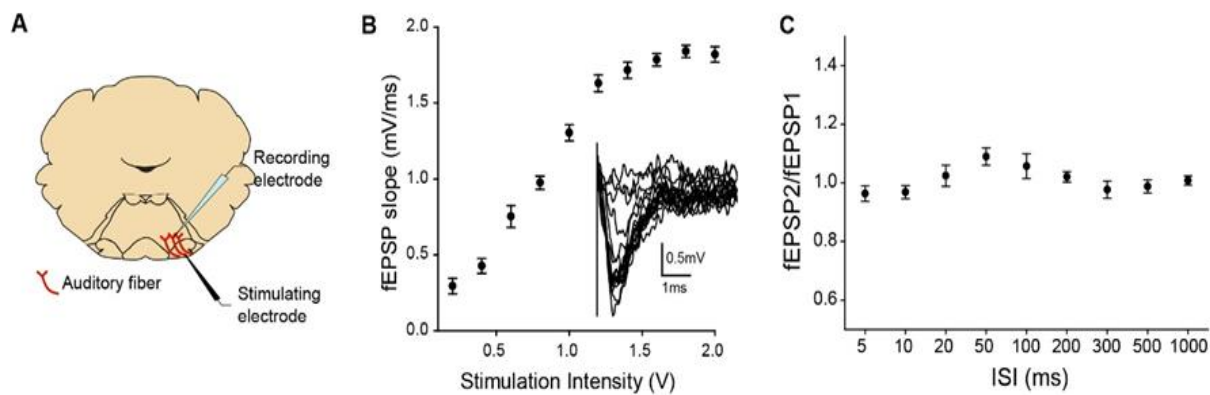


Figure 3.12. Electrical stimulation of auditory fibers elicit fEPSPs in the PnC. (A) Diagram of a coronal slice at the level of the PnC showing the placement of the recording electrode (within the PnC; delineated by major landmarks) and stimulating electrode (ventral to the superior olivary complex) to stimulate auditory fibers. (B) Basal synaptic transmission plotted as fEPSP slope as a function of stimulation intensity (N=7, n=21). Inset, Superimposed sample fEPSP traces elicited by the electrical stimulation of auditory fibers, at increasing intensities. (C) Graph of paired-pulse ratios (fEPSP2/fEPSP1) recorded at auditory fibers-PnC synapses (N=7, n=21). Data are represented as mean \pm SEM.

If CeA-PnC synapses contribute to PPI *in vitro*, optical activation of CeA fibers prior (mimicking a “prepulse”) to stimulation of auditory fibers should decrease the *in vitro* ASR (Figure 3.13A). Interestingly, photo-stimulation 20-200ms before auditory fiber stimulation attenuated electrically-evoked fEPSPs in the PnC (N=7, n=21; ANOVA, $F_{(1,8)}=5.574$, $p<0.001$; Figure 3.13B, C). In contrast, at shorter (10ms: $t=1.021$, $p=1.000$) and longer ISI (300, 500 and 1000ms: $F_{(1,3)}=0.0661$, $p=0.977$), photo-stimulation of CeA fibers had

no significant effect on the electrically-evoked fEPSPs (Figure 3.13C). This finding suggests that the CeA-PnC connection may contribute to PPI *in vivo*.

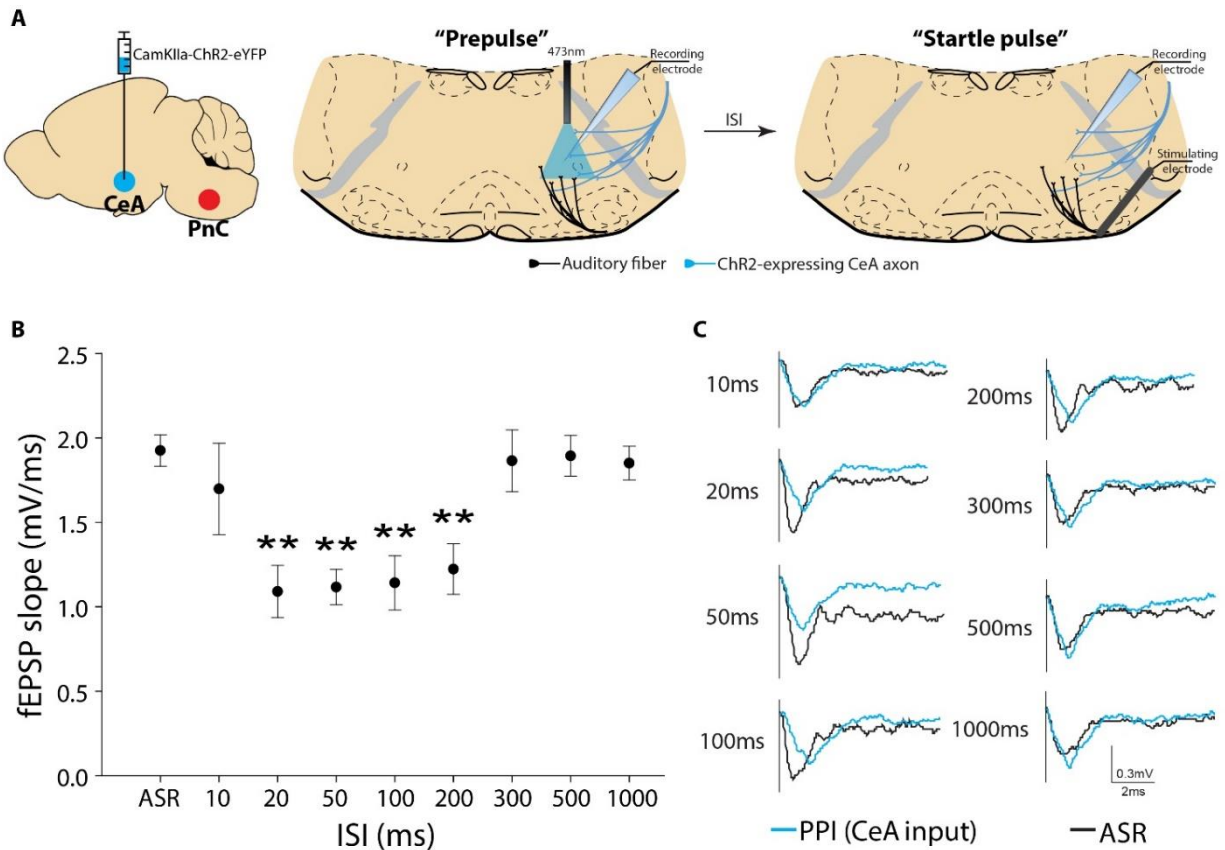


Figure 3.13. Excitatory CeA input to the PnC contributes to PPI *in vitro*. (A) PPI *in vitro* consisted on recording the effect of CeA excitatory input photo-stimulation ("prepulse") on fEPSPs in the PnC, which were elicited by electrical stimulation of auditory fibers ("startle pulse") at different ISI. (B) When compared to electrical stimulation alone ("ASR"), photo-activation of CeA fibers 20-200ms before the "startle pulse" significantly attenuated the electrically-evoked fEPSPs in the PnC. (C) Representative traces at all tested ISI. Electrical stimulation only traces are shown in black; blue traces represent electrical stimulation preceded by photostimulation. Data are represented as mean \pm SEM. ** $p < 0.01$.

Lastly, we investigated whether CeA excitatory inputs suppress transmission of auditory information in the PnC via a presynaptic mechanism (Figure 3.14A). Since PPR reflect the probability of presynaptic neurotransmitter release, we examined if photostimulation of CeA fibers altered PPR values from paired auditory fiber stimulation. Paired fEPSPs were first recorded in response to auditory fibers stimulation alone (labeled as "control"; N=7, n=14), with ISI of 50ms (Figure 3.14B, C) and 100ms (Figure

3.14D, E) between electric pulses. Then, CeA excitatory fibers were photo-stimulated prior to the paired auditory fiber electrical stimulation. Different ISI between the end of CeA fibers photo-stimulation and auditory fiber stimulation were tested to explore any possible presynaptic effect. Photo-stimulation of CeA fibers did not affect the paired pulse ratio at ISI of 50ms (Figure 3.14B, C; $F_{(1,7)}=0.510$, $p=0.824$) or 100ms (Figure 3.14D, E; $F_{(1,7)}=0.839$, $p=0.559$), suggesting that CeA excitatory fibers do not act on the synaptic terminals of auditory afferent fibers in the PnC at these ISI.

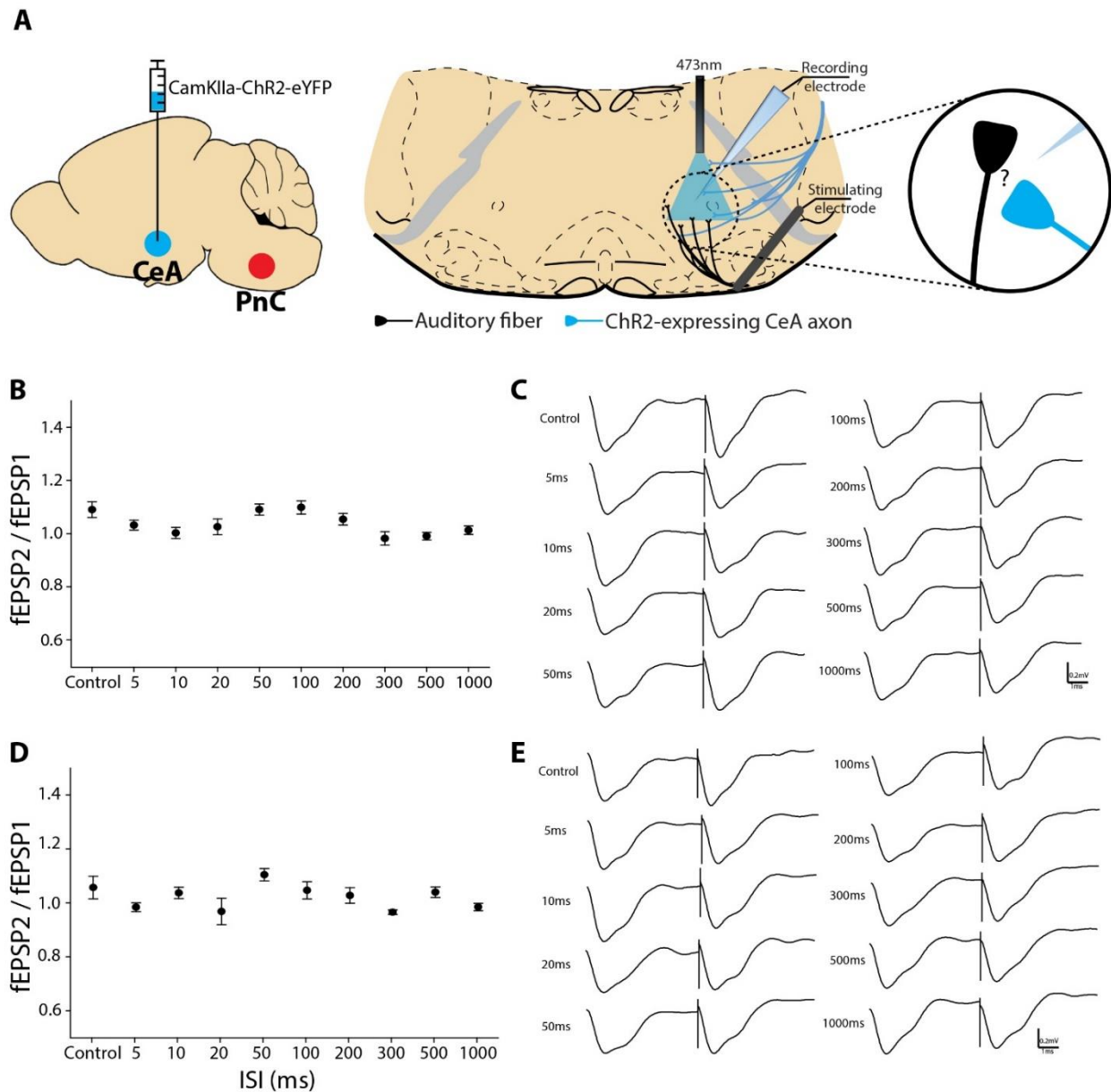


Figure 3.14. CeA inputs do not inhibit vesicle release from auditory fibers in the PnC. (A) In PnC coronal slices of mice injected with ChR2 in the CeA, Photo-stimulation of CeA excitatory fibers preceded paired electrical stimulation of auditory fibers at 50ms and 100ms to reveal any presynaptic filtering mechanisms. (B) Plot of 50ms PPR of auditory fibers stimulation without (denoted as “Control”) and preceded by photo-stimulation of CeA fibers in the PnC at different intervals. (C) Representative traces from 50ms paired-pulses preceded by photostimulation at the indicated ISI. (D) Plot of 100ms PPR of auditory fibers stimulation without (denoted as “Control”) and preceded by the photo-stimulation of CeA fibers in the PnC at different intervals. (E) Representative traces from 50ms paired-pulses preceded by photostimulation at the indicated ISI. Scale: (C, E) 0.2mV/ms

3.3 Optogenetic manipulation of the CeA-PnC excitatory pathway during PPI *in vivo*: mimicking a sensorimotor gating deficit?

Typically known for its role in fear conditioning, the CeA can potentiate the startle response during states of fear in rats (Rosen *et al.*, 1989). Such potentiation occurs via a CeA-PnC direct pathway. This observation, as well as our previous results, suggest that the CeA can directly regulate startle activity in the PnC. Nevertheless, whether the CeA through its PnC connection, contribute to non-associative learning behaviors, such as PPI, has yet to be investigated. Here, we explored the role of the CeA-PnC excitatory connection in PPI *in vivo*. To do so, we used optogenetics to manipulate the CeA-PnC excitatory synapses during the ASR and PPI tasks. AAV vectors were injected in the CeA and an optical fiber was implanted in the PnC of mice (Figures 3.15, 3.16).

3.3.1 Excitatory CeA-PnC connection does not alter the basal ASR

Since PPI is the attenuation of the ASR, changes in basal ASR by any sort of manipulation can be interpreted as a PPI effect. Therefore, we first assessed the role of the excitatory CeA-PnC connection in ASR.

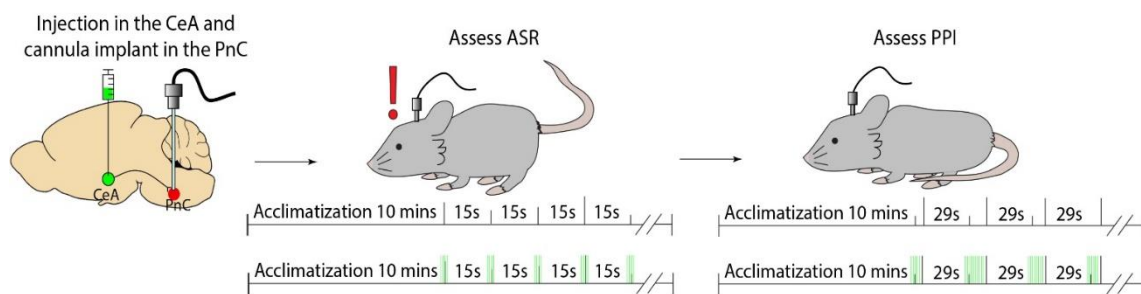


Figure 3.15. Optogenetic manipulation of CeA-PnC synapses during behavioral testing. The opsin viral vector was injected in the CeA, and an optic fiber was implanted in the PnC. Mice were then subjected to the ASR and PPI tasks with and without light (represented by green bars) during sound pulse or prepulse presentation (depicted by vertical black lines).

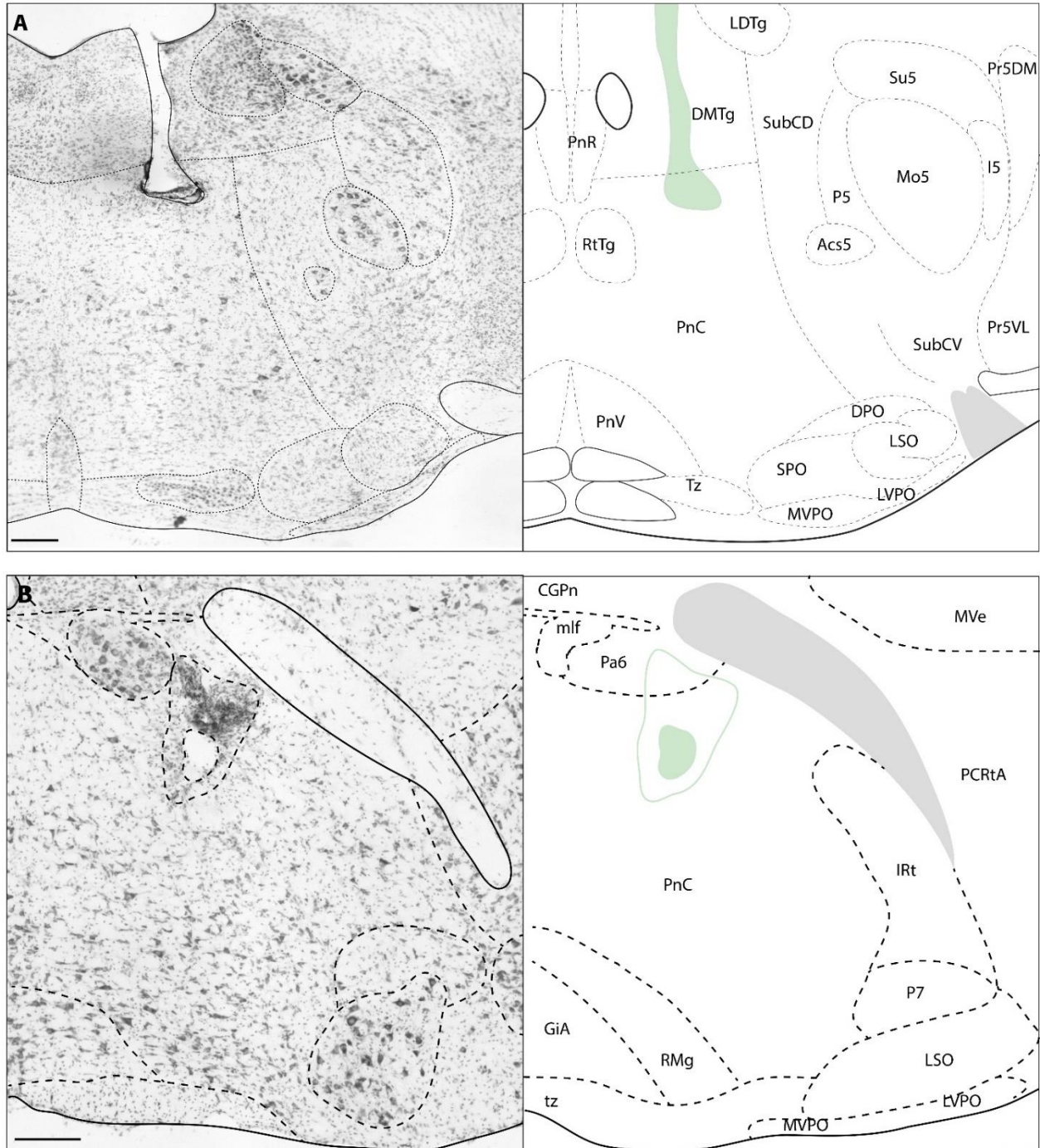


Figure 3.16. Representative PnC coronal sections with lesions from optic fiber implants. (A, B) Nissl-stained PnC coronal sections of two subjects showing lesions from optic fiber implants used for photo-manipulation during behavioral testing. Lesions were mapped on their corresponding anatomical levels (A: 75; B: 78) of the Paxinos and Franklin Mouse brain Atlas to confirm implant within the PnC. Scale bar: (A, B) 500µm

When compared to the control groups (non-injected, N=10; and EYFP-only, N=4), silencing the CeA-PnC excitatory connection with Arch3.0; N=8) had no effect on the ASR, regardless of the vector used ($F_{(1,11)}=1.417$, $p=0.268$), light ($F_{(1)}=0.00155$, $p=0.969$) or the sound intensity and light interaction ($F_{(1,6)}=0.206$, $p=0.974$; Figure 3.17A). Since prolonged Arch3.0-mediated photo-inhibition has been observed to elicit EPSPs (Mahn, *et al.* 2016; Wiegert *et al.*, 2017), ASR trials were also performed in mice injected with another inhibitory opsin, Halorhodopsin (NpHR3.0, N=8). Similar to the observation in the Arch3.0 group, the ASR of the group injected with NpHR3.0 was not altered by the vector used ($F_{(1,11)}=1.935$, $p=0.115$), light ($F_{(1)}=0.00297$, $p=0.958$) or by the sound intensity and light interaction ($F_{(1,6)}=0.102$, $p=0.996$; Figure 3.18A).

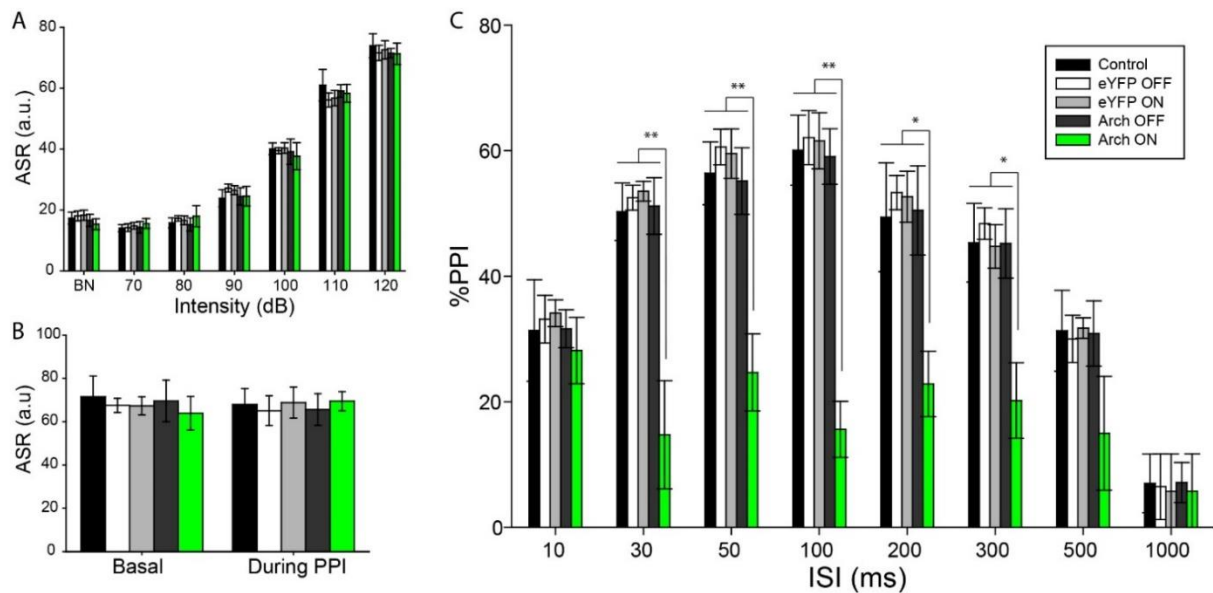


Figure 3.17. Arch3.0 photoinhibition of CeA-PnC synapses reduces PPI *in vivo*. (A) Basal ASR increased as sound intensity increased, and remained unaltered when the excitatory CeA-PnC connection was silenced. (B) Basal ASR was not affected during the PPI task among groups. (C) Photo-inhibition of the excitatory CeA-PnC connection during the presentation of the prepulse significantly decreased PPI at 30-300ms ISI. Data are represented as mean \pm SEM. * $p<0.05$, ** $p<0.01$.

These results suggest photo-inhibition of the CeA-PnC connection did not alter basal ASR. In all groups, sound intensities beyond 90dB elicited an exponential increase of the startle response (Arch3.0: $F_{(1,6)}=325.867$, $p<0.001$; NpHR3.0: $F_{(1,6)}=357.202$, $p<0.001$). On the other hand, when compared to background noise (BN=65dB), sound intensities of 70dB and 80dB did not elicit a startle response (Arch3.0: $F_{(1,2)}=1.495$, $p=0.229$; NpHR3.0: $F_{(1,2)}=2.641$, $p=0.079$), despite light (Arch3.0: $F_{(1)}=0.358$, $p=0.551$; NpHR3.0: $F_{(1)}=0.0447$, $p=0.833$) or the sound intensity and light interaction (Arch3.0: $F_{(1,2)}=0.521$, $p=0.596$; NpHR3.0: $F_{(1,2)}=0.00323$, $p=0.997$).

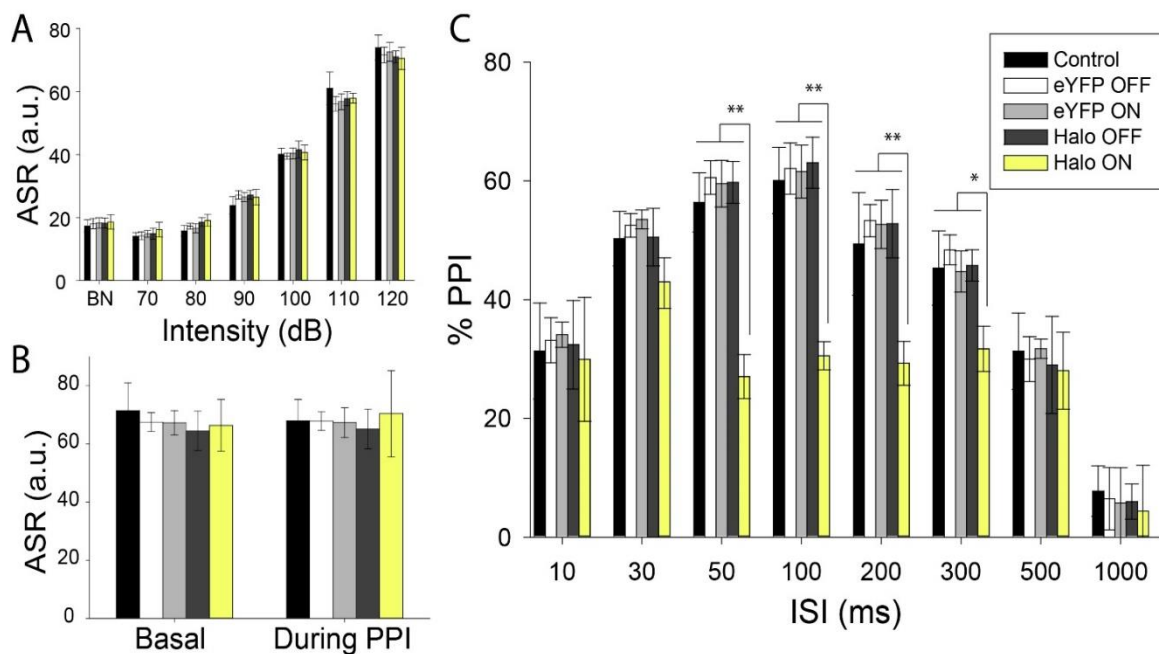


Figure 3.18. NpHR3.0 photoinhibition of CeA-PnC synapses reduces PPI *in vivo*. (A) Basal ASR increased as sound intensity increased, and remained unaltered when the excitatory CeA-PnC connection was silenced. (B) Basal ASR was not affected during the PPI task among groups. (C) Photo-inhibition of the excitatory CeA-PnC connection during the presentation of the prepulse significantly decreased PPI at 50-300ms ISI. Data are represented as mean \pm SEM. * $p<0.05$, ** $p<0.01$.

Similarly, in mice injected with the excitatory opsin, ChR2-stimulation of CeA-PnC excitatory synapses did not modify basal ASR regardless of the vector (Figure 3.19A,

$N=14$, $F_{(1,2)}=1.417$, $p=0.247$) or the vector and sound intensity interaction ($F_{(1,12)}=0.413$, $p=0.956$). Also, sound intensities beyond 90dB significantly incremented the ASR ($F_{(1,6)}=118.344$, $p<0.001$); while 70-80dB did not evoke an ASR ($F_{(1,6)}=1.113$, $p=0.364$).

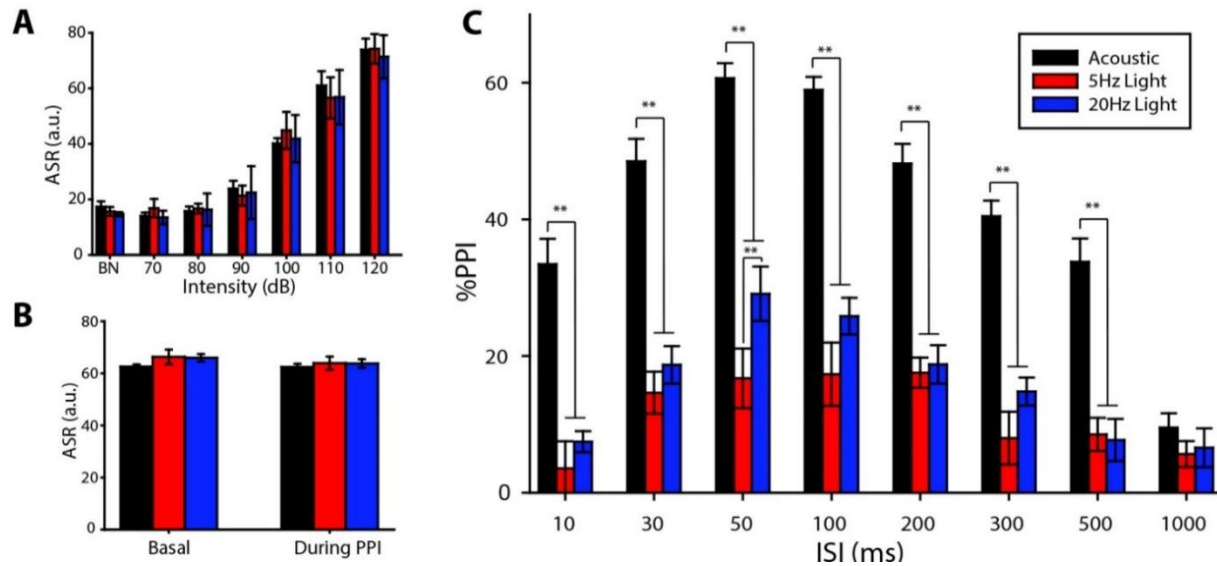


Figure 3.19. Photostimulation of CeA-PnC synapses as a prepulse elicits a PPI effect. (A) Basal ASR increased as sound intensity increased, and remained unaltered with 5Hz and 20Hz photostimulation. **(B)** Basal ASR was not affected during the PPI task among groups at both photostimulation frequencies used. **(C)** PPI elicited using the light prepulse was performed by photostimulating CeA-PnC excitatory synapses at 5Hz (red bars) and 20Hz (dark blue bars), and was compared to the PPI elicited using the acoustic prepulse (black bars). Both types of PPI assays were compared in the same mice and resulted in a PPI effect at ISI between 10ms and 500ms.

Overall, photostimulation or photoinhibition of the CeA-PnC excitatory connection did not alter basal ASR. Based on these observations and previous studies, we selected a prepulse sound intensity of 75 dB and a 120dB startling pulse to be used in the PPI task.

3.3.2 Excitatory CeA input to the PnC contributes to PPI

Based on our results from the ASR task, we then examined the effect of silencing the CeA-PnC connection during the PPI task. We hypothesized that if the CeA-PnC excitatory

connection is a neural substrate of PPI, then it should be activated when the non-startling prepulse is presented, as we observed no effect when the ASR was presented alone. When compared to control groups, the light (Arch3.0: $F_{(1)}=10.201$, $p=0.009$; NpHR3.0: $F_{(1)}=5.371$, $p=0.041$) and the light and ISI interaction (Arch3.0: $F_{(1,7)}=4.057$, $p<0.001$; NpHR3.0: $F_{(1,7)}=3.692$, $p=0.002$) significantly affected PPI in the two opsin groups. In the Arch3.0 group, photo-inhibition of the CeA-PnC connection attenuated PPI by 25-43% when the prepulse was presented 30-300ms before the startle pulse (Figure 3.17C). Similarly, PPI of the NpHR3.0 group was reduced by 16-29% at 50-300ms ISI (Figure 3.18C). Furthermore, to validate the exclusive effect on PPI of the photoinhibition, basal ASR before or during the PPI task was measured. Because none of the 2 inhibitory opsins altered the ASR (Arch3.0: $F_{(1)}=3.124$, $p=0.105$, Figure 3.17B; NpHR3.0: $F_{(1)}=0.394$, $p=0.543$, Figure 3.18B). This suggests that photoinhibition of CeA-PnC altered the processing of the acoustic prepulse.

To confirm the efficacy of the inhibitory optogenetic tool used, whole-cell patch clamp recordings were performed in mice injected with NpHR3.0 in the vHPC (Figure 3.20; $N=3$, $n=6$). We took advantage of the easy access of CamKII α -dependent fluorescent cell bodies of vHPC neurons in the pyramidal layer (Figure 3.20B). Injections of depolarizing currents triggered action potentials on the virally infected cells; while shining yellow light successfully hyperpolarized their membrane potential (1-way RM ANOVA, $F_{(1,2)}=25.729$, $p<0.001$), abolished their firing rate (1-way RM ANOVA, $F_{(1,2)}=10.905$, $p=0.003$), and both recovered in the absence of yellow light (Figure 3.20C-E).

Finally, to determine if the CeA excitatory inputs can potentiate PPI, we photo-stimulated this connection during the presentation of the acoustic prepulse in mice

injected with CamKII α -ChR2. Photo-stimulation did not alter PPI (Figure 3.21; N=6, 1-way ANOVA, $F=0.757$, $p=0.399$), suggesting that the CeA-PnC excitatory component exists in a maximally activated state *in vivo*.

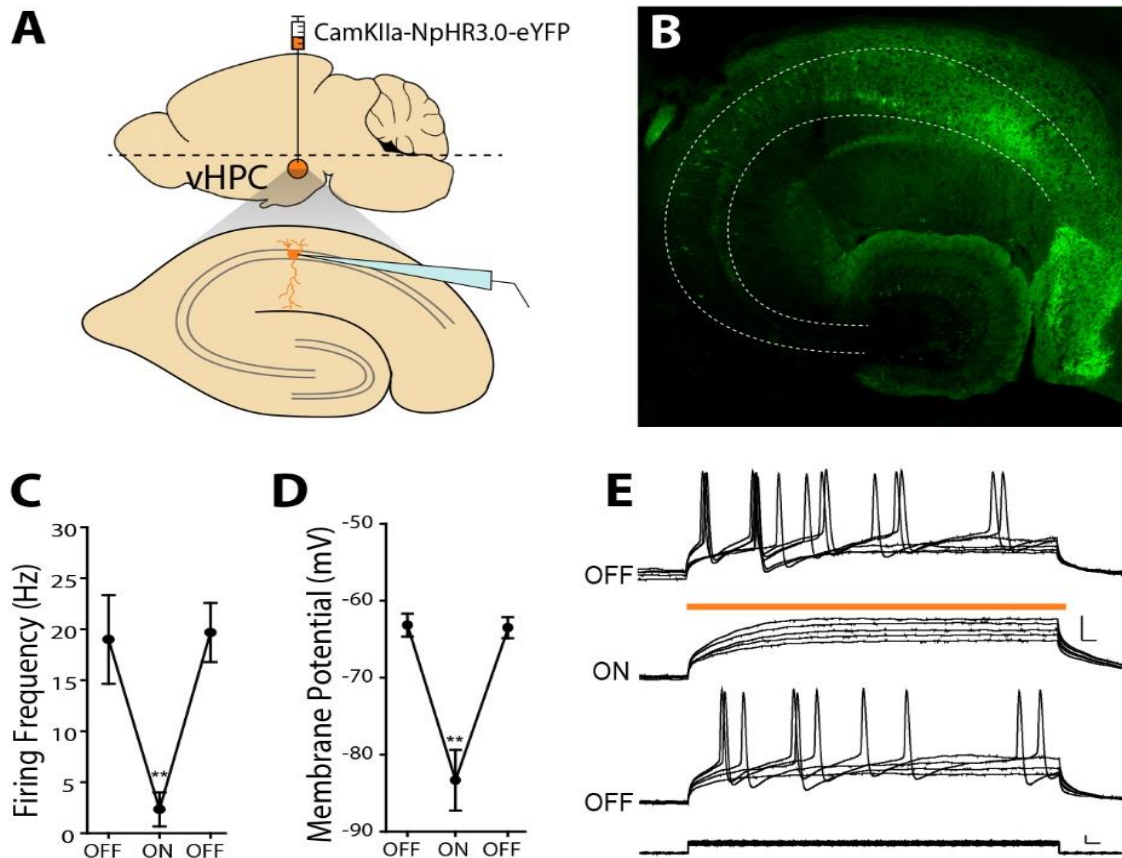


Figure 3.20. NpHR3.0 photoinhibition of hippocampal neurons. (A) Horizontal section of the ventral hippocampus (vHPC) showing the injection site (top) and the site of whole cell-recordings (bottom) (B) Representative horizontal vHPC slice from a mouse injected with CamKII α -NpHR3.0 showing eYFP fluorescence (green) in the pyramidal cell layer (delineated by the white dotted lines). (C) Orange light decreased the firing frequency and (D) the membrane potential of NpHR3.0-expressing hippocampal neurons activated by depolarizing currents injections. (E) Voltage traces obtained under current clamp conditions showing the effect of orange light (orange line) on spiking activity induced by injection of depolarizing currents (N=3; n=6). Scale bars: (B) 100 μ m, (E) Top: 20mV/10ms, Bottom: 100pA/10ms. Data are represented as mean \pm SEM. ** $p<0.01$.

Because of this, we then tested whether the photo-stimulation of the CeA-PnC excitatory synapses alone could mimic the PPI effects elicited by acoustic prepulses in mice injected with CamKII α -ChR2 in the CeA. To assess this, we performed PPI *in vivo*

by replacing the acoustic prepulse with the photo-stimulation of the targeted synapses with blue light pulses (at 5Hz or 20Hz), followed by an acoustic startling stimulation. In the same mice, PPI was also elicited by using the classic acoustic prepulse followed by the acoustic startling pulse paradigm. As shown in Figure 3.19C, photo-stimulation as a prepulse resulted in a PPI effect at ISI between 10ms and 500ms (N=8; ANOVA, $F_{(1,14)}=6.152$, $p<0.001$). Light-evoked PPI was enhanced when the CeA photo-stimulation frequency was increased from 5Hz to 20Hz, at the 50ms ISI ($q=4.376$, $p=0.007$). In fact, the PPI effect elicited by photo-stimulation of CeA afferents represented 18-41% of the PPI elicited by the acoustic prepulse, depending on the interval tested. Taken together, these results suggest that, with these photostimulation parameters, the excitatory CeA-PnC connection contributes to PPI alongside other neuronal pathways in the PnC.

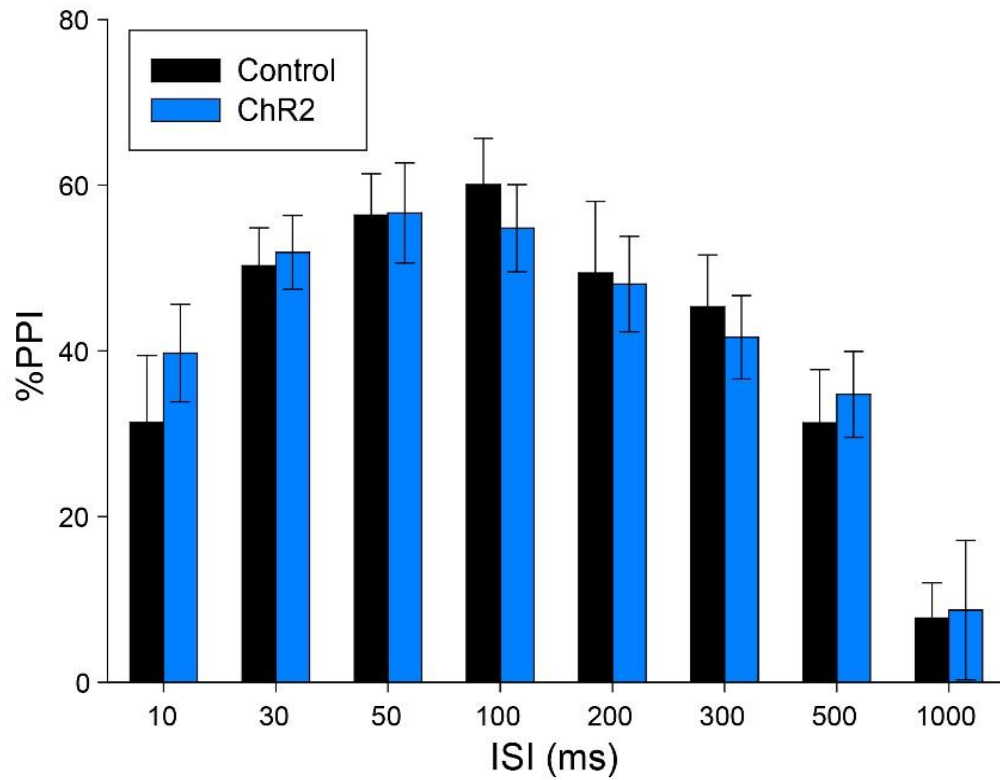


Figure 3.21. Photostimulation of CeA-PnC synapses does not potentiate acoustic PPI. (A) Photo-stimulation of the excitatory CeA-PnC connection during the presentation of the prepulse did not alter PPI. Data are represented as mean \pm SEM.

3.4 Unraveling the identity of the PnC cells receiving CeA excitatory inputs

Intriguingly, our results suggest that excitatory CeA-PnC connection contributes to PPI, an inhibitory mechanism. Therefore, to understand the role of the CeA-PnC excitatory synapses in PPI, we next investigated the cellular substrate in the PnC activated by CeA excitatory input. We hypothesize that excitatory CeA inputs activate inhibitory PnC interneurons, which in turn, inhibit startle neurons. To this end, we used tract-tracing with imaging analyses in a transgenic mouse line that expresses eGFP under the control of the GlyT2 promoter. Complementarily, we performed whole-cell recordings with photostimulation in a mouse line that expresses Cre under the GlyT2 promoter.

3.4.1 Distribution of GlyT2⁺ neurons in the PnC: a mapping analysis

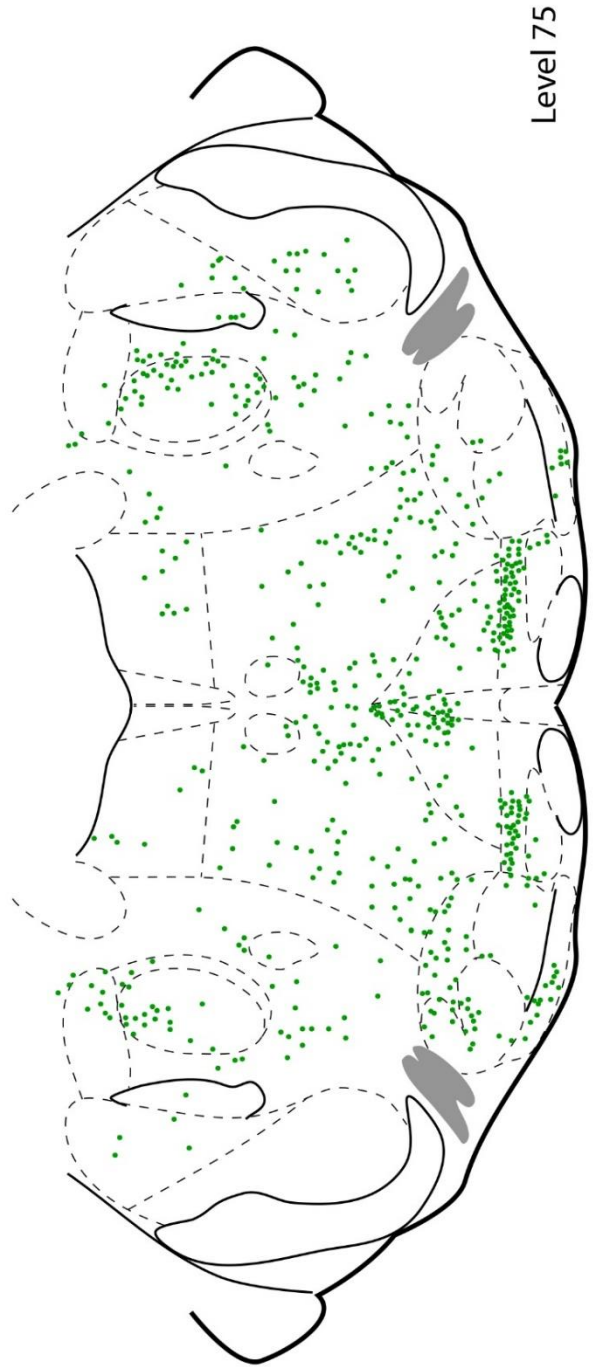
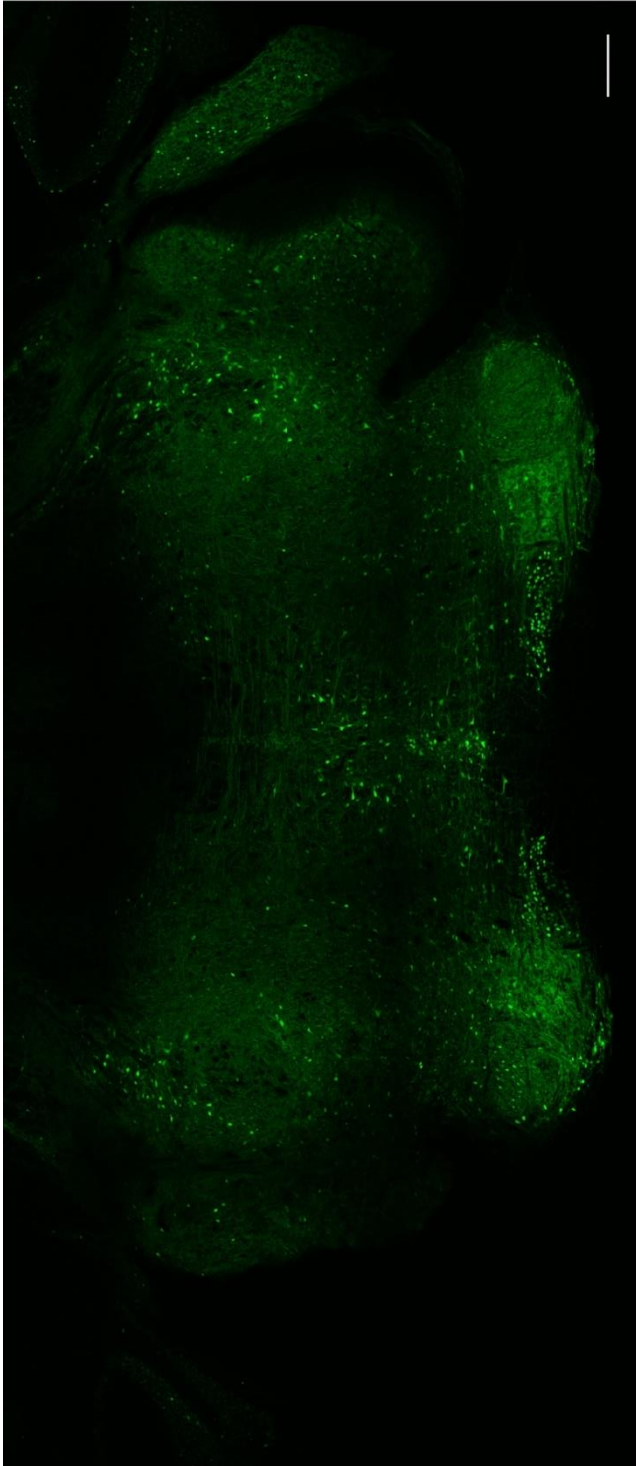
In the study where the GlyT2-eGFP transgenic mouse line was established, Zeilhofer and colleagues (2005) identify the brain regions containing GlyT2⁺ neuron, which included the PnC (Rampon 1996). First, we further validated this transgenic mouse line to be used for the proposed experiments. To do so, we performed a histological analysis and mapped the distribution of GlyT2⁺ neurons in the five more caudal anatomical levels containing the PnC (levels 75-78; Paxinos and Franklin, 2004; Figure 3.22). In doing so, we were able to evaluate if GlyT2⁺ neurons were located at PnC sites where we had previously observed excitatory CeA axonal projections. We only considered the more caudal PnC anatomical levels, where the 7n serves as the primary cytoarchitectural landmark that delineates the PnC. In fact, we use the 7n landmark when collecting acute thick sections for the electrophysiological experiments. It is noteworthy that GlyT2⁺ neurons are also present in more rostral anatomical levels (73-74), where the boundary between the PnC and its rostral counterpart, the PnO, is not clearly identifiable. Also, glycinergic and GABAergic fibers from the PnO to the intralaminar thalamic nuclei

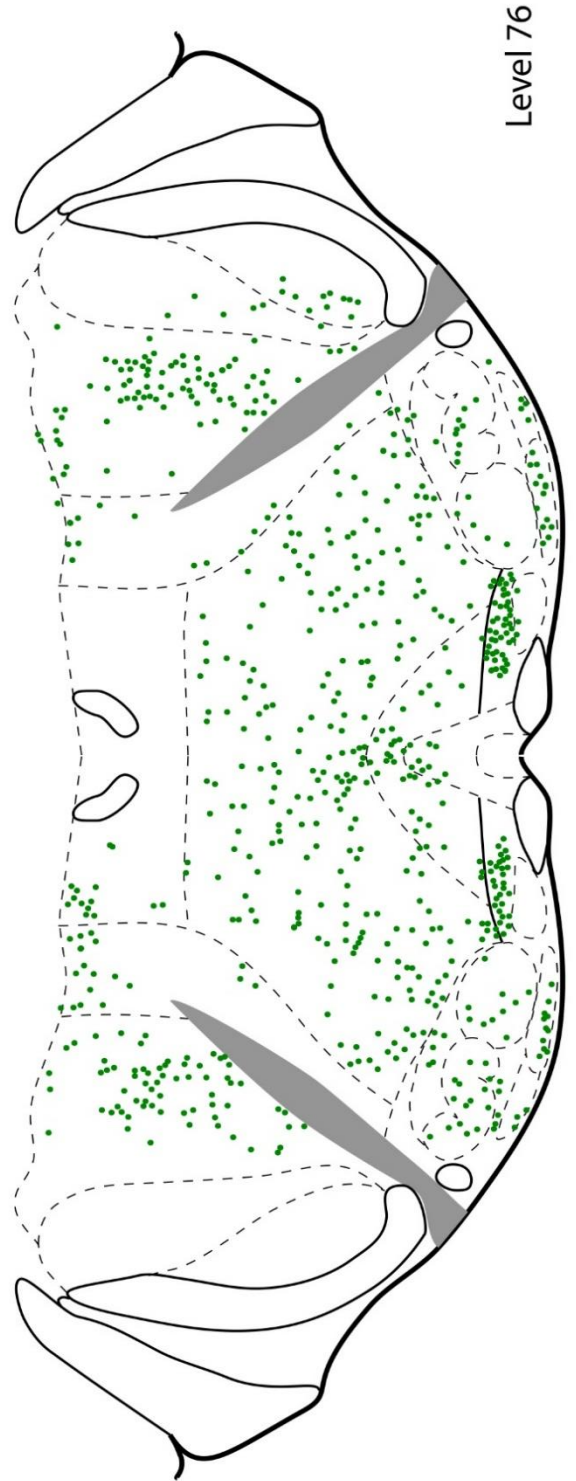
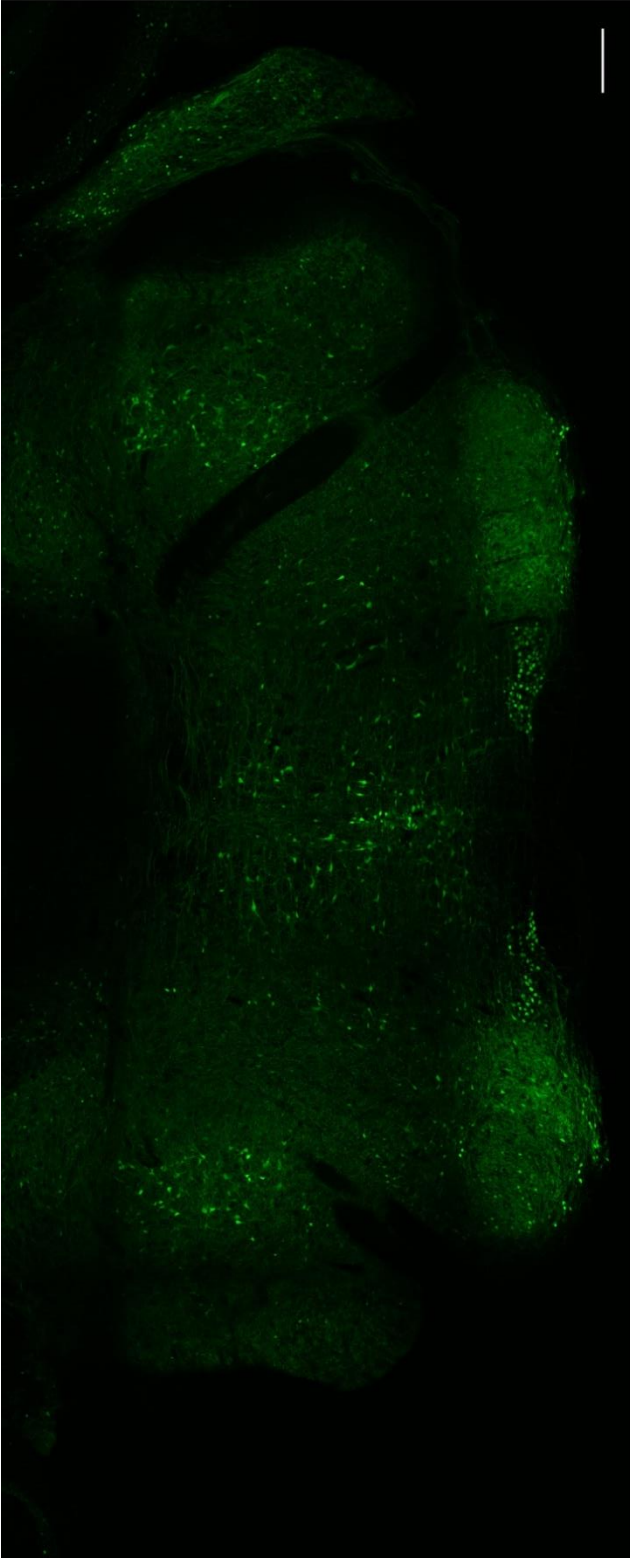
regulate freezing behavior (Giber *et al.*, 2015), a possible confounding factor when targeting GlyT2 PnC interneurons during PPI assessment. In all levels assessed, we observed numerous GlyT2⁺ neurons scattered throughout the extent of the PnC (Figure 3.22). Several GlyT2⁺ neurons clustered in close proximity to each other along the midline of the PnC. Most importantly, throughout all PnC levels, we observed several GlyT2⁺ neurons in the lateroventral part of the PnC, where excitatory CeA fibers were most densely observed. Besides the PnC, GlyT2⁺ neurons were also observed in several adjacent brainstem regions at the coronal level of the PnC, such as areas of the olivary complex, Pr5, PCRtA, CGPn, GiA, RMg and DMTg. For the following tract tracing, immunohistochemistry and electrophysiological experiments, we targeted the GlyT2⁺ neurons within the PnC, medial to 7n and dorsal to the olivary complex.

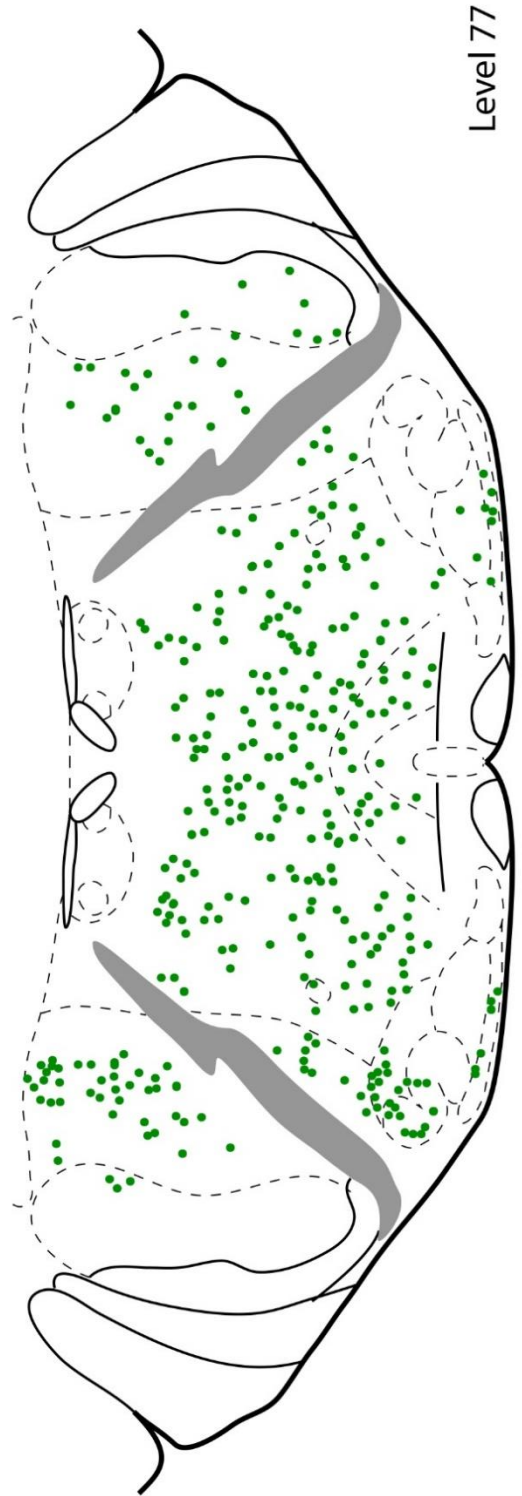
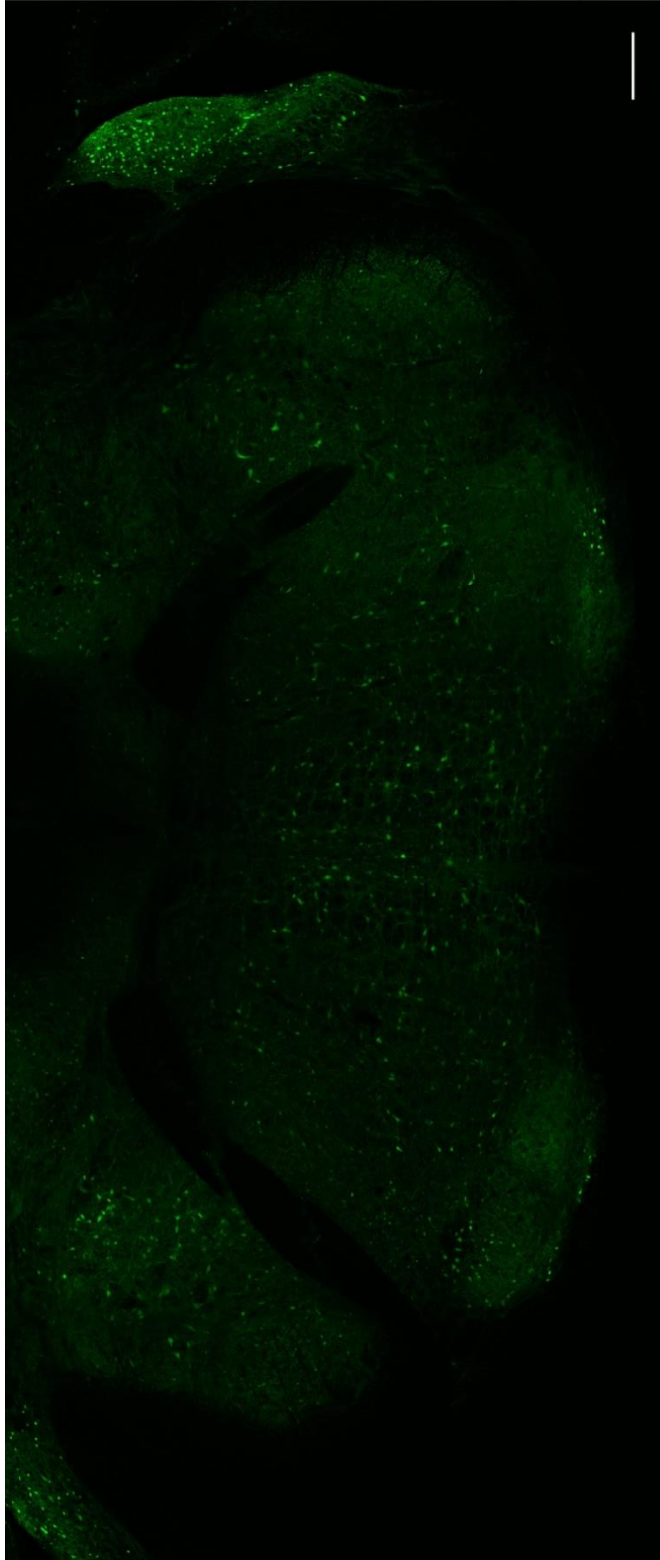
3.4.2 A PPI-relevant neurochemical profile of PnC GlyT2⁺ neurons

Since we hypothesize that excitatory CeA input may activate an inhibitory component in the PnC, we examined the potential of GlyT2⁺ to receive excitatory input. To do so, we probed PnC tissue slices of GlyT2-eGFP mice for PSD-95, a post-synaptic scaffolding protein present only at excitatory synapses. In the sections imaged and anatomical levels assessed, we observed that all PnC GlyT2⁺ interneurons expressed PSD-95, suggesting that these neurons receive excitatory input (Figure 3.23). We also observed other non-green neurons that were delineated by PSD-95 expression/staining (Figure 3.23B).

We then elaborated on the neurochemical profile of the PnC GlyT2⁺ neurons by probing for PV and PRODH, two markers that might underlie sensorimotor gating deficits and contribute to the schizophrenia pathology. Within the PnC, neurons were GlyT2⁺-only, GlyT2⁺/PV⁺/PRODH⁺ or PV⁺/PRODH⁺ (Figure 3.24).







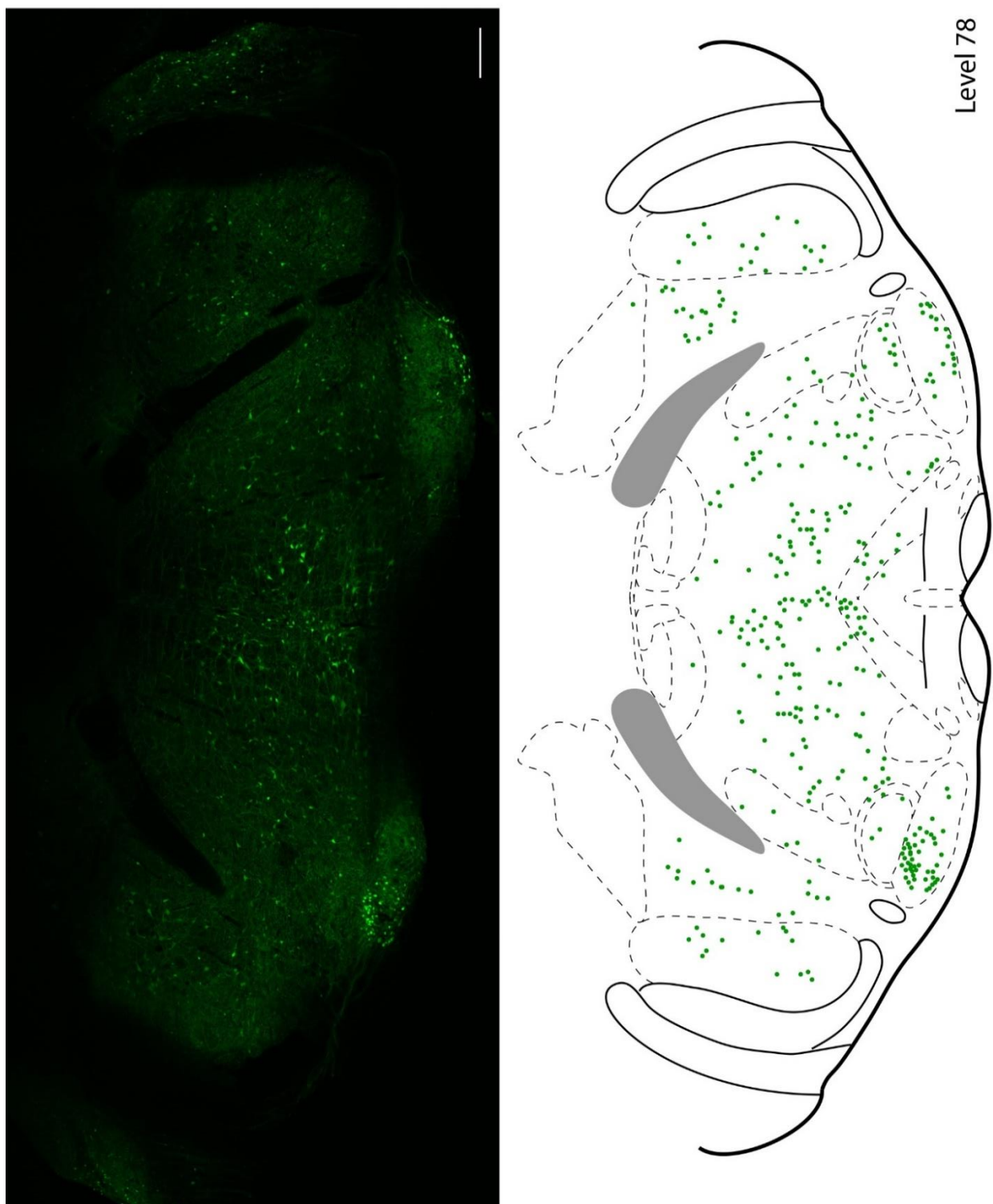


Figure 3.22. Distribution of GlyT2⁺ interneurons in the PnC and adjacent regions. Representative distribution of GlyT2 interneurons (green) in the ventral portion of PnC coronal slices mapped on anatomical levels 75-78 of the Paxinos and Franklin Mouse Brain Atlas (2004). Scale bars: 500µm.

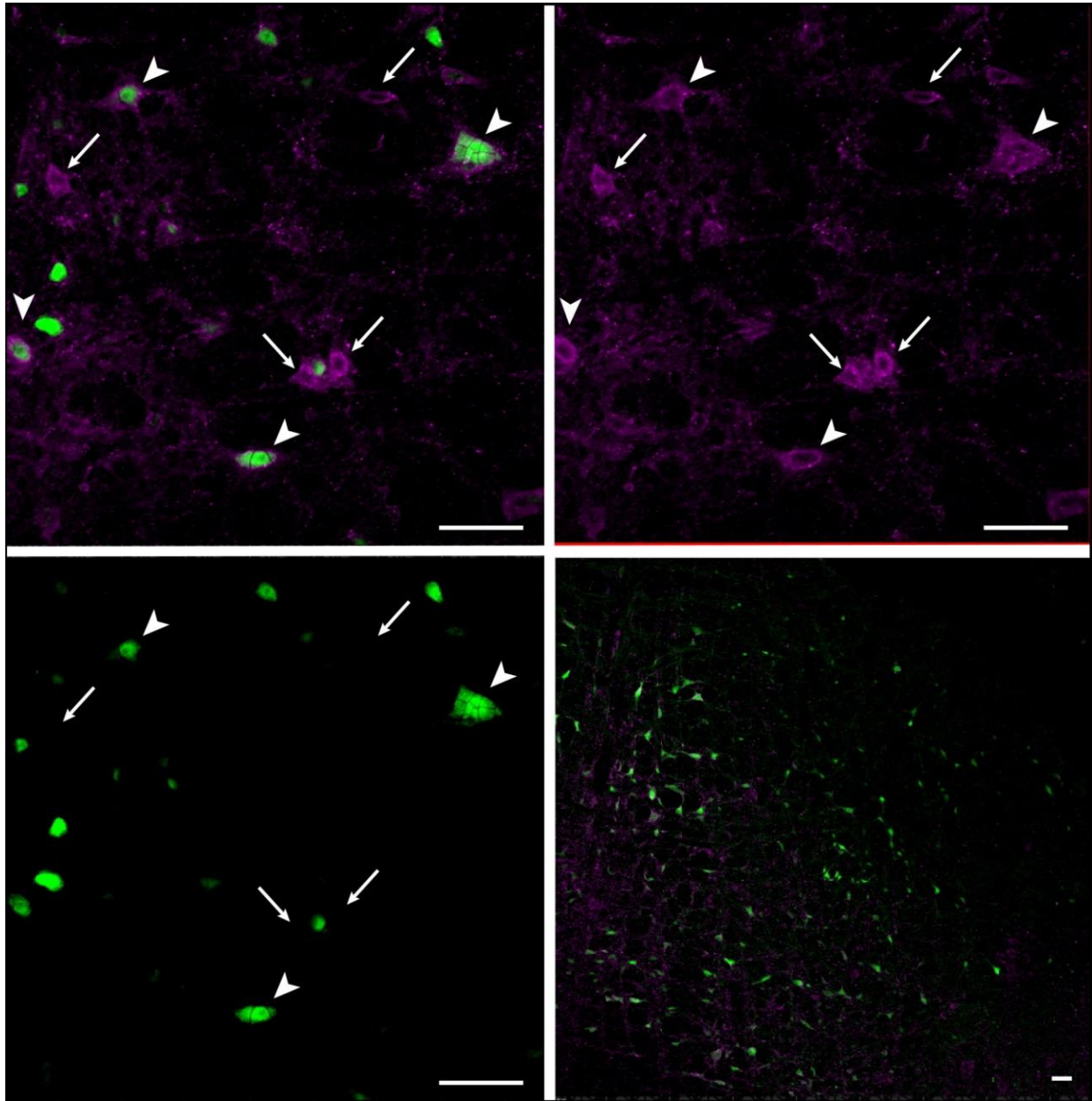


Figure 3.23. PnC GlyT2⁺ interneurons express PSD-95. (A) Low magnification image of a hemisphere of the PnC with the midline on the left end, the 7n in the upper right corner and GlyT2-EGFP cell bodies within the PnC. (B-D) High magnification image of GlyT2-EGFP cell bodies (green) delineated by PSD-95 expression (magenta; arrowheads). Other non-GlyT2 neurons were also outlined by PSD-95 expression (arrows). Scale bars: (A-D) 50μm.

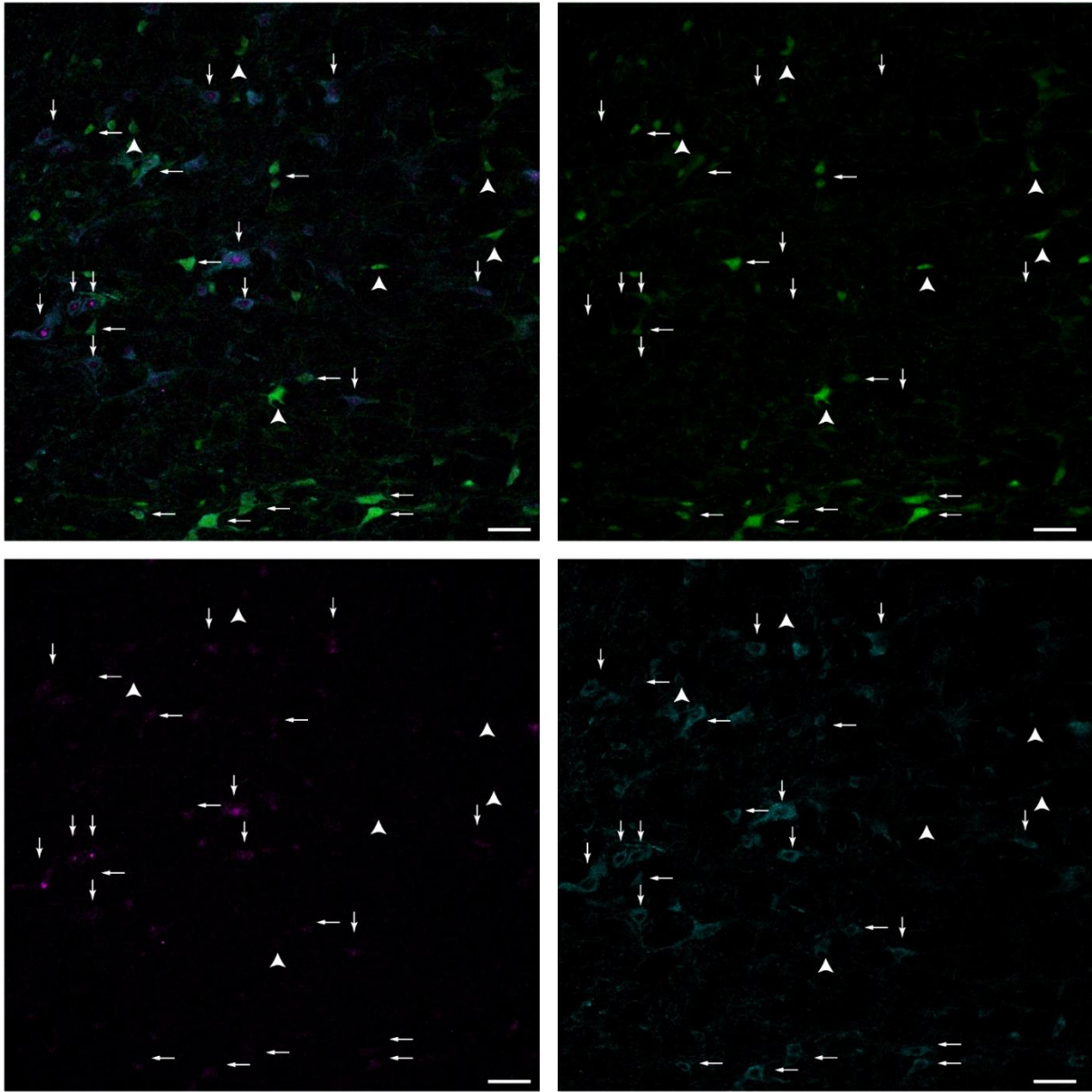


Figure 3.24. PnC GlyT2⁺ interneurons express PV and PRODH. Three phenotypes were observed in the PnC: 1) GlyT2⁺ cells (green; arrowheads); 2) GlyT2⁺/PV⁺/PRODH⁺ cells (left arrows); and 3) PV⁺/PRODH⁺ cells (down arrows). Scale bars: (A-D) 50μm.

These findings make PnC GlyT2⁺ interneurons a potential candidate to receive excitatory inputs from the CeA, to be involved in sensorimotor gating, and possibly abnormal in disease states.

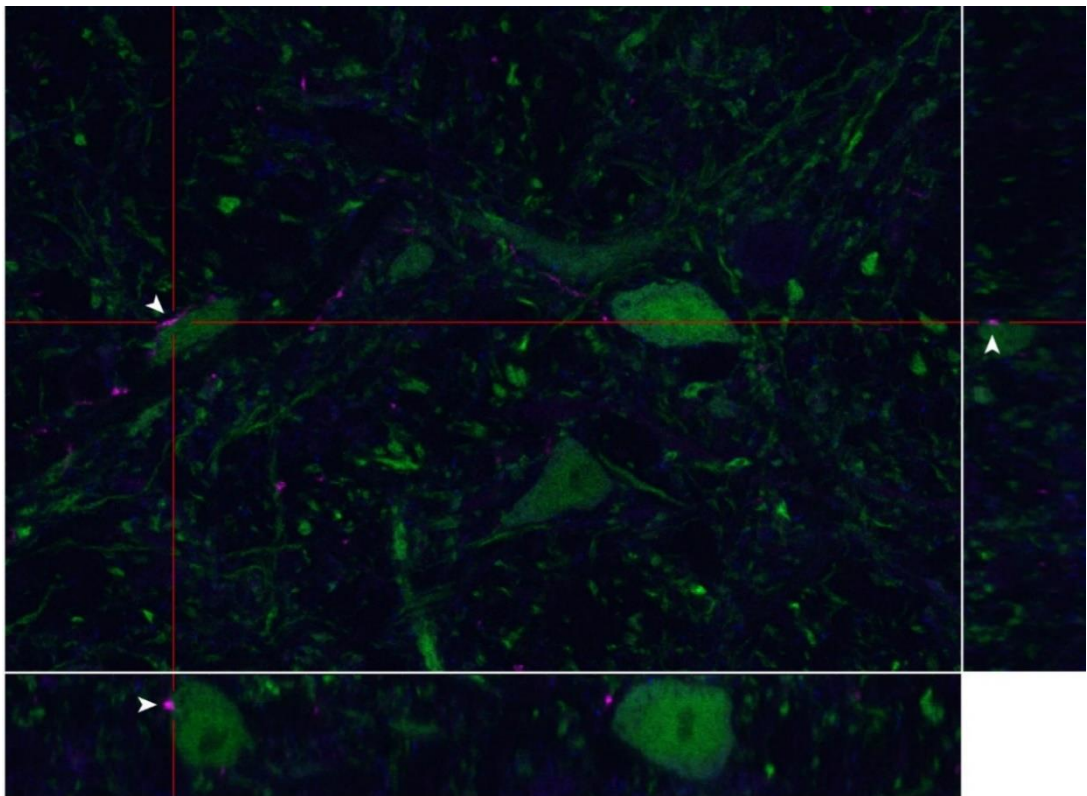
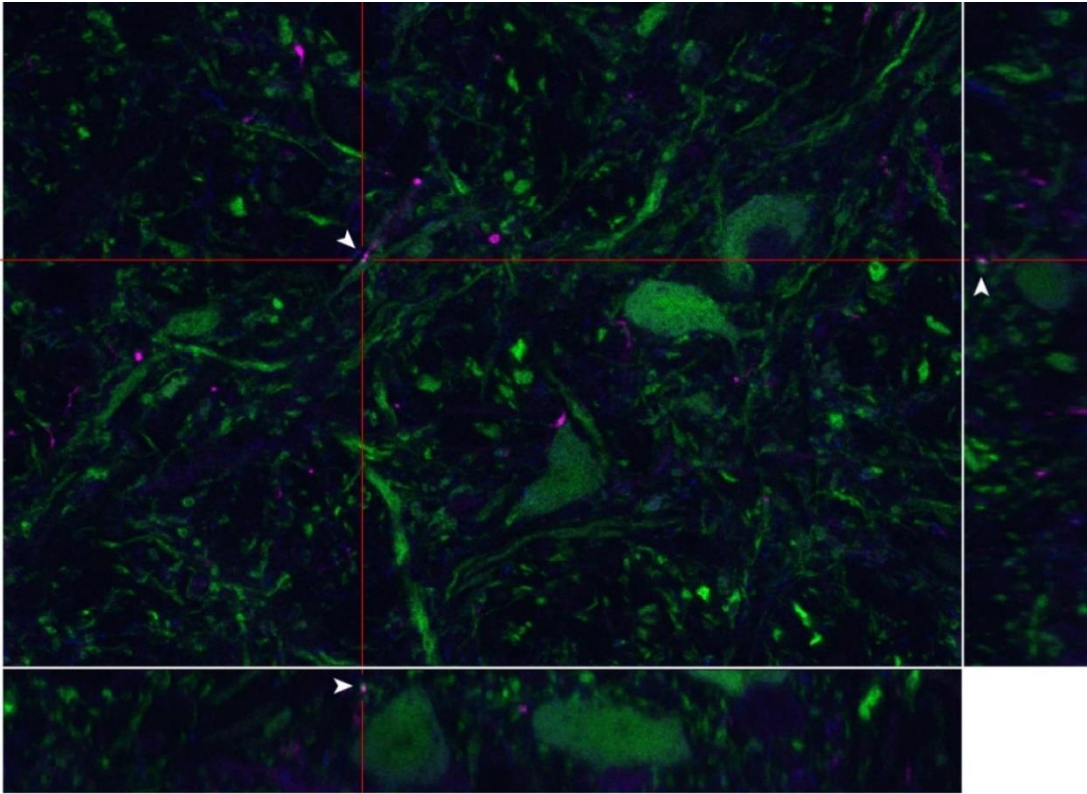
3.4.3 Putative synaptic contacts: Imaging CamKII α CeA fibers on PnC GlyT2 neurons

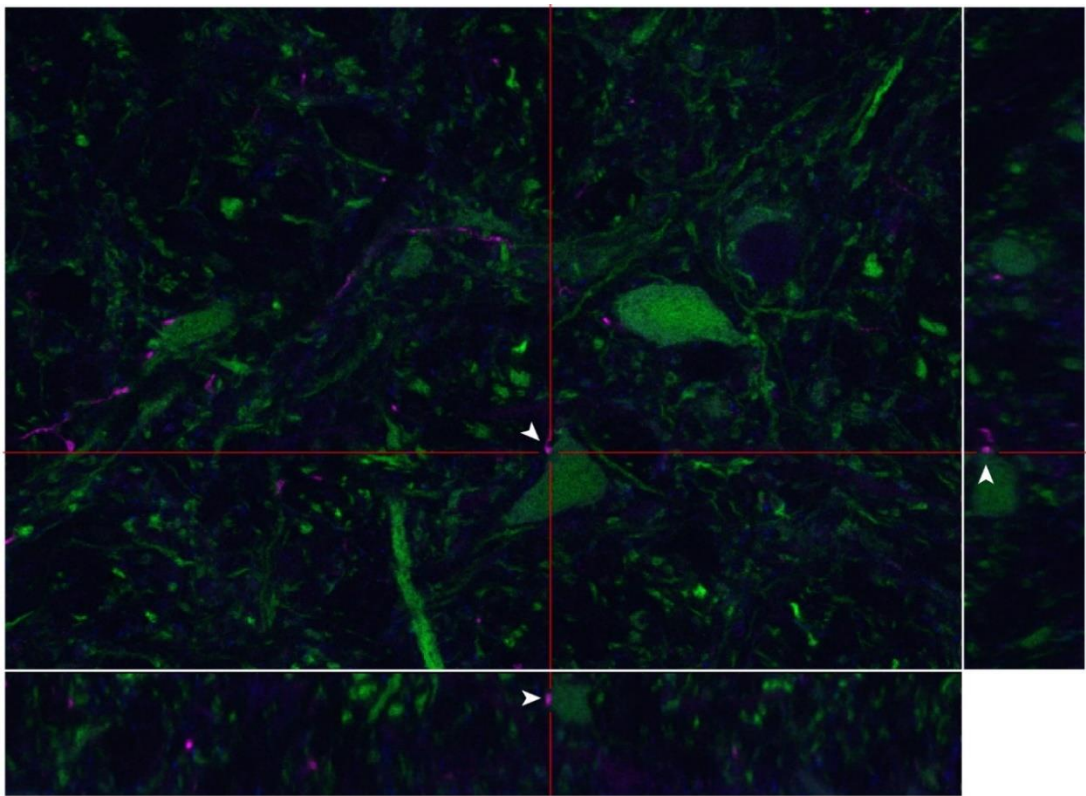
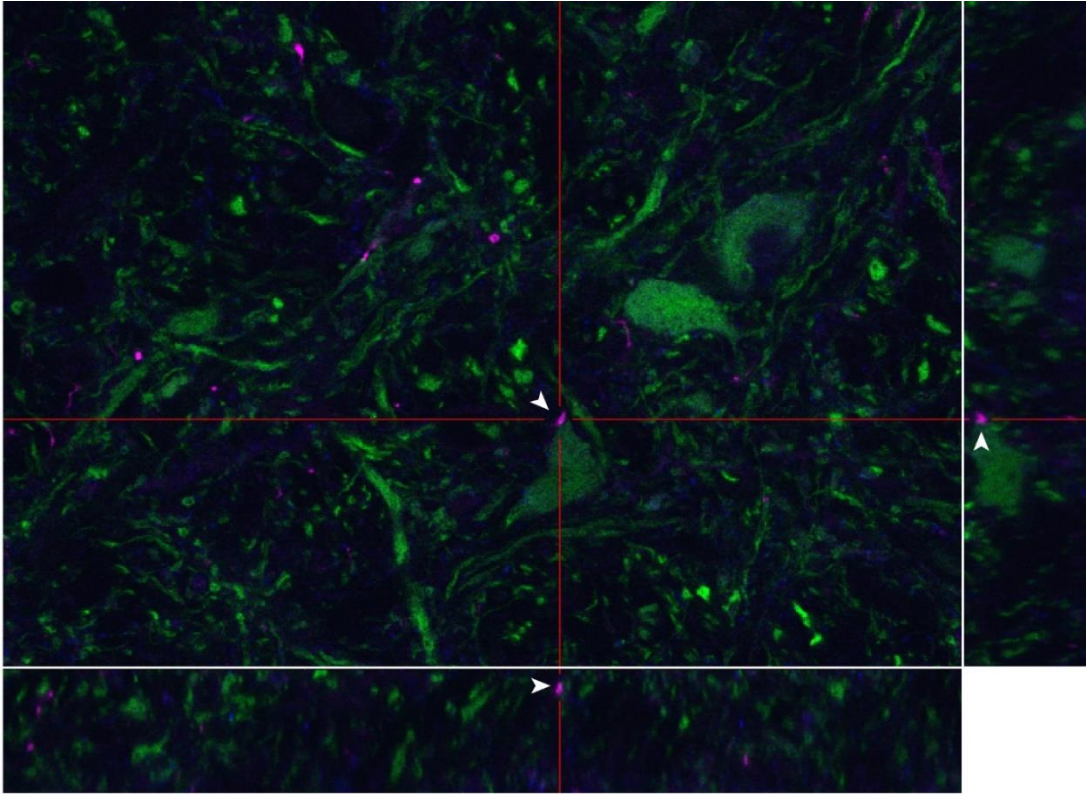
The tract tracing strategy used here consisted of a unilateral injection of AAV-CamKII α -mCherry in the CeA of GlyT2-eGFP mice. Tissue slices at the level of the PnC were then immunostained for PSD-95. In this manner, we were able to image close PSD-95-positive appositions between CeA (mCherry-labeled) axonal projections and GlyT2⁺ (eGFP-labeled) interneurons. Figure 3.25 shows orthogonal views of representative close appositions (and putative synaptic contacts) between CamKII α -dependent CeA excitatory fibers and GlyT2⁺ cell bodies or neurites in the PnC. Three-dimensional reconstructions, volume rendering and angled sectioning show, in more detail, promising putative synaptic contacts between CeA excitatory fibers and GlyT2⁺ structures in the PnC (Figure 3.26). Other close appositions did not show PSD-95 staining (Figure 3.26B).

3.4.4 CamKII α CeA input activates PnC GlyT2 cells

To confirm whether the observed close appositions between CeA axonal projections and PnC GlyT2⁺ cell bodies are synaptic contacts, we performed whole cell recordings of GlyT2⁺ neurons with photo-stimulation of CeA fibers. To do so, GlyT2-Cre mice were injected with CamKII α -ChR2-EYFP and Cre-tdTomato viral vectors in the CeA and PnC, respectively. In this manner, we were able to detect and record from GlyT2⁺ cell bodies in the PnC with optical stimulation of excitatory CeA inputs (Figure 3.27).

The passive electrical properties of a neuron dictate synaptic integration, signal conduction and excitability; therefore, these inherent membrane properties of PnC GlyT2 neurons were first measured (Table 3.1). Statistical analysis showed no significant differences in the access resistance (R_a), membrane resistance (R_m), membrane capacitance (C_m), time constant (τ) and the holding current (I_h) of light responsive and





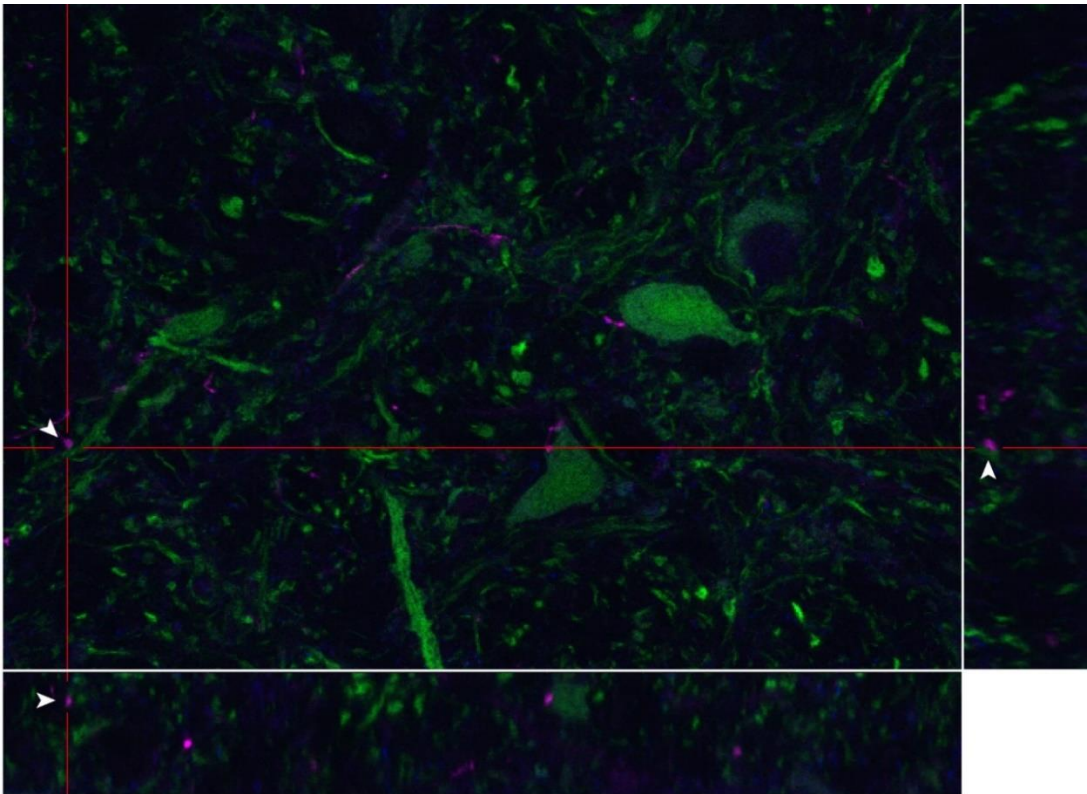
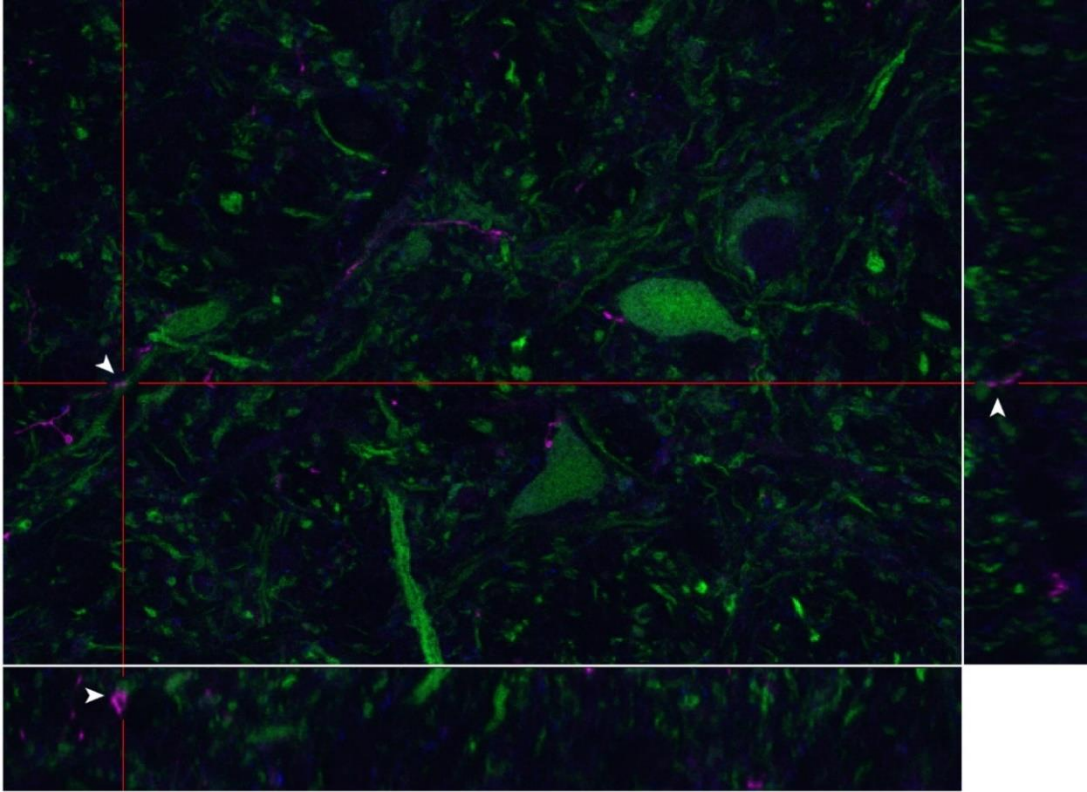


Figure 3.25. Putative synaptic appositions between CeA fibers and PnC interneurons. Orthogonal views showing six different close appositions (arrowheads) between CeA fibers expressing CamKII α -dependent mCherry (magenta) and PnC GlyT2⁺ cell bodies and neurites (green). The close apposition shown in the main X-Y axis (large square) is pinpointed on the X-Z axis (bottom rectangle) and Y-Z axis (right side rectangle) by the red lines. PSD-95 expression (blue) at each close apposition was further analyzed.

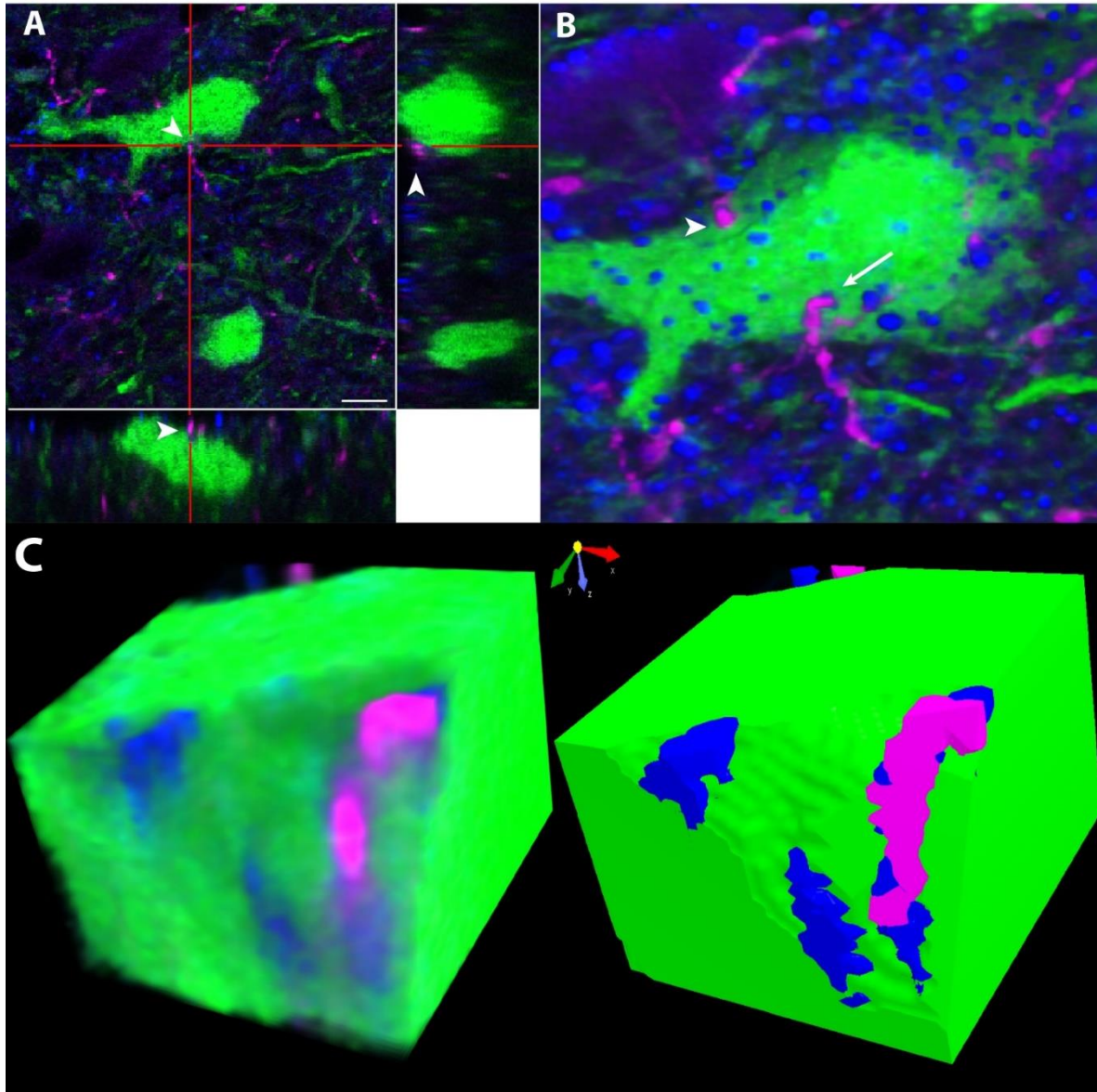


Figure 3.26 Imaging analysis of a putative synaptic contact. (A) Orthogonal view of a close apposition between CeA excitatory fibers (magenta) and a GlyT2⁺ cell body. (B) Three-dimensional reconstruction of putative synaptic contacts with PSD-95 (blue; arrow) co-localization. Other putative synaptic appositions did not show PSD-95 staining (arrowheads). (C) Volume rendering and angular sectioning of the PSD-95-positive putative synaptic contact shown in B. Scale bars: (A) 50 μ m

unresponsive cells. We then measured the spontaneous synaptic transmission and neuronal excitability capabilities of GlyT2⁺ neurons. sEPSC were recorded at resting membrane potential (-70mV); while IPSCs were recorded at the reversal potential of EPSCs (~0mV). The AP firing rate of GlyT2⁺ neurons was evaluated by injection of depolarizing current steps. Light pulses were then delivered at -70mV and 0mV to record light-evoked excitatory and inhibitory events, respectively. With this approach, we categorized the recorded GlyT2⁺ cells as light unresponsive (no light-evoked events) or light responsive. As shown in Figure 3.28, further analyses on these two groups showed that light responsive cells displayed larger mean sEPSC (n=18, t=2.538, p=0.011) and IPSC (t=2.434, p=0.025) amplitudes when compared to light unresponsive cells (n=20). More importantly, these neurons receive both excitatory and inhibitory inputs. Then, to measure neuronal excitability, AP firing rate was measured as a function of the current injected. Both groups showed similar spiking rate at every current step applied (2-way ANOVA, F=1.119, p=0.327; Figure 3.29).

Table 3.1: Passive membrane properties of PnC GlyT2⁺ cells

Group	R _a	R _m	C _m	τ (ms)	I _H (pA)
Light unresponsive (n=20)	65.33±5.69	212.24±21.61	28.5±4.15	1.5	-8.53±2.64
Light responsive (n=18)	49.59±6.88	188.28±24.56	26.06±3.9	1.5	-5.21±3.44
t-value (p-value)	-1.76 (0.1)	-0.73 (0.47)	0.43 (0.67)	-	-0.77 (0.46)

In accordance with our neuroanatomical analysis of the CeA-PnC connection, spatial distribution of GlyT2⁺ neurons within the PnC influenced whether a cell was light unresponsive or responsive. We previously observed that CamKIIα⁺ axonal projections from the CeA were most densely present in the lateroventral area of the PnC. Precisely,

cells located in this area, closer to the 7n, elicited light-evoked APs (n=6), and more medially located lateroventral PnC cells displayed light-evoked EPSPs (n=12). On the other hand, cells closer to the midline (n=16) or contralateral to the injection site were not photo-stimulated (n=4; Figure 3.30). These findings further suggest ipsilateral innervation of CeA excitatory synaptic inputs to the lateroventral PnC.

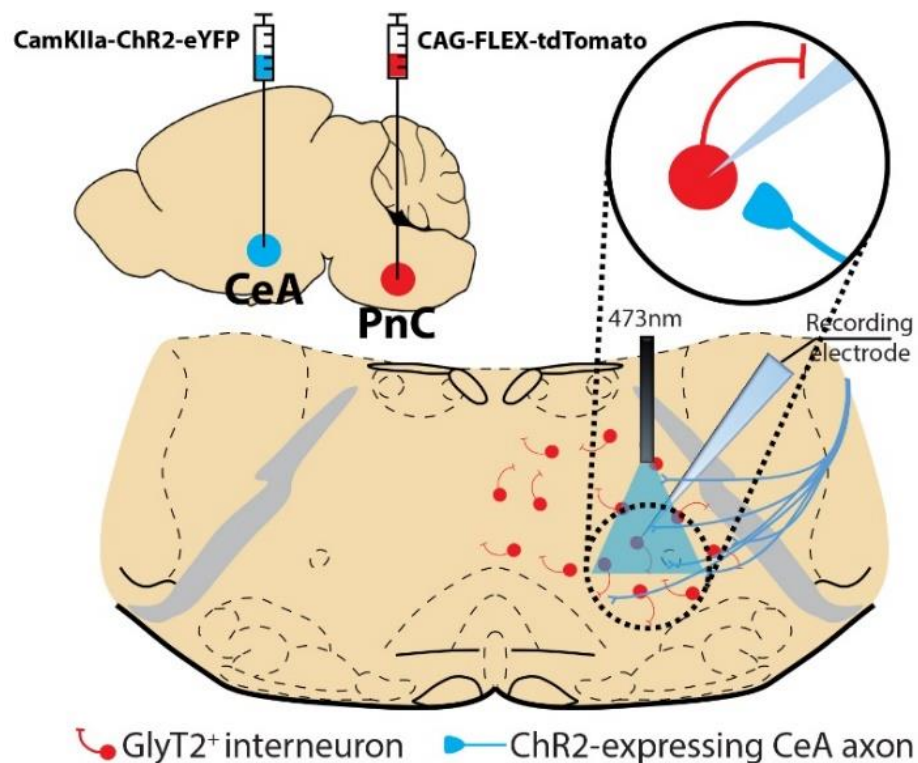


Figure 3.27 Strategy for whole-cell patch-clamp recordings of PnC GlyT2 neurons. In GlyT2-Cre mice, CamKIIα-ChR2 was injected in the CeA to photo-stimulate fibers in the PnC; and Cre-dependent tdTomato in the PnC was used to label GlyT2⁺ cells.

In light responsive cells, basal neurotransmission and short-term plasticity were then assessed. All light-evoked events had a short latency (i.e., 1-2ms after photostimulation), further suggesting a monosynaptic connection between the ChR2-expressing CeA fibers and GlyT2⁺ PnC interneurons (Figure 3.31). Using a stimulation-response protocol, we

then measured basal light-evoked neurotransmission at these synapses, and observed that light-evoked EPSCs reached their maximum amplitude at 4rlu (49.55 ± 7.64 mV; Figure 3.31A).

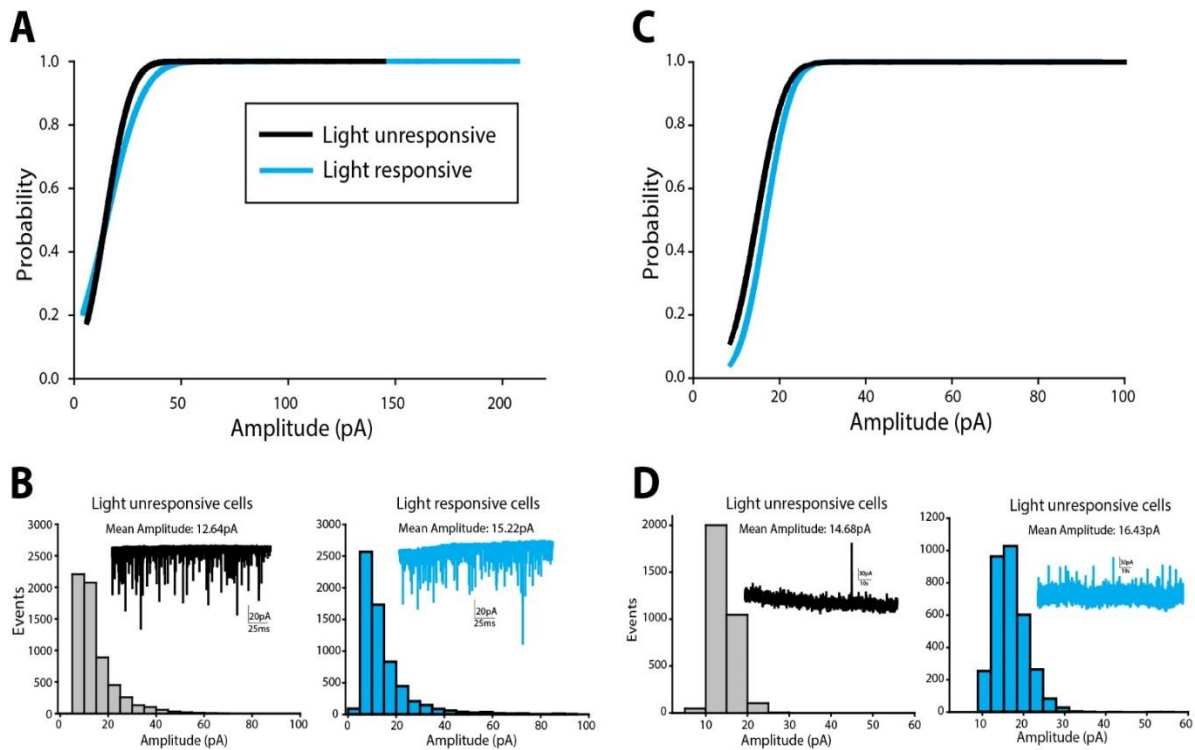


Figure 3.28 sEPSC and IPSC amplitude distribution of PnC GlyT2 interneurons. (A) Cumulative distribution plot showing larger sEPSC amplitude in light responsive cells. (B) Histograms showing the sEPSC amplitude distribution of events in light unresponsive (Left; $n=20$) and responsive (Right; $n=18$) cells. (C) Cumulative distribution plot showing larger IPSC amplitude in light responsive cells. (D) Histograms showing IPSC amplitude distribution of events in light unresponsive (Left; $n=20$) and responsive (Right; $n=18$) cells. Insets: Representative traces. $N=10$, $n=38$. Data represented as mean \pm SEM.

Therefore, 3rlu of intensity, which elicited half of the maximum response (16.02 ± 13.78 mV), were used to then test the vesicle release efficacy of CeA-PnC excitatory synapses. Similar to our findings in the field recording experiments, the PPR for the EPSPs and EPSCs at 50 and 100ms ISI were greater than 1, indicating synaptic facilitation due to a relatively low vesicle release probability following the first stimulus, and allowing a relatively big pool of vesicles to be released in response to the second

stimulus (Figure 3.31B, EPSP PPR: 50ms=1.09, 100ms=1.13; Figure 3.31C EPSC PPR: 50ms=1.318, 100ms=1.243).

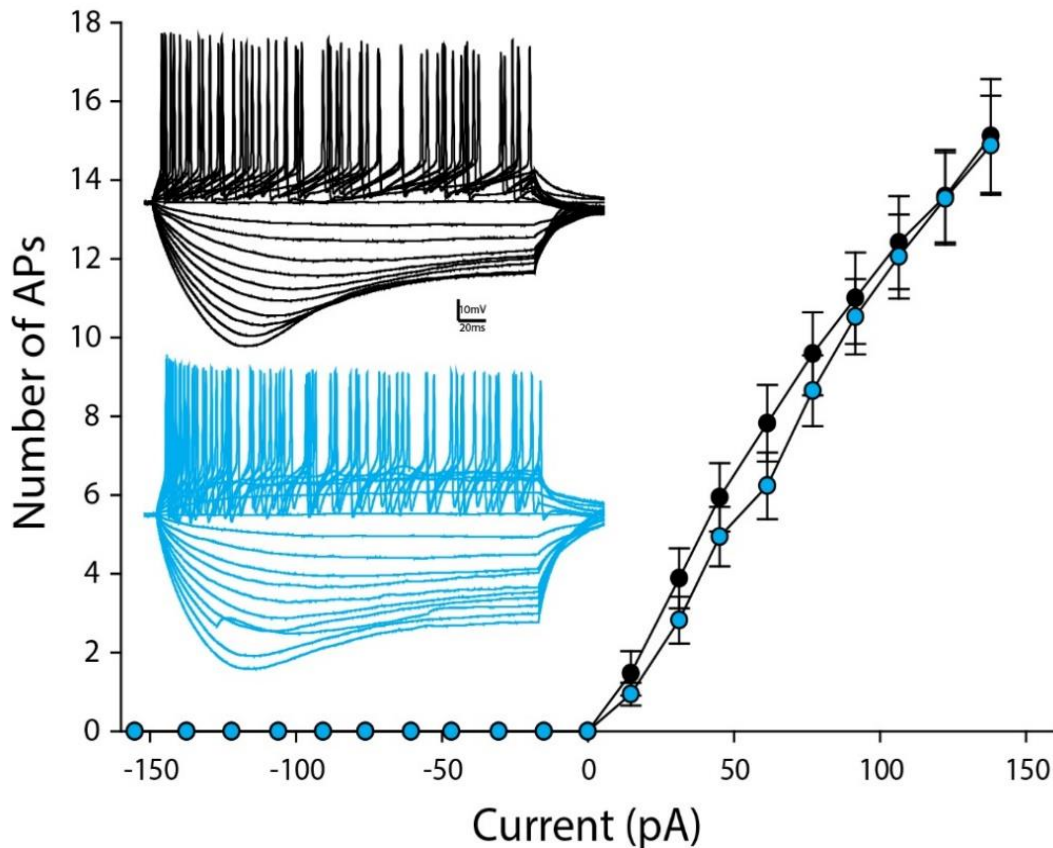


Figure 3.29 Light responsive and unresponsive cells display similar spiking activity.
Both cell groups displayed similar firing rate and threshold current to elicit APs.

Complementarily, to further confirm on the neurochemistry of the CamKII α -dependent CeA inputs to GlyT2⁺ PnC interneurons, we bath-applied AP5 and DNQX. Once more, similar to our extracellular recordings results, light-evoked EPSPs (2.39 ± 0.47 mV) were significantly reduced by AP5 and DNQX (AP5: 0.68 ± 0.17 mV; DNQX: 0.75 ± 0.17 mV; 1-way RM ANOVA, $F=9.463$, $p<0.01$), and recovered washout (2.15 ± 0.75 mV; Figure 3.32A). Similarly, in cells that displayed light-evoked APs, AP5 and DNQX greatly decreased APs amplitude (Figure 3.32B; 1-way RM ANOVA, $F=6.009$, $p<0.01$).

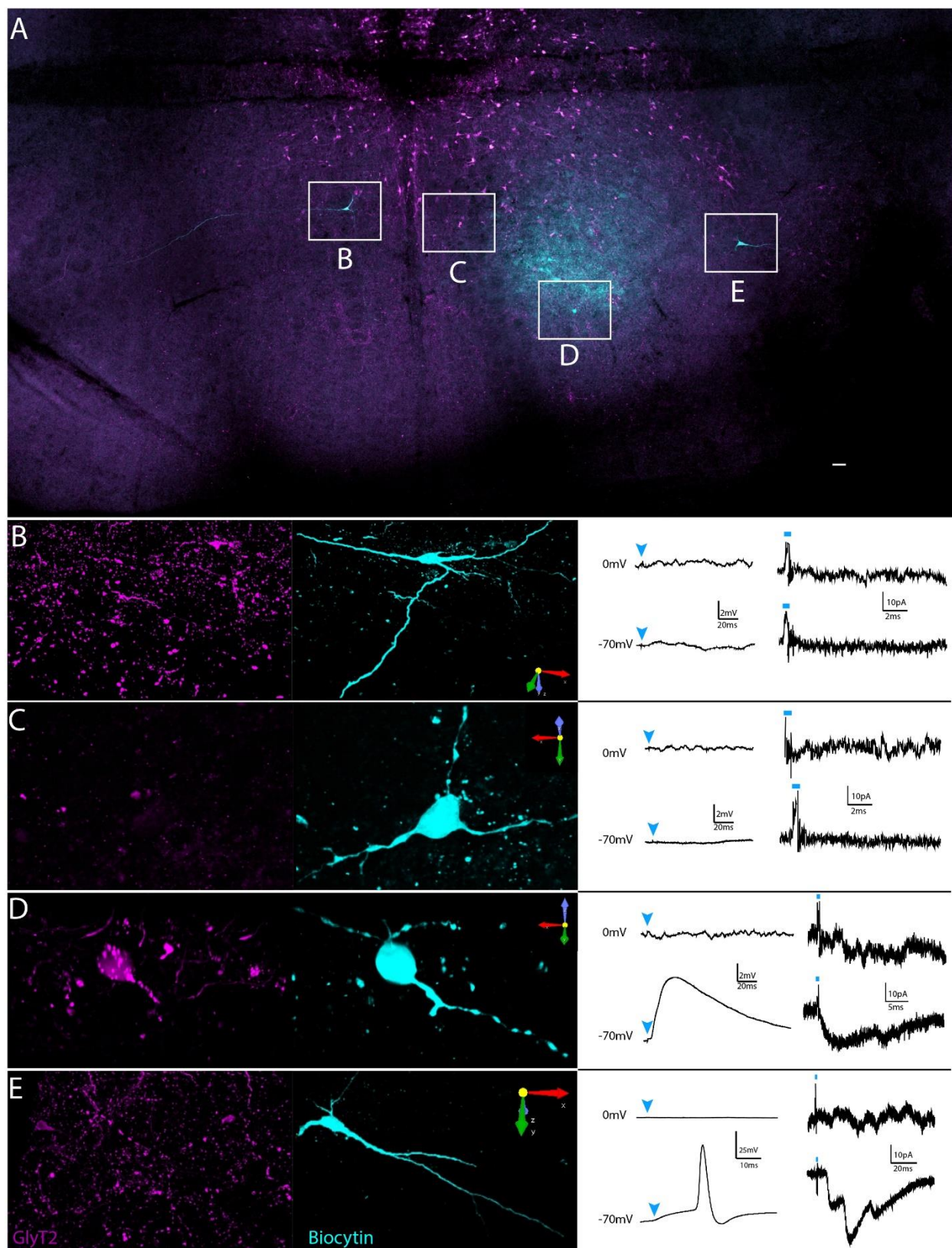


Figure 3.30. Spatial-dependent light-evoked activity of PnC GlyT2 interneurons. (A) Low magnification image of an acute PnC slice showing patched cells (cyan; white rectangles) at different locations within the PnC. Other GlyT2⁺ cells labeled by the extent of the injection site (magenta) are scattered throughout the PnC and adjacent brain regions. (B-E) Morphological reconstructions of recorded cells shown in (A) with their corresponding traces of light-evoked EPSPs/APs and EPSCs at -70mV. Cells contralateral to the injection site (B) and ipsilateral cells closer to the midline (C) showed no light-evoked activity. Ipsilateral cells closer to the 7n (C, D) displayed light-evoked EPSPs/APs and EPSCs. Blue arrowheads and lines indicate photostimulation. Scale bars: (A) 250μm

Lastly, at the injection site, we also characterized the electrophysiological properties, firing capabilities and light-evoked events of CamKIIα⁺ neurons within the CeA (Figure 3.33). These cells presented a sEPSC mean amplitude of 13.26pA, a slower firing rate and a considerably larger maximum light-evoked EPSC ($821.15 \pm 20.3\text{pA}$) than PnC GlyT2⁺ interneurons.

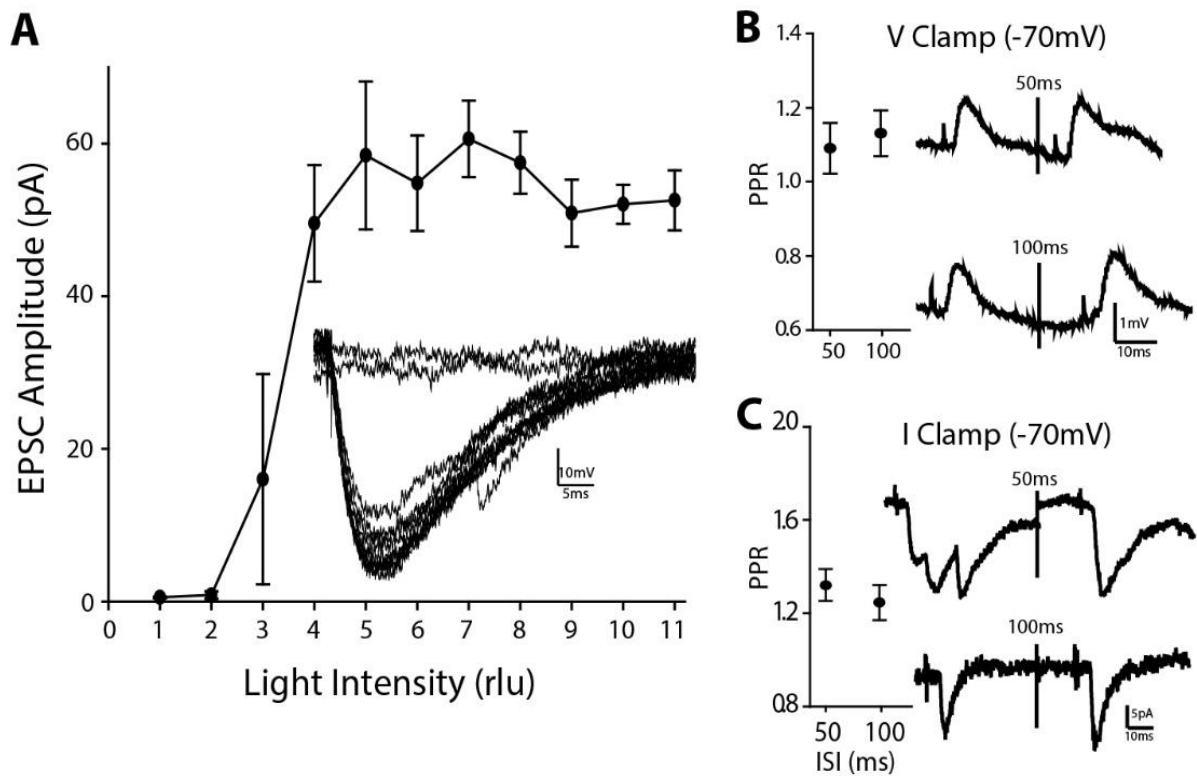


Figure 3.31. Light-evoked activity of PnC GlyT2 interneurons. (A) Input/output curve of light-evoked EPSC. (B, C) Paired-pulse ratios of light-evoked EPSPs (B) and EPSCs (C) indicate an initial low probability of neurotransmitter release. Insets: Representative traces. N=10, n=20. Data are represented as mean \pm SEM.

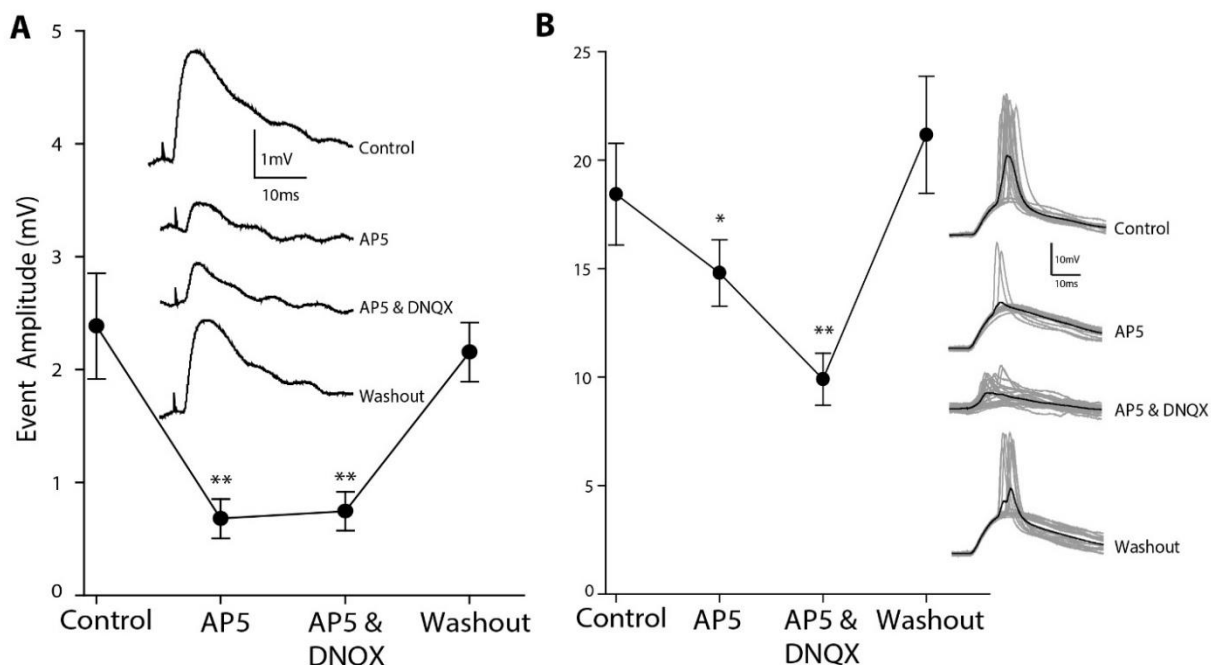


Figure 3.32. CeA excitatory inputs activate ionotropic receptors on GlyT2 interneurons. (A, B) Amplitude of light-evoked EPSPs (A; $n=12$) and APs (B; $n=6$) was significantly decreased by bath-application of AP5 and DNQX, and recovered following washout. Insets: Representative traces. $N=10$, $n=38$. Data are represented as mean \pm SEM. * $P>0.05$, ** $P>0.01$.

In sum, our results suggest that direct, ipsilateral, and CamKII α -dependent axonal projections from the CeA to the PnC mediate PPI in mice. In a feed-forward inhibition fashion, these excitatory projections activate, in part, inhibitory interneurons in the PnC that are likely to then inhibit/gate giant reticulospinal ‘startle’ neurons. Whole-cell patch-clamp recordings on these downstream components of the PPI neural network would further test our proposed pathway. In addition, further efforts should also be aimed to identify the upstream brain regions that undertake the neural computation of the prepulse and are likely to then physiologically activate the CeA. These results substantiate the role in sensorimotor gating of an intermediate and alternative pathway to the classical PPTg-PnC circuits.

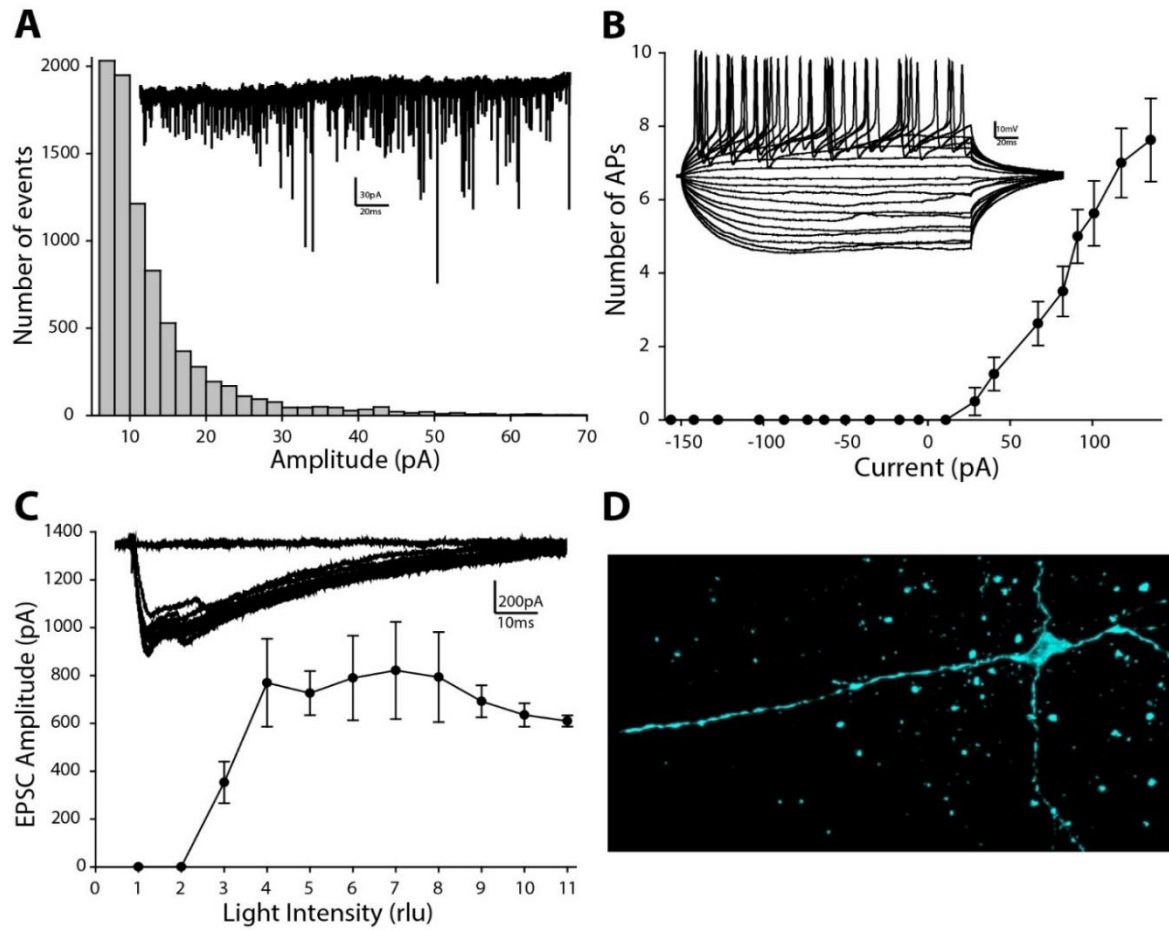


Figure 3.33. sEPSC, spiking and light-evoked activity of CeA CamKII α cells. (A, B) Plots showing the cumulative distribution of sEPSC amplitude (A) and firing rate by depolarizing currents (B). (C) Input/output curve of light-evoked EPSC. (D) Three dimensional reconstruction of a representative patched CeA neuron. Insets: Representative traces. N=10, n=26. Data represented as mean \pm SEM.

Chapter 4: Discussion

Recent studies, revisiting the dogmatic role of pontine cholinergic neurons in PPI, suggest that non-cholinergic PPTg neurons are crucial for PPI (Azzopardi *et al.*, 2018; Fulcher *et al.*, 2019; MacLaren *et al.*, 2014; Schmid *et al.*, 2011). Interestingly, an increasing number of evidence highlights the importance of GABAergic and glutamatergic signaling circuits in PPI. Numerous studies have shown that PPI changes occur when GABAergic and glutamatergic neurotransmission are altered in several brain regions, such as the prefrontal cortex (Kohl *et al.*, 2013), substantia nigra (Koch *et al.*, 2000), amygdala (Forcelli *et al.*, 2012; Howland *et al.*, 2007; Wan and Swerdlow, 1997), hippocampus (Harrison *et al.*, 2003; Ma and Leung, 2011; Nguyen *et al.*, 2014), superior colliculus (Fendt, 1999), PPTg (Azzopardi *et al.*, 2019; Bergeron *et al.*, 2015; MacLaren *et al.*, 2014; Tabor *et al.*, 2019) and NAcc (Swerdlow *et al.*, 1990). Some of these brain regions also exhibit anatomical and functional abnormalities in neuropsychiatric disorders associated to sensorimotor gating deficits. Therefore, in order to reconcile impaired sensory filtering in disease, a better understanding of the neuronal elements and circuits underlying PPI is needed. In that respect, the study presented here sheds light on the neuroanatomical, neurochemical and mechanistic bases of a connection centrally positioned to contribute to sensorimotor gating, alternative to the well-studied CSPP network.

Outlined in the aims presented in Chapter 3, the main findings from this project are: 1) an excitatory, ipsilateral, and directly-connected set of CeA projections elicit synaptic activity in the PnC; 2) this subset of CeA fibers can attenuate PnC activity elicited by auditory fiber stimulation *in vitro*; 3) CeA-PnC excitatory synapses do not alter basal ASR,

and contribute to PPI *in vivo*; and 4) excitatory CeA inputs activate PnC inhibitory interneurons, which then likely inhibit 'startle' neurons.

4.1 Neuroanatomy and neurochemistry of an excitatory CeA-PnC connection

Our analyses suggest that the CeA sends, in part, direct, excitatory and ipsilateral inputs to inhibitory interneurons in the PnC of mice. These CamKII α -dependent CeA fibers were most densely observed in the lateroventral area of the ipsilateral PnC, adjacent to the 7th nerve fibers and the olivary complex. The lateroventral area of the PnC is also innervated by cochlear nuclei fibers conveying acoustic startle input to PnC reticulospinal neurons (Bosch and Schmid, 2006; Davis *et al.*, 1982; Gomez-Nieto *et al.*, 2014). A closer mapping analysis indicated that the PnC neurons activated by CeA excitatory inputs are principally distributed in this PnC area, vital for acoustic startle information processing. In fact, unilateral electrolytic lesions to the lateroventral PnC greatly attenuate the acoustic startle reflex (Lee *et al.*, 1996). Interestingly, previous studies in healthy and schizophrenia subjects have shown that a monaural acoustic prepulse exerts a stronger inhibition of the eye blink reflex, a component of the ASR in humans, compared to a binaural prepulse (Kumari *et al.*, 2007; Marsh *et al.*, 1976). Also, unilateral GABAergic inhibition of the BLA was demonstrated to be sufficient to decrease baseline ASR and PPI (Forcelli *et al.*, 2012). Similarly, here, we show that unilateral photo-inhibition of CeA-PnC CamKII α synapses was sufficient to induce a robust decrease in PPI.

At the level of the CeA, we demonstrate that cell bodies anatomically connected to the PnC are confined to the medial CeA; while no cell bodies projecting to the PnC in the lateral and capsular CeA were detected. The medial CeA is one of the major amygdalar

output stations conveying integrated information to several premotor hindbrain regions that drive both innate and learned defensive behaviors (Isosaka *et al.*, 2015; Swanson and Petrovich, 1998; Tillman *et al.*, 2018). In these circuits, sensory information is integrated in the CeA, relayed directly (and indirectly) to premotor regions (e.g., PAG and PCRtA), which then activate motor neurons that elicit a response. In the PPI neural pathway proposed here, CamKII α cells in the medial CeA process the prepulse sensory information from still unidentified upstream neural substrates, and relay the integrated information to the PnC, where the startle input is gated resulting in an attenuated activation of motor neurons and response.

On the neurochemical basis of this connection, our results first demonstrate that CeA cell bodies directly connected to the PnC are not cholinergic. These observations are in line with previous studies demonstrating no cholinergic neurons in the CeA (Ichikawa *et al.* 1997), and that cholinergic inputs to the PnC originate from the mesopontine tegmental nuclei, such as the PPTg (Semba *et al.* 1989; Semba *et al.*, 1990). We then observe that CamKII α -EYFP-expressing cell bodies in the medial CeA project directly to the PnC. Preferentially expressed in excitatory neurons, previous studies detected CamKII α -driven expression in GABAergic neurons (Nathanson *et al.*, 2009). In addition, taking into consideration that the CeA is a largely GABAergic nucleus; here, we show that Gabazine did not affect light-evoked events in the PnC. Complementarily, we observed no light-evoked events at membrane potentials where inhibitory events are isolated (~ 0 mV). On the other hand, field and single-cell light-evoked events in the PnC were greatly reduced by ionotropic glutamate receptor antagonists. Taken together, these results suggest that CamKII α neurons in the medial CeA send glutamatergic inputs that activate ionotropic

receptors on PnC neurons. Although not as abundant as GABAergic neurons, glutamatergic cells have been documented in the CeA (Hur *et al.*, 2005; Poulin *et al.*, 2008). Noteworthy, CamKII α -independent GABAergic projections from the CeA may also regulate PnC activity. We observed more FluoroGold-labeled than CamKII α -eYFP-expressing neurons, which may be partially explained by the unclear retrograde tracing specificity of FluoroGold. Nonetheless, the CeA sends GABAergic inputs to several brainstem regions adjacent to the PnC (Han *et al.*, 2017; Jungling *et al.*, 2015; Swanson and Petrovich, 1998; Ozawa *et al.*, 2017). Furthermore, altered GABAergic neurotransmission is hallmark of schizophrenia (Benes and Beretta, 2001; Lewis *et al.*, 2005), and it is closely associated with abnormal ASR and PPI (Forcelli *et al.*, 2012; Koch *et al.*, 2000; Ma and Leung, 2011; Fendt, 1999; Swerdlow *et al.*, 1990). Overall, these observations make the CeA an intriguing hub for future studies on the emerging role of GABAergic and glutamatergic systems in sensorimotor gating.

4.2 Synaptic properties of CeA-PnC connection and their relevance to sensorimotor gating

Assessing the probability of neurotransmitter release of CamKII α -dependent CeA-PnC synapses, we observed that light-evoked fEPSPs facilitated at ISI of 50-200ms. Such events are typical of facilitating synapses, presumably displaying a presynaptic enhancement of transmitter quanta release on the hundreds of milliseconds time scale (Zucker and Regehr, 2002). Similar observations were recorded at the single cell level, where PnC inhibitory interneurons displayed facilitating light-evoked EPSPs and EPSCs at ISI of 50 and 100ms. The synaptic properties described here will serve as baseline for

future studies on the CeA-PnC connection in animal models of disorders associated with sensorimotor gating deficits.

Deficient plasticity has been long suspected to be compromised and contribute to the cognitive deficits observed in schizophrenia patients and animal models. Genetic screening for susceptibility schizophrenia genes elucidated several loci coding for proteins and microRNAs with prominent neurodevelopmental and functional roles in synapses, such as DGCR8 (Fenelon, *et al.*, 2011; Fenelon *et al.*, 2013), neuregulins (Law *et al.*, 2004; Law *et al.*, 2006; Li *et al.*, 2006; Ozaki *et al.*, 2001), dysbindin (Talbot *et al.*, 2011), PRODH (Crabtree, *et al.*, 2016) and cadherins (Singh *et al.*, 2010), among myriad of other genes. Like so, mutant mouse lines with altered expression of several presynaptic machinery components display a schizophrenic phenotype. Transgenic mouse lines with reduced expression of presynaptic scaffolding proteins, such as neuregulins (Chen *et al.*, 2008), DISC1 (Maher and LoTurco, 2012), RIM1a, synaptotagmin and Rab3A (Blundell *et al.*, 2010) and neurexin (Etherton *et al.*, 2009) exhibit PPI deficits, among other cognitive impairments correlated to schizophrenia patients. Furthermore, mice with a heterozygous null mutation of the excitatory presynaptic protein, CamKII α , display several behavioral deficits closely associated with schizophrenia, such as reduced working memory (Frankland *et al.*, 2008; Miyakawa *et al.*, 2008). In this extensive study by Miyakawa and colleagues (2008), reduced levels of phosphorylated CamKII α were measured in the amygdala and cingulate cortex, among other regions. Although, no significant changes in PPI were observed in this mutant mice, different parameters were used in this study, such as a recording period for a startle response of only 140ms after the startling sound was presented, and only one ISI (100ms) between the prepulse and

pulse was tested. Regardless, along with their essential presynaptic role during neurotransmission, all of the aforementioned proteins have been shown to be critical in neurodevelopmental processes dysregulated in schizophrenia, including neurogenesis, neuronal maturation and migration, axonal guidance and network formation (Fenelon *et al.*, 2011; Mukai *et al.*, 2015; Windrem *et al.*, 2015). Taken together, these observations highlight the importance of characterizing the presynaptic mechanisms of the CamKII α -dependent CeA-PnC connection, which are likely to contribute to PPI.

4.3 CeA-PnC connection as a gating substrate

Here, we observed that optogenetic inhibition of CeA-PnC glutamatergic synapses greatly attenuated PPI *in vivo*; while photostimulating this connection in lieu of an acoustic prepulse contributed to a significant percentage of the total acoustic PPI. Similarly, in a pair of elegant studies in zebrafish, ablation of Gsx1 neurons in a region homologous to the mammal PPTg greatly reduced PPI; while photostimulation of these neurons as a prepulse elicited a PPI effect at ISI of 400ms (Bergeron *et al.*, 2015, Tabor *et al.*, 2018). This paradoxical role of PPTg glutamate neurons was recently replicated in a rat model. Using a VGLUT2-Cre line, chemogenetic inhibition of PPTg glutamatergic neurons significantly decreased PPI at ISI of 30 and 100ms (Fulcher *et al.*, 2019).

4.3.1 Presynaptic filtering

The puzzling contribution of an excitatory input in PPI, an inhibitory phenomenon, is the focus of current investigations. First described in the aforementioned study by Frost and colleagues (2003), a prepulse-activated interneuron hyperpolarizes the presynaptic sensory efferent fiber reducing the activation of startle cells and the subsequent startle

response. This presynaptic filtering mechanism, which mediates PPI in *Tritonia*, occurs via hyperpolarizing chloride currents that inhibit the axon terminal of the sensory cells. In the zebrafish studies, the inhibition occurred via presynaptic filtering of the output from the auditory fibers of the VIIIth nerve to the startle Mauthner cells (Tabor *et al.*, 2018). However, in this case presynaptic glutamatergic inputs activated by the prepulse drive the presynaptic filtering mechanism. Although the precise molecular mechanisms are yet to be identified, it was speculated that these glutamatergic neurons activate presynaptic glutamate ionotropic receptors on auditory efferents, which then inhibit presynaptic neurotransmitter release via voltage-gated Ca^{2+} channels and metabotropic mechanisms (Oshima-Takago *et al.*, 2017; Takago *et al.*, 2005; Wu and Saggau, 1997). Alternatively, NMDA receptors are also thought to shunt action potential propagation and inhibit synaptic neurotransmission by inactivating presynaptic Na^+ and Ca^{2+} channels (Bardoni *et al.*, 2004; MacDermott *et al.*, 1999). Regardless, further investigation will elucidate the precise molecular signaling pathways underlying excitatory presynaptic filtering.

We contemplated a similar mechanism, in which CeA glutamatergic inputs filter output of cochlear (auditory) fibers to the lateroventral PnC. However, we observed that photostimulation of CeA fibers as a prepulse did not alter the probability of neurotransmitter release from auditory terminals suggesting no presynaptic filtering, at least in this part of the circuit.

4.3.2 Post-synaptic gating

Alternatively, to provide mechanistic evidence and reconcile our *in vitro* field recordings and *in vivo* results, we explored the possibility of post-synaptic gating through feed-forward inhibition. In this pathway, the gating signal (prepulse) activates inhibitory

interneurons, which then inhibit the subsequent activation of the PnC startle neurons. The presynaptic inhibitory mechanism investigated by Frost and colleagues (2003) was mediated by a prepulse-activated interneuron, which then ‘filtered’ sensory input to startle neurons. In addition, in this same *Tritonia* study, authors also identified a “prepulse-elicited post-synaptic inhibition” circuit also mediated by an interneuron. This post-synaptic neuronal pathway hinges on an excitatory interneuron that is activated by sensory input. Then, the excitatory interneuron activates an “unidentified” inhibitory interneuron, which then inhibits a motor component in the central pattern generator. In addition, the excitatory interneuron also recruits the inhibitory interneuron responsible for the presynaptic filtering mechanism (described in the previous section); therefore, strengthening the inhibition of the escape swim startle response (Frost *et al.*, 2003).

In a similar manner, other brain circuits in rodents also rely on interneuron-mediated post-synaptic mechanisms to distil information and shape behavior. Interneurons are orchestrators that fine-tune afferent input to micro-circuits and regulate activity within a brain region. For example, the myriad of cortical GABAergic interneurons gate input to pyramidal neurons and mediate their synchronous firing to properly process sensory information (Stober *et al.*, 2009). Principally mediated by vHPC glutamate efferents to the mPFC, working memory is further modulated by thalamic-striatal inputs that, through ‘rhythmic’ activation of mPFC GABA interneurons, refine hippocampal glutamatergic inputs to mPFC pyramidal cells (Cardin *et al.*, 2009, Floresco *et al.*, 1999; Miller, 2000). In a similar manner, the vHPC also sends glutamatergic projections to GABA-PV interneurons and medium spiny neurons (MSNs) in the NAcc. (Pennartz and Kitai, 1991; Scudder *et al.*, 2018). In this feed-forward inhibition circuit, vHPC regulates the

excitatory/inhibitory activity of MSNs in the NAcc and shapes reward-seeking behavior. The vHPC also recruits GABA-PV interneurons in the IL mPFC that inhibit efferents to the amygdala. In doing so, the vHPC triggers fear renewal to an extinguished conditioned stimulus (Marek *et al.*, 2018).

Inhibitory GlyT2-expressing interneurons were previously described in the PnC of rodents (Rampon *et al.*, 1996, Zeilhofer *et al.*, 2005); however, their function remains unknown. Furthermore, these GlyT2-expressing neurons in auditory brainstem regions corelease GABA and glycine (Moore and Trussel, 2017). Histological studies in macaques also identified medium-sized excitatory and inhibitory neurons clustered in the dorsomedial PnC that received SC input and contributed of eye-saccades (Horn, 2006; Sakai *et al.*, 2009; Strassman *et al.*, 1986). We observed a similar distribution pattern of densely clustered GlyT2 neurons along the midline of the PnC, which also expressed PV and PRODH, in all anatomical levels analyzed. Whether these neurons receive input from the SC and are involved in eye-saccades, as in macaques, is yet to be investigated. More importantly, these inhibitory interneurons were also present in the lateroventral PnC, an area critical for acoustic startle information processing and where we observed the most CeA innervation (Davis *et al.*, 1982; Lee *et al.*, 1996). Interestingly, in the discussion of the tract-tracing study by Rosen and colleagues (1991) where the CeA-PnC connection was first described, the authors commented on the fact that CeA fibers are in close proximity to small-to-medium-sized cell bodies, as opposed to giant reticulospinal neurons. Here, we imaged and dissected putative synaptic PSD95-expressing appositions between excitatory CeA axonal projections and small-to-medium-sized GlyT2 interneurons. Complementarily, whole-cell patch-clamp recordings confirmed that CeA

glutamatergic inputs activate PnC inhibitory interneurons. To reconcile these findings with the *in vivo* results, we hypothesize that these interneurons inhibit the startle-activated PnC reticulospinal neurons. In this manner, the output to motor neurons is inhibited ('gated') resulting in an attenuated startle response. Our hypothesis is supported by previous studies demonstrating that PnC giant neurons express GABA_A and glycine receptors (Waldvogel *et al.*, 2010), and application of GABA and glycine can attenuate cochlear-evoked activity of these PnC reticulospinal neurons (Geis and Schmid, 2011; Yeomans *et al.*, 2010).

The post-synaptic gating mechanism contributing to sensorimotor gating proposed here employs inhibitory interneurons, a common and dysfunctional denominator of the neuropsychiatric disorders closely associated with sensorimotor gating deficits. Post-mortem studies on brain tissue from schizophrenia patients show reduced levels of several inhibitory interneuron and GABAergic signaling markers, such as GAD67, reelin, PV, GABA receptors and vGAT (Bastrup and Larsen, 2017; Beasley and Reynolds, 1997; Benes and Beretta, 2001; Stober *et al.*, 2009; Woo *et al.*, 1998; Zhang and Reynolds, 2002). The resulting abnormal GABAergic neurotransmission in cortical and limbic circuits is thought to contribute, and possibly underlie, the neuropathology of schizophrenia. This hypothesis is further supported by mutation studies in rodents, where impaired expression of GABAergic markers results in schizophrenia-related phenotypic behaviors. A PV-expressing and fast-spiking subset of GABA interneurons has been widely investigated due to their vast presence in cortical and limbic regions, where they regulate the synchronous neuronal firing responsible for higher cognitive processes (Amilhon *et al.*, 2015; Cardin *et al.*, 2009; Lewis *et al.*, 2005; Lovett-Barron *et al.*, 2012). Rodents with

reduced PV expression or targeted inhibition of PV-expressing interneurons manifest impaired schizophrenia-related behaviors, including sensorimotor gating deficits, impaired working memory, anxiety, hyperlocomotor activity and social withdrawal (Brown *et al.*, 2015; Lewis *et al.*, 2005; Nguyen *et al.*, 2014 Yeung *et al.*, 2018). Although the comorbidity of PV interneuron hypofunction and PPI deficits was thought to mainly originate in the hippocampus (Nguyen *et al.*, 2014); the contribution of hippocampus to sensorimotor gating is still debated (Fendt *et al.*, 1999; Ma and Leung, 2011; Swerdlow and Light, 2016). In fact, an isomorphic mouse model of the 22q11.2 microdeletion syndrome presents sensorimotor gating deficits and PV interneuron hypofunction, which impairs hippocampus-dependent tasks (Drew *et al.*, 2011; Marissal *et al.*, 2018). Interestingly, systemic administration of neuregulin-1 rescued function of hippocampal PV neurons and restored sensorimotor gating; while neuregulin-1 administration local to the hippocampus failed to restore it (Marissal *et al.*, 2018). Therefore, it is hypothesized that a potential detrimental effect of PV interneuron hypofunction on sensorimotor gating may originate in other brain region underlying PPI. In fact, the mPFC is a brain region with intrinsic microcircuits and projections whose activity are highly dependent on interneuron gating. Additionally, in conjunction with sensorimotor gating deficits, a concomitant endophenotype of schizophrenia is PV interneuron hypofunction. Animal models with reduced PV function in the mPFC and patients diagnosed with schizophrenia show impairments in sensorimotor gating mPFC-mediated tasks, such as working memory (Benes and Berretta, 2001; Enomoto *et al.*, 2011; Murray *et al.*, 2015; Shin *et al.*, 2019; Yeung *et al.*, 2018).

In light of this, inhibitory neurons in PPI relevant regions, such as the GlyT2 neurons observed in the PnC, are an interesting substrate underlying post-synaptic sensory gating mechanisms. Therefore, PnC GlyT2 interneurons hypofunction might contribute to sensorimotor gating deficits resulting in neocortical sensory overload and development of schizophrenia symptoms.

4.4 Proposed amygdalar control underlying sensorimotor gating

Integrating the results presented here into the body of literature on the role of the amygdala on sensorimotor gating, we propose that the BLA regulates both the ASR and PPI through distinct parallel pathways (Figure 4.1). Besides the well-understood primary startle pathway, the ASR is modulated by a BLA-NAcc-VP neural circuit that converges in the PPTg (Figure 4.1; in red); thus, integrated to the canonical CSPP network underlying PPI (Figure 4.1; in grey). In contrast, parallel to the CSPP network, the BLA-CeA-PnC neuronal pathway also mediates PPI (Figure 4.1; in blue). Along these two pathways, there are brain regions where the pathways converge, integrate sensory information from upstream neural substrates and contribute to both ASR and PPI (Figure 4.1; in purple).

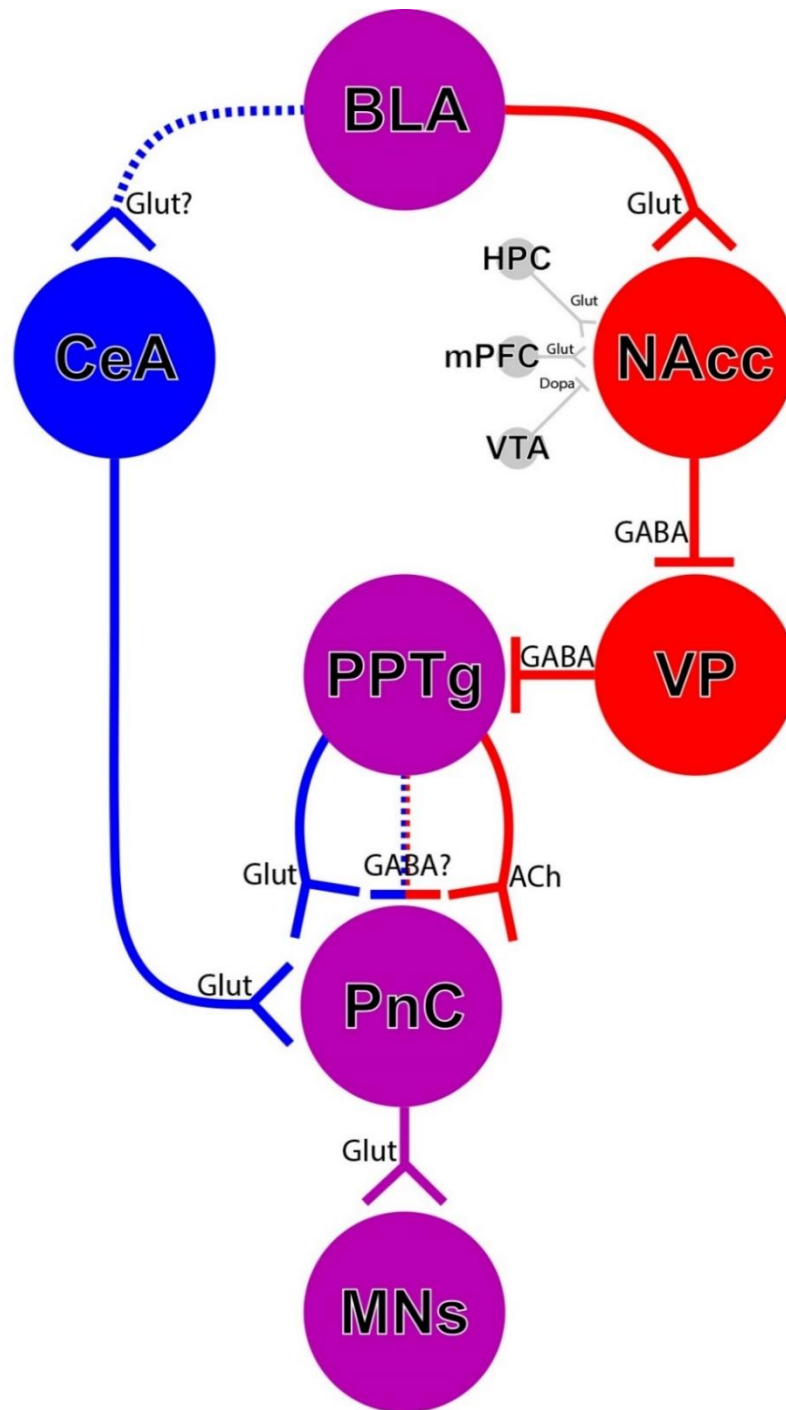


Figure 4.1 Proposed parallel amygdalar pathways regulating ASR and PPI. In red, the BLA-nucleus accumbens-ventral pallidum neural circuit regulate the ASR and converge in the PPTg. In blue, the BLA-CeA-PnC neuronal pathway mediate PPI. In purple, the BLA, PPTg and PnC integrate sensory information from upstream brain regions and mediate both ASR and PPI. In grey, the more cortical regions of CSPP network modulate PPI. Dotted lines indicate pathways that are yet to be tested with the ASR and PPI behavioral paradigms.

4.5 Methodological considerations

For TEM analysis, optimal ultrastructural preservation of tissue samples starts with a transcardial perfusion of Karnovsky's fixative, tissue sectioning (~1mm), overnight immersion fixation of the tissue sections, and then processed as described in *Section 2.2*. However, the tissue sections used in the pilot TEM analysis presented here were collected for electrophysiological analysis (as described in *Section 2.8*) without immediate fixation. In future analysis, tissue can be processed for electrophysiological recordings followed by an immediate immersion fixation (*section 2.12*) or flash freezing (Watanabe *et al.*, 2013).

Despite earlier studies demonstrating the promiscuity of the CamKII α promoter (Nathanson *et al.*, 2009); here, we show that CamKII α -dependent CeA inputs to the PnC are not GABAergic. However, other CamKII α -independent GABAergic inputs from the CeA may project to PPI substrates. As mentioned before, the CeA sends GABAergic efferents to several brainstem nuclei. To circumvent the lack of a viral vector with a GABA promoter, a Cre-dependent optogenetic approach on a VGAT-Cre mouse line could be applied to investigate the influence of GABAergic input from the CeA to the PPI pathway.

In our initial *in vivo* findings, we observed that optical inhibition of CeA-PnC synapses greatly reduced PPI, reminiscing PPI deficits measured in patients and animal models of schizophrenia (Braff *et al.*, 1978; Stark *et al.*, 2008). With the guileless premise that photo-stimulation of CeA-PnC synapses as a prepulse should then reveal their functional contribution to PPI, we were prompted to perform these experiments. Briefly, we observed that optical stimulation of CeA-PnC synapses elicited a smaller PPI effect that forms part of the overall acoustic PPI effect. We specifically targeted CeA synaptic inputs at the PnC, instead of somatic photo-stimulation at the CeA, since the latter might activate other

pathways and elicit behaviors that would likely mask an actual PPI contribution. However, even results from optogenetic stimulation at the synaptic level must be carefully interpreted, as to not fall prey to the caveats of this approach. Optogenetic stimulation targeting the axon terminal can elicit antidromic APs, which can activate synapses throughout the axonal projection and cell body (Tye *et al.*, 2011). In addition, optical stimulation of a neuronal pathway might not mimic its physiological activation. On the other hand, antidromic signaling does not occur with optogenetic inhibition, which we used to mimic a potential neuronal dysfunction that might be present in disorders associated with sensorimotor gating deficits. Altogether, these findings suggest that the subset of CeA-PnC synapses studied here contribute to PPI.

To test the optogenetic inhibition used in the behavioral tasks, we used *in vitro* whole cell patch clamp recordings with NpHR3.0 inhibition in the vHPC. Briefly, we observed that light pulses hyperpolarize the resting membrane potential and abolish the firing rate of NpHR3.0-expressing neurons. Despite this, the drastic behavioral effect is our only readout for the inhibition of the CeA axon terminals during our *in vivo* experiments. In a sophisticated and targeted approach, Cal-light relies on the calcium influx triggered by neuron activation and light pulses to elicit the expression of reporter or opsin genes. In this manner, only neurons underlying a certain behavior express the opsin gene, and can then be activated to elicit the behavior (Lee *et al.*, 2017). This recent technology provides a specific contribution at a cellular level. However, opsin expression is evoked by repetitive stimulation (Wang *et al.*, 2019). In the case of ASR and PPI, repetitive stimulation can lead to habituation, a behavior controlled by a distinct neural network (Abel *et al.*, 1998; Gerwitz and Davis, 1995). Furthermore, Cal-light has only been tested

in 'slow' learned behaviors, as opposed to the innate ASR and PPI elicited in the millisecond scale. In fact, the innate nature of ASR and PPI makes c-Fos expression also an inaccurate readout for cell activation without several appropriate controls. Separate animal control cohorts subjected to only background noise, startle pulses, prepulses, and optical manipulation. For future experiments, a less convoluted alternative using an optrode can provide a real-time readout of the effect of optical manipulations on local field potentials during behavioral tasks.

4.6 Future directions

Results from this project postulate an excitatory connection as an alternative pathway mediating PPI. This pathway is an intermediary component of the network underlying sensorimotor gating. Therefore, the upstream neural substrates that physiologically activate the CeA by the prepulse presentation are yet to be identified. We hypothesize that following the prepulse, glutamatergic inputs from the BLA activate the CeA. The BLA projects to all three subnuclei of the CeA (Kim *et al.*, 2016; Kim *et al.*, 2017; Swanson and Petrovich, 1998; Zhang *et al.*, 2018). BLA input to distinct populations of GABAergic neurons in the CeA differentially regulates appetitive behaviors in mice (Kim *et al.*, 2016; Kim *et al.*, 2017). Additionally, glutamatergic BLA input to the CeA mediates defensive behaviors under states of stress (Zhang *et al.*, 2018). Despite this, further upstream substrates that activate the BLA and modulate both the ASR and PPI (Forcelli *et al.*, 2012) remain to be identified, which can be achieved with the methodologies applied in this project. Similarly, it remains to be elucidated if PnC reticulospinal ‘startle’ neurons are a downstream substrate and are inhibited by activated GlyT2 neurons. Earlier studies suggest that these startle neurons are inhibited by GABA and glycine (Geis and Schmid, 2011; Yeomans *et al.*, 2010); however, the physiological source of this inhibitory inputs, if any, remains to be investigated. In previous studies in rats, whole-cell patch clamp recordings of the ‘startle’ neurons were successfully performed at post-natal day (PND) 12 to 19, with the premise that the success rate is radically abolished after PND 19. Age-specific stereotaxic injections and transduction period of optogenetic vectors make our electrophysiological/optogenetics approaches challenging to address this hypothesis. Alternative to the borderline impossible whole-cell recordings of PnC ‘startle’ neurons, *in vitro* calcium or voltage imaging with ChR2-stimulation of CeA fibers can be performed

(Quicke *et al.*, 2017; Schauer *et al.*, 2012). Doing so will elucidate the overall effect of CeA glutamatergic input on the PnC output to motor neurons.

Also, to further test pathway proposed here, the precise contribution of PnC GlyT2 neurons to ASR and PPI needs to be investigated. First, PnC GlyT2 neurons can be optically inhibited and stimulated during the ASR and PPI behavioral tasks. Then to identify their connectivity to the PPI network, a Cre-dependent retrograde tract-tracing strategy can be applied. Described by Wall and colleagues (2010), a restricted tract-tracing approach using a Cre-driver line can reveal monosynaptic projections to Cre-expressing neurons. In the GlyT2-Cre mouse line used here, an AAV vector carrying a plasmid coding for Cre-dependent TVA, G (glycoprotein) and a reporter gene (e.g. mCherry) is injected in the PnC (Callaway and Luo, 2015). In this manner, only GlyT2-Cre cells will express TVA, G and mCherry. Following an adequate transduction period, a glycoprotein-deleted with EnvA rabies viral vector coding for EGFP (EnvA+RVdG-EGFP) is then injected in the PnC. The TVA-EnvA complex is needed for rabies viral particles entry and transduction, which will be evident by the co-expression of mCherry and EGFP only in GlyT2-Cre cells. The RVdG will then replicate, use the membrane-bound G to move in a retrograde manner across synapses, and only (EGFP) label cell bodies directly connected to PnC GlyT2-Cre cells (Callaway and Luo, 2015; Wall *et al.*, 2010).

Lastly, disease modeling offers a unique platform to recapitulate pathological conditions, understand pathology development and test therapeutic approaches in an “ethically reasonable” manner. For example, *Df(16)A^{+/-}* mouse line are an isomorphic animal model of the human 22q11.2 deletion syndrome, the highest genetic risk factor to

develop schizophrenia-associated (Drew *et al.*, 2011). Humans and mice with this homologous microdeletion display neuroanatomical and behavioral schizophrenia phenotypes, such as amygdalar abnormalities and sensorimotor gating deficits (Ellegood *et al.*, 2014; Fenelon *et al.*, 2011; Fenelon *et al.*, 2013; Mukai *et al.*, 2015; Scarborough *et al.*, 2019; Stark *et al.*, 2008). The results and methods presented here can serve as guidelines for future studies on animal models of diseases associated with sensorimotor gating deficits.

References

- Abel, K., Waikar, M., Pedro, B., Hemsley, D., & Geyer, M. (1998). Repeated testing of prepulse inhibition and habituation of the startle reflex: a study in healthy human controls. *J Psychopharmacol*, 12(4), 330-337. doi:10.1177/026988119801200402
- Ahmari, S. E., & Dougherty, D. D. (2015). Dissecting Ocd Circuits: From Animal Models to Targeted Treatments. *Depress Anxiety*, 32(8), 550-562. doi:10.1002/da.22367
- Ahmari, S. E., Risbrough, V. B., Geyer, M. A., & Simpson, H. B. (2012). Impaired sensorimotor gating in unmedicated adults with obsessive-compulsive disorder. *Neuropsychopharmacology*, 37(5), 1216-1223. doi:10.1038/npp.2011.308
- Akmaev, I. G., Kalimullina, L. B., & Sharipova, L. A. (2004). The central nucleus of the amygdaloid body of the brain: cytoarchitectonics, neuronal organization, connections. *Neurosci Behav Physiol*, 34(6), 603-610. doi:10.1023/b:neab.0000028292.14402.ad
- Amilhon, B., Huh, C. Y., Manseau, F., Ducharme, G., Nichol, H., Adamantidis, A., & Williams, S. (2015). Parvalbumin Interneurons of Hippocampus Tune Population Activity at Theta Frequency. *Neuron*, 86(5), 1277-1289. doi:10.1016/j.neuron.2015.05.027
- Azzopardi, E., Louttit, A. G., DeOliveira, C., Laviolette, S. R., & Schmid, S. (2018). The Role of Cholinergic Midbrain Neurons in Startle and Prepulse Inhibition. *J Neurosci*, 38(41), 8798-8808. doi:10.1523/JNEUROSCI.0984-18.2018
- Bardoni, R., Torsney, C., Tong, C. K., Prandini, M., & MacDermott, A. B. (2004). Presynaptic NMDA receptors modulate glutamate release from primary sensory neurons in rat spinal cord dorsal horn. *J Neurosci*, 24(11), 2774-2781. doi:10.1523/JNEUROSCI.4637-03.2004

Bastrup, J., & Larsen, P. H. (2017). Optimized CLARITY technique detects reduced parvalbumin density in a genetic model of schizophrenia. *J Neurosci Methods*, 283, 23-32. doi:10.1016/j.jneumeth.2017.03.011

Beasley, C. L., & Reynolds, G. P. (1997). Parvalbumin-immunoreactive neurons are reduced in the prefrontal cortex of schizophrenics. *Schizophr Res*, 24(3), 349-355. doi:10.1016/s0920-9964(96)00122-3

Benes F. M., & Berretta, S. (2001). GABAergic interneurons: implications for understanding schizophrenia and bipolar disorder. *Neuropsychopharmacology* 25(1):1-27

Bergeron, S. A., Carrier, N., Li, G. H., Ahn, S., & Burgess, H. A. (2015). Gsx1 expression defines neurons required for prepulse inhibition. *Mol Psychiatry*, 20(8), 974-985. doi:10.1038/mp.2014.106

Bloss, E. B., Cembrowski, M. S., Karsh, B., Colonell, J., Fetter, R. D., & Spruston, N. (2016). Structured Dendritic Inhibition Supports Branch-Selective Integration in CA1 Pyramidal Cells. *Neuron*, 89(5):1016-30. doi: 10.1016/j.neuron.2016.01.029. Epub 2016 Feb 18. PubMed PMID: 26898780

Blumenthal, T. D. (1996). Inhibition of the human startle response is affected by both prepulse intensity and eliciting stimulus intensity. *Biol Psychol*, 44(2), 85-104. doi:10.1016/0301-0511(96)05214-3

Blumenthal, T. D., Schicatano, E. J., Chapman, J. G., Norris, C. M., & Ergenzinger, E. R., Jr. (1996). Prepulse effects on magnitude estimation of startle-eliciting stimuli and startle responses. *Percept Psychophys*, 58(1), 73-80. doi:10.3758/bf03205477

Blundell, J., Kaeser, P. S., Sudhof, T. C., & Powell, C. M. (2010). RIM1alpha and interacting proteins involved in presynaptic plasticity mediate prepulse inhibition and

additional behaviors linked to schizophrenia. *J Neurosci*, 30(15), 5326-5333. doi:10.1523/JNEUROSCI.0328-10.2010

Boland, M. J., Hazen, J. L., Nazor, K. L., Rodriguez, A. R., Martin, G., Kupriyanov, S., & Baldwin, K. K. (2012). Generation of mice derived from induced pluripotent stem cells. *J Vis Exp* (69), e4003. doi:10.3791/4003

Bolino, F., Manna, V., Di Cicco, L., Di Michele, V., Daneluzzo, E., Rossi, A., & Casacchia, M. (1992). Startle reflex habituation in functional psychoses: a controlled study. *Neurosci Lett*, 145(2), 126-128. doi:10.1016/0304-3940(92)90002-o

Booker, S. A., Song, J., & Vida, I. (2014). Whole-cell patch-clamp recordings from morphologically- and neurochemically-identified hippocampal interneurons. *J Vis Exp*(91), e51706. doi:10.3791/51706

Bosch, D., & Schmid, S. (2006). Activation of muscarinic cholinergic receptors inhibits giant neurones in the caudal pontine reticular nucleus. *Eur J Neurosci*, 24(7), 1967-1975. doi:10.1111/j.1460-9568.2006.05085.x

Bosch, D., & Schmid, S. (2008). Cholinergic mechanism underlying prepulse inhibition of the startle response in rats. *Neuroscience*, 155(1), 326-335. doi:10.1016/j.neuroscience.2008.04.018

Braff, D. L., & Geyer, M. A. (1990). Sensorimotor gating and schizophrenia. Human and animal model studies. *Arch Gen Psychiatry*, 47(2), 181-188. doi:10.1001/archpsyc.1990.01810140081011

Braff, D. L., Callaway, E., & Naylor, H. (1977). Very short-term memory dysfunction in schizophrenia. Defective short time constant information processing in schizophrenia. *Arch Gen Psychiatry*, 34(1), 25-30. doi:10.1001/archpsyc.1977.01770130027002

Braff, D. L., Geyer, M. A., & Swerdlow, N. R. (2001). Human studies of prepulse inhibition of startle: normal subjects, patient groups, and pharmacological studies. *Psychopharmacology (Berl)*, 156(2-3), 234-258. doi:10.1007/s002130100810

Braff, D., Stone, C., Callaway, E., Geyer, M., Glick, I., & Bali, L. (1978). Prestimulus effects on human startle reflex in normals and schizophrenics. *Psychophysiology*, 15(4), 339-343. doi:10.1111/j.1469-8986.1978.tb01390.x

Britt, J. P., Benaliouad, F., McDevitt, R. A., Stuber, G. D., Wise, R. A., & Bonci, A. (2012). Synaptic and behavioral profile of multiple glutamatergic inputs to the nucleus accumbens. *Neuron*, 76(4), 790-803. doi:10.1016/j.neuron.2012.09.040

Brown, J. A., Ramikie, T. S., Schmidt, M. J., Baldi, R., Garbett, K., Everheart, M. G., & Mirnics, K. (2015). Inhibition of parvalbumin-expressing interneurons results in complex behavioral changes. *Mol Psychiatry*, 20(12), 1499-1507. doi:10.1038/mp.2014.192

Burgess, H. A., & Granato, M. (2007). Sensorimotor gating in larval zebrafish. *J Neurosci*, 27(18), 4984-4994. doi:10.1523/JNEUROSCI.0615-07.2007

Callaway, E. M., & Luo, L. (2015). Monosynaptic Circuit Tracing with Glycoprotein-Deleted Rabies Viruses. *J Neurosci*, 35(24), 8979-8985. doi:10.1523/JNEUROSCI.0409-15.2015

Cardin, J. A., Carlen, M., Meletis, K., Knoblich, U., Zhang, F., Deisseroth, K., & Moore, C. I. (2009). Driving fast-spiking cells induces gamma rhythm and controls sensory responses. *Nature*, 459(7247), 663-667. doi:10.1038/nature08002

Cardno, A. G., & Owen, M. J. (2014). Genetic relationships between schizophrenia, bipolar disorder, and schizoaffective disorder. *Schizophrenia bulletin*, 40(3), 504–515. doi:10.1093/schbul/sbu016

Carter, R. J., Lione, L. A., Humby, T., Mangiarini, L., Mahal, A., Bates, G. P., & Morton, A. J. (1999). Characterization of progressive motor deficits in mice transgenic for the human Huntington's disease mutation. *J Neurosci*, 19(8), 3248-3257. Retrieved from <https://www.ncbi.nlm.nih.gov/pubmed/10191337>

Cassell, M. D., Gray, T. S., & Kiss, J. Z. (1986). Neuronal architecture in the rat central nucleus of the amygdala: a cytological, hodological, and immunocytochemical study. *J Comp Neurol*, 246(4), 478-499. doi:10.1002/cne.902460406

Cavanna, A. E., Black, K. J., Hallett, M., & Voon, V. (2017). Neurobiology of the Premonitory Urge in Tourette's Syndrome: Pathophysiology and Treatment Implications. *J Neuropsychiatry Clin Neurosci*, 29(2), 95-104. doi:10.1176/appi.neuropsych.16070141

Chen, Y. J., Johnson, M. A., Lieberman, M. D., Goodchild, R. E., Schobel, S., Lewandowski, N., & Role, L. W. (2008). Type III neuregulin-1 is required for normal sensorimotor gating, memory-related behaviors, and corticostriatal circuit components. *J Neurosci*, 28(27), 6872-6883. doi:10.1523/JNEUROSCI.1815-08.2008

Chieng, B. C., Christie, M. J., & Osborne, P. B. (2006). Characterization of neurons in the rat central nucleus of the amygdala: cellular physiology, morphology, and opioid sensitivity. *J Comp Neurol*, 497(6), 910-927. doi:10.1002/cne.21025

Chong, H. Y., Teoh, S. L., Wu, D. B., Kotirum, S., Chiou, C. F., & Chaiyakunapruk, N. (2016). Global economic burden of schizophrenia: a systematic review. *Neuropsychiatr Dis Treat*, 12, 357-373. doi:10.2147/NDT.S96649

Clark, S. D., Alderson, H. L., Winn, P., Latimer, M. P., Nothacker, H. P., & Civelli, O. (2007). Fusion of diphtheria toxin and urotensin II produces a neurotoxin selective for cholinergic neurons in the rat mesopontine tegmentum. *J Neurochem*, 102(1), 112-120. doi:10.1111/j.1471-4159.2007.04529.x

Clements, J.R., & Grant, S. (1990). Glutamate-like immunoreactivity in neurons of the laterodorsal tegmental and pedunculo pontine nuclei in the rat. *Neurosci Lett*, 120,70-73

Cloutier, M., Aigbogun, M. S., Guerin, A., Nitulescu, R., Ramanakumar, A. V., Kamat, S. A., DeLucia, M., Duffy, R., Legacy, S. N., Henderson, C., Francois, C., & Wu, E. (2016). The Economic Burden of Schizophrenia in the United States in 2013. *J Clin Psychiatry*, 77(6):764-71. doi: 10.4088/JCP.15m10278. PubMed PMID: 27135986

Crabtree, G. W., Park, A. J., Gordon, J. A., & Gogos, J. A. (2016). Cytosolic Accumulation of L-Proline Disrupts GABAergic Transmission through GAD Blockade. *Cell Rep*, 17(2), 570-582. doi:10.1016/j.celrep.2016.09.029

Curtin, P. C., & Preuss, T. (2015). Glycine and GABAA receptors mediate tonic and phasic inhibitory processes that contribute to prepulse inhibition in the goldfish startle network. *Front Neural Circuits*, 9, 12. doi:10.3389/fncir.2015.00012

Cyr, M., Parent, M. J., Mechawar, N., Rosa-Neto, P., Soucy, J. P., Clark, S. D., Aghourian, M., & Bedard, M. A. (2015). Deficit in sustained attention following selective cholinergic lesion of the pedunculo pontine tegmental nucleus in rat, as measured with both post-mortem immunocytochemistry and in vivo PET imaging with [(1)(8)F]fluoroethoxybenzovesamicol. *Behav Brain Res*, 278:107-114

Davis, M. (1984). The Mammalian Startle Response. In: Eaton R.C. (eds) *Neural Mechanisms of Startle Behavior*. Springer, Boston, MA.

Davis, M. (1997). Neurobiology of fear responses: the role of the amygdala. *J Neuropsychiatry Clin Neurosci*, 9(3), 382-402. doi:10.1176/jnp.9.3.382

Davis, M., Falls, W. A., Campeau, S., & Kim, M. (1993). Fear-potentiated startle: a neural and pharmacological analysis. *Behav Brain Res*, 58(1-2), 175-198. doi:10.1016/0166-4328(93)90102-v

Davis, M., Gendelman, D. S., Tischler, M. D., & Gendelman, P. M. (1982). A primary acoustic startle circuit: lesion and stimulation studies. *J Neurosci*, 2(6), 791-805. Retrieved from <https://www.ncbi.nlm.nih.gov/pubmed/7086484>

Davis, M., Walker, D. L., & Lee, Y. (1997). Amygdala and bed nucleus of the stria terminalis: differential roles in fear and anxiety measured with the acoustic startle reflex. *Philos Trans R Soc Lond B Biol Sci*, 352(1362), 1675-1687. doi:10.1098/rstb.1997.0149

Dawson, M. E., Hazlett, E. A., Filion, D. L., Nuechterlein, K. H., & Schell, A. M. (1993). Attention and schizophrenia: impaired modulation of the startle reflex. *J Abnorm Psychol*. 102(4):633-41. PubMed PMID: 8282934

Decker, M. W., Curzon, P., & Brioni, J. D. (1995). Influence of separate and combined septal and amygdala lesions on memory, acoustic startle, anxiety, and locomotor activity in rats. *Neurobiol Learn Mem*, 64(2), 156-168. doi:10.1006/nlme.1995.1055

Desai, P. R., Lawson, K. A., Barner, J. C., & Rascati, K. L. (2013a). Identifying patient characteristics associated with high schizophrenia-related direct medical costs in community-dwelling patients. *J Manag Care Pharm*. (6):468-77. PubMed PMID: 23806061

Desai, P. R., Lawson, K. A., Barner, J. C., & Rascati, K. L. (2013b). Schizophrenia-related costs for community-dwellers. *Journal of Pharmaceutical Health Services Research*, 4: 187-194. doi:10.1111/jphs.12027

Diederich, K., & Koch, M. (2005). Role of the pedunculo pontine tegmental nucleus in sensorimotor gating and reward-related behavior in rats. *Psychopharmacology (Berl)*, 179(2), 402-408. doi:10.1007/s00213-004-2052-y

Drew, L. J., Crabtree, G. W., Markx, S., Stark, K. L., Chaverneff, F., Xu, B., Mukai, J., Fenelon, K., Hsu, P.K., Gogos, J. A., & Karayiorgou, M. (2011). The 22q11.2 microdeletion: fifteen years of insights into the genetic and neural complexity of psychiatric disorders. *International journal of developmental neuroscience: the official journal of the International Society for Developmental Neuroscience*, 29(3), 259–281. doi:10.1016/j.ijdevneu.2010.09.007

Duvarci, S., Popa, D., & Pare, D. (2011). Central amygdala activity during fear conditioning. *J Neurosci*, 31(1), 289-294. doi:10.1523/JNEUROSCI.4985-10.2011

Eaton, R. C. (1984). *Neural mechanisms of startle behavior*. New York: Plenum.

Eaton, R. C., DiDomenico, R., & Nissanov, J. (1991). Role of the Mauthner cell in sensorimotor integration by the brain stem escape network. *Brain Behav Evol*, 37(5), 272-285. doi:10.1159/000114365

Ellegood, J., Markx, S., Lerch, J. P., Steadman, P. E., Genç, C., Provenzano, F., Kushner, S. A., Henkelman, R. M., Karayiorgou, M., & Gogos, J. A. (2014). Neuroanatomical phenotypes in a mouse model of the 22q11.2 microdeletion. *Molecular psychiatry*, 19(1), 99–107. doi:10.1038/mp.2013.112

Enomoto, T., Tse, M. T., & Floresco, S. B. (2011). Reducing prefrontal gamma-aminobutyric acid activity induces cognitive, behavioral, and dopaminergic abnormalities that resemble schizophrenia. *Biol Psychiatry*, 69(5), 432-441. doi:10.1016/j.biopsych.2010.09.038

Etherton, M. R., Blaiss, C. A., Powell, C. M., & Sudhof, T. C. (2009). Mouse neurexin-1alpha deletion causes correlated electrophysiological and behavioral changes consistent with cognitive impairments. *Proc Natl Acad Sci U S A*, 106(42), 17998-18003. doi:10.1073/pnas.0910297106

Fadok, J. P., Markovic, M., Tovote, P., & Luthi, A. (2018). New perspectives on central amygdala function. *Curr Opin Neurobiol*, 49, 141-147. doi:10.1016/j.conb.2018.02.009

Falgairolle, M., & O'Donovan, M. J. (2015). Pharmacological Investigation of Fluoro-Gold Entry into Spinal Neurons. *PLoS One*, 10(6), e0131430. doi:10.1371/journal.pone.0131430

Fast, C. D., & McGann, J. P. (2017). Amygdalar Gating of Early Sensory Processing through Interactions with Locus Coeruleus. *J Neurosci*, 37(11), 3085-3101. doi:10.1523/JNEUROSCI.2797-16.2017

Fendt, M. (1999). Enhancement of prepulse inhibition after blockade of GABA activity within the superior colliculus. *Brain Res*, 833(1), 81-85. doi:10.1016/s0006-8993(99)01525-5

Fendt, M., Koch, M., & Schnitzler, H. U. (1997). Corticotropin-releasing factor in the caudal pontine reticular nucleus mediates the expression of fear-potentiated startle in the rat. *Eur J Neurosci*, 9(2), 299-305. doi:10.1111/j.1460-9568.1997.tb01400.x

Fendt, M., Li, L., & Yeomans, J. S. (2001). Brain stem circuits mediating prepulse inhibition of the startle reflex. *Psychopharmacology (Berl)*, 156(2-3), 216-224. doi:10.1007/s002130100794

Fenelon, K., Mukai, J., Xu, B., Hsu, P. K., Drew, L. J., Karayiorgou, M., & Gogos, J. A. (2011). Deficiency of *Dgcr8*, a gene disrupted by the 22q11.2 microdeletion, results in altered short-term plasticity in the prefrontal cortex. *Proc Natl Acad Sci U S A*, 108(11), 4447-4452. doi:10.1073/pnas.1101219108

Fenelon, K., Xu, B., Lai, C. S., Mukai, J., Markx, S., Stark, K. L., & Gogos, J. A. (2013). The pattern of cortical dysfunction in a mouse model of a schizophrenia-related

microdeletion. *J Neurosci*, 33(37), 14825-14839. doi:10.1523/JNEUROSCI.1611-13.2013

Flaten, M. A., Nordmark, E., & Elden, A. (2005). Effects of background noise on the human startle reflex and prepulse inhibition. *Psychophysiology*, 42(3), 298-305. doi:10.1111/j.1469-8986.2005.00293.x

Flint, J., & Munafò, M. R. (2007). The endophenotype concept in psychiatric genetics. *Psychological medicine*, 37(2), 163–180. doi:10.1017/S0033291706008750

Floresco, S. B., & Grace, A. A. (2003). Gating of hippocampal-evoked activity in prefrontal cortical neurons by inputs from the mediodorsal thalamus and ventral tegmental area. *J Neurosci*, 23(9), 3930-3943. Retrieved from <https://www.ncbi.nlm.nih.gov/pubmed/12736363>

Forcelli, P. A., West, E. A., Murnen, A. T., & Malkova, L. (2012). Ventral pallidum mediates amygdala-evoked deficits in prepulse inhibition. *Behav Neurosci*, 126(2), 290-300. doi:10.1037/a0026898

Frankland, P. W., Sakaguchi, M., & Arruda-Carvalho, M. (2008). Starting at the endophenotype: A role for alpha-CaMKII in schizophrenia? *Molecular brain*, 1, 5. doi:10.1186/1756-6606-1-5

Frankland, P. W., Scott, B. W., & Yeomans, J. S. (1995). Axons and synapses mediating electrically evoked startle: collision tests and latency analysis. *Brain Res*, 670(1), 97-111. doi:10.1016/0006-8993(94)01220-c

Frost, W. N., Tian, L. M., Hoppe, T. A., Mongeluzi, D. L., & Wang, J. (2003). A cellular mechanism for prepulse inhibition. *Neuron*, 40(5), 991-1001. doi:10.1016/s0896-6273(03)00731-1

Fulcher, N., Azzopardi, A., De Oliveira, C., Hudson, R., Laviolette, S., & Schmid, S. (2019). Double dissociation of two PPTg neuron population mediating prepulse inhibition and reward. Society for Neuroscience 2019. DP15/W30

Gallagher, M., & Holland, P. C. (1994). The amygdala complex: multiple roles in associative learning and attention. *Proceedings of the National Academy of Sciences of the United States of America*, 91(25), 11771–11776. doi:10.1073/pnas.91.25.11771

GBD 2016 Disease and Injury Incidence and Prevalence Collaborators. Global, regional, and national incidence, prevalence, and years lived with disability for 328 diseases and injuries for 195 countries, 1990-2016: a systematic analysis for the Global Burden of Disease Study 2016. 2017. *Lancet*. 390(10100):1211-1259. doi: 10.1016/S0140-6736(17)32154-2. Erratum in: *Lancet*. 2017 Oct 28;390(10106):e38. PubMed PMID: 28919117; PubMed Central PMCID: PMC5605509

Geis, H. R., & Schmid, S. (2011). Glycine inhibits startle-mediating neurons in the caudal pontine reticular formation but is not involved in synaptic depression underlying short-term habituation of startle. *Neurosci Res*, 71(2), 114-123. doi:10.1016/j.neures.2011.06.007

Gewirtz, J. C., & Davis, M. (1995). Habituation of prepulse inhibition of the startle reflex using an auditory prepulse close to background noise. *Behav Neurosci*, 109(3), 388-395. doi:10.1037//0735-7044.109.3.388

Geyer, M. A., & Dulawa, S. C. (2003). Assessment of murine startle reactivity, prepulse inhibition, and habituation. *Curr Protoc Neurosci*, Chapter 8, Unit 8 17. doi:10.1002/0471142301.ns0817s24

Giber, K., Diana, M. A., Plattner, V., Dugue, G. P., Bokor, H., Rousseau, C. V., Acsady, L. (2015). A subcortical inhibitory signal for behavioral arrest in the thalamus. *Nat Neurosci*, 18(4), 562-568. doi:10.1038/nn.3951

Gomez-Nieto, R., Horta-Junior Jde, A., Castellano, O., Millian-Morell, L., Rubio, M. E., & Lopez, D. E. (2014). Origin and function of short-latency inputs to the neural substrates underlying the acoustic startle reflex. *Front Neurosci*, 8, 216. doi:10.3389/fnins.2014.00216

Graham, F. K. (1975). Presidential Address, 1974. The more or less startling effects of weak prestimulation. *Psychophysiology*, 12(3), 238-248. doi:10.1111/j.1469-8986.1975.tb01284.x

Gray T.S., & Magnuson D.J. (1987). Neuropeptide neuronal efferents from the bed nucleus of the stria terminalis and central amygdaloid nucleus to the dorsal vagal complex in the rat. *J Comp Neurol* 262(3):365-74.

Greenwood, T. A., Lazzeroni, L. C., Murray, S. S., Cadenhead, K. S., Calkins, M. E., Dobie, D. J., & Braff, D. L. (2011). Analysis of 94 candidate genes and 12 endophenotypes for schizophrenia from the Consortium on the Genetics of Schizophrenia. *Am J Psychiatry*, 168(9), 930-946. doi:10.1176/appi.ajp.2011.10050723

Groenewegen, H. J., van den Heuvel, O. A., Cath, D. C., Voorn, P., & Veltman, D. J. (2003). Does an imbalance between the dorsal and ventral striatopallidal systems play a role in Tourette's syndrome? A neuronal circuit approach. *Brain Dev*, 25 Suppl 1, S3-S14. doi:10.1016/s0387-7604(03)90001-5

Groves, P. M., & Thompson, R. F. (1970). Habituation: a dual-process theory. *Psychol Rev*. 77(5):419-50. PubMed PMID: 4319167.

Gupta, T., Marquart, G. D., Horstick, E. J., Tabor, K. M., Pajevic, S., & Burgess, H. A. (2018). Morphometric analysis and neuroanatomical mapping of the zebrafish brain. *Methods*, 150, 49-62. doi:10.1016/j.ymeth.2018.06.008

Gut, N.K., & Winn, P. (2016). The pedunculo pontine tegmental nucleus-A functional hypothesis from the comparative literature. *Mov Disord*, 31:615-62

Han, W., Tellez, L. A., Rangel, M. J., Jr., Motta, S. C., Zhang, X., Perez, I. O., & de Araujo, I. E. (2017). Integrated Control of Predatory Hunting by the Central Nucleus of the Amygdala. *Cell*, 168(1-2), 311-324 e318. doi:10.1016/j.cell.2016.12.027

Harris, K. M., & Weinberg, R. J. (2012). Ultrastructure of synapses in the mammalian brain. *Cold Spring Harb Perspect Biol*, 4(5). doi:10.1101/cshperspect.a005587

Harrison, P. J., Law, A. J., & Eastwood, S. L. (2003). Glutamate receptors and transporters in the hippocampus in schizophrenia. *Ann N Y Acad Sci*, 1003, 94-101. doi:10.1196/annals.1300.006

Hitchcock, J. M., & Davis, M. (1991). Efferent pathway of the amygdala involved in conditioned fear as measured with the fear-potentiated startle paradigm. *Behav Neurosci*, 105(6), 826-842. doi:10.1037//0735-7044.105.6.826

Hoening, K., Hochrein, A., Quednow, B. B., Maier, W., & Wagner, M. (2005). Impaired prepulse inhibition of acoustic startle in obsessive-compulsive disorder. *Biol Psychiatry*, 57(10), 1153-1158. doi:10.1016/j.biopsych.2005.01.040

Hoffman, H. S., & Fleshler, M. (1963). Startle Reaction: Modification by Background Acoustic Stimulation. *Science*, 141(3584), 928-930. doi:10.1126/science.141.3584.928

Hoffman, H. S., & Searle, J. L. (1965). Acoustic variables in the modification of startle reaction in the rat. *Journal of Comparative and Physiological Psychology*, 60(1), 53-58

Hoffman, H. S., & Searle, J. L. (1968). Acoustic and temporal factors in the evocation of startle. *J Acoust Soc Am*, 43(2), 269-282. doi:10.1121/1.1910776

Hoffman, H. S., & Wible, B. L. (1969). Temporal parameters in startle facilitation by steady background signals. *J Acoust Soc Am*, 45(1), 7-12. doi:10.1121/1.1911377

Hoffman, H. S., & Wible, B. L. (1970). Role of weak signals in acoustic startle. *J Acoust Soc Am* 47:489–497

Hoffman, H.S., & Ison, J.R. (1980). Reflex modification in the domain of startle: I. Some empirical findings and their implications for how the nervous system processes sensory input. *Psychol Rev.* 87(2):175-89. PubMed PMID: 7375610

Holland, P. C., & Gallagher, M. (1993). Amygdala central nucleus lesions disrupt increments, but not decrements, in conditioned stimulus processing. *Behav Neurosci*, 107(2), 246-253. doi:10.1037//0735-7044.107.2.246

Holstein, D. H., Vollenweider, F. X., Geyer, M. A., Csomor, P. A., Belser, N., & Eich, D. (2013). Sensory and sensorimotor gating in adult attention-deficit/hyperactivity disorder (ADHD). *Psychiatry Res.* 205(1-2):117-26. doi: 10.1016/j.psychres.2012.08.013. Epub 2012 Sep 25. PubMed PMID: 23017654

Horn, A. K. (2006). The reticular formation. *Prog Brain Res.*151:127-55. PubMed PMID: 16221588

Howland, J. G., Hannesson, D. K., Barnes, S. J., & Phillips, A. G. (2007). Kindling of basolateral amygdala but not ventral hippocampus or perirhinal cortex disrupts sensorimotor gating in rats. *Behav Brain Res* 177(1):30-36

Hsieh, M. H., Swerdlow, N. R., & Braff, D. L. (2006). Effects of background and prepulse characteristics on prepulse inhibition and facilitation: implications for neuropsychiatric research. *Biol Psychiatry*, 59(6), 555-559. doi:10.1016/j.biopsych.2005.07.032
<http://dx.doi.org/10.1037/0735-7044.109.5.912>

Hur, E. E., & Zaborszky, L. (2005). Vglut2 afferents to the medial prefrontal and primary somatosensory cortices: a combined retrograde tracing in situ hybridization study [corrected]. *J Comp Neurol*, 483(3), 351-373. doi:10.1002/cne.20444

Iacono W. G. (2018). Endophenotypes in psychiatric disease: prospects and challenges. *Genome medicine*, 10(1), 11. doi:10.1186/s13073-018-0526-5

Ichikawa, T., Ajiki, K., Matsuura, J., & Misawa, H. (1997). Localization of two cholinergic markers, choline acetyltransferase and vesicular acetylcholine transporter in the central nervous system of the rat: in situ hybridization histochemistry and immunohistochemistry. *J Chem Neuroanat*, 13(1), 23-39. doi:10.1016/s0891-0618(97)00021-5

Ison, J. R., & Hammond, G. R. (1971). Modification of the startle reflex in rat by changes in the auditory and visual environments. *J Comp Physiol Psychol* 75:452

Ison, J. R., McAdam, D. W., & Hammond, G. R. (1973). Latency and amplitude changes in the acoustic startle reflex of the rat produced by variation in auditory prestimulation. *Physiol Behav* 10:1035–1039

Isosaka, T., Matsuo, T., Yamaguchi, T., Funabiki, K., Nakanishi, S., Kobayakawa, R., & Kobayakawa, K. (2015). Htr2a-Expressing Cells in the Central Amygdala Control the Hierarchy between Innate and Learned Fear. *Cell*, 163(5), 1153-1164. doi:10.1016/j.cell.2015.10.047

Iwata, J., LeDoux, J. E., Meeley, M. P., Arneric, S., & Reis, D. J. (1986). Intrinsic neurons in the amygdaloid field projected to by the medial geniculate body mediate emotional responses conditioned to acoustic stimuli. *Brain Res*, 383(1-2), 195-214. PubMed PMID: 3768689

Javanbakht, A. (2006). Sensory gating deficits, pattern completion, and disturbed fronto-
limbic balance, a model for description of hallucinations and delusions in schizophrenia.
Med Hypotheses, 67(5), 1173-1184. doi:10.1016/j.mehy.2006.03.054

Jungling, K., Lange, M. D., Szkudlarek, H. J., Lesting, J., Erdmann, F. S., Doengi, M., &
Pape, H. C. (2015). Increased GABAergic Efficacy of Central Amygdala Projections to
Neuropeptide S Neurons in the Brainstem During Fear Memory Retrieval.
Neuropsychopharmacology, 40(12), 2753-2763. doi:10.1038/npp.2015.125

Kamali, A., Sair, H. I., Blitz, A. M., Riascos, R. F., Mirbagheri, S., Keser, Z., & Hasan, K.
M. (2016). Revealing the ventral amygdalofugal pathway of the human limbic system
using high spatial resolution diffusion tensor tractography. *Brain Struct Funct*, 221(7),
3561-3569. doi:10.1007/s00429-015-1119-3

Kandel, E. R. (1976). *Cellular basis of behavior: An introduction to behavioral
neurobiology*. Oxford, England: W. H. Freeman.

Keifer, O. P., Jr., Hurt, R. C., Ressler, K. J., & Marvar, P. J. (2015). The Physiology of
Fear: Reconceptualizing the Role of the Central Amygdala in Fear Learning. *Physiology
(Bethesda)*, 30(5), 389-401. doi:10.1152/physiol.00058.2014

Kendler, K. S., & Neale, M. C. (2010). Endophenotype: a conceptual analysis. *Molecular
psychiatry*, 15(8), 789–797. doi:10.1038/mp.2010.8

Kennedy, M. B. (2000). Signal-processing machines at the postsynaptic density. *Science*,
290(5492), 750-754. doi:10.1126/science.290.5492.750

Kim, E., & Sheng, M. (2004). PDZ domain proteins of synapses. *Nat Rev Neurosci*,
5(10):771-81. Review. PubMed PMID: 15378037

Kim, H., Ahrlund-Richter, S., Wang, X., Deisseroth, K., & Carlen, M. (2016). Prefrontal Parvalbumin Neurons in Control of Attention. *Cell*, 164(1-2), 208-218. doi:10.1016/j.cell.2015.11.038

Kim, J., Zhang, X., Muralidhar, S., LeBlanc, S. A., & Tonegawa, S. (2017). Basolateral to Central Amygdala Neural Circuits for Appetitive Behaviors. *Neuron*, 93(6), 1464-1479 e1465. doi:10.1016/j.neuron.2017.02.034

Knott, G.W., Quairiaux, C., Genoud, C., & Welker, E. (2002). Formation of dendritic spines with GABAergic synapses induced by whisker stimulation in adult mice. *Neuron*, 34(2):265-73. PubMed PMID: 11970868

Knudsen, E.I., & Knudsen, P.F. (1985). Vision guides the adjustment of auditory localization in young barn owls. *Science*. 230(4725):545-8. PubMed PMID: 4048948

Koch, M. (1999). The neurobiology of startle. *Prog Neurobiol*, 59(2), 107-128. doi:10.1016/s0301-0082(98)00098-7

Koch, M., & Ebert, U. (1993). Enhancement of the acoustic startle response by stimulation of an excitatory pathway from the central amygdala/basal nucleus of Meynert to the pontine reticular formation. *Exp Brain Res*, 93(2), 231-241. doi:10.1007/bf00228390

Koch, M., & Schnitzler, H. U. (1997). The acoustic startle response in rats--circuits mediating evocation, inhibition and potentiation. *Behav Brain Res*, 89(1-2), 35-49. doi:10.1016/s0166-4328(97)02296-1

Koch, M., Fendt, M., & Kretschmer, B. D. (2000). Role of the substantia nigra pars reticulata in sensorimotor gating, measured by prepulse inhibition of startle in rats. *Behav Brain Res*, 117(1-2), 153-162. doi:10.1016/s0166-4328(00)00299-0

Koch, M., Kungel, M., & Herbert, H. (1993). Cholinergic neurons in the pedunculo pontine tegmental nucleus are involved in the mediation of prepulse inhibition of the acoustic startle response in the rat. *Exp Brain Res*, 97(1), 71-82. doi:10.1007/bf00228818

Kodsi, M. H., & Swerdlow, N. R. (1995). Prepulse inhibition in the rat is regulated by ventral and caudodorsal striato-pallidal circuitry. *Behavioral Neuroscience*, 109(5), 912-928

Kodsi, M. H., & Swerdlow, N. R. (1997). Reduced prepulse inhibition after electrolytic lesions of nucleus accumbens subregions in the rat. *Brain Res*, 773(1-2), 45-52. doi:10.1016/s0006-8993(97)00869-x

Kodsi, M.H., & Swerdlow, N.R. (1994). Quinolinic acid lesions of the ventral striatum reduce sensorimotor gating of acoustic startle in rats. *Brain Res*, 643(1-2):59-65. PubMed PMID: 8032933

Kohl, S., Heekeren, K., Klosterkotter, J., & Kuhn, J. (2013). Prepulse inhibition in psychiatric disorders--apart from schizophrenia. *J Psychiatr Res*, 47(4), 445-452. doi:10.1016/j.jpsychires.2012.11.018

Koster, R., & Sassen, W. A. (2015). A molecular toolbox for genetic manipulation of zebrafish. *Advances in Genomics and Genetics*. doi:10.2147/agg.S57585

Kroeger, D., Ferrari, L. L., Petit, G., Mahoney, C. E., Fuller, P. M., Arrigoni, E., & Scammell, T. E. (2017). Cholinergic, Glutamatergic, and GABAergic Neurons of the Pedunculo pontine Tegmental Nucleus Have Distinct Effects on Sleep/Wake Behavior in Mice. *J Neurosci*, 37(5), 1352-1366. doi:10.1523/JNEUROSCI.1405-16.2016

Kumari, V., Fannon, D., Sumich, A.L., & Sharma, T. (2007). Startle gating in antipsychotic-naïve first episode schizophrenia patients: one ear is better than two. *Psychiatry Res*, 151(1-2):21-8

Kumari, V., Soni, W., & Sharma, T. (2001). Influence of cigarette smoking on prepulse inhibition of the acoustic startle response in schizophrenia. *Hum Psychopharmacol* 16, 321-326

Kuramashi, A., Abe, H., Koganemaru, G., Matsuo, H., Ikeda, T., Ebihara, K., & Ishida, Y. (2013). Effect of blonanserin on methamphetamine-induced disruption of latent inhibition and c-Fos expression in rats. *Neurosci Lett*, 549, 97-102. doi:10.1016/j.neulet.2013.06.020

Landis C., & Hunt W. (1939). The startle pattern. Oxford, England: Farrar & Rinehart.

Landis, D. M., Hall, A. K., Weinstein, L. A., & Reese, T. S. (1988). The organization of cytoplasm at the presynaptic active zone of a central nervous system synapse. *Neuron*, 1: 201–209

Law, A. J., Lipska, B. K., Weickert, C. S., Hyde, T. M., Straub, R. E., Hashimoto, R., Weinberger, D. R. (2006). Neuregulin 1 transcripts are differentially expressed in schizophrenia and regulated by 5' SNPs associated with the disease. *Proc Natl Acad Sci U S A*, 103(17), 6747-6752. doi:10.1073/pnas.0602002103

Law, A. J., Shannon Weickert, C., Hyde, T. M., Kleinman, J. E., & Harrison, P. J. (2004). Neuregulin-1 (NRG-1) mRNA and protein in the adult human brain. *Neuroscience*, 127(1), 125-136. doi:10.1016/j.neuroscience.2004.04.026

LeDoux, J. E., Iwata, J., Cicchetti, P., & Reis, D. J. (1988). Different projections of the central amygdaloid nucleus mediate autonomic and behavioral correlates of conditioned fear. *J Neurosci*, 8(7), 2517-2529. Retrieved from <https://www.ncbi.nlm.nih.gov/pubmed/2854842>

Lee, D., Hyun, J. H., Jung, K., Hannan, P., & Kwon, H. B. (2017). A calcium- and light-gated switch to induce gene expression in activated neurons. *Nat Biotechnol*, 35(9), 858-863. doi:10.1038/nbt.3902

Lee, Y., Lopez, D. E., Meloni, E. G., & Davis, M. (1996). A primary acoustic startle pathway: obligatory role of cochlear root neurons and the nucleus reticularis pontis caudalis. *J Neurosci*, 16(11), 3775-3789. Retrieved from <https://www.ncbi.nlm.nih.gov/pubmed/8642420>

Lewis, D. A., Volk, D. W., & Hashimoto, T. (2004). Selective alterations in prefrontal cortical GABA neurotransmission in schizophrenia: a novel target for the treatment of working memory dysfunction. *Psychopharmacology (Berl)*, 174(1), 143-150. doi:10.1007/s00213-003-1673-x

Li, D., Collier, D. A., & He, L. (2006). Meta-analysis shows strong positive association of the neuregulin 1 (NRG1) gene with schizophrenia. *Hum Mol Genet*, 15(12), 1995-2002. doi:10.1093/hmg/ddl122

Li, H., Penzo, M. A., Taniguchi, H., Kopec, C. D., Huang, Z. J., & Li, B. (2013). Experience-dependent modification of a central amygdala fear circuit. *Nat Neurosci*, 16(3), 332-339. doi:10.1038/nn.3322

Li, L., Du, Y., Li, N., Wu, X., & Wu, Y. (2009). Top-down modulation of prepulse inhibition of the startle reflex in humans and rats. *Neurosci Biobehav Rev*, 33(8), 1157-1167. doi:10.1016/j.neubiorev.2009.02.001

Li, L., Korngut, L. M., Frost, B. J., & Beninger, R. J. (1998). Prepulse inhibition following lesions of the inferior colliculus: prepulse intensity functions. *Physiol Behav*, 65(1), 133-139. doi:10.1016/s0031-9384(98)00143-7

Lim, M., Park, D. Y., Kwon, J. S., Joo, Y. H., & Hong, K. S. Prevalence and clinical characteristics of obsessive-compulsive symptoms associated with atypical antipsychotics. *J. Clin. Psychopharmacol.* 2007;27(6):712–3

Lingenhöhl, K., & Friauf, E. (1992). Giant neurons in the caudal pontine reticular formation receive short latency acoustic input: an intracellular recording and HRP-study in the rat. *J Comp Neurol*, 325(4), 473-492. doi:10.1002/cne.903250403

Lingenhöhl, K., & Friauf, E. (1994). Giant neurons in the rat reticular formation: a sensorimotor interface in the elementary acoustic startle circuit? *J Neurosci*, 14(3 Pt 1), 1176-1194. Retrieved from <https://www.ncbi.nlm.nih.gov/pubmed/8120618>

Lovett-Barron, M., Turi, G. F., Kaifosh, P., Lee, P. H., Bolze, F., Sun, X. H., & Losonczy, A. (2012). Regulation of neuronal input transformations by tunable dendritic inhibition. *Nat Neurosci*, 15(3), 423-430, S421-423. doi:10.1038/nn.3024

Ludewig, S., & Ludewig, K. (2003). No prepulse inhibition deficits in patients with unipolar depression. *Depress Anxiety*, 17(4):224-5. PubMed PMID: 12820179

Ludewig, S., Ludewig, K., Geyer, M. A., Hell, D., & Vollenweider, F. X. (2002). Prepulse inhibition deficits in patients with panic disorder. *Depress Anxiety*, 15(2), 55-60. Retrieved from <https://www.ncbi.nlm.nih.gov/pubmed/11891993>

Ma, J., & Leung, L. S. (2011). GABA(B) receptor blockade in the hippocampus affects sensory and sensorimotor gating in Long-Evans rats. *Psychopharmacology (Berl)*, 217(2), 167-176. doi:10.1007/s00213-011-2274-8

MacDermott, A. B., Role, L. W., & Siegelbaum, S. A. (1999). Presynaptic ionotropic receptors and the control of transmitter release. *Annu Rev Neurosci*, 22, 443-485. doi:10.1146/annurev.neuro.22.1.443

MacLaren, D. A., Markovic, T., & Clark, S. D. (2014). Assessment of sensorimotor gating following selective lesions of cholinergic pedunculo pontine neurons. *Eur J Neurosci*, 40(10), 3526-3537. doi:10.1111/ejn.12716

Maddux, J. M., Kerfoot, E. C., Chatterjee, S., & Holland, P. C. (2007). Dissociation of attention in learning and action: effects of lesions of the amygdala central nucleus, medial prefrontal cortex, and posterior parietal cortex. *Behav Neurosci*, 121(1), 63-79. doi:10.1037/0735-7044.121.1.63

Maher, B. J., & LoTurco, J. J. (2012). Disrupted-in-schizophrenia (DISC1) functions presynaptically at glutamatergic synapses. *PloS one*, 7(3), e34053. doi:10.1371/journal.pone.0034053

Mahn, M., Prigge, M., Ron, S., Levy, R., & Yizhar, O. (2016). Biophysical constraints of optogenetic inhibition at presynaptic terminals. *Nat Neurosci*, 19(4), 554-556. doi:10.1038/nn.4266

Marissal, T., Salazar, R. F., Bertollini, C., Mutel, S., De Roo, M., Rodriguez, I., Carleton, A. (2018). Restoring wild-type-like CA1 network dynamics and behavior during adulthood in a mouse model of schizophrenia. *Nat Neurosci*, 21(10), 1412-1420. doi:10.1038/s41593-018-0225-y

Marsh, R. R., Hoffman, H. S., & Stitt, C. L. (1976). Eyeblick inhibition by monaural and binaural stimulation: one ear is better than two. *Science* 192(4237):390-1

Martin, G. F., Holstege, G., & Mehler, W. R. (1990). Reticular formation of the pons and medulla. In *The Human Nervous System*. Academic Press, San Diego, CA

Martina, M., Royer, S., & Pare, D. (1999). Physiological properties of central medial and central lateral amygdala neurons. *J Neurophysiol*, 82(4), 1843-1854. doi:10.1152/jn.1999.82.4.1843

McDonald, A. J. (1982). Cytoarchitecture of the central amygdaloid nucleus of the rat. *J Comp Neurol*, 208(4), 401-418. doi:10.1002/cne.902080409

Medan, V., & Preuss, T. (2014). The Mauthner-cell circuit of fish as a model system for startle plasticity. *J Physiol Paris*, 108(2-3), 129-140. doi:10.1016/j.jphysparis.2014.07.006

Melia, K. R., Sananes, C. B., & Davis, M. (1992). Lesions of the central nucleus of the amygdala block the excitatory effects of septal ablation on the acoustic startle reflex. *Physiol Behav*, 51(1), 175-180. doi:10.1016/0031-9384(92)90220-v

Mena, A., Ruiz-Salas, J. C., Puentes, A., Dorado, I., Ruiz-Veguilla, M., & De la Casa, L. G. (2016). Reduced Prepulse Inhibition as a Biomarker of Schizophrenia. *Front Behav Neurosci*, 10, 202. doi:10.3389/fnbeh.2016.00202

Miller E. K. (2000). The prefrontal cortex and cognitive control. *Nat Rev Neurosci*, 1:59–65

Miserendino, M. J., & Davis, M. (1993). NMDA and non-NMDA antagonists infused into the nucleus reticularis pontis caudalis depress the acoustic startle reflex. *Brain Res*, 623(2), 215-222. doi:10.1016/0006-8993(93)91430-z

Moore, L. A., & Trussell, L. O. (2017). Corelease of Inhibitory Neurotransmitters in the Mouse Auditory Midbrain. *J Neurosci*, 37(39), 9453-9464. doi:10.1523/JNEUROSCI.1125-17.2017

Mukai, J., Tamura, M., Fenelon, K., Rosen, A. M., Spellman, T. J., Kang, R., & Gogos, J. A. (2015). Molecular substrates of altered axonal growth and brain connectivity in a mouse model of schizophrenia. *Neuron*, 86(3), 680-695. doi:10.1016/j.neuron.2015.04.003

Murray, A. J., Woloszynowska-Fraser, M. U., Ansel-Bollepalli, L., Cole, K. L., Foggetti, A., Crouch, B., & Wulff, P. (2015). Parvalbumin-positive interneurons of the prefrontal cortex support working memory and cognitive flexibility. *Sci Rep*, 5, 16778. doi:10.1038/srep16778

Nathanson, J. L., Yanagawa, Y., Obata, K., & Callaway, E. M. (2009). Preferential labeling of inhibitory and excitatory cortical neurons by endogenous tropism of adeno-associated virus and lentivirus vectors. *Neuroscience*, 161(2), 441-450. doi:10.1016/j.neuroscience.2009.03.032

National Alliance for Mental Illness (NAMI). Schizophrenia. Accessed Nov. 11, 2019 on <https://www.nami.org/learn-more/mental-health-conditions/schizophrenia>

Nguyen, R., Morrissey, M. D., Mahadevan, V., Cajanding, J. D., Woodin, M. A., Yeomans, J. S., & Kim, J. C. (2014). Parvalbumin and GAD65 interneuron inhibition in the ventral hippocampus induces distinct behavioral deficits relevant to schizophrenia. *J Neurosci*, 34(45), 14948-14960. doi:10.1523/JNEUROSCI.2204-14.2014

Oshima-Takago, T., & Takago, H. (2017). NMDA receptor-dependent presynaptic inhibition at the calyx of Held synapse of rat pups. *Open Biol*, 7(7). doi:10.1098/rsob.170032

Ozaki, M. (2001). Neuregulins and the shaping of synapses. *Neuroscientist*, 7(2), 146-154. doi:10.1177/107385840100700209

Ozawa, T., Ycu, E. A., Kumar, A., Yeh, L. F., Ahmed, T., Koivumaa, J., & Johansen, J. P. (2017). A feedback neural circuit for calibrating aversive memory strength. *Nat Neurosci*, 20(1), 90-97. doi:10.1038/nn.4439

Pauls, D. L. (2008). The genetics of obsessive compulsive disorder: a review of the evidence. *Am J Med Genet C Semin Med Genet*, 148C(2), 133-139. doi:10.1002/ajmg.c.30168

Paxinos G., & Franklin, K. B. J. (2004). *The mouse brain in stereotaxic coordinates*, (Elsevier Academic Press).

Pei, Z., Wang, B., Chen, G., Nagao, M., Nakafuku, M., & Campbell, K. (2011). Homeobox genes *Gsx1* and *Gsx2* differentially regulate telencephalic progenitor maturation. *Proc Natl Acad Sci U S A*, 108(4), 1675-1680. doi:10.1073/pnas.1008824108

Pennartz, C. M., & Kitai, S. T. (1991). Hippocampal inputs to identified neurons in an in vitro slice preparation of the rat nucleus accumbens: evidence for feed-forward inhibition. *The Journal of neuroscience: the official journal of the Society for Neuroscience*, 11(9), 2838–2847. doi:10.1523/JNEUROSCI.11-09-02838.1991

Peterson, B. W., & Felpel, L. P. (1971). Excitation and inhibition of reticulospinal neurons by vestibular, cortical and cutaneous stimulation. *Brain Res*, 27(2):373-6. PubMed PMID: 5552178

Pilz, P. K., & Schnitzler, H. U. (1996). Habituation and sensitization of the acoustic startle response in rats: amplitude, threshold, and latency measures. *Neurobiol Learn Mem*, 66(1), 67-79. doi:10.1006/nlme.1996.0044

Poulin, J. F., Castonguay-Lebel, Z., Laforest, S., & Drolet, G. (2008). Enkephalin co-expression with classic neurotransmitters in the amygdaloid complex of the rat. *J Comp Neurol*, 506(6), 943-959. doi:10.1002/cne.21587

Prasad, S. E., Howley, S., & Murphy, K. C. (2008). Candidate genes and the behavioral phenotype in 22q11.2 deletion syndrome. *Dev Disabil Res Rev*, 14(1), 26-34. doi:10.1002/ddrr.5

Quicke, P., Barnes, S. J., & Knöpfel, T. (2017). Imaging of Brain Slices with a Genetically Encoded Voltage Indicator. *Methods in molecular biology* (Clifton, N.J.), 1563, 73–84. doi:10.1007/978-1-4939-6810-7_5

Rampon, C., Luppi, P. H., Fort, P., Peyron, C., & Jouvett, M. (1996). Distribution of glycine-immunoreactive cell bodies and fibers in the rat brain. *Neuroscience*, 75(3), 737-755. doi:10.1016/0306-4522(96)00278-3

Reyes, B. A., Carvalho, A. F., Vakharia, K., & Van Bockstaele, E. J. (2011). Amygdalar peptidergic circuits regulating noradrenergic locus coeruleus neurons: linking limbic and arousal centers. *Experimental neurology*, 230(1), 96–105. doi:10.1016/j.expneurol.2011.04.001

Rosen, J. B., & Davis, M. (1988a). Enhancement of acoustic startle by electrical stimulation of the amygdala. *Behav Neurosci*, 102(2), 195-202, 324. doi:10.1037//0735-7044.102.2.195

Rosen, J. B., & Davis, M. (1988b). Temporal characteristics of enhancement of startle by stimulation of the amygdala. *Physiol Behav*, 44(1), 117-123. doi:10.1016/0031-9384(88)90354-x

Rosen, J. B., & Davis, M. (1990). Enhancement of electrically elicited startle by amygdaloid stimulation. *Physiol Behav*, 48(2), 343-349. doi:10.1016/0031-9384(90)90325-x

Rosen, J. B., Hitchcock, J. M., Sananes, C. B., Miserendino, M. J., & Davis, M. (1991). A direct projection from the central nucleus of the amygdala to the acoustic startle pathway: anterograde and retrograde tracing studies. *Behav Neurosci*, 105(6), 817-825. doi:10.1037/0735-7044.105.6.817

Saha, S., Batten, T. F., Henderson, Z. (2000). A GABAergic projection from the central nucleus of the amygdala to the nucleus of the solitary tract: a combined anterograde tracing and electron microscopic immunohistochemical study. *Neuroscience* 99(4):613-26

Sakai, S. T., Davidson, A. G., & Buford, J. A. (2009). Reticulospinal neurons in the pontomedullary reticular formation of the monkey (*Macaca fascicularis*). *Neuroscience*, 163(4), 1158-1170. doi:10.1016/j.neuroscience.2009.07.036

Sananes, C. B., & Davis, M. (1992). N-methyl-D-aspartate lesions of the lateral and basolateral nuclei of the amygdaloid block fear-potentiated startle and shock sensitization of startle. *Behavioral Neuroscience*, 106(1), 72-80. <http://dx.doi.org/10.1037/0735-7044.106.1.72>

Scarborough, J., Mueller, F., Weber-Stadlbauer, U., Richetto, J., & Meyer, U. (2019). Dependency of prepulse inhibition deficits on baseline startle reactivity in a mouse model of the human 22q11.2 microdeletion syndrome. *Genes Brain Behav*, 18(4), e12523. doi:10.1111/gbb.12523

Schauer, C., & Leinders-Zufall, T. (2012). Imaging calcium responses in GFP-tagged neurons of hypothalamic mouse brain slices. *Journal of visualized experiments: JoVE*, (66), e4213. doi:10.3791/4213

Schmajuk, N. A., Larrauri, J. A., Hagenbuch, N., Levin, E. D., Feldon, J., & Yee, B. K. (2006). Startle and prepulse inhibition as a function of background noise: a computational and experimental analysis. *Behav Brain Res*, 170(2), 182-196. doi:10.1016/j.bbr.2006.02.021

Schmid, S., Azzopardi, E., De Jaeger, X., Prado, M. A., & Prado, V. F. (2011). VACHT knock-down mice show normal prepulse inhibition but disrupted long-term habituation. *Genes Brain Behav*, 10(4), 457-464. doi:10.1111/j.1601-183X.2011.00686.x

Schmid, S., Simons, N. S., & Schnitzler, H. U. (2003). Cellular mechanisms of the trigeminally evoked startle response. *Eur J Neurosci*, 17(7), 1438-1444. doi:10.1046/j.1460-9568.2003.02565.x

Scudder, S. L., Baimel, C., Macdonald, E. E., & Carter, A. G. (2018). Hippocampal-Evoked Feedforward Inhibition in the Nucleus Accumbens. *The Journal of neuroscience: the official journal of the Society for Neuroscience*, 38(42), 9091–9104. doi:10.1523/JNEUROSCI.1971-18.2018

Sechenov, I. M. (1965). *Reflexes of the Brain* (Translated by S. Belsky, ed by G. Gibbons) Cambridge, Mass.: The Massachusetts Institute of Technology Press.

Semba, K., Reiner, P. B., & Fibiger, H.C. (1990). Single cholinergic mesopontine tegmental neurons project to both the pontine reticular formation and the thalamus in the rat. *Neuroscience*, 38(3):643-54. PubMed PMID: 2176719

Semba, K., Reiner, P.B., McGeer, E.G., & Fibiger, H.C. (1989). Brainstem projecting neurons in the rat basal forebrain: neurochemical, topographical, and physiological distinctions from cortically projecting cholinergic neurons. *Brain Res Bull*, 2(3):501-9. PubMed PMID: 2469525

Singh, S. M., Castellani, C., & O'Reilly, R. (2010). Autism meets schizophrenia via cadherin pathway. *Schizophr Res*, 116(2-3), 293-294. doi:10.1016/j.schres.2009.09.031

St Andre, J., & Reilly, S. (2007). Effects of central and basolateral amygdala lesions on conditioned taste aversion and latent inhibition. *Behav Neurosci*, 121(1), 90-99. doi:10.1037/0735-7044.121.1.90

Stark, K. L., Xu, B., Bagchi, A., Lai, W. S., Liu, H., Hsu, R., Wan, X., Pavlidis, P., Mills, A. A., Karayiorgou, M., & Gogos, J. A. (2008). Altered brain microRNA biogenesis

contributes to phenotypic deficits in a 22q11-deletion mouse model. *Nat Genet*, 40(6):751-60. doi: 10.1038/ng.138. Epub 2008 May 11. PubMed PMID: 1846981

Stefansson, H., Meyer-Lindenberg, A., Steinberg, S., Magnusdottir, B., Morgen, K., Arnarsdottir, S., Bjornsdottir, G., Walters, G.B., Jonsdottir, G.A., Doyle, O. M., Tost, H., Grimm, O., Kristjansdottir, S., Snorrason, H., Davidsdottir, S. R., Gudmundsson, L. J., Jonsson, G. F., Stefansdottir, B., Helgadottir, I., Haraldsson, M., Jonsdottir, B., Thygesen, J. H., Schwarz, A. J., Didriksen, M., Stensbøl, T. B., Brammer, M., Kapur, S., Halldorsson, J. G., Hjreidarsson, S., Saemundsen, E., Sigurdsson, E., & Stefansson, K. (2014). CNVs conferring risk of autism or schizophrenia affect cognition in controls *Nature*, 505(7483):361-6. doi: 10.1038/nature12818. Epub 2013 Dec 18. PubMed PMID: 24352232

Steidl, S., Faerman, P., Li, L., & Yeomans, J. S. (2004). Kynurenate in the pontine reticular formation inhibits acoustic and trigeminal nucleus-evoked startle, but not vestibular nucleus-evoked startle. *Neuroscience*, 126(1), 127-136. doi:10.1016/j.neuroscience.2004.03.020

Steinkellner, T., Yoo, J. H., & Hnasko, T. S. (2019). Differential Expression of VGLUT2 in Mouse Mesopontine Cholinergic Neurons. *eNeuro*, 6(4). doi:10.1523/ENEURO.0161-19.2019

Stober, G., Ben-Shachar, D., Cardon, M., Falkai, P., Fonteh, A. N., Gawlik, M., & Riederer, P. (2009). Schizophrenia: from the brain to peripheral markers. A consensus paper of the WFSBP task force on biological markers. *World J Biol Psychiatry*, 10(2), 127-155. doi:10.1080/15622970902898980

Strassman, A., Highstein, S. M. & McCrea, R. A. (1986). Anatomy and physiology of saccadic burst neurons in the alert squirrel monkey. II. Inhibitory burst neurons. *J. Comp. Neurol*, 249: 358-380. doi:10.1002/cne.902490304

Swanson, L. W., & Petrovich, G. D. (1998). What is the amygdala? *Trends Neurosci*, 21(8), 323-331. doi:10.1016/s0166-2236(98)01265-x

Swerdlow, N. R. (1993). Sensorimotor gating in Tourette Syndrome. (1993). Tourette Association of America, <https://tourette.org/grant/sensorimotor-gating-in-tourette-syndrome>

Swerdlow, N. R. (2013). Update: studies of prepulse inhibition of startle, with particular relevance to the pathophysiology or treatment of Tourette Syndrome. *Neurosci Biobehav Rev*, 37(6), 1150-1156. doi:10.1016/j.neubiorev.2012.09.002

Swerdlow, N. R., & Geyer, M. A. (1993). Prepulse inhibition of acoustic startle in rats after lesions of the pedunculopontine tegmental nucleus. *Behav Neurosci*, 107(1), 104-117. doi:10.1037//0735-7044.107.1.104

Swerdlow, N. R., & Light, G. A. (2016). Animal Models of Deficient Sensorimotor Gating in Schizophrenia: Are They Still Relevant? *Curr Top Behav Neurosci*, 28, 305-325. doi:10.1007/7854_2015_5012

Swerdlow, N. R., Blumenthal, T. D., Sutherland, A. N., Weber, E., & Talledo, J. A. (2007). Effects of prepulse intensity, duration, and bandwidth on perceived intensity of startling acoustic stimuli. *Biol Psychol*, 74(3), 389-395. doi:10.1016/j.biopsycho.2006.10.001

Swerdlow, N. R., Braff, D. L., & Geyer, M. A. (1990). GABAergic projection from nucleus accumbens to ventral pallidum mediates dopamine-induced sensorimotor gating deficits of acoustic startle in rats. *Brain Res*, 532(1-2):146-50. PubMed PMID: 2282510

Swerdlow, N. R., Braff, D. L., & Geyer, M. A. (1999). Cross-species studies of sensorimotor gating of the startle reflex. *Ann N Y Acad Sci*, 877, 202-216. doi:10.1111/j.1749-6632.1999.tb09269.x

Swerdlow, N. R., Caine, S. B., & Geyer, M. A. (1992). Regionally selective effects of intracerebral dopamine infusion on sensorimotor gating of the startle reflex in rats. *Psychopharmacology (Berl)*, 108(1-2), 189-195. doi:10.1007/bf02245306

Swerdlow, N. R., Geyer, M. A., & Braff, D. L. (2001). Neural circuit regulation of prepulse inhibition of startle in the rat: current knowledge and future challenges. *Psychopharmacology (Berl)*, 156(2-3), 194-215. doi:10.1007/s002130100799

Swerdlow, N. R., Paulsen, J., Braff, D. L., Butters, N., Geyer, M. A., & Swenson, M. R. (1995). Impaired prepulse inhibition of acoustic and tactile startle response in patients with Huntington's disease. *J Neurol Neurosurg Psychiatry*, 58(2), 192-200. doi:10.1136/jnnp.58.2.192

Swietek, B., Gupta, A., Proddutur, A., & Santhakumar, V. (2016). Immunostaining of Biocytin-filled and Processed Sections for Neurochemical Markers. *J Vis Exp*(118). doi:10.3791/54880

Szechtman, H., Ahmari, S. E., Beninger, R. J., Eilam, D., Harvey, B. H., Edemann-Callesen, H., & Winter, C. (2017). Obsessive-compulsive disorder: Insights from animal models. *Neurosci Biobehav Rev*, 76(Pt B), 254-279. doi:10.1016/j.neubiorev.2016.04.019

Tabor, K. M., Smith, T. S., Brown, M., Bergeron, S. A., Briggman, K. L., & Burgess, H. A. (2018). Presynaptic Inhibition Selectively Gates Auditory Transmission to the Brainstem Startle Circuit. *Curr Biol*, 28(16), 2527-2535 e2528. doi:10.1016/j.cub.2018.06.020

Takago, H., Nakamura, Y., & Takahashi, T. (2005). G protein-dependent presynaptic inhibition mediated by AMPA receptors at the calyx of Held. *Proc Natl Acad Sci U S A*, 102(20), 7368-7373. doi:10.1073/pnas.0408514102

Takahashi, M., Inoue, M., Tanimoto, M., Kohashi, T., & Oda, Y. (2017). Short-term desensitization of fast escape behavior associated with suppression of Mauthner cell activity in larval zebrafish. *Neurosci Res*, 121, 29-36. doi:10.1016/j.neures.2017.03.008

Talbot, K., Louneva, N., Cohen, J. W., Kazi, H., Blake, D. J., & Arnold, S. E. (2011). Synaptic dysbindin-1 reductions in schizophrenia occur in an isoform-specific manner indicating their subsynaptic location. *PLoS One*, 6(3), e16886. doi:10.1371/journal.pone.0016886

Tillman, R. M., Stockbridge, M. D., Nacewicz, B. M., Torrisi, S., Fox, A. S., Smith, J. F., & Shackman, A. J. (2018). Intrinsic functional connectivity of the central extended amygdala. *Hum Brain Mapp*, 39(3), 1291-1312. doi:10.1002/hbm.23917

Toresson, H., & Campbell, K. (2001) A role for Gsh1 in the developing striatum and olfactory bulb of Gsh2 mutant mice. *Development*, 28(23):4769-80. PubMed PMID: 11731457.

Tsai, J., & Rosenheck, R. A. (2013). Psychiatric comorbidity among adults with schizophrenia: a latent class analysis. *Psychiatry research*, 210(1), 16–20. doi:10.1016/j.psychres.2013.05.013

Tye, K. M., Prakash, R., Kim, S. Y., Fenno, L. E., Grosenick, L., Zarabi, H., & Deisseroth, K. (2011). Amygdala circuitry mediating reversible and bidirectional control of anxiety. *Nature*, 471(7338), 358-362. doi:10.1038/nature09820

Valentino, R. J., & Van Bockstaele, E. (2008). Convergent regulation of locus coeruleus activity as an adaptive response to stress. *European journal of pharmacology*, 583(2-3), 194–203. doi:10.1016/j.ejphar.2007.11.062

Valsamis, B., & Schmid, S. (2011). Habituation and prepulse inhibition of acoustic startle in rodents. *J Vis Exp*(55), e3446. doi:10.3791/3446

Waldvogel, H. J., Baer, K., Eady, E., Allen, K. L., Gilbert, R. T., Mohler, H., Faull, R. L. (2010). Differential localization of gamma-aminobutyric acid type A and glycine receptor subunits and gephyrin in the human pons, medulla oblongata and uppermost cervical segment of the spinal cord: an immunohistochemical study. *J Comp Neurol*, 518(3), 305-328. doi:10.1002/cne.22212

Wall, N. R., Wickersham, I. R., Cetin, A., De La Parra, M., & Callaway, E. M. (2010). Monosynaptic circuit tracing in vivo through Cre-dependent targeting and complementation of modified rabies virus. *Proceedings of the National Academy of Sciences of the United States of America*, 107(50), 21848–21853. doi:10.1073/pnas.1011756107

Walters, J. T., & Owen, M. J. (2007). Endophenotypes in psychiatric genetics. *Mol Psychiatry*, 12(10), 886-890. doi:10.1038/sj.mp.4002068

Wan, F. J., & Swerdlow, N. R. (1997). The basolateral amygdala regulates sensorimotor gating of acoustic startle in the rat. *Neuroscience*, 76(3), 715-724. doi:10.1016/s0306-4522(96)00218-7

Wang, H. L., & Morales, M. (2009). Pedunculopontine and laterodorsal tegmental nuclei contain distinct populations of cholinergic, glutamatergic and GABAergic neurons in the rat. *Eur J Neurosci*, 29(2), 340-358. doi:10.1111/j.1460-9568.2008.06576.x

Wang, W., Kim, C. K., & Ting, A. Y. (2019). Molecular tools for imaging and recording neuronal activity. *Nat Chem Biol*, 15(2), 101-110. doi:10.1038/s41589-018-0207-0

Watanabe, S., Rost, B. R., Camacho-Pérez, M., Davis, M. W., Söhl-Kielczynski, B., Rosenmund, C., & Jorgensen, E. M. (2013). Ultrafast endocytosis at mouse hippocampal synapses. *Nature*, 504(7479), 242–247. doi:10.1038/nature12809

Weber, M., Schmitt, A., Wischmeyer, E., & Doring, F. (2008). Excitability of pontine startle processing neurones is regulated by the two-pore-domain K⁺ channel TASK-3 coupled to 5-HT_{2C} receptors. *Eur J Neurosci*, 28(5), 931-940. doi:10.1111/j.1460-9568.2008.06400.x

Weber, M., Schnitzler, H. U., & Schmid, S. (2002). Synaptic plasticity in the acoustic startle pathway: the neuronal basis for short-term habituation? *Eur J Neurosci*, 16(7), 1325-1332. doi:10.1046/j.1460-9568.2002.02194.x

Wiegert, J. S., Mahn, M., Prigge, M., Printz, Y., & Yizhar, O. (2017). Silencing Neurons: Tools, Applications, and Experimental Constraints. *Neuron*, 95(3), 504-529. doi:10.1016/j.neuron.2017.06.050

Wilensky, A. E., Schafe, G. E., Kristensen, M. P., & LeDoux, J. E. (2006). Rethinking the fear circuit: the central nucleus of the amygdala is required for the acquisition, consolidation, and expression of Pavlovian fear conditioning. *J Neurosci*, 26(48), 12387-12396. doi:10.1523/JNEUROSCI.4316-06.2006

Wilson, C. J., Groves, P. M., Kitai, S. T., & Linder, J. C. (1983). Three-dimensional structure of dendritic spines in the rat neostriatum. *The Journal of neuroscience: the official journal of the Society for Neuroscience*, 3(2), 383–388. doi:10.1523/JNEUROSCI.03-02-00383.1983

Windrem, M. S., Osipovitch, M., Liu, Z., Bates, J., Chandler-Militello, D., Zou, L., Goldman, S. A. (2017). Human iPSC Glial Mouse Chimeras Reveal Glial Contributions to Schizophrenia. *Cell Stem Cell*, 21(2), 195-208 e196. doi:10.1016/j.stem.2017.06.012

Wu EQ, Shi L, Birnbaum H, Hudson T, & Kessler R. (2006). Annual prevalence of diagnosed schizophrenia in the USA: a claims data analysis approach. *Psychol Med* 36(11), 1535-40. Epub 2006 Aug 15. PubMed PMID: 16907994

Wu, L. G., & Saggau, P. (1997). Presynaptic inhibition of elicited neurotransmitter release. *Trends Neurosci*, 20(5), 204-212. doi:10.1016/s0166-2236(96)01015-6

Wu, M.F., Jenden, D.J., Fairchild, M.D., & Siegel, J.M. (1993). Cholinergic mechanisms in startle and prepulse inhibition: effects of the false cholinergic precursor N-aminodeanol. *Behav Neurosci*, 107(2), 306-16. PubMed PMID: 8097917

Wyszynski, M., Valtschanoff, J. G., Naisbitt, S., Dunah, A. W., Kim, E., Standaert, D. G., Weinberg, R. & Sheng, M. (1999). Association of AMPA receptors with a subset of glutamate receptor-interacting protein in vivo. *The Journal of neuroscience: the official journal of the Society for Neuroscience*, 19(15), 6528–6537. doi:10.1523/JNEUROSCI.19-15-06528.1999

Xiao, C., Cho, J. R., Zhou, C. Y., Treweek, J. B., Chan, K., McKinney, S. L., Yang, B., & Gradinaru, V. (2016). Cholinergic Mesopontine Signals Govern Locomotion and Reward through Dissociable Midbrain Pathways. *Neuron* 90:333-347

Yamasaki, N., Maekawa, M., Kobayashi, K., Kajii, Y., Maeda, J., Soma, M., Miyakawa, T. (2008). Alpha-CaMKII deficiency causes immature dentate gyrus, a novel candidate endophenotype of psychiatric disorders. *Molecular brain*, 1, 6. doi:10.1186/1756-6606-1-6

Yeomans, J. S., & Pollard, B. A. (1993). Amygdala efferents mediating electrically evoked startle-like responses and fear potentiation of acoustic startle. *Behav Neurosci*, 107(4), 596-610. doi:10.1037//0735-7044.107.4.596

Yeomans, J. S., Bosch, D., Alves, N., Daros, A., Ure, R. J., & Schmid, S. (2010). GABA receptors and prepulse inhibition of acoustic startle in mice and rats. *Eur J Neurosci*, 31(11), 2053-2061. doi:10.1111/j.1460-9568.2010.07236.x

Yeomans, J. S., Lee, J., Yeomans, M. H., Steidl, S., & Li, L. (2006). Midbrain pathways for prepulse inhibition and startle activation in rat. *Neuroscience*, 142(4), 921-929. doi:10.1016/j.neuroscience.2006.06.025

Yeomans, J. S., Li, L., Scott, B. W., & Frankland, P. W. (2002). Tactile, acoustic and vestibular systems sum to elicit the startle reflex. *Neurosci Biobehav Rev*, 26(1), 1-11. doi:10.1016/s0149-7634(01)00057-4

Yeung, R. K., Xiang, Z. H., Tsang, S. Y., Li, R., Ho, T. Y. C., Li, Q., Xue, H. (2018). Gabrb2-knockout mice displayed schizophrenia-like and comorbid phenotypes with interneuron-astrocyte-microglia dysregulation. *Transl Psychiatry*, 8(1), 128. doi:10.1038/s41398-018-0176-9

Young, B. J., & Leaton, R. N. (1996). Amygdala central nucleus lesions attenuate acoustic startle stimulus-evoked heart rate changes in rats. *Behav Neurosci*, 110(2), 228-237. doi:10.1037//0735-7044.110.2.228

Zebardast, N., Crowley, M. J., Bloch, M. H., Mayes, L. C., Wyk, B. V., Leckman, J. F., Swain, J. E. (2013). Brain mechanisms for prepulse inhibition in adults with Tourette syndrome: initial findings. *Psychiatry Res*, 214(1), 33-41. doi:10.1016/j.psychresns.2013.05.009

Zeilhofer, H. U., Studler, B., Arabadzisz, D., Schweizer, C., Ahmadi, S., Layh, B., Fritschy, J. M. (2005). Glycinergic neurons expressing enhanced green fluorescent protein in bacterial artificial chromosome transgenic mice. *J Comp Neurol*, 482(2), 123-141. doi:10.1002/cne.20349

Zhang, X., Ge, T. T., Yin, G., Cui, R., Zhao, G., & Yang, W. (2018). Stress-Induced Functional Alterations in Amygdala: Implications for Neuropsychiatric Diseases. *Front Neurosci*, 12, 367. doi:10.3389/fnins.2018.00367

Zhang, Z. J., & Reynolds, G. P. (2002). A selective decrease in the relative density of parvalbumin-immunoreactive neurons in the hippocampus in schizophrenia. *Schizophr Res* 55(1-2):1-10. PubMed PMID: 11955958.

Zucker, R. S., Regehr, W. G. (2002). Short-term synaptic plasticity. *Annu Rev Physiol*, 64:355-405.

Appendix

Recipes and Reagents

10x Tris-Buffered Saline (TBS; 1L)

500ml Autoclaved Milli-Q water

24.2g Tris Base (#T1503-1KG, Sigma Aldrich)

87.6g Sodium chloride (NaCl; #S7653-5KG, Millipore sigma)

pH to 7.5 with Hydrochloric acid (HCl; #H1758-500ML, Sigma Aldrich)

Bring volume up to 1L with autoclaved Milli-Q water

1x TBS (1L)

100ml 10x TBS

900ml Autoclaved Milli-Q water

5x Phosphate-Buffered Saline (PBS; 1L)

500 ml Autoclaved Milli-Q water

40g NaCl

1g Potassium chloride (KCl; #P9333-1KG, Sigma Aldrich)

5.75g Sodium phosphate dibasic dihydrate ($\text{Na}_2\text{HPO}_4 \cdot 2\text{H}_2\text{O}$; #71643-1KG Sigma Aldrich)

1g Potassium phosphate monobasic (KH_2PO_4 ; #795488-1KG, Sigma Aldrich)

Bring volume up to 1L with autoclaved Milli-Q water

1x PBS (1L)

200ml 5x PBS

800ml Autoclaved Milli-Q water

0.9% Saline solution (1L)

9g NaCl

1L Autoclaved Milli-Q water

0.12M PBS for EM (1L)***Solution A***

22.6g Sodium phosphate monobasic monohydrate ($\text{NaH}_2\text{PO}_4 \cdot \text{H}_2\text{O}$; #71507-250G, Sigma Aldrich)

1L DI water

Solution B

25.2g Sodium hydroxide pellets (NaOH; #S399-1, Fischer Scientific)

1L DI water

Sucrose Solution

4g Sucrose (#S7903-5KG; Sigma Aldrich)

100ml DI water

PBS solution

415ml Solution A

85 ml Solution B

50ml Sucrose solution

25g Calcium chloride dihydrate ($\text{CaCl}_2 \cdot 2\text{H}_2\text{O}$; #C5080-1KG, Sigma Aldrich)

1. Mix Solution A and Solution B
2. Remove 50ml of mix

3. Add 50ml of Sucrose solution
4. Add 25g of CaCl₂ for each 100 ml of PBS buffer
5. pH to 7.4 with Solution B
6. Bring volume up to 1L with DI water
7. Store at 4°C

0.06M PBS for EM (1L)

500ml 0.12M PBS

500ml DI water

Karnovsky's fixative modified with 2% Paraformaldehyde (PFA; 50ml)

25ml 1xPBS

10ml 10% Aqueous PFA (#15712, Electron Microscopy Sciences)

5ml 25% Aqueous Glutaraldehyde (#16220, Electron Microscopy Sciences)

Bring volume up to 50ml with DI water

2% Osmium tetroxide (50ml)

25ml 4% Osmium tetroxide (#19170, Electron Microscopy Sciences)

25ml 0.12M PBS

Store at 4°C in glass bottle wrapped in aluminum foil

2% Uranyl acetate for en bloc stain

2g Uranyl acetate (#22400, Electron Microscopy Sciences)

100ml DI water

Store at 4°C in glass bottle wrapped in aluminum foil

2.5% Uranyl acetate for post-fixation stain

2.5g Uranyl acetate

100ml DI water

Store at 4°C in glass bottle wrapped in aluminum foil

Reynold's Lead citrate (50ml)

100ml of dH₂O

1.33g Lead nitrate (#17900, Electron Microscopy Sciences)

1.76g Sodium citrate (#21140, Electron Microscopy Sciences)

8 ml 1N NaOH (#21170-01, Electron Microscopy Sciences)

1. Boil 100 ml of dH₂O to remove dissolved CO₂
2. Cool to RT
3. Add 30ml of CO₂-less water in a volumetric flask
4. Add the 1.33g of Lead nitrate
5. Add the 1.76g of Sodium citrate
6. Shake vigorously for 1min, then every 5min for a 30min period
7. Add the 8ml of 1N NaOH to clear solution
8. Bring volume up to 50ml
9. Store at 4°C in glass bottle

4% PFA solution (1L)

700ml 1X PBS

40g granular PFA (#19210, Electron Microscopy Sciences)

NaOH pellets

Glacial acetic acid (#ARK2183, Sigma Aldrich)

1. Heat PBS to 65°C

2. Add and dissolve the 40g of PFA for 5mins with a magnetic stirrer
3. Add 2 NaOH pellets to completely dissolve PFA
4. pH to 9.5 with NaOH and glacial acetic acid
5. Bring volume up to 1L with 1xPBS
6. Store at 4°C in an aluminum wrapped container

12% sucrose in PFA solution (100ml)

12g of Sucrose

100ml PFA solution

Sodium bicarbonate-buffered glycerol mounting media (1L)

500 ml Autoclaved Milli-Q water

8.4 g Sodium bicarbonate (#S5761-1KG, Sigma Aldrich)

500 ml Glycerol (#BP229-1, Fisher Scientific)

pH to 8.62

Cryoprotectant (4L)

Solution A

82.8g Sodium phosphate dibasic dihydrate

2L Autoclaved Milli-Q water

Bring volume up to 3L with Autoclaved Milli-Q water

Solution B

99.4g Sodium phosphate monobasic monohydrate

2L Autoclaved Milli-Q water

Bring volume up to 3L with Autoclaved Milli-Q water

Solution C

440ml Solution A

3.2L of Solution B

pH to 7.4

Final solution

1L Autoclaved Milli-Q water

1L Solution C

1.2L Ethylene glycol (#324558-1L, Sigma Aldrich)

800ml Glycerol

Test solution in a petri dish at -20°C (solution must remain liquid)

Subbing Solution to gel-coat glass slides (1L)

750ml Autoclaved Milli-Q water

10g Gelatin (Knor)

1g Chromium (III) potassium sulfate dodecahydrate (#60151-500G, Sigma Aldrich)

1. Heat water and regulate to 40°C
2. Slowly add the 10g of gelatin
3. Stir until dissolved
4. Add the 1g of chromium potassium sulfate dodecahydrate
5. Bring volume up to 1L
6. Filter and maintain at 40°C

Gel coating

1. Place glass slides on metal racks
2. Clean glass slides with running DI water for 5mins
3. Blot and air-dry glass slides
4. Once completely dry, place metal racks inside the subbing solution at 40°C for 4min
5. Remove metal racks from subbing solution
6. Blot excess and place on underpad with plastic lining for drying
7. Place racks in a container with an underpad in a 37°C oven for 24 hours

Thionin acetate for Nissl stain (1L)

800ml Autoclaved Milli-Q water

11ml Glacial acetic acid

2g of NaOH pellets

5g Thionin acetate (#229840050, Acros Organics, Fisher Scientific)

1. Add the 11ml of glacial acetic acid to water
2. Add and dissolve the 2g of NaOH pellets
3. pH to 4.5
4. Heat up solution until steaming while stirring
5. Turn off heat
6. Add and dissolve the 5g of thionin acetate for 30min
7. Filter solution
8. Store solution at 60°C in glass bottle wrapped with aluminum-foiled
9. Filter before use

Blocking solution for immunohistochemistry (50ml)

48.5ml 1xTBS

1ml Normal Donkey Serum (#D9663, Sigma Aldrich)

50µl Triton X-100 (#T8787-50ML, Sigma Aldrich)

1.25% FluoroGold

3.125mg FluoroGold (#H22845, Invitrogen, ThermoFisher Scientific)

250µl 0.9% Saline solution

Sonicate, if necessary

Store at -20°C

Dissection stock solution (1L)

700ml Autoclaved Milli-Q water

2.922g NaCl

333.743g Sucrose

0.69g NaH₂PO₄

0.932g KCl

1. While stirring, add and completely dissolve the 2.922g of NaCl
2. Slowly add 100g of sucrose at a time while solution is being stirred
3. Add the 0.69g of NaH₂PO₄ and the 0.932g of KCl
4. Bring volume up to 1L with Autoclaved Milli-Q water
5. Store at 4°C

Recording stock solution (2L)

1400ml Autoclaved Milli-Q water

289.862g NaCl

5.52g NaH_2PO_4

7.45g KCl

1. While stirring, slowly add 100g of NaCl at a time while solution is being stirred
2. Add the 5.52g of NaH_2PO_4 and the 7.45g of KCl
3. Bring volume up to 2L with Autoclaved Milli-Q water
4. Store at 4°C

1M Calcium Chloride solution (250ml)

100ml Autoclaved Milli-Q water

29.4g CaCl_2

Bring volume up to 200ml with autoclaved Milli-Q water

Store at 4°C

1M Magnesium Sulfate Solution (250ml)

50ml of Autoclaved Milli-Q water

24.648g Magnesium sulfate heptahydrate ($\text{MgSO}_4 \cdot 7\text{H}_2\text{O}$; #63138-1KG, Sigma Aldrich)

Bring volume up to 100ml with autoclaved Milli-Q water

Store at 4°C

Glucose Solution (1L)

800ml Autoclaved Milli-Q water

72.08g D-Glucose (#G8270-1KG, Sigma Aldrich)

Bring volume up to 1L with autoclaved Milli-Q water

Store at 4°C

Dissection solution for extracellular field recordings (1L)

600ml Autoclaved Milli-Q water

200ml Dissection stock solution

25ml Glucose solution

2.1g Sodium bicarbonate

4ml 1M MgSO_4 solution

0.5ml 1M CaCl_2 solution

1. Pour 600ml Autoclaved Milli-Q water in a 1L graduated cylinder
2. Mix the Dissection stock solution and Glucose solution in a separate cylinder
3. While stirring, add the Dissection stock and Glucose solutions to the 600ml of water
4. Add the 2.1g of Sodium bicarbonate
5. Add the 4ml of MgSO_4 solution and the 0.5ml of CaCl_2 solution
6. Bring volume up to 1L with autoclaved Milli-Q water
7. Bubble with 95% O_2 /5% CO_2 for 5min
8. Store at 4°C

Recording solution for extracellular field recordings (aCSF; 2L)

1700ml Autoclaved Milli-Q water

100ml Dissection stock solution

50ml Glucose solution

4.2g Sodium bicarbonate

2ml 1M MgSO_4 solution

4ml 1M CaCl_2 solution

1. Pour 1700ml Autoclaved Milli-Q water in a 2L graduated cylinder
2. Mix the Recording stock solution and Glucose solution in a separate cylinder

3. While stirring, add the Recording stock and Glucose solutions to the 1700ml of water
4. Add the 4.2g of Sodium bicarbonate
5. Add the 2ml of MgSO_4 solution
6. Add the 4ml of CaCl_2 solution
7. Bring volume up to 2L with autoclaved Milli-Q water
8. Bubble with 95% O_2 /5% CO_2 for 5min

Dissection solution for whole-cell recordings (1L)

600ml Autoclaved Milli-Q water

71.89g Sucrose

2.18g Sodium bicarbonate

190mg Magnesium chloride (#M8266-100G, Sigma-Aldrich)

160mg Potassium phosphate monobasic (#795488-1KG, Sigma-Aldrich)

150mg Potassium chloride

1.8g Glucose

540mg Myo-inositol (#J60828, Alfa Aesar)

220mg Sodium pyruvate (#A11148, Alfa Aesar)

70mg Ascorbic acid (#A4544-25G, Sigma-Aldrich)

1. Pour 600ml Autoclaved Milli-Q water in a 1L graduated cylinder
2. Add and dissolve compounds one at a time (do not add the CaCl_2)
3. Bring volume up to 1L with autoclaved Milli-Q water
4. Bubble with 95% O_2 /5% CO_2 for 30mins
5. Measure pH
6. If pH is 7.3-7.4, add CaCl_2
7. Store at 4°C

Recording solution for whole-cell recordings (aCSF; 1L)

1700ml Autoclaved Milli-Q water

100ml Dissection stock solution

50ml Glucose solution

4.2g Sodium bicarbonate

2ml 1M MgSO₄ solution

80μl 1M CaCl₂ solution

1840μl 1M CaCl₂ solution

1. Pour 1700ml Autoclaved Milli-Q water in a 2L graduated cylinder
2. Mix the Recording stock solution and Glucose solution in a separate cylinder
3. While stirring, add the Recording stock and Glucose solutions to the 1700ml of water
4. Add the 2.1g of Sodium bicarbonate
5. Add the 2ml of MgSO₄ solution
6. Bring volume up to 2L with autoclaved Milli-Q water
7. Bubble with 95%O₂/5%CO₂ for 30mins
8. If pH is 7.3-7.4, pour 80ml in a 100ml beaker of the recording solution
9. Add 80μl of CaCl₂ solution to the beaker with 80ml of recording solution
10. Add 1840μl of CaCl₂ solution to the container with 920ml of recording solution

50μM AP5 solution

50mg DL-AP5 sodium salt (#3693, Tocris, Biotechnne)

4564μl Autoclaved Milli-Q water

1. Dissolve the 50 mg of D-AP5 with the 4564μl of water (50mM AP5)
2. Prepare 100μl aliquots of 50mM AP5 solution
3. Store at -20°C

4. When ready to use, thaw and add a 100µl aliquot to 200ml of aCSF

25µM CNQX solution

50mg CNQX disodium salt (#1045, Tocris, Biotechne)

3622µl Autoclaved Milli-Q water

1. Dissolve the 50 mg of CNQX disodium salt with the 3622µl of water (50mM CNQX)
2. Prepare 100µl aliquots of 50mM CNQX solution
3. Store at -20°C
4. When ready to use, thaw and add a 100µl aliquot to 200ml of aCSF

25µM DNQX solution

50mg DNQX disodium salt (#2312, Tocris, Biotechne)

3377µl Autoclaved Milli-Q water

5. Dissolve the 50 mg of DNQX disodium salt with the 1689µl of water (50mM DNQX)
6. Prepare 100µl aliquots of 50mM DNQX solution
7. Store at -20°C
8. When ready to use, thaw and add a 100µl aliquot to 200ml of aCSF

10µM Gabazine solution

50mg Gabazine (or SR95531, #ab120042, abcam)

5431µl Dimethyl sulfoxide (DMSO, #D8418-100ML, Sigma-Aldrich)

1. Dissolve the 50 mg of Gabazine with the 5.43ml of DMSO (25mM Gabazine)
2. Prepare 100µl aliquots of 25mM Gabazine solution
3. Store at -20°C
4. When ready to use, thaw and add a 100µl aliquot to 250ml of aCSF

Flunixin (analgesic; 2.5mg/kg)

100µl Flunixin meglumine (50mg/ml; Norbrook)

9900µl 0.9% Saline solution

1. Store at -20°C
2. After surgery, inject 0.125ml subcutaneously

Gentamicin (antibiotic; 2-4mg/kg)

50µl Gentamicin sulfate solution (100mg/ml; NDC 50989-318-12, Vedco)

9950µl 0.9% Saline solution

1. Store at -20°C
2. After surgery, inject 0.1ml subcutaneously

Internal solution for whole-cell recordings***V-clamp/I-clamp***

50ml Autoclaved Milli-Q water

0.83875g Potassium methanesulfonate (125mM KMeSO₄; #83000-25G-F, Sigma Aldrich)

0.03728g KCl (10mM)

0.11915g HEPES (10mM; #H4034-500G, Sigma Aldrich)*

0.01169g NaCl (4mM)*

0.0019g EGTA (0.1mM; #06522-500ML, Sigma Aldrich)*

0.10144g Adenosine 5'-triphosphate magnesium (4mM MgATP; #A9187-1G, Sigma Aldrich)*

0.00785g Adenosine 5'-triphosphate sodium (0.3mM Na₂ATP; #A2383-1G, Sigma Aldrich)*

0.12755g Phosphocreatine disodium salt hydrate (10mM; #P7936-1G, Sigma Aldrich)

0.05g Biocytin (0.1%; # B1758-250MG, Sigma Aldrich)

pH: 7.2 (adjust it with 1M KOH solution)

Osmolarity: 285-300MΩ

Prepare 1ml aliquots

Store at -20°C

**Since the amount used of these reagents was too small to be measured precisely, concentrated solutions to be used in internal solution preparation were made as follows.*

MgATP

1g MgATP

19.7ml Autoclaved Milli-Q water

Use 2ml to make 50ml of internal solution

HEPES

2.38g HEPES

10ml Autoclaved Milli-Q water

Prepare 500μl aliquots

Use 500μl to make 50ml of internal solution

NaCl

5.84g NaCl

100ml Autoclaved Milli-Q water

Prepare 200μl aliquots

Use 200μl to make 50ml of internal solution

EGTA

3.804g EGTA

100ml Autoclaved Milli-Q water

Use 300µl to make 50ml of internal solution

Na₂GTP

0.25g Na₂GTP

9.55ml Autoclaved Milli-Q water

Prepare 200µl aliquots

Use 200µl to make 50ml of internal solution

1M KOH (to pH internal solution to 7.2)

2.8g Potassium hydroxide (KOH; #484016-1KG, Sigma Aldrich)

50ml Autoclaved Milli-Q water

Agarose Salt Bridges***3M KCl solution***

44.73g KCl

200ml Autoclaved Milli-Q water

Store at 4°C

3% Agarose in KCl solution

3g Agarose

100ml 3M KCl solution

Warm 3M KCl solution

Add agarose while stirring

Bridge preparation

Keep agarose solution warm while preparing bridges

Fill capillary glass tubes with agarose solution

Use a Bunsen burner to bend capillary glass tubes in to an “L” shape about 1/3 from one end

Store bridges in 3M KCl solution at 4°C

DPX Mountant for histology (#06522-500ML, Sigma Aldrich)

EMbed-812 embedding media kit (#14121, Electron Microscopy Sciences)

Ethanol, histological grade (A405P-4, Fisher Scientific)

Isoflurane, USP (Isosol, Vedco; IsoFlo, Zoetis)

Hexanes (#H292-500, Fisher Scientific)

Xylenes (#534056-4L, Sigma Aldrich)

Vita

Jose Carlos Cano Rodriguez graduated with a Bachelor of Science in Biomedical Sciences and a minor in Chemistry from The University of Texas at El Paso (UTEP) in May of 2010. During his undergraduate studies, Jose investigated the ultrastructural effects of alcohol in hepatic mouse tissue under the mentorship of Dr. Joanne T. Ellzey. Jose then worked as research assistant in the Analytical Cytology Core Facility of Dr. Ellzey (2012-2014) using transmission electron microscopy (TEM) techniques to image biological and inorganic samples at high resolution. In 2014, Jose started his Ph.D. in Biological Sciences with a focus in Neuroscience at UTEP in the laboratory of Dr. Karine Fenelon. For his dissertation research project, Jose investigated the neural bases of a novel substrate involved in a pre-attentive processing mechanism. Under the mentorship of Dr. Fenelon, Jose then attended UMass Amherst (2018-2019) to acquire further technical skills and complete his dissertation research project. Jose was the inaugural recipient of the Ellzey Scholars Research Fellowship (August 2014-August 2016), the Dodson Research Grant (Fall 2016), and is the first UTEP student to receive the NIH Blueprint Diversity Specialized Predoctoral to Postdoctoral Advancement in Neuroscience (D-SPAN) Award (F99/K00; 2018-2024). At UTEP, Jose taught undergraduate laboratory courses of Anatomy and Physiology, Topics in Study of Life, Organismal Biology and a graduate/undergraduate laboratory course on TEM techniques. The dissertation research project of Jose yielded two publications (one under journal review and a second one in preparation). Jose also collaborated in a research project that yielded one publication. In April of 2020, Jose will start a post-doctoral training in the laboratory of Dr. Steven Goldman at the University of Rochester Medical Center, Rochester, NY.

Permanent address: 2317 Tierra Sol, El Paso, TX 79938

This dissertation was written by Jose Carlos Cano Rodriguez